Frequency Response Analysis of Heat and Mass Transfer in Adsorbent Composites and Simplified Performance Estimation for Heat Transformation Applications

Vom Promotionsausschuss der
Technischen Universität Hamburg

zur Erlangung des akademischen Grades

Doktor-Ingenieur (Dr.-Ing.)

genehmigte Dissertation

von
Eric Laurenz

aus
Coesfeld

2021

https://doi.org/10.15480/882.3836

https://orcid.org/0000-0002-9805-620X

Creative Commons License Agreement

The text is licensed under the Creative Commons Attribution 4.0 (CC BY 4.0) license unless otherwise noted. This means that it may be reproduced, distributed and made publicly available, including commercially, provided that the author, the source of the text and the above license are always mentioned. The exact wording of the license can be found at https://creativecommons.org/licenses/by/4.0/.

Gutachter:

1. Prof. Dr.-Ing. Gerhard Schmitz

2. Prof. Dr. Roger Gläser

Vorsitzender des Prüfungsausschusses:

Prof. Dr.-Ing. Alfons Kather

Tag der mündlichen Prüfung: 8. Oktober 2021

Acknowledgements

I would like to express my deepest appreciation to Prof. Dr.-Ing. Gerhard Schmitz for his willingness to supervise this work academically and for his continuous support. He awakened my fascination for thermodynamics and its applications many years ago. I thank Prof. Dr. Roger Gläser for his role as second referee and for his valuable confirmation of my adsorption and mass transfer related results.

This thesis was written at the Department of Heating and Cooling Technologies at Fraunhofer ISE in Freiburg. I am extremely grateful to Dr.-Ing. Lena Schnabel and especially Dr. Gerrit Füldner for their constant and appreciative support with a profound belief in my work. I had the great chance to build up on many years of their practical experience and deep scientific knowledge in the field of adsorption dynamics, which allowed me to learn so much and eventually enabled me to go one little step further with the frequency response. Moreover, thanks to them, I was able to access great hardware resources and enjoy a wonderful open and collegial atmosphere in the department.

A scholarship from the Heinrich Böll Foundation supported me financially during this time and provided me with intellectual input far beyond the boundaries of the technical sciences through an inspiring accompanying programme. Most of the lab work was funded by the Fraunhofer Zukunftsstiftung as part of the "Harvest" project.

I would like to thank Dr. Andreas Velte for collaborating on the kinetics test setup, for the many stimulating discussions on adsorption dynamics, the simulations in the time domain and regular reasons to celebrate. My thanks go to Dr. Harry Kummer for the invaluable contribution to sample preparation, the measurement of particle size distributions and his extensive knowledge in MOF chemistry. Georg Hagelstein and Philipp Hügenell supported the work by performing "strange" DSC and adsorption measurements with great patience. Without the highly accurate and reliable design and assembly work of Paolo Di Lauro and Hannes Seifarth and the miraculous abilities in electrical debugging of Daniel Sonnekalb, FRA measurements would never have happened. In addition, many large and small inspiring conversations about the energy balance of adsorption or the politics of the global energy transition have enjoyably accompanied this work. Among the many people throughout the department, I would especially like to thank my office colleagues Dr.-Ing. Ursula Wittstatt, Dr.-Ing. Constanze Bongs and Dr.-Ing. Katharina Morawietz for this.

Thanks also goes to Michael Schubert, Max Fuchs, Harsono, Florian Tönnies, Raffael Wolff, Sri Polimetla and many other scientific assistants for their helpful practical contributions to this work.

I would like to extend my sincere thanks to the consortium of the project "Wassermod2" in the German-Greek Research and Innovation Programme (BMBF) for the discussions of the mass transfer results and passionate excursions into the world of diffusion, especially Takis Kolokathis for disentangling the structural data of Alfum. I would like to thank Yuri Aristov and his working group at the BIC in Novosibirsk for the great hospitality and the brief insight into their extraordinary work as well as the provision of “salt in porous matrix” samples. Unfortunately, salt hydrates have (yet) successfully resisted an investigation with the FRA and, despite intensive preliminary work, ultimately did not find their way into this work.

Last but not least, my thanks go to my parents, who have given me a lot of important things for life and have always supported me, and especially to my wife Jennyfer and my three boys Jonathan, Leo and Jaron. You have endured a lot and reminded me with incredible energy of the really important things in life.

Summary

Adsorption chillers, heat pumps and storages offer solutions for the valorisation of waste or solar heat for cooling and heating demands and for thermal energy storage. While these adsorption heat transformation (AHT) applications are environmentally friendly and are potentially important in a sustainable energy system, they currently maintain a niche status in the market due to costly and bulky appliances. A mayor issue to be addressed, in order to overcome this status, is the improvement of the core component, the adsorption heat exchanger (Ad-HX) by process intensification. This process is governed by adsorption dynamics: the interaction of heat and mass transfer (HMT) resistances, sorption equilibria, sorption enthalpies and heat capacities.

In this work, the frequency response analysis (FRA) is applied to quantitatively investigate the governing heat and mass transfer mechanisms for 30–60 °C in aluminium fumarate coatings of 140–610 µm thickness. This metal–organic framework has attracted recent interest for AHT due to its exceptional water adsorption properties for low temperature driven applications and potentially low production costs. For the FRA, realised in a custom built setup, a coating sample is placed in a small chamber whose volume is changed sinusoidally, while the pressure and the sample surface temperature is measured. The evolution of this response over the excitation frequency is compared to specifically derived models.

Based on a model with discretised heat transfer and linear driving force (LDF)-simplified micropore diffusion, the thermal conductivity of the samples was identified as about 0.07 W/(m K), and the LDF time constant between 0.1 and 3 s^{-1} at 40 °C with a U-shaped loading dependency and an Arrhenius-type temperature dependency. Macropore diffusion and the thermal coating–support contact are not limiting. Additionally, manometric uptake measurements and – to derive the adsorption enthalpy with a novel approach – small isothermal and isochoric state changes are carried out in the same apparatus. The isotherm confirms the step-like form known for aluminium fumarate with a temperature dependent inflection point at $p_{\mathrm{rel}} \approx 0.25$, 0.28 and 0.33 for 30, 40 and 60 °C. The calculated differential enthalpy of adsorption is found to be 2.90 ± 0.05 MJ/kg (52.2 ± 1.0 kJ/mol) on average, which is about 10–15% higher than expected by a simple Dubinin approximation, with no significant loading or temperature dependency. The loading dependent specific heat capacity of the coating is measured by DSC, revealing values for the dry coating of 1.1–1.2 kJ/(kg K) between 30 and 90 °C and a concave loading dependency, which deviates from the common approximation (assuming the c_p of pure water for the adsorbate) by up to 20%.

The parametrised model is successfully validated by comparing a measured large temperature jump experiment to the results from a non-linear simulation informed solely by these parameters obtained from the new FR-based method.

The concept of effective thermal resistances is introduced and further extended to directly interpret the obtained transfer parameters in terms of their relevance for AHT applications and for rough estimates of principle performance indicators. This analysis shows that for thinner coatings the mass transfer, and for thicker coatings the heat transfer is limiting, with overall effective thermal resistances of 1–4 (m^2 K)/kW. This reflects an improvement of about one order of magnitude compared to values reported for a state-of-the-art silica-gel granular bed. Based on a heat exchanger design case study, the expected specific cooling power on heat exchanger level is in the range of 0.2–0.7 kW/l with a coefficient of performance between 0.54 and 0.67, for typical boundary conditions of a data centre cooling application.

Table of Content

List of Figures

List of Tables

Nomenclature

List of Abbreviations

Ad-HX	Adsorption heat exchanger
AHT	Adsorption heat transformation
Alfum	Aluminium fumarate
CAS	Computer algebra system
CNRS	Centre national de la recherche scientifique
cont	continued
COP	Coefficient of performance
CPU	Central processor unit
DA	Dubinin–Astakhov
DAQ	Data acquisition
DR	Dubinin–Radushkevich
DSC	Differential scanning calorimetry
EOS	Equation of state
FEM	Finite element method
FFT	Fast Fourier transformation
FR	Frequency response
FRA	Frequency response analysis
GUM	Guide to the expression of uncertainty in measurement (JCGM, 2008)
HMT	Heat and mass transfer
HT	Heat transfer
HTF	Heat transfer fluid
HX	Heat exchanger
IAPWS	International Association of the Properties of Water and Steam
IR	Infrared
LDF	Linear driving force
LIMSI	Laboratoire d'informatique pour la mécanique et les sciences de l'ingénieur
LPF	Low-pass filter
LPJ	Large pressure jump
LTJ	Large temperature jump
LVDT	Linear variable differential transformer
maD	Macropore diffusion

miD	Micropore diffusion
MOF	Metal–organic framework
MSCP	Mass specific cooling power
NETD	Noise equivalent temperature difference
ODE	Ordinary differential equation
PDE	Partial differential equation
PFG-NMR	Pulsed field gradient nuclear magnetic resonance
PI	Parameter identification
RMSD	Root mean square deviation
SCP	Specific cooling power
SPJ	Small pressure jump
TFR	Thermal frequency response
TG	Thermogravimetry
VSCP	Volume specific cooling power
VSFR	Volume swing frequency response

List of Symbols

A	Surface area (m^2), adsorption potential (J/kg$_\mathrm{a}$), Amplitude (any unit)
Bi	Biot number (-)
C	Heat capacity (J/K)
c	Concentration (mol/m^3)
COP	Coefficient of performance (for cooling, unless otherwise specified) (-)
c_p	Specific heat capacity (J/(kg K))
D	Diffusivity (m^2/s)
d	Layer thickness, diameter (m)
E	Error functional, weighted root mean squared difference (-)
E_a	Activation energy (J/mol)
F	F-distribution (-)
f	Frequency (Hz), arbitrary function (any unit)
g	Specific Gibb’s free energy (J/kg)
G_{pV}	Complex pressure volume transfer function (Pa/m^3)
G_{TV}	Complex temperature volume transfer function (K/m^3)
G_{TX}	Complex temperature loading transfer function (K/(kg/kg))
G_{XV}	Complex loading volume transfer function ((kg/kg)/m^3)

h	Heat transfer coefficient (W/(m^{2}K)), specific enthalpy (J/kg)
H	Enthalpy (J)
Δh_s	Differential adsorption enthalpy (J/kg$_\mathrm{a}$)
$\boldsymbol{I}$	Identity matrix (-)
j	Imaginary unit (-)
$\boldsymbol{k}$	Vector of individual measurands over all frequencies (any unit)
k	Kinetic coefficient (1/s)
K_c	Slope of the isotherm per concentration ((kg/kg)/(mol/m^3))
Kn	Knudsen number (-)
K_p	Slope of the isotherm per pressure ((kg/kg)/Pa)
K_T	Slope of the isobar ((kg/kg)/K)
M	Molar mass (kg/mol)
m	Mass (kg)
$\dot{m}$	Mass flow (kg/s)
N	Number of observations (-)
n	Amount of substance (mol), number (-)
$\dot{n}$	Molar flux (mol/(m^2 s))
p	Pressure (Pa)
$\boldsymbol{P}$	Vector of identified parameters (any unit)
$\dot{q}$	Heat flux (W/m^2)
Q	Amount of heat (J)
R	Universal gas constant (J/(mol K)), thermal resistance (K/kW)
r	Radius (m)
R^A	Effective thermal resistance related to area ((m^2 K)/kW)
R^m	Effective thermal resistance related to mass ((kg K)/kW)
R^V	Effective thermal resistance related to volume ((m^3 K)/kW)
R_w	Specific gas constant of water (J/(kg K))
S	Entropy (J/K)
s	Laplace variable (1/s), specific entropy (J/(kg K))
Sh	Sherwood number (-)
T	Temperature (K)
t	Time (s)
U	Overall heat transfer coefficient (W/(m^{2}K))
$u(y)$	Measurement uncertainty of quantity y (same unit as y)
V	Volume (m^3)

v	Specific volume (m^3/kg)
$\boldsymbol{W}$	Weighing matrix (any unit)
W	Specific volume of the adsorbed phase (m^3/kg)
w_{vrt}	Virtual work (J)
X	Loading ($\mathrm{kg_a}/\mathrm{kg_s}$)
$\dot{X}$	Temporal loading change ($\mathrm{kg_a}/(\mathrm{kg_s}\ \mathrm{s})$)
x	Space variable (m), arbitrary quantity (any unit)
X_{eff}	Effective loading ($\mathrm{kg_a}/\mathrm{kg_{cmp,dry}}$)
$\boldsymbol{y}$	Vector of all measurands per frequency (any unit)
y	Arbitrary quantity (any unit)
z	Reference quantity (any unit)
α	Model coefficient: $\alpha = K_p \rho_{\mathrm{eff}} R_{\mathrm{w}} T_0 / \varepsilon_{\mathrm{P}}$ (-)
β	Model coefficient: $\beta = \left(Ah + c_p m_{\mathrm{s}} s\right) / \Delta h_s K_T m_s$ (1/s)
Γ	Thermodynamic factor (-)
γ	Model coefficient: $\gamma = 1 + s/k_{\mathrm{LDF}}$ (-), LDF form factor: $\gamma = \sigma(\sigma + 2)$ (-)
ε_{P}	Marco porosity ($\mathrm{m}^3/\mathrm{m}^3$)
η	Dynamic viscosity (Pa s)
ϑ	Temperature (alternative symbol) (K)
λ	Thermal conductivity (W/(m K))
λ_{MFP}	Molecular mean free path (m)
μ	Tortuosity (-)
ρ	Density (kg/m^3)
σ	Measurement uncertainty (any unit), curvature factor (slab/flat plate: 1, cylinder: 2, sphere: 3)
τ	Time constant (s)
ϕ	Phase shift (rad)
χ	Loading (alternative symbol) ($\mathrm{kg_a}/\mathrm{kg_s}$)
ψ	Empty chamber pressure correction factor (-)
ω	Angular velocity (rad/s)

List of Indices and Superscripts

$\tilde{}$	Laplace transformed of the deviation from the temporal mean value
$\hat{}$	Amplitude, deviation from the temporal mean, best estimate
$\bar{}$	Spatial mean value, differential adsorbed state (c.f. Section 2.1.2)

′	Saturated liquid, first derivative of a function of a single variable
″	Saturated vapour
0	Temporal mean value
a	Adsorbate
ad	Adsorbate diffusion
AdHX	Adsorption heat exchanger
b	(Surface) Barrier resistance
blw	Bellow (modulates the measuring chamber volume)
bnd	Binder
btm	Bottom of the composite (at the interface to the sample support)
C	Carnot
cal	At calibration conditions, blank measurement
ch	(Measuring) chamber, characteristic
cldPlt	Cold plate
cmp	Composite
cor	Corrected
ct	Coating
D	Dosing chamber
drv	Driving difference
e	Evaporator
EC	Evaporator/condenser
eff	Effective
eq	At equilibrium
err	Error
exp	Experimental
f	Per Frequency
g	Gas
H	High level
HT	Heat transfer, heat transformation cycle
HX	Heat exchanger
init	Initial conditions
Kn	Knudsen (diffusion)
L	Low level, liquid
LDF	Linear driving force
lft	Lift

M	Medium level, measuring chamber
m	Intermediate
maD	Macropore diffusion
mat	Material level (in contrast to heat exchanger or appliance level)
max	Maximal, maximum
mi, miD	Micropore (diffusion)
min	Minimal, minimum
MKS	Related to the capacitive pressure sensor MKS Baratron 627B
msr	Measured
MT	Mass transfer
p	Parameter
rel	Relative
s	(Ad)sorbent, (ad)sorption
s+a	Combined property of the adsorbent–adsorbate system
sat	At saturation condition (liquid-vapour equilibrium)
smpSrf	Sample surface
srf	Surface of the composite/sample
STS	Related to the piezo-resistive pressure sensor STS ATM
thr	Thrust
v	Vaporisation
vis	Viscous (flow)
w	Water
σ	Surface excess quantity

1. Introduction

Cooling for goods and buildings is a pre-requisite for the satisfaction of many basic human needs. However, it is strongly coupled with primary energy consumptions and greenhouse gas emissions, and thus an important driver of global warming. At the same time, increasing global temperatures and thriving economies in hot regions of the earth are expected to drastically increase cooling demand in the coming decades (IEA, 2018).

Especially in low and middle income countries, refrigeration for food and medical products as well as air conditioning for improved productivity are basics for development. Meeting this demand, while mitigating climate change, requires alternatives to the pathway of fossil-fuel-based industrialisation. While these questions are political and global-economic in principle, innovative technology can contribute significantly.

Adsorption chillers and heat pumps are among those technological parts of the solutions. They allow for the environmentally friendly valorisation of waste or solar heat for cooling demands, avoiding problematic refrigerants or pressure on the electrical grid. The working principle allows a simple, robust and scalable design: The affinity of solid adsorbents to a refrigerant, like water, is used to provide the required low pressure to a cold-producing evaporator – replacing the suction side of a mechanical vapour compressor. After saturation, the adsorbent is regenerated by applying heat, while the refrigerant is conducted with the required high pressure to a condenser – replacing the pressure side of the compressor.

The same principle may be employed for thermally driven heat pumps and thermal energy storage (Pinheiro *et al.*, 2020). Adsorption chillers and heat pumps have been applied successfully for different applications like solar thermal cooling of buildings (Meunier, 2013), gas adsorption heat pumps (Metcalf *et al.*, 2012; Wittstadt *et al.*, 2017) and more (Wang *et al.*, 2010; Pang *et al.*, 2013). All these applications are summarized as adsorption heat transformation (AHT). (IEA, 2012)

1.1 Motivation

Despite the important role AHT can play in a sustainable energy system, the technology suffers from a low level of development and has currently a niche status (Stryi-Hipp & Dias, 2014). The fundamental motivation for this PhD project is derived from the resulting research needs. Further development aims at safe and cost-effective operation.

In order to overcome this niche status of the state-of-the-art technologies, the cost and size of appliances need to be reduced, while keeping stability and efficiency high. Activities targeting theses aspects include improving materials, heat exchangers, appliance designs and control strategies (Teng *et al.*, 2016).

The improvement of the core component, the adsorbent covered adsorption heat exchanger (Ad-HX), has been identified as mayor issue to be addressed by process intensification in order to reduce size, weight and cost (Aristov, 2017a). This process is governed in large parts by adsorption dynamics: the interaction of heat and mass transfer (HMT), sorption equilibria, sorption enthalpies and heat capacities in adsorbent composites. This interaction is marked by a strong and non-linear coupling between heat and mass transfer, which make adsorption dynamics – simply speaking – being somewhat complicated. This might be a primary reason why Ad-HX are often found to be designed using an experimental trial-and-error approach instead of a targeted design and optimization method, as deplored by several authors recently (Pinheiro *et al.*, 2018; Aristov, 2020; Graf *et al.*, 2020). Pinheiro *et al.* (2018) focus on the process of selecting and interpreting simulation parameters for a given Ad-HX model using design of experiment and response surface methodology, in order to reduce the number of simulations required for a given optimisation task. However, actual experimental assessments of the adsorption dynamics are not taken into account, thus, the elaborated statistical methods stand on a weakly validated basis. In contrast to this, Graf *et al.* (2016; 2020) suggest using small-scale experiments to calibrate a transient adsorption dynamic model, which then is used to predict the performance of a full-scale Ad-HX. A similar approach has been developed at Fraunhofer ISE (Schnabel *et al.*, 2018). However, these approaches have two shortcomings, which this work is addressing:

- The dependency on the thermodynamic state of the fitted adsorption dynamics can – if at all – be resolved only very coarsely. Due to its principle design, the experimental method applied, the large temperature jump (LTJ), struggles with clearing up this dependency on temperature, pressure and refrigerant-loading of the adsorbent. Moreover, the method requires fitting non-linear transient models in the time domain through numerical solutions, demanding time-consuming implementations and computations.
- The performance prediction for an Ad-HX requires transient, non-linear and often space discretised models to be solved, which is a time consuming and error-prone task.

The frequency response analysis (FRA), a proven method for the analysis of various mass transport phenomena in adsorbents, is based on periodic excitations of an adsorbent material and the analysis of the frequency spectrum of the responses to these excitations (Kärger *et al.*, 2012). It allows distinguishing different transfer mechanisms, since they manifest in different characteristic patterns at different frequencies depending on their time constant and physical nature. Beneath several practical advantages, with the FRA the dependency of transfer parameters on the thermodynamic state may be determined, as during one measurement the sample is kept in a small and well-defined state region.

A simplified method for the performance prediction of Ad-HX based on heat and mass transfer parameters has not yet been established. However, there are approaches to quantitatively compare heat and mass transfer, by mapping the mass transfer resistance to an equivalent heat transfer resistance. This has been first suggested by Wittstadt *et al.* (2017) and then further elaborated by Ammann *et al.* (2018) for the phenomenological interpretation of gramm-scale experimental data.

The development of new adsorbent materials has been a research interest for many years. Beneath practical considerations, like safety, stability and economic availability, adsorbents with a high refrigerant-uptake in a narrow range of thermodynamic states allow for best performances in terms of efficiency and compactness for applications with given temperature boundary conditions (Aristov, 2013). Amongst the materials, exhibiting such an S- or step-shaped isotherm, aluminium fumarate (Alfum), a metal-organic framework (MOF), has attracted increasing interest for thermal applications in recent years (Jeremias *et al.*, 2014; Kummer *et al.*, 2017b). Alfum is especially interesting for applications with low driving temperature levels (Lenzen *et al.*, 2019). While not yet available at low enough prices for AHT, this material is potentially a cost-effective material due to widely available educts (Al-salts and fumaric acid) and water based synthesis route (Kiener *et al.*, 2009). A promising approach to increase compactness in Ad-HX is to use binder-based adsorbent coatings to allow for a substantially better heat transfer to the heat exchanger structure in comparison to loose grain beds, the state of the art solution (Freni *et al.*, 2015). While the manufacturability of such an Alfum-coated Ad-HX has been proven (Kummer *et al.*, 2017b), detailed knowledge about the adsorption dynamics is still missing. For this reason, these coatings have been chosen as exemplary material to be analysed in this work.

1.2 Research Question

This work focusses on two principal questions derived from the motivation above:

1. What are the relevant transfer parameters for the adsorption dynamics of binder-based Alfum coatings, with a special focus on their dependency on the thermodynamic state?
2. How can the resulting heat and mass transfer parameters be presented in a simplified form, allowing a direct interpretation of their relevance for AHT and rough estimates of principle performance indicators for efficiency and compactness?

For the analysis of the adsorption dynamics, a FRA-based method is developed and applied, that extends the conventional FRA in two ways: Firstly, the method, classically designed and used for the investigation of mass transfer phenomena, is extended to investigate heat transfer effects in detail, in order to differentiate thermal conductivity and contact resistances. This includes developing and analytically solving new heat and mass transfer models. Secondly, the FRA is embedded in a measurement procedure that allows, in a single measurement run, to determine the adsorption equilibrium properties and the adsorption enthalpies at exactly the same thermodynamic state of the same sample. This reduces effort for and possible conversion errors of separated measurements.

Further, this first question is extended to whether it is possible to use the obtained transfer parameters and equilibrium properties to properly predict the behaviour of the sample under application-like, i.e. strongly non-linear and transient, conditions.

For the simplified parameter interpretation and performance estimation, the concept of effective thermal resistances is suggested. It extends the idea of equivalent heat transfer resistances, which were derived from experimental data, by theoretically relating the effective resistance directly to heat and mass transfer parameters. Further, the overall performance of an AHT can be estimated directly from an Ohm's-law-like relationship between the effective resistances and an overall driving temperature difference. This temperature difference may be easily calculated by subtracting temperature differences of external temperature boundary conditions and an internal characteristic temperature difference, deduced from the adsorption equilibrium in a concise and compact form.

This second question is completed by showing to what extent this simplified performance prediction on Ad-HX level is comparable to the prediction from commonly used LTJ experiments.

1.3 Structure of the Work

This work is structured as follows:

The second chapter 'Fundamentals' provides the required background from the state of the art, including a critical review of key aspects. The AHT theory is built up starting from basic equilibrium thermodynamics, through the different aspects of adsorption dynamics up to the AHT on appliance level. The chapter includes an overview on sorption materials, without going into the details of material chemistry and synthesis.

The third chapter 'Theory and Model' comprises the two theoretical pillars developed within the scope of this work: The extended FRA including novel heat and mass transfer models with their solutions in the Laplace domain and the parameter identification method, and the concept of effective thermal resistances.

In the fourth chapter 'Experiment' details about the experimental work undertaken are given. After defining the samples investigated, the extended FRA comprises the mayor part of this chapter as the principal experimental method used and developed in the frame of this work. This includes the experimental setup, measurement procedure, data processing and a thorough uncertainty analysis. Additionally, the way how established methods are employed is specified, namely the differential scanning calorimetry (DSC) and the LTJ.

Results and discussions are regrouped in Chapter 5. These are the relevant equilibrium thermodynamic material properties and the experimental FRA results alongside with the identified transport parameters obtained from the model derived in Chapter 3. The later includes an in-depth interpretation and the LTJ-based overall validation of the approach. Further, the expected Ad-HX performance is presented based on the concept of effective thermal resistances.

Finally, conclusion and outlook may be found in Chapter 6.

2. Fundamentals

This chapter provides the required background from the state of the art, including a critical review of key aspects. The AHT theory is built up starting from basic equilibrium thermodynamics, through the different aspects of adsorption dynamics up to the AHT on appliance level. Finally, this chapter will give an overview on sorption materials, without going into the details of material chemistry and synthesis.

While the field of adsorption theory is typically a basis for process engineering applications like catalysis or gas separation, for AHT the focus is slightly different. Thus, questions regarding the energy balance and heat transfer problems are dealt with in depth, including especially the role of the adsorption enthalpy and the specific heat capacity.

Special attention is paid to the experimental techniques available to access the physical parameters introduced in the following.

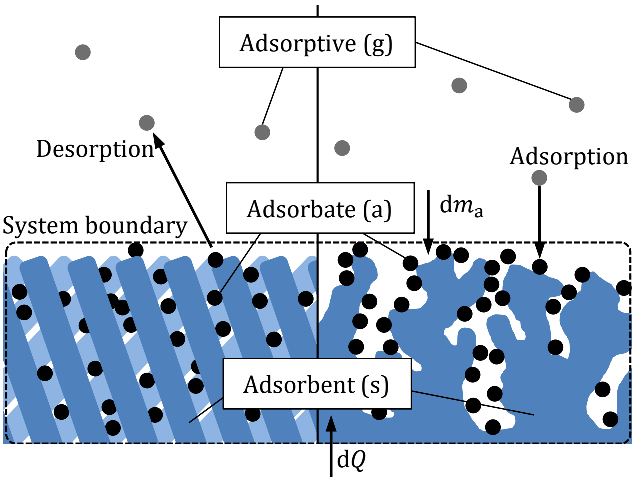

Figure 1: Schematic microscopic adsorbent–adsorbate system of a single-component adsorbate on two principal types of adsorbents: either regular microporous crystalline like a zeolite or a MOF (left half of the schematic) or irregular like a silica gel or an activated carbon (right half), with key terms and variable indexes

2.1 Adsorption Thermodynamics

Adsorption thermodynamics aims to describe the equilibrium relations coupled with the physical phenomenon of adsorption.

Adsorption and desorption, as depicted in Figure 1, are the processes of binding and releasing molecules or atoms between a fluid phase, the *adsorptive*, and the surface of a solid, the *adsorbent*. Often, the terms sorbent or (ad)sorption material are used interchangeably instead of adsorbent. The bound molecules or atoms are referred to as *adsorbate*. In the context of AHT the adsorptive will always be assumed to be a gas phase of a single constituent, also referred to as the refrigerant or working fluid. Further, the adsorbent is a porous material, which might host parts of the gas phase inside its pores – in contrast to the bulk gas phase that is outside of any porous structure.

Adsorption thermodynamics, as understood here, is the most general description of adsorption without any assumption about the nature of the adsorption process. Details of this process, like the properties of the adsorbed molecules, the adsorbent pore structure, or the nature of the adsorption forces, are highly relevant to material science but beyond the scope of this work.

The state of an adsorbent–adsorbate system with a single-component adsorbate is defined by three state variables, which are commonly chosen as: the pressure p (or the relative pressure $p_{\mathrm{rel}} = p/p_{\mathrm{sat}}(T)$), the temperature T and, as additional variable, the loading

$$X = \frac{m_{\mathrm{a}}}{m_{\mathrm{s}}}. \tag{1}$$

A third state variable is, according to Gibbs phase rule, required for this system of two constituents (adsorbent and refrigerant) and two phases with two degrees of freedom.

Classically, the adsorbent (denoted by index “s”) and the adsorbate (“a”) are assumed to be two different phases with following properties (Kast, 1988):

1. The adsorbent is inert. Thus, any thermodynamic property Z of the adsorbent is independent of the loading and only a function of p and T, i.e. the adsorbent has always the same property as the fully desorbed “dry” adsorbent: $Z_{\mathrm{s}}(X, T, p) = Z_{\mathrm{s}}(X = 0, T, p)$.
2. The adsorbate is a “two dimensional phase” in equilibrium with the gas phase.

This concept leads to two fundamental problems. First, not all adsorbents are truly inert. They might undergo structural changes und the influence of the adsorbate. While these changes might be small, their energetic effects can be important. With the assumption of an inert adsorbent, these non-inert properties of the adsorbent are attributed to the “adsorbed phase” with possibly irritating consequences, like negative heat capacities in the worst case (Schwamberger & Schmidt, 2013). Secondly, the term “phase” is difficult for the adsorbate as it does, e.g., not fulfil the homogeneity requirement of a phase in the thermodynamic sense (Baehr & Kabelac, 2009). This requirement implies that any intensive property should remain constant if phase is extended. However, if the adsorbed phase is extended ($m_{\mathrm{a2}} > m_{\mathrm{a1}}$), while the adsorbent mass is kept constant ($m_{\mathrm{s1}} = m_{\mathrm{s2}}$), the loading is changed ($X_2 > X_1$) and thus the thermodynamic state of the systems. The “adsorbed phase” does not exist independently from the adsorbent.

These problems are avoided by treating the adsorbate as an abstract “surface excess” , originally proposed by Gibbs in the 1870s (Rouquerol *et al.*, 2014). This concept does not assume any microscopic model for the physical properties of an actual adsorbate. It defines an imaginary interface, the Gibbs dividing surface, of area A_{s}, between the gas phase and the solid adsorbent, where the state variables of the gas phase are influenced in the vicinity. The influence vanishes for distances larger than z. The deviation from the gas properties are the surface excess quantities (index σ). The surface excess is not any “phase” in the thermodynamic sense, nor is there anything like an excess volume ($V_\sigma = 0$). E.g., for the concentration of the adsorbable species, the excess concentration is the difference between the total concentration (under adsorption influence) and the free gas concentration in equilibrium, but far away: $c_\sigma = c - c_{\mathrm{g}}$. The excess mass, e.g., is expressed as integral along x, perpendicular to the interface:

$$m_\sigma = M A_{\mathrm{s}} \int_0^{\mathrm{z}} c_\sigma \mathrm{d}x \tag{2}$$

The total mass adsorbed is the sum of the excess mass and the gas mass close to the interface:

$$m_\mathrm{a} = MA_\mathrm{s} \int_0^\mathrm{z} \left(c_\sigma + c_\mathrm{g}\right) \mathrm{d}x \tag{3}$$

If z is small and the pressure is low, the gas phase close to the interface may be neglected as $c_\sigma \gg c_\mathrm{g}$, thus $m_\mathrm{a} \approx m_\sigma$. Rouquerol et al. suggest this approximation for pressures up to 1 bar, which is far above the pressure region of 0–100 mbar considered in this work. Thus, this approximation will be assumed in the following. For improved readability, the term “adsorbate” will often be used instead of “surface excess”. As the interface is imaginarily defined, the concept is still valid if defining and measuring a real surface becomes challenging, which is, e.g., the case for microporous adsorbent like zeolites or MOFs.

An equilibrium thermodynamic description requires at least a thermal and a caloric equation of state (EOS), typically derived from fundamental equations. As, up to now, no consistent fundamental equations are available for the adsorbent–adsorbate system that would allow computing these EOS with sufficient accuracy (Aristov, 2012), these terms are little common in adsorption thermodynamics. The thermal EOS is rather referred to as adsorption equilibrium. And instead of a consistent caloric EOS, their derivatives, the differential adsorption enthalpy and specific heat capacity, are used and mostly described empirically based on direct measurements.

2.1.1 Adsorption equilibrium

The adsorption equilibrium describes the relationship between the three state variables pressure, temperature and loading. It is typically formulated as $X = f(T, p)$, as with the principal experimental methods either T or – less popular – p are kept constant. For the simplified description of these isotherms or isobars, the literature offers a variety of different theoretical approaches. Examples are the “Langmuir isotherm” (Langmuir, 1918), the simplest and oldest model derived from the idea of a well-defined surface covered with an adsorbate monolayer, or the BET surface (Brunauer *et al.*, 1938), which extends the Langmuir model for adsorbate multilayers, up to more complex models based on statistical thermodynamics, of which, e.g., a good overview is given by Llano-Restrepo & Mosquera (2009).

This work will focus on the “Dubinin approach”, as the most popular in the context of AHT (Aristov, 2012), and the Clausius–Clapeyron-based approach, which will be used later. These two approaches will be shortly presented in the following, while a detailed overview and discussion of the other different approaches can be found elsewhere (Velte, 2019).

All these approaches have in common that they do not account for any hysteresis in the adsorption equilibrium as they assume uniqueness in the relation between loading, pressure and temperature. Although, hysteresis is commonly observed in adsorption equilibria, which is explained by different phenomena always associated to pore condensation (Kast, 1988). Pore condensation becomes relevant mostly at high relative pressures, e.g., for water adsorbed on activated carbons at $p_\mathrm{rel} > 0.4$ (Kast, 1988). As these high relative pressures are irrelevant to heat transformation applications, hysteresis is disregarded here in a first approximation. However, its existence cannot be fully excluded and should be verified experimentally.

Dubinin's theory of volume filling of micropores

For microporous adsorbents with pores sizes similar to the size of the guest molecules the concept of a "surface", the basis of the classical Langmuir or BET models, becomes vague. This motivated Dubinin to develop the "Theory of Volume Filling of Micropores" (Dubinin, 1975). This theory initially aimed at describing the adsorption on nonpolar adsorbents like activated carbon and was then further extended to zeolites.

In this framework, the equilibrium data is transformed from the bivariate $X(T,p)$ to the univariate $W(A)$ with the adsorption potential

$$A = -RT \ln p_{\mathrm{rel}} \tag{4}$$

and the specific volume of the adsorbed phase

$$W = \frac{X(T,p)}{\rho_{\mathrm{a}}(T,X)}. \tag{5}$$

The basic idea is that the degree of filling of the pore volume, which is easier to assign for microporous adsorbents, replaces the notion of surface coverage. Dubinin found that for many materials in the W over A plot all data points were, within the measurement uncertainty, on a single curve, irrespective of the actual p and T conditions. This curve is known as the "characteristic curve" and may be derived theoretically from the assumption of the temperature invariance of A: $(\partial A/\partial T)_W = 0$. This assumption and thus the coincidence of all equilibrium data points on one curve is a fundamental pre-requisite for the Dubinin formalism as a tool for the reduction of experimental data. It is, however, only valid for non-polar adsorbents in small temperature ranges.

Specific ansaetze have proven helpful to describe $W(A)$ with as little parameters as possible also to reduce the number of required experiments. The most popular are the Dubinin–Radushkevich (DR) equation

$$W = W_0 \exp\left[-\left(\frac{A}{\beta E}\right)^2\right] \tag{6}$$

and its generalisation, the Dubinin–Astakhov (DA) equation

$$W = W_0 \exp\left[-\left(\frac{A}{\beta E}\right)^m\right], \tag{7}$$

with three or four parameters, respectively.

However, these equations are not well suited to represent a number of working pairs relevant to AHT. This lead to a "generalized Dubinin" (Núñez, 2001) with an arbitrary function for $W(A)$, e.g. the ratio of two polynomials, without claiming any physical meaning of the parameters. Since a long time, but contrary to the practical situation of Dubinin in the 1970s, the communication and evaluation of functions with ten or more parameters is not a disadvantage anymore.

Despite being “a rather crude approximation” (Dubinin & Astakhov, 1971) for adsorption on polar adsorbents over a wide temperature range, this approach has for its compactness become popular for modelling AHT (Aristov, 2012), including, e.g., adsorption on zeolites (Riffel *et al.*, 2010; Wittstadt *et al.*, 2015; Ammann *et al.*, 2019) and MOFs (Kummer *et al.*, 2017a; Lenzen *et al.*, 2019).

Clausius–Clapeyron Based Approach

A more generic approach is based on the Clausius–Clapeyron equation

$$\left(\frac{\partial p}{\partial T}\right)_X = \frac{\Delta h_\mathrm{s}(X,T)}{T\left(v_\mathrm{g} - v_\mathrm{a}\right)} \approx \frac{\Delta h_\mathrm{s}(X,T)}{R_\mathrm{w}} \frac{p}{T^2}, \tag{8}$$

which is valid for any two phases in equilibrium as it is directly derived from the fundamental equilibrium criterion of equal Gibbs potentials (Baehr & Kabelac, 2009). For the second step in Eq. (8) ideal gas behaviour and the negligibility of the adsorbate volume ($v_\mathrm{g} \gg v_\mathrm{a}$) are assumed, which is both well-met for the case of this work. With the common transformation, the linear relation

$$\left(\frac{\partial \ln\left(\frac{p}{p_0}\right)}{\partial\left(-\frac{1}{T}\right)}\right)_X \approx \frac{\Delta h_\mathrm{s}(X,T)}{R_\mathrm{w}} \tag{9}$$

is obtained, which is the basis for creating Clausius–Clapeyron plots with $\ln(p/p_0)$ over $-1/T$.

This allows to construct an isostere, i.e. a line of constant loading, from a single point if the differential adsorption enthalpy $\Delta h_\mathrm{s}(X,T)$ is known. This single point may, e.g., be obtained from a tabulated or (arbitrarily) fitted well known isotherm.

This approach may be seen as a generalisation of the “thermodynamic approach” for the adsorption isotherm (Kast, 1988) that requires no specific assumption about the adsorbent. It has the advantage of being independent on any assumption about the physical nature of the adsorption mechanism. It is especially useful if Δh_s can be assumed constant.

However, it is less compact compared to other methods and it requires knowledge of Δh_s. Moreover, if Δh_s may not be assumed constant, it is numerically useful only for computing $p(X,T)$ and less for $X(p,T)$ as here $\Delta h_\mathrm{s}(X,T)$ results in an implicit expression requiring iterative numerical solutions in most cases. Though for computer based calculations and in the context of AHT where thorough knowledge of $\Delta h_\mathrm{s}(X,T)$ must be given anyway, the advantage of precision and consistency seem to outweigh these drawbacks. If necessary, e.g. for detailed transient simulations, the numerically expensive solution of iterative expressions can be performed once to fill a detailed look-up table, from where values are interpolated at the simulation runtime.

2.1.2 Adsorption enthalpy

The description of changes in enthalpy associated with adsorption depends, especially, on the aforementioned issue of whether the adsorbent is treated as inert or not. As an alternative to the inert-adsorbent model the concept of surface excess properties was introduced above. While the latter is preferred here for its physical consistency, the following derivations will also be discussed in the context of the inert-adsorbent model – simply for its wide popularity in literature.

To start with, consider the adsorbent–adsorbate system (Figure 1) with a constant mass of adsorbent m_s, variable temperature T and mass of adsorbate m_a at a defined equilibrium pressure $p(X,T) = p(m_\mathrm{a},T)$. Then, the enthalpy change of the system is

$$\mathrm{d}H_\mathrm{s+a} = \left(\frac{\partial H_\mathrm{s+a}}{\partial T}\right)_{m_\mathrm{s},m_\mathrm{a}} \mathrm{d}T + \left(\frac{\partial H_\mathrm{s+a}}{\partial m_\mathrm{a}}\right)_{m_\mathrm{s},T} \mathrm{d}m_\mathrm{a} \qquad (10)$$

where, for the low pressure regime considered here, the enthalpy of the gas phase in the system can be neglected (Rouquerol *et al.*, 2014). The gas mass is by several orders of magnitude smaller than the adsorbate or the adsorbent mass. The assumption of an inert adsorbent ($\partial H_\mathrm{s}/\partial m_\mathrm{a} = 0$) allows separating $\mathrm{d}H_\mathrm{s+a}$ into an adsorbent part

$$\mathrm{d}H_\mathrm{s} = \left(\frac{\partial H_\mathrm{s}}{\partial T}\right)_{m_\mathrm{s}} \mathrm{d}T \qquad (11)$$

and the enthalpy change of the adsorbate (Schwamberger & Schmidt, 2013):

$$\mathrm{d}H_\mathrm{a} = \left(\frac{\partial H_\mathrm{a}}{\partial T}\right)_{m_\mathrm{s},m_\mathrm{a}} \mathrm{d}T + \left(\frac{\partial H_\mathrm{a}}{\partial m_\mathrm{a}}\right)_{m_\mathrm{s},T} \mathrm{d}m_\mathrm{a}. \qquad (12)$$

Without the inert-adsorbent assumption, this separation may also be done in theory but it is not helpful as $\partial H_\mathrm{s}/\partial m_\mathrm{a}$ may not be separated from $\partial H_\mathrm{a}/\partial m_\mathrm{a}$ experimentally.

The temperature derivatives in Eqs. (10) and (12) refer to the heat capacity (Section 2.1.3). The mass derivatives are the differential enthalpy of the adsorbent–adsorbate system $\bar{h}_\mathrm{s+a} = (\partial H_\mathrm{s+a}/\partial m_\mathrm{a})_{m_\mathrm{s},T}$ for a non-inert adsorbent, or the mass derivative is the differential enthalpy of the adsorbate $\bar{h}_\mathrm{a} = (\partial H_\mathrm{a}/\partial m_\mathrm{a})_{m_\mathrm{s},T}$ for an inert adsorbent (Rouquerol *et al.*, 2014). Simplified and only for an inert adsorbent, $\bar{h}_\mathrm{a}$ may be seen as the specific enthalpy at the boundary to the gas phase, that decreases with X towards the specific enthalpy of the free liquid phase h' (Kast, 1988), or, more general, the differential surface excess enthalpy. This differential state will be referred to as the differential adsorbed state in the following, denoted with an overbar. For the low pressures considered here, the effect of the adsorbate volume on the energy balance may be neglected, so that $H_\mathrm{a} \approx U_\mathrm{a}$ and thus $\bar{h}_\mathrm{a} = \bar{u}_\mathrm{a}$ may be assumed (Rouquerol *et al.*, 2014).

The differential adsorption enthalpy may then be written as

$$\Delta h_\mathrm{s} = h_\mathrm{g} - \bar{h}_\mathrm{s+a} \qquad (13)$$

or, for the inert adsorbent, as

$$\Delta h_\mathrm{s} = h_\mathrm{g} - \bar{h}_\mathrm{a}. \tag{14}$$

From the energy balance of the adsorbent–adsorbate system (Figure 1) follows, that in both cases Δh_s is equal to $(-\mathrm{d}Q)$, the amount of heat released by an open isothermal system (Figure 1) per infinitesimal mass $\mathrm{d}m_\mathrm{a}$ changing from gas to adsorbed state (c.f. Appendix A.1).

The quantity characterizing the adsorbate as a whole is the integral specific enthalpy of the adsorbate. It can be calculated for an inert adsorbent by isothermal integration:

$$h_\mathrm{a}(X,T) = \frac{H_\mathrm{a}}{m_\mathrm{a}} = \frac{1}{X}\int_0^X \bar{h}_\mathrm{a}(\chi,T)\mathrm{d}\chi. \tag{15}$$

Relation to the Adsorption Equilibrium

For the equilibrium between the gas and the adsorbed phase the Clapeyron equation (i.e. assuming for the specific volumes: $v_\mathrm{g} - \bar{v}_\mathrm{a} \approx v_\mathrm{g}$) may be applied without any further assumptions:

$$\left(\frac{\partial p}{\partial T}\right)_X = \frac{\Delta h_\mathrm{s}}{v_\mathrm{g} T}. \tag{16}$$

This relates Δh_s to the isostere slope, which explains its designation as isosteric heat of adsorption, a term that is discouraged by IUPAC to strictly separate enthalpy and heat as state and process variables (Rouquerol *et al.*, 2014). The differential adsorption enthalpy Δh_s is not to be confounded with the *differential heat of adsorption*, a term earlier used for $\Delta u_\mathrm{s} = u_\mathrm{g} - (\partial u_\mathrm{a}/\partial m_\mathrm{a})_{m_\mathrm{s},T}$, i.e. the difference between the internal energy of the gas phase and the differential internal energy of the adsorbed phase (Clark, 1970; Llano-Restrepo & Mosquera, 2009).

Eq. (16) may be further simplified assuming an ideal gas ($v_\mathrm{g} = R_\mathrm{w}T/p$) to yield the Clausius–Clapeyron equation

$$\begin{gathered}\left(\frac{\partial p}{\partial T}\right)_X = \frac{\Delta h_\mathrm{s} p}{R_\mathrm{w} T^2} \\ \left(\frac{\partial \ln(p/p_0)}{\partial T^{-1}}\right)_X = \frac{\Delta h_\mathrm{s}}{R_\mathrm{w}}\end{gathered} \tag{17}$$

where p_0 is a constant reference pressure, which is set by convention to 10^5 Pa.

The deviation of v_g between the IAPWS formulation (Wagner *et al.*, 2000) and the ideal gas are below 0.3% for water under the operating conditions within the scope of this work ($20\ °\mathrm{C} < T < 80\ °\mathrm{C}$, $p_\mathrm{rel} < 0.5$ and $p < 100$ mbar).

With the general relation between the state variables partial derivatives

$$\left(\frac{\partial X}{\partial p}\right)_T \left(\frac{\partial p}{\partial T}\right)_X \left(\frac{\partial T}{\partial X}\right)_p = -1 \tag{18}$$

and Eq. (17), the differential adsorption enthalpy can be related to the slopes of the isotherm and the isobar which are experimentally directly available (c.f. Section 4.2.2.2):

$$\Delta h_s = -\frac{R_\mathrm{w} T^2}{p} \left(\frac{\mathrm{d}X}{\mathrm{d}T}\right)_p \left(\frac{\mathrm{d}X}{\mathrm{d}p}\right)_T^{-1} \tag{19}$$

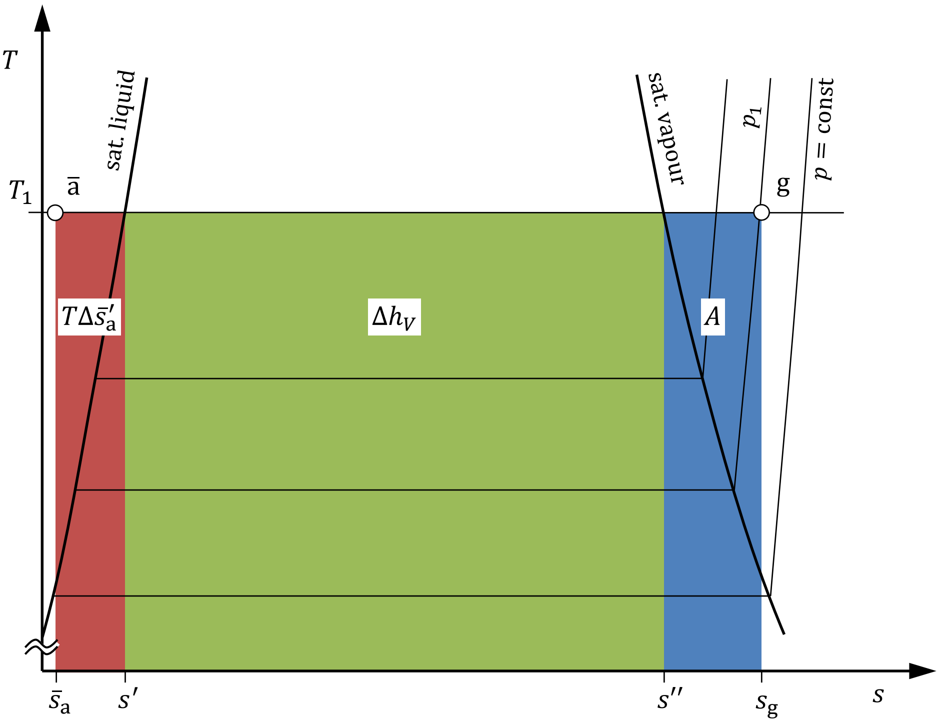

Figure 2: Illustration of the Dubinin approach for the differential adsorbed state “ā”, and the adsorption enthalpy ($\Delta h_\mathrm{s} = T\Delta s_\mathrm{a}' + \Delta h_\mathrm{v} + A$) in the T-s-diagram for water at moderate temperatures (T < 100 °C)

Relation to the Dubinin Formalism

In the Dubinin formalism the adsorbed state is related to the saturated liquid at the adsorption temperature, as an arbitrary reference state. The adsorption enthalpy can be calculated as (Dubinin, 1975)

$$\Delta h_\mathrm{s} = \Delta h_\mathrm{v} + A + T\Delta\bar{s}_\mathrm{a}'. \tag{20}$$

It is directly related to the adsorption potential A, the enthalpy of vaporisation $\Delta h_\mathrm{v} = h'' - h'$, and an “entropy term” $T\Delta\bar{s}_\mathrm{a}'$, as depicted in the T-s-diagram (Figure 2).

The adsorption potential A is by definition the enthalpy difference between the unsaturated gas state “g” and the saturated vapour at adsorption temperature. This is equivalent to the work required for an reversible isothermal compression from p to $p_\mathrm{sat}(T)$.

In the "entropy term" of Eq. (20), $\Delta\bar{s}_\mathrm{a}'$ is the difference between the saturated liquid at the adsorption temperature, and the differential entropy of the adsorbate $\bar{s}_\mathrm{a} = (\partial S_\mathrm{a}/\partial m_\mathrm{a})_{m_\mathrm{s},T}$. It is directly related to the temperature variance of A. This follows from Gibb's fundamental equation, and the definition of $A = \bar{g}_\mathrm{a} - g'$, as the difference between the differential Gibb's free energy of the adsorbate and the specific Gibb's free energy of the saturated liquid (Dubinin, 1975):

$$\Delta\bar{s}_\mathrm{a}' = s' - \bar{s}_\mathrm{a} = -\left(\frac{\partial A}{\partial T}\right)_X \tag{21}$$

Note that here $\Delta\bar{s}_\mathrm{a}'$ is differently defined and corresponds to $(-\Delta S)$ in Dubinin's work.

For the case of a temperature-invariant characteristic curve, $(\partial A/\partial T)_W = 0$, this simplifies to (Dubinin, 1975; Núñez, 2001)

$$\Delta\bar{s}_\mathrm{a}' = -\alpha\left(\frac{\partial A}{\partial \ln W}\right) \tag{22}$$

where α is the thermal coefficient of limiting adsorption. As α is mostly unknown, it may be approximated by the thermal coefficient of the saturated liquid at adsorption temperature. In this case, and especially for a step-like isotherm where $\partial A/\partial \ln W$ becomes small, $T\Delta\bar{s}_\mathrm{a}'$ is below the order of 1% of Δh_v, and can be neglected. In this case $s_\mathrm{a} \approx s'$ and Eq. (20) reduces to the simple Dubinin approximation

$$\Delta h_\mathrm{s} = \Delta h_\mathrm{v} + A. \tag{23}$$

While being well confirmed for many classical adsorbents (Aristov, 2012), the temperature invariance is not well met for, e.g., SAPO-34 with water, which is a much investigated working pair for adsorption heat transformation. Already small deviations from the temperature-invariance conditions have important consequences on the adsorption enthalpy, at least for water: At 300 K, $T\Delta\bar{s}_\mathrm{a}'$ reaches 0.8 kJ/kg (this is 10% of Δh_v) already when A deviates by just 8 kJ/kg over a temperature difference of 10 K. For the p_rel range of 0.1–0.3, which is common for heat transformation applications, this equates to a relative deviation of 2.5%–4.9% in A over 10 K. Thus, the deviation may easily be hidden by the measurement uncertainty of uptake experiments, unless isotherms over a wide temperature range are considered. In this case it does especially not make sense to take into account Eq. (22), as this corrects a tiny deviation, while the major effect of the unmet temperature invariance is missed.

2.1.3 Specific heat capacity

The heat capacity of the adsorbent–adsorbate system (Figure 1) may be defined as

$$c_{p,\mathrm{s+a}}(T,X) = \frac{1}{m_\mathrm{s}}\left(\frac{\partial H_\mathrm{s+a}}{\partial T}\right)_{m_\mathrm{s},m_\mathrm{a}}. \tag{24}$$

For convenience $c_{p,\mathrm{s+a}}$ is referred to the adsorbent dry mass, which is constant throughout the process. The total mass specific heat capacity is $(1+X)^{-1}c_{p,\mathrm{s+a}}$.

For an inert adsorbent this may be further differentiated into

$$c_{p,\mathrm{s+a}}(T,X) = c_{p,\mathrm{s}}(T) + Xc_{p,\mathrm{a}}(T,X) \tag{25}$$

with the heat capacity of the adsorbent, and of the adsorbate:

$$\begin{aligned} c_{p,\mathrm{s}}(T) &= \frac{1}{m_\mathrm{s}}\left(\frac{\partial H_\mathrm{s}}{\partial T}\right)_{m_\mathrm{s}} \\ c_{p,\mathrm{a}}(T,X) &= \frac{1}{m_\mathrm{a}}\left(\frac{\partial H_\mathrm{a}}{\partial T}\right)_{m_\mathrm{s},m_\mathrm{a}}. \end{aligned} \tag{26}$$

This assumption allows using a single value of $c_{p,s}$, e.g. from a measurement at $X=0$, for the whole loading range. The heat capacity of the adsorbate must then be approximated, e.g. by the properties of the adsorptive (Velte *et al.*, 2017), of bulk water (Graf *et al.*, 2016; Ammann *et al.*, 2019), or calculated from the adsorption enthalpy through the energy balance. For the latter Schwamberger and Schmidt (2013), building upon work from Walton an LeVan (2005), relate the specific heat capacity to the specific heat capacity of the gas and the temperature dependency of the differential adsorption enthalpy, both averaged over the isotherm:

$$c_{p,\mathrm{a}} = \frac{1}{X}\int_0^X \left[\left(\frac{\partial h_\mathrm{g}(p(\chi,T),T)}{\partial T}\right)_\chi - \left(\frac{\partial \Delta h_\mathrm{s}(\chi,T)}{\partial T}\right)_\chi\right]\mathrm{d}\chi. \tag{27}$$

Which can be derived from Eq. (26) with the definition of the differential adsorption enthalpy Eq. (14) and the integral specific enthalpy of the adsorbate Eq. (15). For the case of an ideal gas, where h_g only depends on temperature, this simplifies to

$$\begin{aligned} c_{p,\mathrm{a}} &= \frac{1}{X}\int_0^X \left[c_{p,\mathrm{g}}(T) - \left(\frac{\partial \Delta h_\mathrm{s}(\chi,T)}{\partial T}\right)_\chi\right]\mathrm{d}\chi \\ &= c_{p,\mathrm{g}}(T) - \frac{1}{X}\int_0^X \left(\frac{\partial \Delta h_\mathrm{s}(\chi,T)}{\partial T}\right)_\chi \mathrm{d}\chi \\ &= c_{p,\mathrm{g}}(T) - \frac{\partial}{\partial T}\frac{1}{X}\int_0^X \Delta h_\mathrm{s}(\chi,\mathrm{T})\mathrm{d}\chi \end{aligned} \tag{28}$$

where in the last step it was made use of a special case of Leibniz's rule as X is independent of T. In Eq. (28) $\frac{1}{X}\int_0^X \Delta h_\mathrm{s}(\chi,\mathrm{T})\mathrm{d}\chi$ is the integral adsorption enthalpy. This illustrates the analogy to a single component with ideal gas and incompressible liquid, where $c_{p,\mathrm{l}} = c_{p,\mathrm{g}} - \partial\Delta h_\mathrm{v}/\partial T$.

A simple mean to ensure a consistent energy balance in modelling, is to neglect the temperature dependency of the adsorption enthalpy (integral or differential), as this yields $c_{p,\mathrm{a}} = c_{p,\mathrm{g}}$. Using the heat capacity of bulk water for $c_{p,\mathrm{a}}$, and a temperature-invariant adsorption enthalpy, necessarily leads to an inconsistent energy balance as Eq. (27) is violated. The practical problem of using Eqs. (27) or (28) is the high uncertainty associated to $\partial\Delta h_\mathrm{s}/\partial T$ from either experimental data or theoretical considerations. This can lead to $c_{p,\mathrm{a}}$ having rather a compensatory function, to ensure consistent energy balances with imperfect assumptions for Δh_s (e.g. from an assumed temperature invariance of the characteristic curve, c.f. Section 2.1.2), than an actual physical meaning (Schwamberger & Schmidt, 2013). From this point of view, appropriate measurements of $c_{p,\mathrm{a}}$, that then may be used to derive the temperature dependency of Δh_s, are expected to be more robust in terms of uncertainty.

Based on calorimetric measurements, Vučelić & Vučelić (1983) found strongly temperature dependent results for $c_{p,\mathrm{a}}$, for fully saturated samples of silica gel, activated carbon, and CaA-zeolite. The values were close to those of ice, for lower temperatures, and close to those of bulk water, for higher temperatures.

Beyond the adsorbent–adsorbate system, the specific heat capacities of all other materials that undergo temperature changes, like binders, additives, or the heat exchanger support structure, are relevant to design and operation of adsorption heat transformers. For these truly inert materials no special adsorption-related attention is required.

2.1.4 Measurement methods

Overviews about the experimental approaches to adsorption equilibrium and adsorption enthalpy are, e.g., given by Rouquerol *et al.* (2002; 2014).

Adsorption equilibrium

Adsorption equilibrium is most commonly measured as adsorption isotherms. The amount adsorbed is either determined manometrically, through the measurement of the pressure in a calibrated control volume, or directly gravimetrically. For historical reasons the manometry is still often referred to as volumetry.

For adsorption manometry, a material sample is placed in a glass adsorption cell, and connected to a temperature controlled vacuum setup with the calibrated volume, which also serves as manifold to the pressure transducer(s), a vacuum pump and an adsorptive reservoir. The adsorption bulb is typically placed in a temperature controlled bath, or, for nitrogen measurement, in a liquid nitrogen filled dewar. After initial degassing under vacuum at high temperatures, adsorptive is successively dosed in until equilibrium is reached. The change in the amount adsorbed is calculated based on the thermal equation of state of the adsorptive and the mass balance of the calibrated volume, and the total uptake by cumulating all changes. Once a set maximum relative pressure, typically close to 1, is reached, the desorption branch is measured by successively dosing adsorptive out of the adsorption cell. This approach has become the standard method for adsorption characterisation with automated devices commercially available from several manufacturers. Though seemingly simple to operate, leak-tightness must be ensured and appropriate sample size and equilibration criteria chosen. The incremental procedure results in a high resolution of the isotherm to the cost of an accumulation of uncertainties during a measurement. Alternatively, configurations with reservoir and double pressure measurement allow for measuring specific points of the isotherm with low measurement uncertainty (Rouquerol & Rouquerol, 2014).

Adsorption gravimetry is a special kind of thermogravimetry (TG), that may be conducted either “open” under atmospheric pressure, with the adsorptive mixed to a non-adsorbing carrier gas, e.g. humidified nitrogen, or closed under a pure adsorptive atmosphere, i.e. under vacuum conditions for water adsorption. A comparison with many practical considerations for water adsorption measurements can, e.g., be found in Henninger (2008). The adsorbent is placed in a crucible hanging on a microbalance. The concept is not limited to isothermal measurements, but may be employed for isobaric measurements, or the simulation of any application relevant pressure and temperature condition. In principle, closed loop control would also allow measurements with defined loading, e.g. isosteres, although this is not common. Both, open and closed TG, are established methods with automated devices commercially available, although more so for the open TG. Practically, the humidity control and measurement required for open TG may pose problems, especially for very low partial pressures (Henninger, 2008). For closed TG temperature control can be a critical point, given the extremely low thermal contact of a sample hung in a vacuum environment. This may also lead to very long equilibration times, or low equilibrium quality.

Commercially available devices for manometrical or gravimetrical adsorption measurements are designed for samples in form of granules or powders in the 10–100 mg scale.

Adsorption enthalpy

Adsorption enthalpy may either be calculated from adsorption equilibrium measurement results, or directly measured calorimetrically. Calculation is based on interpolating several points of the same isostere from isobars and isotherms and application of the Clausius–Clapeyron equation (Eq. (17), p29) on the slope derived by the linear regression. This relatively simple method relies on the quality of the initial adsorption equilibrium, the interpolation precision, and a sufficiently large temperature difference for the significance of the linear regression, which contradicts a high temperature resolution. The calculation of adsorption enthalpy may be implemented as automatic procedure in commercially available manometric adsorption measurement devices.

Calorimetric measurements of adsorption enthalpy are less reported in literature than equilibrium measurement. The state of the art method is experiments based on isothermal (a.k.a. static) microcalorimeters (Fubini, 1988; Handy *et al.*, 1993; Rouquerol & Rouquerol, 2014) with heat-flowmeters based on principles first described by Tian (1923) and later improved by Calvet and Prat (1963). These Tian–Calvet thermopiles completely encapsulate a measurement cell with up to 1000 thermocouples allowing for precise heat flow measurements, even for the relatively large measurement cells that are required to provide reversible sealing and a vacuum connection necessary for adsorption experiments. Typically, two measurement cells are used with thermopiles connected in differences. This differential assembly allows for measuring the difference between the heat flows to a surrounding thermostat of a measurement and a reference cell. For sample pre-conditioning and uptake measurement, the cells need to be connected to an appropriate manometric adsorption measurement apparatus. With this approach, e.g., Jänchen et al. (2005) have determined differential adsorption enthalpies as a function of loading for water on LiLSX, SAPO-34 and $CaCl_2$ impregnated attapulgite meant for thermochemical heat storage.

A slightly different method is the differential scanning calorimetry coupled with a thermogravimetric device (TG-DSC). With this method, the measurement plate of a DSC may be either hanging with the sample on a microbalance, or embedded in a tube surrounding a freely hanging crucible. Microbalance and DSC are both exposed to the atmosphere conditioned for the experiment, typically at ambient pressure (i.e. open TG). This method is more versatile and involving less experimental effort but less precise (Pires *et al.*, 2000). The same restrictions apply as for TG measurements. TG-DSC is described as a fast method for screening purposes (Jänchen *et al.*, 2005) with less information about the loading dependency of the differential adsorption enthalpy (Pires *et al.*, 2000).

Recently, a group at the University of Duisburg-Essen developed a sensor gas calorimeter (Bläker *et al.*, 2016; Bläker *et al.*, 2017) to replace the complicated thermopiles of the Tian–Calvet microcalorimeter. For this approach, the adsorption and reference cell are embedded in two gas-filled containers, which are immerged in a temperature controlled bath. The pressure in both containers is measured and its temporal evolution calibrated to the heat released during adsorption.

Specific Heat Capacity

The measurement of the heat capacity of the adsorbent–adsorbate is often limited to the dry adsorbent (Brancato *et al.*, 2015; Uddin *et al.*, 2018), while loading dependent measurements are rarely found in literature. Heat capacity measurements of the loaded adsorbent are challenging due to bias from ad- or desorption processes. To reduce this effect, adsorbent samples may be conditioned to a set loading and hermetically sealed with as little void volume as possible (Aristov *et al.*, 1997; Cacciola *et al.*, 1998; Aristov, 2012).

The heat capacity may then be measured by DSC, where a measurement cell is embedded in a tightly temperature controlled block. Typical DSC measurement cells are equipped with a single thermocouple between a sample and a reference crucible instead of a complex Tian-Calvet thermopile. Given that calibration routines are carried out repeatedly, this simple approach allows precise measurement of the heat flow into the sample. This is possible, due to small and well defined crucibles. The differential configuration, with two identical crucibles, ensures that the heat flow component resulting from the heat capacity of the crucibles is cancelled out. The specific heat capacity is deduced from the measured heat flow applying the energy balance of the adsorbent–adsorbate system (c.f. Appendix A.1) under controlled temporal evolution of the thermostat temperature, which is either a constant temperature slope (referred to as “heating rate”) or a step-wise temperature change. The actual sample temperature is unknown and may, especially for large temperature slopes, deviate considerably from the thermostat temperature. This temperature lag is avoided in the step-wise mode.

With this approach Aristov *et al.* (1997) measured the specific heat capacity of a $CaCl_2$ impregnated silica gel at nine different loadings in the range of 0–0.41 kg/kg for the temperature range of 40–110 °C, and Cacciola *et al.* (1998) for the specific heat capacity of 4A zeolite at 0.01–0.20 kg/kg and 40–115 °C. The same method was used later on SWS-8L ($Ca(NO_3)_2$-impregnated silica) with water in the loading and temperature range of 0–0.25 kg/kg and 20–100 °C, respectively (Freni *et al.*, 2012).

For reduction of the temperature and loading dependent data, this empirical fit has proven useful (Aristov, 2012):

$$c_{p,\mathrm{s+a}}(T,X) = (a_0 + a_1 X + a_2 X^2) + (b_0 + b_1 X + b_2 X^2)T. \qquad (29)$$

The specific heat capacity of the adsorbate can only be deduced from Eq. (25) by assuming an inert adsorbent ($\partial H_s/\partial m_\mathrm{a} = 0$):

$$c_{p,\mathrm{a}}(T,X) = \frac{1}{X}\Big(c_{p,\mathrm{s+a}}(T,X) - c_{p,\mathrm{s}}(T)\Big). \tag{30}$$

Here $c_{p,s}(T)$ is the measured specific heat capacity of the dry adsorbent. Explorative application of Eq. (30) on available literature data yields, e.g. $c_{p,\mathrm{a}} \approx 5.5$ kJ/(kg K) for water on $CaCl_2$ impregnated silica gel (Aristov *et al.*, 1997), or $c_{p,\mathrm{a}} \approx 4.6$–$5.4$ kJ/(kg K) for 4A zeolite (Cacciola *et al.*, 1998), which is substantially larger than the values from the liquid or gas state (i.e. about 4.2 or 1.9 kJ/(kg K), respectively), which are typically assumed for $c_{p,\mathrm{a}}$ (c.f. Section 2.1.3).

Further, a low temperature vacuum adiabatic calorimeter was used to study the heat capacity of $CaCl_2$ impregnated silica gel in the temperature range of 6–300 K at two water loadings: 0 mol/mol and 2.04 mol/mol (Aristov *et al.*, 2011). This approach is especially suited for addressing fundamental questions related to the behaviour close to absolute zero, while it remains of limited relevance for engineering purposes.

2.2 Adsorption Dynamics

In addition to the thermodynamic equilibrium properties, information about the dynamics of the adsorption process is crucial for any technical application. In AHT the overall dynamics are a result of the interplay between the different components, typically the Ad-HX, and the evaporator or condenser. The adsorption dynamics cover the processes occurring in the Ad-HX.

Intrinsic adsorption kinetics, the process of microscopically-local changes between the gas and the adsorbed state, occur at a time scale orders of magnitude faster than any processes visible at macroscopic scale (Kärger *et al.*, 2012). Thus, adsorption dynamics relevant to any AHT application are entirely determined by heat and mass transfer phenomena and their interplay with external boundary conditions and the thermodynamics equilibrium.

These heat and mass transfer phenomena are transient due to the cyclic operation, strongly coupled through the adsorption equilibrium and typically highly non-linear. Unlike for most adsorption applications, the thermal effects are the fundamental motivation for any AHT application. Thus, the heat transfer is an inherent and possibly dominant part of the adsorption dynamics, which needs to be assessed in detail, and the otherwise common assumption of an iso-thermal system is impossible.

For technical applications, adsorbents need to be shaped, either as granules, as binder-based coating, or through direct synthesis on the Ad-HX surface. This shape and the resulting heterogeneous geometry on microscopic and macroscopic scale are as important determinants for the overall adsorption dynamics as the local transport coefficients (diffusivities, thermal conductivities). While the latter are material properties, the lumped transfer coefficients are not, since they are only valid for a specific geometrical configuration. Moreover, for heterogeneous materials it might be necessary to define effective transport coefficients, which are material properties of, e.g., composite materials, valid only for a specific composition.

The model of an adsorption process in a composite material with microporous adsorbent particles embedded into some kind of macroscopic arrangement (composite matrix, granular bed) consists of several mass and heat transfer steps:

1. Diffusion through the macropores of the macroscopic arrangement
2. Entry into the micropores of the adsorbent
3. Diffusion through the micropores of the adsorbent
4. Conduction of the heat that was released by the adsorption through the adsorbent
5. Heat conduction through the macroscopic arrangement
6. Heat conduction in the heat exchanger structure and, eventually, heat transfer to a heat transfer fluid (HTF) on the secondary side of the Ad-HX

These processes are typically temperature, loading or pressure dependent. Further, the heat transfer and the mass transfer are tightly coupled through the adsorption equilibrium. The transient equations used for the respective models are the heat equation and the diffusion equation, as will be detailed in the following.

2.2.1 Heat transfer

Heat transfer in adsorption processes may be modelled in different levels of detail, depending on the actual configuration and the resolution required for the specific question.

It consists of heat conduction in different materials, contact resistances, convective heat transfer in the gas phase and the heat exchanger fluid, and radiative heat transfer. Convective and radiative heat transfers in the gas phase are negligible, given the low density and the low temperature level as well as the small temperature differences considered here.

Contact resistances result from heat transfer through the gas phase on microscopic level. It depends on the comparably low thermal conductivity of the gas phase, which may be superimposed by an additional effect: For the low pressure conditions of water based systems, the small gas filled cavities may easily have similar dimensions as the water molecule's mean free path. At the typical application condition range of 1–10 kPa and 10–100 °C the mean free path of water is in the range of 0.4–5 µm. For this setting the pressure independence of the gas thermal conductivity is lost and a Knudsen effect needs to be taken into account. The concept of thermal conductivity becomes inapplicable and the heat transfer decreases considerably depending on the gas pressure and temperature (Kaganer, 1969). As the information about the microgeometry, required in order to model this effect in detail, are typically not available, the Knudsen effect is included in (p and T dependent) effective parameters at higher levels.

The simplest, and – apart from assuming isothermal conditions – most popular way to model heat transfer in the adsorption context is to assume a single adsorbent temperature varying in time but not in space (Yong & Sumathy, 2002). With this lumped heat transfer approach, the energy balance of the adsorbent writes

$$mc_p \frac{\partial T_\mathrm{s}}{\partial t} = UA(T_0 - T_\mathrm{s}) + \Delta h_\mathrm{s} m_\mathrm{s} \frac{\partial X}{\partial t}, \tag{31}$$

where UA summarises any heat transfer between the ambient (e.g. a heat exchanger surface) at T_0, and the average adsorbent at T_s, i.e. the effective heat conduction in the adsorbent/adsorbent composite, and any contact resistance in between or to a heat exchanger surface. The source term couples the heat transfer to the loading change with the implicit assumption that the adsorptive enters the adsorbent already at T_s. Even if the adsorptive enters at 30 K less, like e.g. in a chiller application, the associated error is just of about 2%, for water as a refrigerant.

If the uncertainty associated with the assumption of an uniform adsorbent temperature becomes too large, the heat transport is discretised in space with Fourier's law:

$$\rho c_p \frac{\partial T_s}{\partial t} = \nabla(\lambda \nabla T) + \rho_\mathrm{s} \Delta h_s \frac{\partial X}{\partial t}. \tag{32}$$

Here ρ and c_p have the same mass reference, as well as ρ_s and X. Generally, all parameters have a temperature and loading dependency, which may be neglected for the densities. To some extent, this assumption may also be made for the thermal conductivity λ and the differential adsorption enthalpy Δh_s, though not for c_p, which even in the simplest model depends on X (c.f. Eq. (25), p32). Together with the effect of the adsorption equilibrium, this makes the heat transfer per se to a non-linear problem unless the loading and temperature variations are kept small, unlike under application conditions. For the heterogeneous structures considered for AHT, like granular beds or any kinds of composites, the thermal conductivity λ is an effective quantity, taking into account the geometry, the conductivities of the different constituents, and any contact resistances in between. As such, it is not a material property of the adsorbent.

Through the source term, the discretised heat transfer in combination with a mass transfer model also accounts for a special kind of heat pipe effect: Adsorbate is desorbed ("consuming" heat) at one place in the composite, transferred to another place and directly adsorbed ("releasing" heat) there.

As opposed the lumped case, a contact resistance R to a heat exchanger wall at x_0 needs to be considered separately through a Cauchy boundary condition

$$-\lambda \frac{\partial T(x_0)}{\partial x} = -h(T(x_0) - T_0) \tag{33}$$

where $h = 1/R$ is the contact heat transfer coefficient, and x is the direction normal to the boundary.

The decision whether the discretised heat transfer model is meaningful may be made based on the Biot number

$$\mathrm{Bi} = \frac{hd}{\lambda}, \tag{34}$$

here for a plane composite layer with thickness d. For $\mathrm{Bi} \ll 1$ the lumped heat transfer model with $h = U$ is sufficient and discretisation does not yield any advantage.

The heat transfer in the massive parts of an Ad-HX may be treated as in any other engineering application. However, due to the low pressure regime, contact resistances that are negligible at atmospheric pressure, may become relevant due to the Knudsen effect described above.

The Buckingham π theorem (Buckingham, 1914) may be applied in order to reduce data on the heat transfer in adsorbent composites to a set of dimensionless numbers, similar to convective heat transfer. This approach was applied to reduce 4-dimensional FEM-simulation results for the heat transfer between a monolayer pellet bed and a flat surface to a 2-dimensional relation of dimensionless numbers (Laurenz *et al.*, 2014).

2.2.2 Mass transfer

Mass transfer in combination with adsorption occurs on different, interconnected levels with accordingly different mechanisms as enumerated above. These diverse transfer processes may be classified into several distinct categories such as the macropore diffusion in the voids between the adsorbent particles and the micropore diffusion inside the adsorbent. In addition, the viscous flow in a super structure at larger scale, e.g. between the HX fins, and local mass transfer resistances at surfaces, e.g. through a barrier layer of inert gas, or through an adverse structure at the “pore mouth” on the adsorbent outer surface, need to be taken into account.

While thorough overviews about these processes in general (Kärger *et al.*, 2012) and for AHT with water as refrigerant, (Füldner, 2015) are available elsewhere, in the following some basic considerations for the two mayor transport cases, the macropore and the micropore diffusion, and the transfer through a barrier resistance are summarised. These two domains are characterised by their pore size relative to the size of the guest molecule ($d_{\mathrm{H_2O}} = 0.3$ nm). The macropores are orders of magnitude larger ($d_{\mathrm{P}} > 50$ nm), so that surface effects (mobility of the adsorbate) may be neglected and only the gas flow is relevant. On the other hand, the micropores are in the same order of magnitude as the size of the guest molecule, thus, the notion of a gas phase is meaningless. The transition between these two cases, the mesoporous region, may be approximated by superimposition (Füldner, 2015). However, this transitional region is irrelevant for the cases handled in this work consisting of microporous adsorbents in a macroporous superstructure.

Macropore diffusion

The mass transfer under confined conditions, like through a porous structure, may be classified based on the Knudsen number, the ratio between the molecules mean free path λ_{MFP} and the pore diameter d_{p}:

$$\mathrm{Kn} = \frac{\lambda_{\mathrm{MFP}}}{d_{\mathrm{p}}}. \tag{35}$$

For a straight cylindrical pore and approximately for any other complex pore geometry, the transfer regimes are classified as follows (Bathen & Breitbach, 2001):

$\mathrm{Kn} < 0.001$	Viscous flow
$0.001 < \mathrm{Kn} < 1$	Slip and transitional flow
$1 < \mathrm{Kn}$	Free molecular flow (pure Knudsen diffusion)

For the viscous flow, the fluid may be treated as continuum with no-slip conditions at the boundaries as the molecule–molecule interactions dominate. For the slip and transitional flow, the molecule–wall interaction become relevant, resulting in gradually rising slip boundary conditions. Here, viscous flow and Knudsen diffusion are superimposed to the Knudsen flow. Finally, for the pure Knudsen diffusion, the molecule–molecule interactions and, thus, the idea of a continuum flow completely vanish.

At the conditions in the context of this work (water vapour at 1–10 kPa and 10–100 °C) λ_{MFP} is in the range of 0.4–5 µm (see above), with $\lambda \sim T$ and $\lambda \sim p^{-1}$. Thus, for pores sizes above 0.5 mm, the viscous flow is the only relevant mechanism. In practice, this applies, e.g., to all macroscopic vapour channels in the mm-range and above. In smaller pores both, viscous flow and Knudsen diffusion, need to be considered, at least for some p, T-conditions, while for pores below 0.04 µm the viscous flow becomes totally irrelevant.

The viscous flow can be described with the Hagen–Poiseuille equation, a particular solution of the Navier–Stokes equations (Kast, 1988), where the volume flow $\dot{V} = \dot{m}/\rho$ is proportional to the pressure gradient ∇p, thus:

$$\dot{m}_{\mathrm{vis}} = -A_{\mathrm{P}} \frac{\rho}{\eta} \frac{d_{\mathrm{P}}^2}{32 \mu_{\mathrm{vis}}} \nabla p. \tag{36}$$

Parameters are the pore cross section A_{P}, the dynamic viscosity η and the tortuosity applicable to the viscous flow μ_{vis}. The latter designates the length of the actual flow path through a winding pore structure compared to that of a straight cylindrical pore.

For the Knudsen diffusion, the molar flow is proportional to the concentration gradient in the gas phase ∇c_{g}:

$$\begin{aligned} \dot{n}_{\mathrm{Kn}} &= -A_{\mathrm{P}} D_{\mathrm{Kn}} \nabla c_{\mathrm{g}} \\ &= -A_{\mathrm{P}} \frac{4}{3} \frac{d_{\mathrm{P}}}{\mu_{\mathrm{Kn}}} \sqrt{\frac{RT}{2\pi}} \nabla c_{\mathrm{g}}. \end{aligned} \tag{37}$$

Here, D_{Kn} is the Knudsen diffusion coefficient and μ_{Kn} the tortuosity applicable to the Knudsen diffusion.

For the slip flow and transitional regime, both flows are superimposed to

$$\dot{n} = \dot{n}_{\mathrm{Kn}} + \dot{n}_{\mathrm{vis}}. \tag{38}$$

Formally, also the viscous flow can be expressed as a diffusion equation with a "viscous diffusion coefficient" D_{vis} (Laurenz, 2012):

$$\begin{aligned} \dot{n} &= -A_{\mathrm{P}} D_{\mathrm{vis}} \nabla c_{\mathrm{g}} \\ &= -A_{\mathrm{P}} \left(\frac{p}{\eta} \frac{d_{\mathrm{P}}^2}{32 \mu_{\mathrm{vis}}} \left[\boldsymbol{I} + \frac{\nabla T}{T} \left(\frac{\nabla c_{\mathrm{g}}}{c_{\mathrm{g}}} \right)^{-1} \right] \right) \nabla c_{\mathrm{g}}, \end{aligned} \tag{39}$$

Unfortunately, the effect of the temperature on the density leads to an undesirable dependency of D_{vis} on the concentration gradient itself. However, this allows summarising both effects as

$$\dot{n} = -A_{\mathrm{P}} D_{\mathrm{eff}} \nabla c_{\mathrm{g}} \tag{40}$$

with an effective diffusion coefficient

$$\begin{aligned} D_{\mathrm{eff}} &= D_{\mathrm{Kn}} + D_{\mathrm{vis}} \\ &= \frac{4}{3}\frac{d_{\mathrm{P}}}{\mu_{\mathrm{Kn}}}\sqrt{\frac{RT}{2\pi}} + \frac{p}{\eta}\frac{d_{\mathrm{P}}^2}{32\mu_{\mathrm{vis}}}\left[\boldsymbol{I} + \frac{\nabla T}{T}\left(\frac{\nabla c_{\mathrm{g}}}{c_{\mathrm{g}}}\right)^{-1}\right] \\ &\approx \frac{4}{3}\frac{d_{\mathrm{P}}}{\mu_{\mathrm{Kn}}}\sqrt{\frac{RT}{2\pi}} + \frac{p}{\eta}\frac{d_{\mathrm{P}}^2}{32\mu_{\mathrm{vis}}}. \end{aligned} \tag{41}$$

For the conditions considered in this work, the common assumption (Füldner, 2015) is made that the impact of the temperature gradient is negligible ($\nabla T/T \ll \nabla c_{\mathrm{g}}/c_{\mathrm{g}}$), allowing for a linearization of Eq. (61) with a constant D_{eff} for a small temperature and pressure range.

Micropore diffusion

For the mass transfer in the micropores with $d_{\mathrm{P}} < 2\ \mathrm{nm}$ (Rouquerol *et al.*, 1994), the notion of a gas flow, be it individual molecules or a continuous phase, loses significance, as the molecular diameter (0.3 nm for water) has the same order of magnitude. All adsorbable molecules are within the direct influence of the adsorbent surface, i.e. in adsorbed state. The mass transfer effect in this, in our case crystalline, domain is referred to as *surface diffusion* or *adsorbate diffusion* with the chemical potential μ as the driving force, which is related to the concentration of the adsorbate c_{a} with assumption of an ideal vapour phase in equilibrium (Kärger *et al.*, 2012). Assuming isothermal conditions, the molar flux in the micropores is

$$\dot{n} = -A_{\mathrm{P}} D_{\mathrm{mi}} \nabla c_{\mathrm{a}} \tag{42}$$

where c_{a} is related to the micropore volume. Given the size of the adsorbent crystals (few µm), their thermal conductivity and the heat fluxes considered here, temperature gradients on this scale are negligible.

The mass balance of the micropore leads to the diffusion equation

$$\frac{\partial c_{\mathrm{a}}}{\partial t} = \nabla(D_{\mathrm{mi}} \nabla c_{\mathrm{a}}). \tag{43}$$

As $c_{\mathrm{a}} = X\rho_s/(M\varepsilon_{\mathrm{mi}})$, with the apparent crystal density ρ_{s}, the molar mass M, and the adsorbent crystal porosity $\varepsilon_{\mathrm{mi}}$ all being constants that can be dropped on both sides of the equation, the diffusion equation may be related to the loading X without further assumptions:

$$\frac{\partial X}{\partial t} = \nabla(D_{\mathrm{mi}} \nabla X). \tag{44}$$

The micro diffusivity D_{mi} is also referred to as transport diffusivity, which can be related to the adsorbate self or tracer diffusivity D_{ad} (Kärger *et al.*, 2003):

$$D_{\mathrm{mi}} = D_{\mathrm{ad}} \frac{\mathrm{d} \ln p}{\mathrm{d} \ln X}. \tag{45}$$

The additional correction factor is referred to as *thermodynamic factor* or *Darken factor*[1] and shows the strong loading dependency of D_{mi} for non-linear isotherms. It can be conveniently related to the slope of the isotherm:

$$\begin{aligned} \Gamma &= \frac{\mathrm{d} \ln p}{\mathrm{d} \ln X} \\ &= \frac{X}{p} \left(\frac{\partial X}{\partial p} \right)^{-1}. \end{aligned} \tag{46}$$

The temperature dependency of the adsorbate diffusivity D_{ad} may be assumed similar, at least in a first approach, to that of diffusion in solids. In solids the diffusivity is proportional to the Boltzmann factor $\exp(-E_{\mathrm{a}}/RT)$, which is the probability of a vibrating atom or molecule to have an energy higher than E_{a}, the activation energy, which is required in order to overcome the energy barrier to a neighbouring site (Kärger *et al.*, 2012). This yields the common Arrhenius type equation

$$\ln D_{\mathrm{ad}} = \ln D_{\mathrm{ad},0} - \frac{E_{\mathrm{a}}}{RT}. \tag{47}$$

Micropore diffusion may be approximated with a linear driving force (LDF) approach by analogy to the isothermal case with linearized equilibrium and homogeneous uptake distribution, i.e. when close to equilibrium (Glueckauf, 1955). In this case, the change in average loading $\bar{X}$ is proportional to its deviation from equilibrium:

$$\frac{\partial \bar{X}}{\partial t} = k_{\mathrm{LDF}} \left(X_{\mathrm{eq}} - \bar{X} \right). \tag{48}$$

Under the above mentioned assumptions and for the case of a step response, being close to equilibrium, Glueckauf (1955) showed that the LDF coefficient k_{LDF} can approximately be related to the diffusivity with

---

[1] Kärger and Ruthven (2012) discussed the origin of the equation and conclude that the common attribution to Darken (1948) is most probably incorrect.

$$D_{\mathrm{mi}} \approx \frac{k_{\mathrm{LDF}}\mathrm{r}^2}{\sigma(\sigma+2)}, \tag{49}$$

where the curvature factor $\sigma = rA/V = 1$ for the flat plate geometry of the 1D channel structure of the aluminium fumarate crystals investigated here. Likewise, values for σ are 2 for cylinder, and 3 for sphere geometries. r is the distance between the surface and the no-flux boundary, i.e. the particle radius for a domain accessible from all sides or the layer thickness for an even layer accessible from only one side.

Surface barrier resistances

In addition to the diffusion in the bulk, a barrier resistance at the surface may exist. This can either be a resistance at the molecular level of the pore mouth for micropore diffusion (Kärger *et al.*, 2012), or a boundary layer of a secondary non-adsorbable species at the macroscopic composite surface (Bathen & Breitbach, 2001). The latter is irrelevant for a single component system at normal operation and disregarded in the following. Although, its impact, when non-adsorbable gases are introduced unintentionally, e.g., due to leakage or outgassing, can be detrimental for AHT at application level (Sapienza *et al.*, 2016).

Barrier resistance at micropore surfaces is a known phenomenon for, e.g. carbon molecular sieves (Jordi & Do, 1993), that can occur as only dominant mechanism, or in parallel to bulk diffusion in the micropores (Qinglin *et al.*, 2003). A barrier resistance is modelled, analogously to the heat transfer contact resistance, as a Cauchy boundary condition of Eq. (43) at the surface (Wang & LeVan, 2011):

$$D_{\mathrm{mi}} \frac{\partial X(x_0)}{\partial x} = k_{\mathrm{b}} \left(X_{\mathrm{eq}} - X(x_0) \right). \tag{50}$$

Here the flux is proportional to the difference between the actual loading and the equilibrium loading X_{eq}, that would settle eventually at the surrounding temperature and pressure conditions. The constant of proportionality is the barrier coefficient k_{b} ($[k_{\mathrm{b}}] = \mathrm{m/s}$).

In reference to the comparison of convective and diffusive mass transfer and similar to the Biot number for heat transfer, a Sherwood number $\mathrm{Sh} = k_{\mathrm{b}} r / D$ can defined in order to differentiate between different limitations. For $\mathrm{Sh} \to \infty$, the surface barrier is negligible (and as such most probably unknown). For $\mathrm{Sh} \to 0$, the micropore diffusion may be neglected. In this case the loading inside the micropore domain is constant in space and the diffusion equation simplifies to

$$\frac{\partial \bar{X}}{\partial t} = \frac{k_{\mathrm{b}} A}{V} \left(X_{\mathrm{eq}} - \bar{X} \right), \tag{51}$$

with A/V being the surface to volume ratio of the microporous domain. This is exactly the LDF equation mentioned above. Thus, for a known geometry of the microporous domain, k_{b} can be directly related to k_{LDF}. It should be noted that for $\mathrm{Sh} \to 0$, Eq. (51) is an exact solution, whereas for $\mathrm{Sh} \to \infty$ the Eqs. (48) and (49) are merely approximations.

An approach for modelling both, surface and gas diffusion, in parallel has been developed by Sun & Meunier (1987) and extended recently (Füldner, 2015). However, in the case of this work, both transport mechanisms are assumed to occur separately at distinct scales. The contribution of surface diffusion on the macro level is assumed negligible, given that the macropores of the investigated composites are in the µm range. Mesoporous materials will not be considered.

2.2.3 Measurement methods

Measurements related to adsorption dynamics are either based on a transient adsorption process in the time or in the frequency domain, or as direct measurements of the transfer properties related to the adsorption dynamics, e.g. diffusivities or thermal conductivity. Depending on the approach and the information of interest, different sample sizes may be used, like whole heat exchangers (large), small representative Ad-HX cut-outs with well-defined geometry (small), or microscopic amounts of adsorbent with undefined geometry (micro).

Measurements on the level of whole appliances are excluded here. Apart of direct prototype performance characterisation, they have been used to inform empirical models allowing to predict impact of varying operation conditions (Schicktanz & Núñez, 2009; Lanzerath, 2013). Though, none of the heat and mass transfer mechanisms introduced above may be resolved at this coarse level.

2.2.3.1 Time domain adsorption measurements

Adsorption-based measurements in the time domain are typically performed as step response analysis, where a large or small sample at a pre-defined equilibrium state is exposed to a sudden change of at least one boundary condition, and subsequently reaches a new equilibrium state with a distinct temporal evolution. For the step response analysis, basically three methods are distinguished in literature: large temperature jump (LTJ), large pressure jump (LPJ), and the small pressure jump (SPJ). A good overview on adsorption-based measurements can be found in a recent review (Aristov, 2020).

The LTJ is the most widely used experimental technique (Aristov, 2020). After pre-conditioning at given temperature and pressure/loading, the temperature boundary condition of the sample is changed as quick as possible. For small samples this may be done by changing the temperature of a cold plate hosting, e.g., a mono- or multi-layer granular bed (Aristov *et al.*, 2008), or a coated composite material (Velte *et al.*, 2017). For complete heat exchangers, the step is applied to the inlet temperature of the HTF (Sapienza *et al.*, 2014; Graf *et al.*, 2016). The temporal evolution of the uptake is measured mostly either manometrically or gravimetrically. Manometrical measurements are restricted to small samples, as a vacuum vessel is required that is large enough to provide the adsorptive while keeping the conditions close to isobaric. For large samples, the gravimetric method is employed. Additionally, the uptake may be estimated through the samples energy balance, either, for small samples, with a heat flux sensor placed between cold plate and sample (Schnabel *et al.*, 2010; Tierney *et al.*, 2016), or, for large samples, with the in- and outlet temperatures of the HTF (Tokarev & Aristov, 2017). In these cases, the caloric mean temperature and the heat capacity of the sample must be measured or estimated in order to close the energy balance which leads to additional uncertainties. Further, stability issues have been reported for heat flux sensors under pure water vapour atmosphere.

For LPJ experiments, the samples temperature conditions (cold plate temperature or HTF inlet temperature) are kept constant, and the gas pressure above the sample is changed by opening a valve to a second vacuum vessel, pre-conditioned with vapour at a different pressure. As for the LTJ, the uptake change is measured manometrically for small samples (Schnabel *et al.*, 2010) or gravimetrically for large samples (Wittstadt *et al.*, 2015).

The SPJ method consists of several small successive pressure jumps performed on small samples, with each step reaching equilibrium. With this approach, the variation of the thermodynamic state of the sample throughout an individual step is minimised to the expense of a limited signal-to-noise ratio. A specific SPJ, where isothermal conditions are assumed throughout, is the isothermal differential step (IDS) method (Kärger *et al.*, 2012).

Temporal uptake evolutions obtained by conventional TG measurements from commercially available devices, which are more accessible compared to the methods mentioned before that require custom built setups, are "strongly discouraged" (Aristov, 2020) for the derivation of HMT parameters. The processes in TG devices are either determined by multi-component diffusion in the surrounding humid gas flow (open TG) or by strong and undefined heat transfer resistance (closed TG). Both effects have nothing to do with the heat and mass transfer processes relevant to adsorption dynamics in AHT. The same applies to other measurements of the temporal evolution of the uptake from a humid gas stream, e.g. by X-ray diffractometry.

In most AHT-related studies adsorption dynamic measurements are performed with the aim to provide some kind of performance evaluation und application-like conditions (Aristov, 2020). The results are interpreted directly and only valid for the boundary conditions and the exact sample measured. The extrapolation to the scale of an actual application, especially from small samples, requires a considerable amount of assumptions and is subject to intensive discussion (Aristov, 2020). No information on HMT parameters is obtained and effects of design parameters or changing boundary conditions may only be included by extensive sample and measurement variation.

However, with parameter identification (PI) adsorption-based measurements are employed with different methodological paradigm. Here, HMT parameters are determined indirectly by comparing the experiment to a model, and trying to minimise the deviation between them. The estimated parameters allow for this minimisation. The estimation of performance under application conditions requires an additional simulation step based on the estimated parameters. While this is more elaborate compared to application mimicking, this approach allows including additional upscaling effects for measurement on small samples, like thermal conduction in the heat exchanger or an heat exchanger fluid with finite heat capacity rate, or changing operation conditions for measurements on both, small and large samples, like mass flow of the HTF, temporal evolution of inlet temperature levels or pressure levels. Here the later may especially be determined from transient evaporator/condenser models.

One of the simplest forms of PI is based on isothermal models with a single Fickian diffusion resistance and consist of linear regression to the initial uptake of SPJ experiments (Ovoshchnikov *et al.*, 2011; Kärger *et al.*, 2012). However, this approach is of limited use for AHT, where the thermal effect is purposely high, as the adverse effect on the supposed isothermal conditions does not decrease with the step size of the SPJ (Sun *et al.*, 1993).

Hence, non-linear time domain models have been used recently by other authors that may only be solved numerically in comparison to LPJ measurements on small samples (Dawoud *et al.*, 2007; Füldner, 2015) and LTJ measurements on small samples (Velte *et* *al.*, 2017) or large samples (Wittstadt *et al.*, 2014; Graf *et al.*, 2016). Moreover, Velte *et al.* (2017) proposed to analyse the heat transfer separately by performing additional LTJ measurements under the inert conditions of a nitrogen atmosphere. LTJ-based PI has generally a limited resolution of the thermodynamic state: Only one set of parameters is identified for the whole range of the step. For smaller steps the precision deteriorates, due to the limited signal-to-noise ratio. Uncertainty reduction by repetition is practically limited through the long equilibration times required for each measurement.

PI, performed on small or large samples, differs in the precision with which parameters may be identified and the amount of transport effects included, thus the amount of assumptions required for extrapolation to actual applications. Small samples, where boundary conditions are tightly controllable with limited spatial variation and edge effects may be neglected, allow for the use of PDE model on simplified geometries which are necessary to identify transfer coefficients, like diffusivities or thermal diffusivities. Measurements on large samples include additional effects from the heat exchanger geometry and both sides of the Ad-HX, i.e. the distribution of the adsorbent (composite) on one side and the HTF on the other side. This makes the results more closely related to the appliance level, while spurious effects from, e.g., mal-condensation or valve switching delays are excluded. The effect of inert gases is also excluded or may be introduced in controlled manner, in order to evaluate its effect (Glaznev & Aristov, 2008; Sapienza *et al.*, 2016). However, the typically complex heat exchanger geometry and coupled variation in boundary conditions on the side of the HTF makes the deduction of local transport properties difficult to impossible.

The identification of effective transport resistances is a different evaluation approach, that has been suggested recently for HMT problems in AHT (Ammann *et al.*, 2018; Ammann *et al.*, 2019). The effective transport resistances lump transfer coefficients and geometry influences, and do not require detailed geometry information nor detailed modelling but just a thorough description of the sorption equilibrium. With an additional temperature measurement they allow for discrimination of heat and mass transfer effect. As explicit geometry information is lacking, the method does not directly allow for model based design optimisation. It is based on the concept of driving temperature equivalent proposed earlier by Wittstadt *et al.* (2017) and will be further elaborated in Section 3.2.

2.2.3.2 Frequency domain adsorption measurements

The FRA is an established (Kärger *et al.*, 2012) method for the determination of heat and mass transfer processes in adsorption systems since the 1960s (Naphtali & Polinski, 1963; Yasuda, 1982; Iglesia & Reyes, 1994; Sun *et al.*, 1994; Sward & LeVan, 2003; Song & Rees, 2008; Giesy *et al.*, 2012): From a set equilibrium state an adsorbent sample is exposed to an, e.g. sinusoidal, periodical fluctuation of one variable (excitation) while the response of one or more other variables is recorded. The experiment is carried out at different frequencies in order to evaluate the response in the frequency domain, i.e. the frequency response (FR). The method has several principal advantages compared to time domain methods:

1. Separation of different transport processes, as they are visible at different frequencies depending on their time constant and with different patterns depending on the transport mechanisms
2. High resolution of the thermodynamic state, as during the experiment the systems is kept in a small region around a constant equilibrium state

3. Easily scalable accuracy by changing the duration of the experiment, i.e. changing the number of periods measured
4. Usage of locally linearised models with constant coefficients without accuracy loss, as in the small state region non-linearities may typically be neglected
5. Measurements in the frequency domain allow for usage of model solutions directly in the Laplace domain, generally easier to obtain compared to the time domain.
6. Computationally inexpensive parameter identification, as for linearized models in the Laplace domain analytical solutions can be derived in most cases

These advantages outweigh the considerable experimental and data processing effort, especially if a quantitative differentiation, between different transport processes for different thermodynamic states (temperature, loading, pressure) of the system, is required.

According to the quantity used for excitation, different FRA types are distinguished in literature: For the *volume swing frequency response* (VSFR) the volume of a closed measuring chamber is varied, e.g., with a mechanically driven bellow, while the pressure fluctuation is recorded. This was the first configuration (Naphtali & Polinski, 1963) and is still the most widely used. Other approaches are the *pressure swing frequency response* (PSFR) (Sward & LeVan, 2003), and the *concentration swing frequency response* (CSFR) (Wang & LeVan, 2008), which are based on flow-through systems. One or more mass flow controllers are used to apply either a pressure excitation for single constituent experiments, or a concentration excitation for multi component experiments. These approaches were, amongst other things, motivated by the reduced temperature fluctuations due to convective heat transfer, in order to allow for the application of isothermal models. Taking into account these temperature fluctuation, also referred to as "heat effect" (Sun *et al.*, 1993; Sun *et al.*, 1994), was also the reason behind the *thermal frequency response* (TFR) (Bourdin *et al.*, 1996a; Bourdin *et al.*, 1996b). With this VSFR setup, developed and operated at the Laboratoire d'informatique pour la mécanique et les sciences de l'ingénieur (LIMSI), a CNRS institute in Orsay near Paris, the response sample surface temperature was measured using a costly high precision fast infrared (IR) detector cooled with liquid helium (Bourdin *et al.*, 1998). The TFR was applied to understand the thermal effects on mass transfer identification. Although, effective thermal resistance where identified, a detailed heat transfer analysis was not the explicit aim of these studies. Since the work at LIMSI, no other TFR reports could be identified in literature.

Extensive overviews over FR apparatus in literature can be found in reviews and text books (Song & Rees, 2008; Kärger *et al.*, 2012), with some instruments being described very detailed in dedicated publications (Bourdin *et al.*, 1998; Turner *et al.*, 2001).

FRA has been applied to a wide variety of adsorbents and adsorptives for all kinds of adsorption applications, e.g., the adsorption kinetics of CO_2 and N_2 in commercial 13X zeolite pellets and O_2, N_2 and Ar in carbon molecular sieves (Giesy & LeVan, 2013; Giesy, 2014; Mohammad Iftekhar Hossain, 2014). However, measurements relevant to AHT, namely with water, are scarce with few exceptions like the investigation of water on NaX zeolite crystals and pellets with the TFR (Bourdin *et al.*, 1996b). A reason could be the strong heat effect, which is problematic for classical FR but required for AHT.

In principle, FR apparatus may also be used to apply a SPJ evaluated in the time domain, which is also referred to as "single step FR" (Song & Rees, 2008), as, e.g., done to assess the diffusion of H_2O in spherical silica gel granules (Gurgel *et al.*, 2001).

A concentration swing FRA has been used to study the mass transfer of water from a humid He stream in the zirconium based MOF UiO-66 (Hossain & Glover, 2019).

Measurements were performed at room temperature, and – in order to distinguish macro and micropore diffusion – on single pelletized granules of different sizes in the mg scale. The results showed a U-shaped loading dependency of the micropore transport diffusivity, presented as the inverse characteristic time D/r^2. The transport diffusivity could not be quantified, due to missing information about the diffusion length.

2.2.3.3 Direct measurements

The HMT transfer parameters relevant to adsorption dynamics may alternatively be measured directly as material properties with approaches that may be independent of an adsorption process.

The measurement of micropore diffusivity in pores is a large field of experimental physics, in which a variety of methods have been developed (Kärger *et al.*, 2012). These methods are applied to phenomena on the scale of several unit cells up to several µm, which is considered as "microscopic" here, and may be differentiated into equilibrium and non-equilibrium techniques. Equilibrium techniques allow the determination of the adsorptive self-diffusivity by tracing the displacement of individual molecules over a specified period of time; either by introducing radioactive isotopes as tracers or by labelling molecules with their magnetic dipole, e.g., with the pulsed field gradient nuclear magnetic resonance (PFG-NMR). Microscopic non-equilibrium methods involve the induction of a transient adsorption process and the measurement of the temporal evolution of concentration profiles, e.g., through IR microscopy (Chmelik *et al.*, 2010). A detailed discussion of these methods and their applicability to AHT problems has been provided by Füldner (2015). A practical issue arises from the extrapolation of microscopically determined diffusivities to the application scale, as this requires detailed information about the geometry at the microscopic level and assumptions about the scale-up effects, like intra- and intercrystalline defects, additional barrier resistances between macro and micro level etc. Moreover, there might be practical experimental restrictions, like the provision of large single crystal for IR microscopy or iron free material samples for PFG-NMR, making these methods inapplicable to certain materials relevant to AHT. However, directly measured diffusivities are important additional information to validate assumptions made for macro scale models and to allow for a holistic understanding of the underlying transfer mechanisms. Especially the mismatch of microscopic and macroscopic results triggers the search for additional transfer effects that eventually might lead to further improvement.

Macropore diffusivity may be measured with permeation experiments in a Wicke–Kallenbach diffusion cell (Wicke & Kallenbach, 1941), where a pressure difference is applied over a macroporous sample while the flux is measured. With measurements at different absolute pressures viscous flow and Knudsen diffusion may be differentiated and quantified. This method is suitable for the investigation of flat samples, accessible from both sides, but not for, e.g. granular samples or coatings too brittle to be detached from a closed support. Still, it has been used to measure macropore diffusion in SAPO-34 coated metallic fibre structures for AHT (Füldner, 2015).

Thermal conductivity may be measured by transient or steady state methods, which have crucial limitations when applied to adsorbent materials for AHT. Transient methods in the time domain, like the hot disc method (Gustavsson *et al.*, 1994) or the laser flash analysis (Parker *et al.*, 1961), or in the frequency domain, like the 3ω method (Cahill & Pohl, 1987), are popular for measuring thermal diffusivities of thin solid samples. However, they all assume a heat equation with no additional source term. As the adsorption-related term in Eq. (32) is tightly coupled to mass transfer properties and thus may not be easily corrected in the analysis, transient methods may not be applied to adsorption materials unless completely desorbed. For steady state methods, the thermal conductivity is derived from heat flux and temperature difference over a known sample thickness. The heat flux through the sample is either measured directly (heat-flux-method) or derived from an electrical heat source making sure that all heat released is conducted through the sample (guarded-hot-plate method). The first method, that requires calibration with a reference material, has been applied under air atmosphere at different temperatures for zeolite 13X composites with different additives (Wang *et al.*, 1999). Contact effects are reported to be included in the calibration. The authors mention the comparative nature of their experiment, as under air the results are likely to differ from application conditions with a pure adsorptive low pressure atmosphere. The second method was for applied for discs of monolithic carbon, also under air atmosphere (Tamainot-Telto & Critoph, 2001). Here, the contact resistance between sample and plates was estimated with an equivalent air gap, based on the sample surface roughness. These steady state measurements required samples in the order of several mm to cm. Measurements under application conditions of AHT could not be found in literature. A reason – beyond the high experimental effort required – might be the contact resistance, which is increased by low pressures, leading to high uncertainties. Hence, at present the determination of thermal conductivities in adsorption material under application conditions is limited to adsorption-based PI methods discussed above.

2.3 Adsorption Heat Transformation

In general, thermally driven heat transformers regroup different kinds of chillers, heat pumps, and thermal energy storages. They use the virtual work, potentially released from a first heat flow dropping from a higher to a lower temperature level, to lift a second heat flow from a lower to a higher temperature level (Figure 4). These appliances may be realized based on the principle of adsorption heat transformation (AHT), which allows simple, robust and scalable designs. For various applications, different cycles have been developed, mainly characterised by the relation between the different temperature levels. In all cases the cycles are intermittent, with a first half-cycle where heat is dropping in temperature, and a second half-cycle where heat is lifted in temperature.

2.3.1 Working principle

The working principle of an adsorption chiller will be explained for the example of data centre cooling (Figure 3). The chiller consists of two Ad-HXs, a condenser and an evaporator in a pure working fluid atmosphere. If temperatures below 0 °C can be excluded, usually water is used as working fluid for its high evaporation enthalpy. The Ad-HXs have a HTF on the primary and a stationary adsorbent material or composite on the secondary side. The process is cyclic: In the first half-cycle the waste heat from the CPUs is used to regenerate the first Ad-HX. The desorbed working fluid is condensed in the condenser which is cooled through a heat rejection to the ambient at, e.g., 30 °C. This part of the cycle is running at a high pressure, above the saturation pressure of the condenser. In the second half-cycle, working fluid is adsorbed on the Ad-HX which is again cooled to the ambient. This allows for a low pressure inducing the evaporation in the evaporator at about 20 °C. For continuous provision of cold, two Ad-HXs are operated alternately. The saturated liquid working fluid flows through a throttle element, where it undergoes an adiabatic expansion from the condenser to the evaporator pressure leading to flash evaporation of a small fraction of the working fluid. With passive check vales between the heat exchangers, this process does not require any mechanically actuated components.

For heat pump applications the same cycle is used, except that the medium-temperature heat is used and the low-temperature heat is provided from an ambient source. As here useful heat is provided during both half-cycles, either from condensation or from adsorption, designs with a combined evaporator–condenser are often used. This design is even simpler, as check valves or throttle elements are unnecessary. However, the thermal mass of the evaporator–condenser is cycled between condension and evaporation temperature, which reduces the overall efficiency.

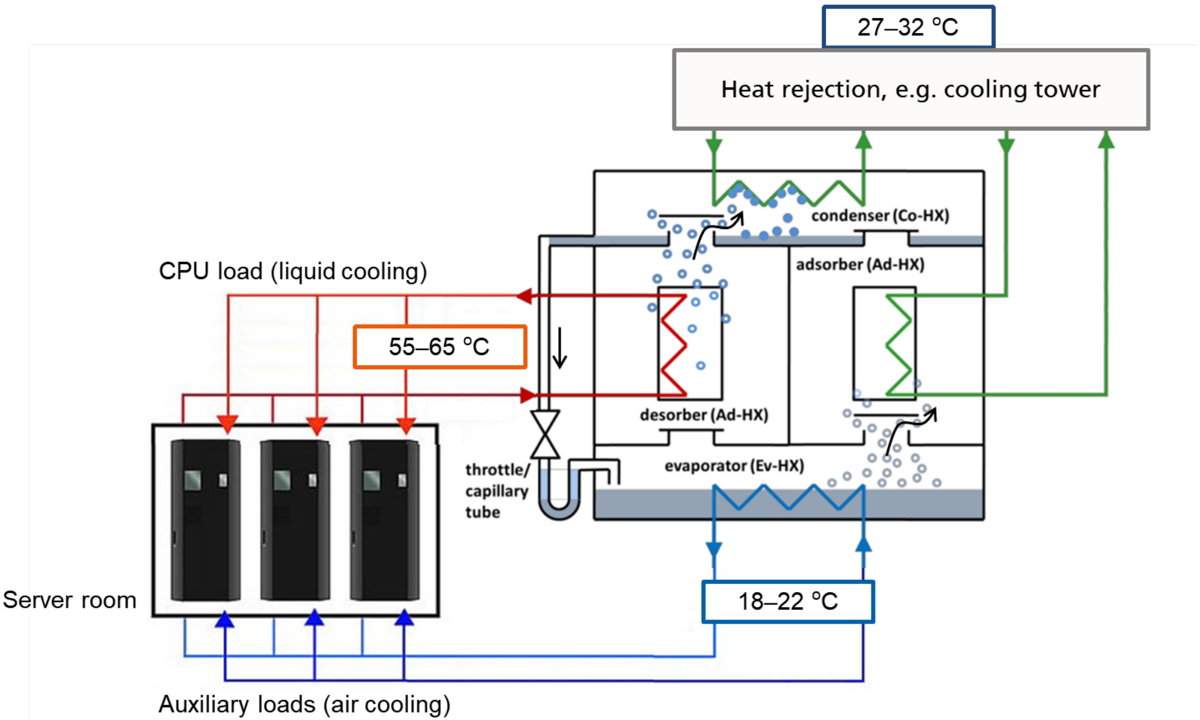

© by Laurenz *et al.*, 2020 / CC BY 4.0

Figure 3: Working principle of an adsorption chiller for the example of data centre cooling: The waste heat recovered from the CPUs by liquid cooling is driving the chiller providing cooling to the auxiliary loads through air cooling

2.3.2 Applications

Adsorption chillers have been successfully applied for cooling of buildings or goods driven by solar heat, excess heat from combined heat and power (CHP) or industrial processes (Deng *et al.*, 2011; Meunier, 2013). Adsorption heat pumps are, e.g., used to efficiently provide heat for space heating or domestic hot water supply. This useful heat is increased by using the temperature difference between the combustion temperature and the usage temperature to lift environmental heat to the usage temperature level (Metcalf *et al.*, 2012; Wittstadt *et al.*, 2017). Similarly, the approach “heat from cold” suggests using the temperature difference between two natural heat reservoirs in very cold climates. Heat from non-frozen waters flowing to the very low temperatures of ambient air could be used to lift heat from the first source to a level useful for space heating (Aristov, 2017b).

The same principle has been used to demonstrate thermal energy storage by interrupting the cycle between the two half-cycles. In this case the temperature levels of the two half cycles are similar, e.g. between a charging temperature level and an environmental reservoir and vice versa. This field has attracted widespread research activities in recent years as summarised in a recent review by Fumey *et al.* (2019), where, in contrast to many other review papers, special attention is payed to the role of the different temperature levels involved. Commercial application of sorption-based thermal energy storage is scarce and yet limited to niche applications like, e.g., temperature controlled transport containers (Rigaud *et al.*, 2015). Despite massive research activities, it remains unclear when, or if at all, applications for the long-term storage of solar thermal energy for buildings will be viable. The German government-funded research project MAKSORE found that with currently available adsorbents several hundred storage cycles per year were necessary in order to reach commercial and ecological (in terms of CO_2-equivalents) viability for this application (Velte *et al.*, 2018). Beneath these commercial and sustainability related questions, the main technological challenges have been summarised as (Aristov, 2017a): "(i) the driving temperature is low, hence temperature losses in adsorbent and heat exchanger unit must be strictly minimized; (ii) solar heat can be highly variable in time, therefore good desorption dynamics is very important to accept high insolation regimes; (iii) the rate of heat recovery during winter time is essentially restricted by low vapour pressure in an evaporator coupled to the ambient."

A novel application of adsorption chillers that has attracted rising interest in recent years is the provision of data centre air cooling driven by heat yielded from water cooled high-temperature CPUs. Current high performance CPUs allow cooling water temperatures of up to 60 °C or more (Zimmermann *et al.*, 2012; Wilde *et al.*, 2017) that can be used to drive adsorption chillers providing cooling for auxiliary loads, e.g. from hard disks and power supplies.

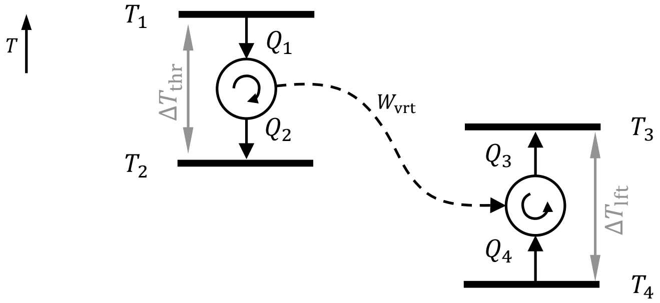

Figure 4: Generic ideal heat transformer as a combination of a clockwise and a counterclockwise Carnot cycle with heat transferred from or to four temperature reservoirs at different arbitrarily chosen levels. Virtual work is exchanged between both half-cycles.

2.3.3 Thermodynamic cycles and performance evaluation

For the analysis of any AHT two thermodynamic cycles are relevant that will be introduced in the following: The Carnot cycle, representing the upper boundary in terms of efficiency, and the ideal adsorption cycle, that takes into account the thermodynamic properties of the adsorbent–refrigerant pair. Two fundamental figures of merit for efficiency and compactness will be introduced.

The ideal thermally driven heat transformation cycle operates between four infinite heat reservoirs at constant temperature (Figure 4). It is a combination of two Carnot cycles: firstly, a clockwise (power) half-cycle operating between T_1 and T_2 that uses the heat Q_1 to provide the virtual work w_{vrt}, while discharging the heat Q_2, and, secondly, a counterclockwise (heat pump and refrigeration) half-cycle operating between T_3 and T_4 that uses w_{vrt} to remove the heat Q_4 and reject the heat Q_3. Here, the virtual work w_{vrt} is a purely theoretical quantity without any relation to any actual physical phenomenon.

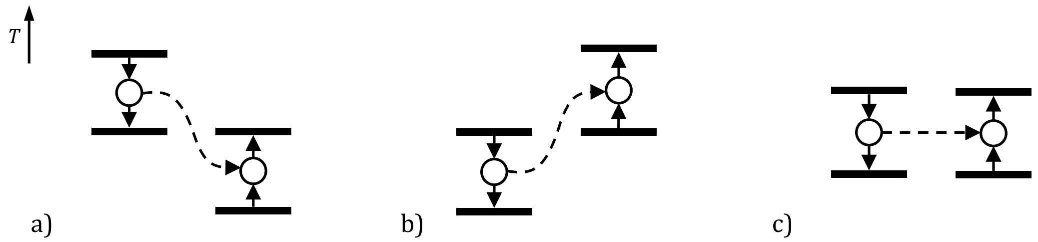

Figure 5: Variation of the ideal heat transformer (c.f. Figure 4): a) Ideal chiller/heat pump cycle, heat from both half-cycles is rejected at the same medium temperature level, b) ideal heat upgrading cycle, both half-cycles are fed from the same medium temperature level, useful heat is provided at elevated temperature level, c) ideal storage cycle, heat from the heat pump half-cycle is rejected at the driving temperature level.

While, in principle, all temperature levels may be chosen independently, three basic variations of the cycle are especially relevant to applications (Figure 5):

a) The first is the ideal thermally driven heat pump and refrigeration cycle, where the heat rejection occurs at the same temperature level. This medium temperature level T_{M} can be either an ambient temperature (chiller) or the useful heating temperature (heat pump).
b) The second is the ideal heat upgrading cycle, where both half-cycles are driven from heat at medium temperature level with some heat being discharged at low temperature, typically to an ambient heat sink, and some heat at a (useful) high temperature level. This cycle is, e.g., the basis of the “heat from cold” concept (Aristov, 2017b).
c) The third is the ideal storage cycle, which is only possible if the two half-cycles may be shifted in time. Both half-cycles, now a charging and discharging half-cycle, operate between the same temperature levels. Depending on whether cold or heat is to be stored, either the upper or lower temperature level is at ambient temperature.

In the following, cycle evaluation parameters, i.e. the figures of merit, are introduced for the example of a chiller application. For the other applications they may be derived accordingly.

The overall cooling efficiency of the ideal heat transformation cycle follows directly from the combination of the both Carnot half-cycles (Figure 4), where the power half-cycle has the efficiency $\eta_{\mathrm{C}} = w_{\mathrm{vrt}}/Q_1$ and the refrigeration half-cycle the coefficient of performance for cooling $\mathrm{COP_C} = Q_4/w_{\mathrm{vrt}}$:

$$\begin{aligned}\mathrm{COP}_{\mathrm{C,HT}} &= \frac{Q_4}{Q_1} \\ &= \eta_{\mathrm{C}}\mathrm{COP}_{\mathrm{C}} \\ &= \frac{T_1 - T_2}{T_1} \cdot \frac{T_4}{T_3 - T_4} \\ &= \frac{T_4}{T_1}\frac{\Delta T_{\mathrm{thr}}}{\Delta T_{\mathrm{lft}}}\end{aligned} \tag{52}$$

Following Ziegler (1999), the first temperature difference is referred to as the temperature thrust $\Delta T_{\mathrm{thr}} = T_1 - T_2$ and the second as the temperature lift $\Delta T_{\mathrm{lft}} = T_3 - T_4$.[2] This formulation shows that the theoretical limit of any actual thermally driven refrigeration cycle only depends on the ratio of the high- and the low-temperature level and the ratio of the two temperature differences.

The ideal adsorption heat transformers are physical realizations of these cycles. While the attribution of heats from the Carnot cycle to the adsorption cycle is somehow arbitrary, it is extremely useful to understand Q_1 as the heat used for desorption, Q_2 as the heat from condensation, Q_3 as the heat from adsorption and Q_4 as the heat used for evaporation. This way, the "power" half-cycle from the Carnot process corresponds to the desorption–condensation half-cycle, and the "heat pump and refrigeration" half-cycle to the adsorption–evaporation half-cycle, which is an important pre-requisite for some of the derivations developed later in Section 3.2. Moreover, e.g., the storage cycle of Figure 5c may be obviously realised as adsorption storage cycle.[3]

Usually, the adsorption cycle is represented in a Clausius–Clapeyron diagram (Figure 6), where $\ln p$ is plotted over $-1/T$. According to the Clausius–Clapeyron equation, Eq. (17), the isosteres and the vapour pressure curve of the pure refrigerant are approximately (assuming ideal gas and constant differential adsorption enthalpy) straight lines. However, this representation has a weakness as it is ambiguous in terms of the caloric state of the working pair. Thus, points may be not well defined thermodynamic states and not all processes are represented by connections between them. This is especially the case on the vapour pressure curve of the pure refrigerant, where the saturated liquid and the saturated vapour are superimposed.

The simple cycle without heat recovery works as follows, assuming that the cycle operates between four ideal heat reservoirs at constant temperature levels, as the Carnot cycle. For analogy with the aforementioned cycle, the description starts at point 3, where the adsorbent is at maximal loading X_2, indicated as "wet", and temperature T_3:

3–1 Isosteric heating of the "wet" adsorbent (3–1'), and isobaric desorption of the refrigerant from the adsorbent down to loading X_1 at pressure p_{c} between temperature $T_{1'}$ and T_1 (1'–1), while the required heat Q_1 is supplied at T_1

1–2 Desuperheating and condensation of the pure working fluid at constant pressure p_{c} and temperature T_2, while releasing the respective heat Q_2 at T_2

---

[2] Here, ΔT_{lft} must not be confounded with the temperature difference between in- and outlet of an open (flow-through) sorption system, which may also be referred to as *temperature lift*, especially in the literature on adsorption thermal energy storage (Hauer, 2002).

[3] However, if the analogy between the adsorption heat pump cycle and the vapour-compression cycle is to be stressed, often the adsorption–desorption process is thought as "thermal compression". In this case the (time-shifted) desorption–adsorption is (implicitly) understood as "power-cycle" driving the heat-pump cycle between evaporation and condensation. As the Carnot cycle does not rely on any actual physics both interpretations are possible.

2–4 Isenthalpic expansion of the saturated liquid refrigerant, including partial flash evaporation

1–3 Isosteric cooling of the "dry" adsorbent (1–3'), and isobaric superheating and adsorption of the working fluid up to loading X_2 at pressure p_e between temperature $T_{3'}$ and T_3 (3'–3), releasing the heat from cooling and adsorption Q_3 at T_3

4–3 Evaporation of the pure working fluid at constant pressure p_e and temperature T_4, while supplying the required heat Q_4 at T_4

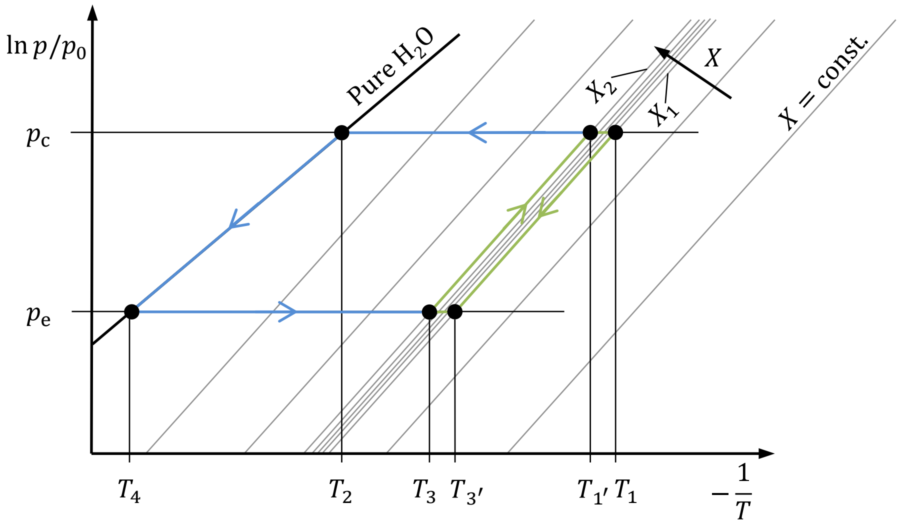

Figure 6: Ideal adsorption heat transformation cycle in the Clausius–Clapeyron plot for a working pair with S-shape isotherm, where the isosteres (grey lines) employed in the cycle form a narrow band and the equilibrium temperatures during ad- and desorption are nearly constant ($T_1 \approx T_1'$ and $T_3 \approx T_3'$)

The first two processes may be seen as the "power" half-cycle and the last two as the "heat pump and refrigeration" half-cycle. In practice, heat recovery might be added, especially between the isosteric heating and cooling phases, e.g. by operating two Ad-HXs shifted in time.

For a sorption material with a perfect step-like isotherm, the temperatures of the de- and adsorption are constant, i.e. $T_1 \approx T_1'$ and $T_3 \approx T_3'$. For this ideal adsorption heat pump and refrigeration cycle, the cooling COP on material level, i.e. without the influence of the thermal mass of any supporting heat exchanger structure, is

$$\mathrm{COP}_\mathrm{mat} = \frac{Q_4}{Q_1} = \frac{(X_2 - X_1)\left(\Delta h_\mathrm{v}(T_4) - \int_{T_4}^{T_2} c_{p,\mathrm{L}}(\vartheta)\mathrm{d}\vartheta\right)}{\int_{\mathrm{X}_1}^{\mathrm{X}_2} \Delta h_\mathrm{s}(\chi, T_1)\mathrm{d}\chi + \int_{T_3}^{T_1} c_{p,s+a}(X_2, \vartheta)\mathrm{d}\vartheta} \tag{53}$$

In the numerator, the integrated specific heat capacity takes into account the effect of the flash evaporation, while the denominator consists of the heat required for the desorption and the isosteric heating.

If the temperature dependency of the specific heat capacities and the loading dependency of the differential adsorption enthalpy Δh_s can be neglected, the integrals may be simplified, which leads to

$$\mathrm{COP_{mat}} = \frac{\Delta X\big(\Delta h_{\mathrm{v}}(T_4) - (T_2 - T_4)c_{p,\mathrm{L}}\big)}{\Delta X \Delta h_{\mathrm{s}}(T_1) + (T_1 - T_3)c_{p,s+a}(X_2)}, \tag{54}$$

with the loading spread $\Delta X = X_2 - X_1$. This material COP is the theoretical upper boundary for any realised adsorption chiller process.

An actual process has, additionally, an Ad-HX with the heat capacity C_{AdHX} and a combined evaporator/condenser with the heat capacity C_{EC} to be considered. For this case and with a single medium temperature level ($T_2 = T_3$) the COP is further reduced:

$$\mathrm{COP_{AC}} = \frac{\Delta X \left(\Delta h_{\mathrm{v}}(T_4) - \Delta T_{\mathrm{lft}}\left(c_{p,\mathrm{L}} + \frac{C_{\mathrm{EC}}}{\Delta X m_{\mathrm{s}}}\right)\right)}{\Delta X \Delta h_{\mathrm{s}}(T_1) + \Delta T_{\mathrm{thr}}\left(c_{p,s+a}(X_2) + \frac{C_{\mathrm{AdHX}}}{m_{\mathrm{s}}}\right)}. \tag{55}$$

For the case of a separated evaporator, the heat capacity of the combined evaporator-condenser C_{EC} is omitted, as the thermal mass of the evaporator is kept at constant temperature.

The efficiency for the heating case, where $Q_3 + Q_2$ are judged “useful”, can be deduced analogously (Schnabel *et al.*, 2018).

The second figure of merit used to evaluate AHT cycles is the specific cooling power (SCP). Depending on the dominant constraint from the application it can either be defined as the volume specific cooling power (VSCP), where compactness and indirectly the amount of auxiliary material counts, or as the adsorbent mass specific cooling power (MSCP), where the amount of adsorbent is relevant.

The VSCP relates the amounts of useful heat to the total cycle time Δt and the reference volume (e.g. of the component) V:

$$\mathrm{VSCP} = \frac{Q_4}{\Delta t \cdot V}. \tag{56}$$

With the same assumptions as above this can be written as:

$$\mathrm{VSCP} = \frac{\Delta X}{\Delta t}\frac{m_{\mathrm{s}}}{V}\left(\Delta h_{\mathrm{v}}(T_4) - \Delta T_{\mathrm{lft}}\left(c_{p,\mathrm{L}} + \frac{C_{\mathrm{EC}}}{\Delta X m_{\mathrm{s}}}\right)\right). \tag{57}$$

Again, the heat capacity of the combined evaporator/condenser C_{EC} is omitted for the case of separated components.

The practical difficulty of Eq. (57) is, that the total cycle time Δt is not available a priori. In contrast to all other variables that determine the COPs, it is not a thermodynamic quantity, but rather a result of the transfer properties of the components, the material properties and the boundary conditions, which is deduced from experiments or simulations. A method for the direct estimation of the SCP without relying on a determination of Δt will be suggested in Section 3.2.

For heating applications, the volume specific heating power can be derived accordingly (Schnabel *et al.*, 2018).

Adsorption heat or cold storage applications may be treated in a similar way in principle, with storage efficiency instead of COP, specific charging and discharging power instead of SCP, and storage density (per volume or mass) as additional parameter (Fumey *et al.*, 2019).

Adsorption heat transformation may also be realised with advanced cycles that may include several effects or stages, or heat recovery. A comparative assessment of these cycles, which are beyond the scope of this work, can be found elsewhere (Velte, 2019).

2.4 Materials

A variety of working pairs, i.e. adsorbent-adsorptive combinations, have been discussed for AHT in literature, that meet the different requirements to different extends (Aristov, 2013; Schnabel *et al.*, 2018).

Working pairs for AHT are primarily characterised by their thermodynamic properties discussed above. Their adsorption equilibrium should allow for a large loading spread under the temperature conditions of the target applications, exhibit a large adsorption enthalpy, a low specific heat capacity. To allow for compact and competitive devices, they should have a high enough density, be easily available at low cost and stable under application conditions. Further, the material should be processable to composites and/or components with good heat and mass transfer properties favourable for high power density with low driving forces.

Overviews of common and promising working pairs are provided, e.g., by Aristov (2013) and Henninger *et al.* (2017), who are discussing all requirements mentioned above.

An adsorptive with a high evaporation enthalpy is crucial for an efficient process, given the cyclic operation and as follows from Eq. (55). Thus, water is the adsorptive of choice, followed by ammonia and methanol, which allow sub-zero evaporation temperatures and avoiding vacuum conditions, to the cost of toxicity and lower evaporation enthalpy.

Silica-gel–water is the working pair, used in most commercial appliances. High stability and a low price compensate the limited uptake, resulting from the linear isotherm. Classical microporous zeolites, like NaX or 4A with water, are especially considered for applications where large ΔT_{lft} are required due to their high hydrophilicity, which on the other hand results in poor performance for most AHT applications, where ΔT_{thr} is limited. Activated carbons, the commercially most relevant material class for classical adsorption applications, have been investigated with ammonia or methanol as a refrigerant (Wang *et al.*, 2009).

S-shaped or step-like isotherms with a large uptake are especially useful for AHT if the application boundary conditions are within narrow bounds (Aristov, 2013). These “discrete sorption materials” allow for cycles with high loading change with small $\Delta T_{\mathrm{thr}}/\Delta T_{\mathrm{lft}}$-ratios, thus, following from Eq. (55), high efficiencies. In the Clausius–Clapeyron-plot (Figure 6) the isosteres of maximal and minimal loading are very close (identical for the case of the ideal step-like isotherm), reducing the adsorption part of the cycle to a small strip. If, however, the temperature conditions are not met, either because of a too high ΔT_{lft}, or a too small ΔT_{thr}, the performance deteriorates completely. This “temperature stiff” behaviour does not occur for materials with a linear isotherm like silica gel or classical zeolites, though large $\Delta T_{\mathrm{thr}}/\Delta T_{\mathrm{lft}}$-ratios are required to allow for sufficient uptake resulting in a difficult trade-off between compactness and efficiency: A large ΔT_{thr} makes efficiency more susceptible to high specific thermal masses of the Ad-HX ($C_{\mathrm{AdHX}}/m_{\mathrm{s}}$ in Eq. (55)), which on the other hand results from power-increasing heat exchanger surface enhancements.

Some metalaluminophosphates exhibit S-shaped isotherms at relative pressures useful for AHT applications. Though more expensive in synthesis, the Chabazite-type silicoaluminophosphate SAPO-34, commercialized as AQSOA FAM-Z02 (Mitsubishi Chemicals), is commercialised currently for AHT applications with $\Delta T_{\mathrm{thr}} \geq 40\,\mathrm{K}$ (Wittstadt *et al.*, 2017). The AFI-type aluminophosphate $AlPO_4$-5 is under investigation for applications requiring lower temperature lifts (and where lower thrusts are available) (Henninger *et al.*, 2017).

In the following two classes of discrete sorption materials are described in details.

2.4.1 Metal–organic frameworks

The most recent class of materials taken into account for AHT applications are metal–organic frameworks (MOFs), porous coordination polymers consisting of metal clusters with organic ligands forming a crystalline porous structure (Henninger *et al.*, 2012). MOFs have attracted considerable research interest in recent years with numerous new materials, exhibiting a preferable S-shape isotherm with high uptakes in an interesting relative pressure range for AHT, and providing the required stability under application conditions. Despite the favourable adsorption properties, MOFs have yet to reach commercially viable prices for actual applications.

Aluminium fumarate, a MOF that attracted increasing interest for thermal applications in recent years, exhibits water adsorption equilibrium properties that fit well to the boundary conditions of adsorptive data centre cooling (Lenzen *et al.*, 2019). Earlier work at Fraunhofer ISE has proven a high hydrothermal cycle stability (Jeremias *et al.*, 2014; Kummer *et al.*, 2017b). Under the temperature conditions depicted in Figure 3 aluminium fumarate undergoes the full uptake step of about 0.3 kg/kg (Jeremias *et al.*, 2014) compared to little more than 0.1 kg/kg for silica gel. This advantage may be used to reduce the amount of adsorbent or to increase the power density by e.g. shorter cycles (Schnabel *et al.*, 2018). The material is potentially a low-cost material due to widely available educts (Al-salts and fumaric acid) and water based synthesis route (Kiener *et al.*, 2009).

Aluminium fumarate has been successfully processed with a polysiloxane-based binder into Ad-HX coatings (Kummer *et al.*, 2017b), which serve as a model adsorbent composite investigated in this work.

The structure of the microporous aluminium fumarate has been analysed by Rietveld refinement (Alvarez *et al.*, 2015). It exhibits a regular pore structure with 1D channels (Figure 7). Chains of Al(OH) octahedrals are connected by fumarate linkers in the cb-plane forming one-dimensional pores with a rhombic cross-section of about $5.7 \times 6.0\ \text{Å}^2$. Water molecules with a diameter of about 3 Å may diffuse through these channels, interacting with the channel walls and each other through hydrogen bonds. In the fully hydrated state, the predicted distance between the water molecules is similar to that of bulk water.

Alvarez at al. estimated the volume of a fully hydrated unit cell, consisting of four Al(OH) octahedral ($m = 4 \cdot 44.0\ \mathrm{u}$) and four fumarate $C_4O_4H_2$ linkers ($m = 4 \cdot 114.1\ \mathrm{u}$), to $990\ \text{Å}^3$, yielding an apparent dry density of the aluminium fumarate crystals of $\rho = 1.06\ \mathrm{g/cm^3}$ (compared to, e.g., $1.50\ \mathrm{g/cm^3}$ for SAPO-34 (Füldner, 2015), and $1.75\ \mathrm{g/cm^3}$ for $AlPO_4$-5 (Qiu *et al.*, 1989; Kolokathis, 2020)). This value does not account for adsorption induced shrinking or swelling, nor for any defects or impurities. A unit cell, consisting of four asymmetric units, is fully hydrated with 14 water molecules, which gives a theoretical maximum loading of about 0.40 kg/kg or 0.42 kg/l at micropore level (compared to, e.g., 0.2 kg/kg or 0.3 kg/l for SAPO-34 (Füldner, 2015), and 0.15 kg/kg or 0.26 kg/l for $AlPO_4$-5 (Pillai & Jasra, 2010)).

The reported adsorption equilibrium (Figure 8) has a coarse resolution in the relevant region of the uptake step and shows inconsistent hysteresis phenomena at different temperatures, which is most likely related to either experimental artefacts (Rouquerol & Rouquerol, 2014), or capillary condensation in mesopores at high relative pressures (Kast, 1988) that are irrelevant to all AHT applications regarded here. Therefore, detailed measurements of the water adsorption equilibrium as relevant for application will be presented in this work (c.f. Section 5.1).

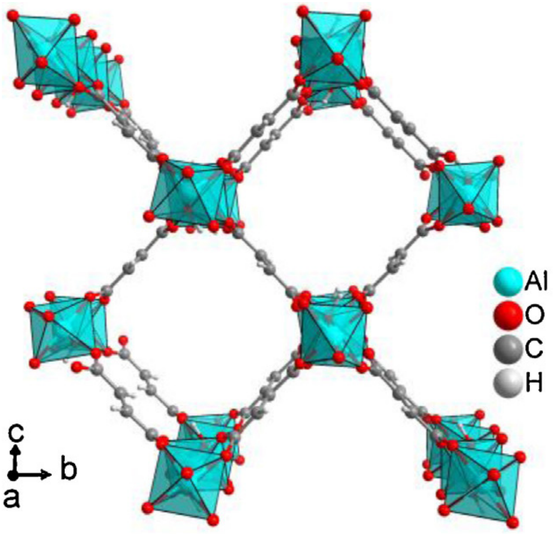

Figure 7: Structure of aluminium fumarate with 1D channels along the *a*-axis (Karmakar *et al.*, 2016)

Reprinted from Karmakar *et al.*, 2016 with permission from Elsevier.

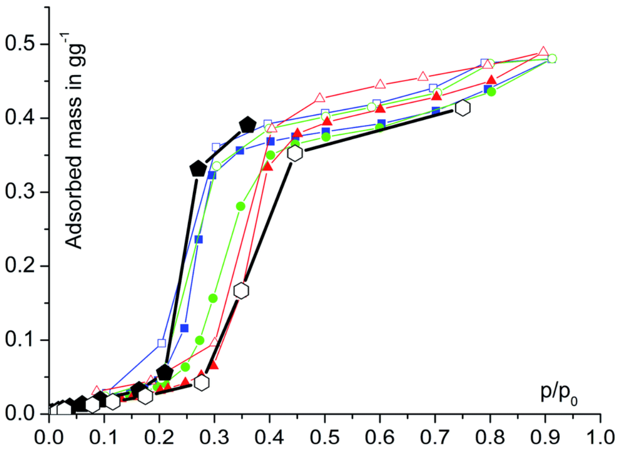

© by Jeremias et al., 2014 / CC BY-NC 3.0

Figure 8: Water dasorption equilibrium of aluminium fumarate (Jeremias *et al.*, 2014) with isotherms at 25 °C (■), 40 °C (●) and 60 °C (▲), and isobars at 12 mbar (L) and 56 mbar (I) (filled symbols: adsorption, empty symbols: desorption)

2.4.2 Hygroscopic salts

Hygroscopic salts are an additional material class for AHT that have a fundamentally different behaviour. Refrigerant molecules, mainly water but also ammonia or methanol, are built into the crystalline structure rather than adsorbed on the inner surface. During this sorption process the crystalline structure is broken up completely, and eventually dissolved, when reaching high relative pressures (the deliquescence relative humidity). Hydration to solid hydrates or the saturated solution takes place in steps, which results in favourable perfect steps in the isotherm, the location of which depends on the salt and the hydration level. The instability of the (micro)geometry throughout the process poses a major problem for application in AHT that has motivated the development of a class of composite materials: salt impregnated porous matrices (Gordeeva & Aristov, 2012). An overview of different salts and their suitability for AHT from a thermodynamic point of view has been presented at the Heat Powered Cycles conference (Laurenz *et al.*, 2016).

3. Theory and Model

This chapter comprises the two theoretical contributions of this work: firstly, the identification of heat and mass transfer (HMT) parameters based on the frequency response analysis (FRA), with a focus on detailed heat transfer modelling and rigorous assessment of the parameter confidence levels, and, secondly, the development of the concept of effective thermal resistances, as a simplified method to roughly estimate performance indicators on application level directly from these transfer parameters. For both parts a distinct theoretical framework is established and applied to a set of specific HMT models with their respective transfer parameters.

3.1 Frequency Response Analysis

The FRA consists of three components (Figure 9): Experiments, mathematical transfer models with solutions under FR boundary conditions, and the combination of both in a fitting procedure, the parameter identification (PI). Typically, the results in the frequency domain cannot be directly interpreted without model comparison. In this section, the transfer models with their analytical solutions and the PI procedure will be developed; the experimental part follows in the next chapter.

From the different FRA methods (c.f. Section 2.2.3.2), a volume swing FRA is employed for the state-dependent determination of the heat and mass transfer processes. This is part of a comprehensive approach that also allows obtaining adsorption equilibria and adsorption enthalpies, alongside with the sorption dynamics, in a single measurement procedure that will be detailed in the next chapter (Section 4.2). The FRA is enhanced with an additional measurement of the surface temperature response to the temperature frequency response (TFR). Prior applications of the TFR principally aimed at mass transfer measurements, where the disturbing heat effect was to be corrected (c.f. Section 2.2.3.2). Here, with AHT as motivating application, the temperature response is even more important, as it allows assessing the heat transfer mechanism in detail, which may be at least as relevant as the mass transfer.

The approach and the models presented in the following, including the analytical solutions, have been published separately before (Laurenz *et al.*, 2021).

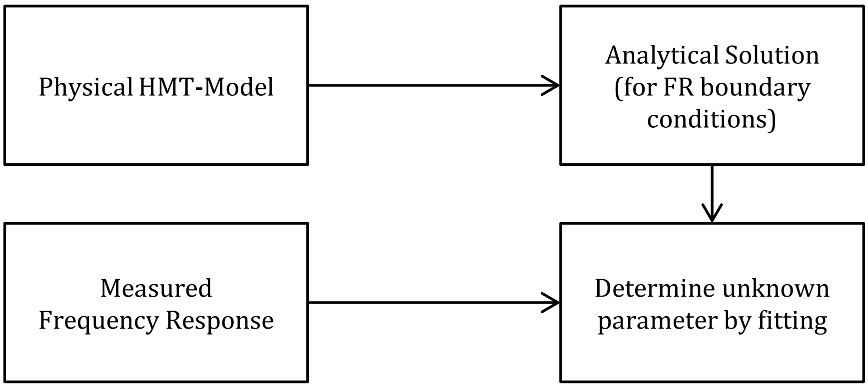

Figure 9: Principal approach of FRA-based parameter identification

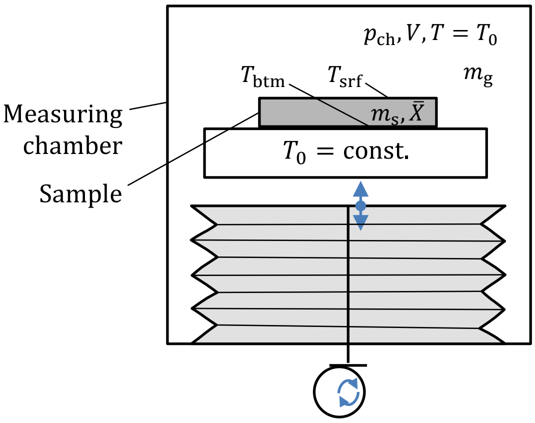

Figure 10: Measuring chamber with principal quantities for FRA: The chamber volume is varied, while the chamber temperature is kept constant ($T = T_0$) and the responses of the sample surface temperature T_{srf} and the chamber pressure p_{ch} are measured.

3.1.1 Modelling framework

Adsorption dynamic modelling for FRA may be structured into a modelling frame work, which comprises the overall mass and energy balances of the sample in the measuring chamber (c.f. Figure 10), and the actual heat and mass transfer models, describing the transport processes inside the sample. The modelling framework is independent of the actual HMT model and defines the boundary conditions of the latter.

Both, the framework and the HMT models are derived in the Laplace domain in order to allow for a direct comparison between the measured and the model-predicted responses in the frequency domain. The response quantities of interest for this comparison are the pressure of the measuring chamber p_{ch} and the sample surface temperature T_{srf}. Both quantities respond with sinusoidal signals to the, again sinusoidal, excitation of the measuring chamber volume V (for readability the index “ch” is omitted for the volume in this section). The responses depend only on the excitation frequency and the thermodynamic state of the system. All three quantities, the volume excitation, the pressure response and the temperature response, can be expressed as a complex quantities, where by definition the phase shift (and thus the imaginary part) of the excitation is zero. The frequency response is the evolution of these complex responses over the excitation frequency. To predict the frequency responses of p_{ch} and T_{srf} directly from the V_{ch} excitation for a given thermodynamic state is the overall aim of the FR modelling.

The modelling framework used here is mainly based on the transfer function approach suggested by Wang and LeVan (2011). The principal assumptions are:

1. Perturbations of the loading, pressure/concentration and temperature are sufficiently small to allow the linearization of all equations with constant coefficients. These coefficients are assumed local for the given mean state but may be different for different mean state, i.e. different experiments.
2. The pressure distribution in the chamber is uniform.
3. The temperature of the gas in the chamber is constant and equal to the temperature of the sample support.
4. Adsorption occurs only on the sample and not on the chamber walls.
5. The chamber contains a pure working fluid atmosphere (single component adsorption).

6. The sample volume is very small compared to the chamber volume, thus the volume displaced by the sample can be neglected.
7. The gas may be described as ideal gas which is a very good approximation for water in the pressure (< 100 mbar) and temperature (20–100 °C) region of interest here. In principle, the models can be extended by different equations of state that are locally linearized. This might be relevant, e.g., for high temperature application, or working fluids, operated in a higher pressure range, like ammonia.

Non-ideal effects contradicting assumptions 2–4 are accounted for in the experiments by applying a pressure correction (see Section 4.2.3.2).

The derivations start with the mass balance of the measurement chamber, which is to be related to the quantities of interest and transformed into the Laplace domain. The balance in the time domain is

$$0 = \frac{\mathrm{d}\bar{X}}{\mathrm{d}t} m_\mathrm{s} + \frac{\mathrm{d}m_\mathrm{g}}{\mathrm{d}t}, \tag{58}$$

where $\bar{X}$ denotes the average loading of the sample (mass of adsorbed working fluid per mass of dry adsorbent), m_s the mass of dry adsorbent, and m_g the gas mass in the chamber. With ideal gas law and constant gas temperature T_0 this becomes:

$$\begin{aligned} 0 &= \frac{\mathrm{d}\bar{X}}{\mathrm{d}t} m_\mathrm{s} + \frac{\frac{\mathrm{d}}{\mathrm{d}t}(p_\mathrm{ch} V)}{R_\mathrm{w} T_0} \\ &= \frac{\mathrm{d}\bar{X}}{\mathrm{d}t} m_\mathrm{s} + \frac{1}{R_\mathrm{w} T_0}\left(V \frac{\mathrm{d}p_\mathrm{ch}}{\mathrm{d}t} + p_\mathrm{ch}\frac{\mathrm{d}V}{\mathrm{d}t}\right). \end{aligned} \tag{59}$$

For a non-ideal gas with the real gas factor $z = pV/(nRT) = f(p_0, T_0)$, R_w may be replaced by zR_w in Eq. (59) and throughout all equations presented in the following.

As the sample volume is about three orders of magnitude smaller than the chamber volume, its effect on the gas phase volume, and thus on the mass balance, may be neglected here. This simplification is especially valid for the low pressure regime considered here. For the same reasons, the amount of gas in the macropores of the sample is not accounted for separately.

A key element of the FR modelling is the transformation of all time-variable quantities into the Laplace domain. To do so, the variables are first expressed as deviations from the temporal mean (index 0) with

$$\begin{aligned} \hat{X}(t) &= X(t) - X_0 \\ \hat{p}(t) &= p(t) - p_0 \\ \hat{c}(t) &= c(t) - c_0 \\ \hat{T}(t) &= T(t) - T_0 \end{aligned} \tag{60}$$

and then Laplace transformed ($\tilde{X}(s) = \mathcal{L}[\hat{X}(t)]$). Thus, the Laplace transformed mass balance is

$$0 = s\tilde{\bar{X}}m_\mathrm{s} + \frac{1}{R_\mathrm{w}T_0}\left(V_0 s\tilde{p}_\mathrm{ch} + p_0 s\tilde{V}\right), \tag{61}$$

where the Laplace transformation of a time derivative ($s\tilde{Z} = \mathcal{L}(\mathrm{d}Z/\mathrm{d}t)$, for an arbitrary variable Z) is applied. This elimination of the time derivatives significantly simplifies the mathematically modelling, which is one of the fundamental advantages of the FRA.

The mass balance can be explicitly solved for the requested relation between the chamber pressure $\tilde{p}_\mathrm{ch}$ and volume $\tilde{V}_\mathrm{ch}$, called the pressure volume transfer function

$$\begin{aligned} G_{pV}(s) = \frac{\tilde{p}_\mathrm{ch}}{\tilde{V}} &= -\left(\frac{\tilde{\bar{X}}}{\tilde{V}}\frac{m_\mathrm{s}R_\mathrm{w}T_0}{V_0} + \frac{p_0}{V_0}\right) \\ &= -\left(G_{XV}(s)\frac{m_\mathrm{s}R_\mathrm{w}T_0}{V_0} + \frac{p_0}{V_0}\right). \end{aligned} \tag{62}$$

That allows calculating the pressure response directly from known constants and the loading volume transfer function $G_{XV}(s) = \tilde{\bar{X}}/\tilde{V}$, i.e. the complex ratio between the average loading and the volume excitation. The form of $G_{XV}(s)$ depends on the actual HMT model that will be introduced in the next section.

For the overall energy balance of the sample, the same approach is used as done by other authors (Sun & Bourdin, 1993; Wang & LeVan, 2011), assuming an effective heat transfer coefficient h between the adsorbent, which has the temperature T_btm at the interface, and the support, which is constantly at the mean temperature T_0. Convective or radiative heat transfer at the adsorbent surface is neglected. The energy balance is then

$$m_\mathrm{s}c_p\frac{\mathrm{d}\bar{T}}{\mathrm{d}t} = m_\mathrm{s}\Delta h_\mathrm{s}\frac{\mathrm{d}\bar{X}}{\mathrm{d}t} - Ah(T_\mathrm{btm} - T_0) \tag{63}$$

with the adsorbent mass specific heat capacity c_p, the enthalpy of adsorption Δh_s and the sample surface area A (i.e. the reference surface for h). Laplace transformation with deviation variables as above yields:

$$m_\mathrm{s}c_p s\tilde{\bar{T}} = m_\mathrm{s}\Delta h_\mathrm{s} s\tilde{\bar{X}} - Ah\tilde{T}_\mathrm{btm}. \tag{64}$$

For models assuming a homogeneous temperature distribution, all temperatures are equal ($\tilde{T} = \tilde{\bar{T}} = \tilde{T}_\mathrm{btm}$) and Eq. (64) simplifies to the form used by Wang & LeVan (2011) that can be solved for $\tilde{T}$directly. This allows formulating the temperature loading transfer function

$$G_{TX}(s) = \frac{\tilde{T}}{\tilde{\bar{X}}} = \frac{m_\mathrm{s}\Delta h_\mathrm{s} s}{m_\mathrm{s}c_p s + Ah}, \tag{65}$$

which is independent of the actual HMT model. The formulation of $G_{TX}(s)$ is slightly different from Wang & LeVan (2011), but more convenient for the calculation of the measured temperature and pressure response directly from $G_{XV}(s)$:

$$\tilde{T} = \underbrace{G_{TX}(s)G_{XV}(s)}_{G_{TV}(s)}\tilde{V} \tag{66}$$

$$\tilde{p} = \underbrace{-\left(G_{XV}(s)\frac{m_\mathrm{s}R_\mathrm{w}T_0}{V_0} + \frac{p_0}{V_0}\right)}_{G_{pV}(s)}\tilde{V}. \tag{67}$$

Thus, $G_{XV}(s)$ is the central transfer function (called a “master curve” by Wang et al.), from which both responses can be computed irrespective of the actual model.

However, in cases where the assumption of a homogeneous temperature distribution for Eq. (65) does not apply, a direct formulation for $G_{TV}(s)$, and likewise for $G_{pV}(s)$, will be required. The reduction to a single transfer function $G_{XV}(s)$ is not possible anymore.

$G_{XV}(s)$ (or $G_{TV}(s)$ and $G_{pV}(s)$) may be computed directly from constants (transport parameters as well as material and setup properties) and the complex variable s according to analytical model solutions that will be derived in the following section. With $s = j2\pi f$ this allows calculating the pressure and temperature FR that can be fitted to the experimental results.

For comparison and transfer to pressure swing FR or in order to use available models here, the loading volume transfer function $G_{XV}(s)$ may be converted to Wang's “adsorbed-phase transfer function” $G_n(s) = \left(\tilde{X}/M\right)/\tilde{p}$ with Eq. (62):

$$G_n(s) = \frac{1}{M}G_{Xp}(s) = -\frac{1}{M}\frac{V_0}{p_0}\left(\frac{m_\mathrm{s}R_\mathrm{w}T_0}{p_0} + G_{XV}(s)^{-1}\right)^{-1}, \tag{68}$$

or, vice versa,:

$$G_{XV}(s) = -p_0\left(\frac{V_0}{M}G_n(s)^{-1} + m_sR_wT_0\right)^{-1}. \tag{69}$$

While, in this work, the pressure response $\tilde{p}_\mathrm{ch}$ is used directly for parameter identification purposes, other data reporting formats are found in literature. Especially in older literature, authors have reported normalised FR results as “in-phase and out-of-phase components” of the pressure (Jordi & Do, 1993; Sun *et al.*, 1993; Sun *et al.*, 1994; Bourdin *et al.*, 1996b):

$$\delta_\mathrm{in} - i\delta_\mathrm{out} = \frac{1}{\beta}\left(\frac{p_0}{\tilde{p}} - 1\right)\frac{\tilde{V}}{V_0}. \tag{70}$$

The dimensionless quantity β describes the ratio of equilibrium mass changes in the sorbent and in the gas phase induced by a pressure change at mean volume:

$$\beta = \frac{\partial m_{\mathrm{a}}/\partial p}{\partial m_{\mathrm{g,0}}/\partial p} = \frac{R_w T}{V_0} m_s \frac{\partial X}{\partial p}. \tag{71}$$

Care must be taken when comparing results, as, in at least one publication (Sun & Bourdin, 1993), β is omitted in the definition of δ_{in} and δ_{out}.

3.1.2 Heat and mass transfer models

The HMT models describe the adsorption dynamics inside the sample with different ODE and PDE approaches, depending on the relevant transport processes occurring or expected inside the adsorbent or the adsorbent composite (c.f. Section 2.2). The modelling approaches are based on different levels of simplifications, mainly regarding lumping, isotropy and symmetry. By comparing different plausible models to the experimental data, the relevant transport mechanisms can be identified alongside with the respective transport parameters. Typically, HMT models need to take into account strongly non-linear effects associated with adsorption dynamics, which typically requires numerical methods to solve. However, with the local linearity assumed above, and the transformation in the Laplace domain, analytical solutions may often be derived for FRA conditions.

In literature, most authors focus on isothermal models, which are simpler but irrelevant to the purpose of this work, while only few solutions are available for non-isothermal conditions. Analytical solutions, in a form of complex transfer function convertible to $G_{XV}(s)$, are available for two non-isothermal cases with different complexity in the mass transfer modelling (Wang & LeVan, 2011):

a) "0DHT_LDF": lumped (zero dimensional) heat transfer with LDF-approximated overall mass transfer,
b) "0DHT_miD_3D": lumped heat transfer with isotropic micropore diffusion in radial symmetric spheres (not applicable for aluminium fumarate).

For the modelling of macropore diffusion in even layers of adsorbent coating and intra crystalline (micropore) diffusion in anisotropic materials with a single preferred diffusion direction, like aluminium fumarate (c.f. Section 2.4.1), the diffusion equation needs to be solved on an even-plate (or slab) geometry. Moreover, to model the heat transfer in a thick coating, a 1D heat transfer model, with conductive heat transfer and contact resistance, is required.

For this work, the FR solutions for differently simplified models were developed that are all plausible for the adsorption dynamics in a binder based coating of aluminium fumarate (c.f. Figure 11):

c) "0DHT_miD": lumped heat transfer with micropore diffusion on a slab geometry (homogeneous concentration in the macropores and homogeneous temperature in the coating),
d) "0DHT_maD": lumped heat transfer with macropore diffusion on flat plate geometry (homogeneous loading in the crystals and homogeneous temperature in the coating),

e) “0DHT_maD_LDF”:	lumped heat transfer with macropore diffusion combined with a LDF-approximated micro-scale mass transfer (homogeneous temperature in the coating)
f) “1DHT_miLDF”:	heat conduction in the coating with a thermal contact resistance to the support and with a LDF-approximated micro-scale mass transfer, neglecting macropore diffusion (same concentration throughout the macropores as in the measurement chamber)

A computer algebra system (CAS) was used (Wolfram Mathematica®) to efficiently solve the systems of ODEs and/or PDEs. The final solutions are summarized together with the models from Wang and LeVan in Table 1 in the form of the transfer function $G_{XV}(s)$. For the detailed derivations please refer to Appendix A.2.

An additional model approach is the combination of model e) and f). This would require a simultaneous space discretization of both, conductive heat transfer and macropore diffusion, which could be solved analytically in principle. However, the straight forward approach, applied for the other cases, fails to produce useful results and is therefore omitted here. The solutions obtained by CAS are so fragmented and extensive that numerical evaluations run into large rounding errors. These approaches are typically found as non-linear models, solved with finite element methods in the time domain (as e.g. in Yong & Sumathy, 2002; Füldner, 2015; Velte *et al.*, 2017). Numerical solutions in the frequency domain are out of scope of this work and are not pursued here. The same applies to non-straightforward CAS-based approaches (Sun & Meunier, 1987), which are left for future studies.

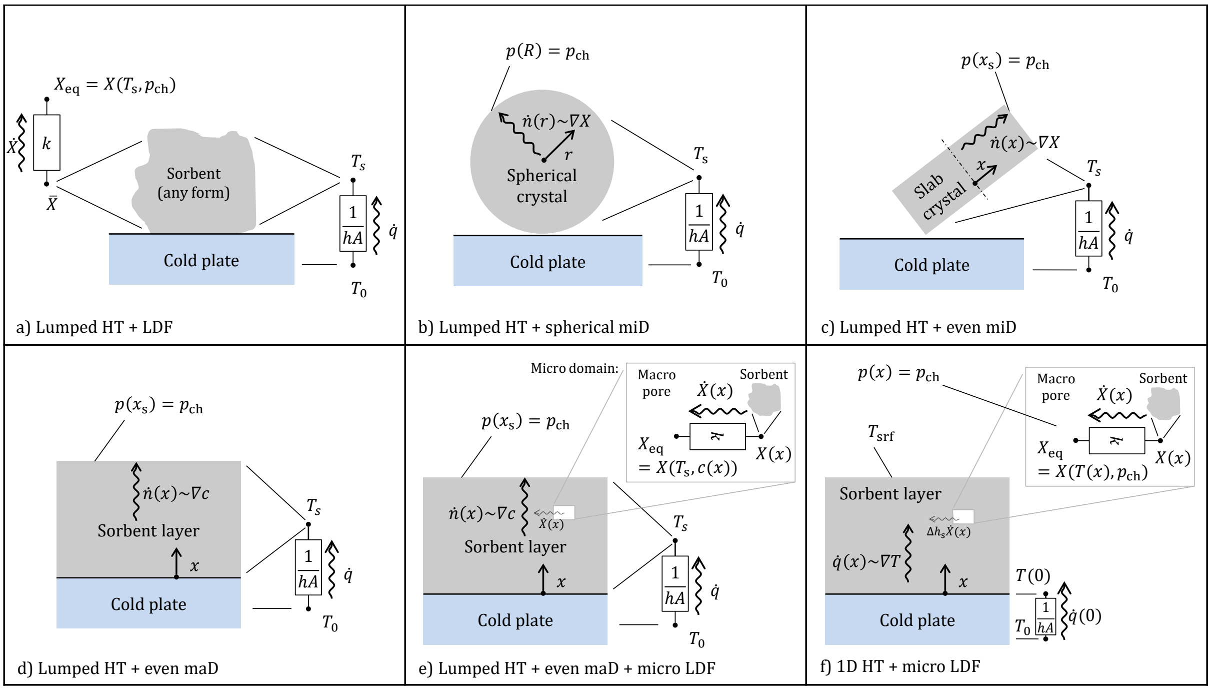

a) Lumped HT + LDF

b) Lumped HT + spherical miD

c) Lumped HT + even miD

d) Lumped HT + even maD

e) Lumped HT + even maD + micro LDF

f) 1D HT + micro LDF

© by Laurenz *et al.*, 2021 / CC BY 4.0

Figure 11: Different non-isothermal approaches for adsorption kinetic modelling with boundary conditions. FR solutions for a) and b) are literature-available (Wang & LeVan, 2011), c)–d) are developed in this work (HT: heat transfer, miD: micro diffusion, maD: macro diffusion, LDF: linear driving force)

Table 1: Summary of FR-model solutions used and/or developed within the scope of this work (HT: heat transfer, miD: micro diffusion, maD: macro diffusion, LDF: linear driving force)

Model	Loading volume transfer function $G_{XV}(s) = \tilde{\tilde{X}}/\tilde{V}$	Reference
a) Lumped HT + LDF	$-\frac{K_p p_0}{V_0}\left[\frac{s}{k_{\mathrm{LDF}}} + 1 + \frac{K_p m_{\mathrm{s}} R_{\mathrm{w}} T_0}{V_0} - \frac{s}{\beta}\right]^{-1}$ with $\beta = \left(Ah + c_p m_{\mathrm{s}} s\right)/(\Delta h_{\mathrm{s}} K_T m_{\mathrm{s}})$	Wang & LeVan (2011)
b) Lumped HT + spherical miD	$-\frac{K_p p_0}{V_0}\left[\frac{s}{3k_{\mathrm{mi}}}\left(\sqrt{\frac{s}{k_{\mathrm{mi}}}}\coth\left(\sqrt{\frac{s}{k_{\mathrm{mi}}}}\right) - 1\right)^{-1} + \frac{K_p m_{\mathrm{s}} R_{\mathrm{w}} T_0}{V_0} - \frac{s}{\beta}\right]^{-1}$ with $k_{\mathrm{mi}} = D_{\mathrm{mi}}/r^2$ and β as above	Wang & LeVan (2011)
c) Lumped HT + even miD	$-\frac{K_p p_0}{V_0}\left[\sqrt{\frac{s}{k_{\mathrm{mi}}}}\coth\left(\sqrt{\frac{s}{k_{\mathrm{mi}}}}\right) + \frac{m_{\mathrm{s}} K_p R_{\mathrm{w}} T_0}{V_0} - \frac{s}{\beta}\right]^{-1}$ with k_{mi}, β as above	Appendix A.2.1
d) Lumped HT + even maD	$-\frac{K_p p_0}{V_0}\left[\sqrt{\frac{s}{k_{\mathrm{ma}}}(1+\alpha)}\left(1 - \frac{s}{\beta(1+\alpha)}\right)\coth\left(\sqrt{\frac{s}{k_{\mathrm{ma}}}(1+\alpha)}\right) + \alpha\left(\frac{\varepsilon_{\mathrm{P}} m_{\mathrm{s}}}{\rho_{\mathrm{eff}} V_0} - \frac{s}{\beta(1+\alpha)}\right)\right]^{-1}$ with $\alpha = K_p \rho_{\mathrm{eff}} R_{\mathrm{w}} T_0/\varepsilon_{\mathrm{P}}$, $k_{\mathrm{ma}} = D_{\mathrm{ma}}/d^2$ and β as above	Appendix A.2.2
e) Lumped HT + even maD + micro LDF	$-\frac{K_p p_0}{V_0}\left[\sqrt{\frac{s}{k_{\mathrm{ma}}}\frac{\alpha+\gamma}{\gamma}}\,\gamma\left(1 - \frac{s}{\beta(\alpha+\gamma)}\right)\coth\left(\sqrt{\frac{s}{k_{\mathrm{ma}}}\frac{\alpha+\gamma}{\gamma}}\right) + \alpha\left(\frac{\varepsilon_{\mathrm{P}} m_{\mathrm{s}}}{\rho_{\mathrm{eff}} V_0} - \frac{s}{\beta(\alpha+\gamma)}\right)\right]^{-1}$ with $\gamma = 1 + s/k_{\mathrm{LDF}}$ and $\alpha, \beta, k_{\mathrm{ma}}$ as above	Appendix A.2.3
f) Even HT + micro LDF	$G_{XV}(s)$ is not usefull in this case. $G_{pV}(s)$ and $G_{TV}(s)$ are given separately in the reference.	Appendix A.2.4

3.1.3 Parameter identification

A generalised weighted least squares method is applied to estimate the parameters for heat and mass transfer, as schematically summarised in Figure 12. The best estimate for the parameter vector $\boldsymbol{P}$ (denoted as $\widehat{\boldsymbol{P}}$) is gained by minimising the error functional $E(\boldsymbol{P})$:

$$\begin{aligned} E\left(\widehat{\boldsymbol{P}}\right) &= \min E(\boldsymbol{P}) \\ &= \min \sqrt{\frac{1}{N}\sum_{i=1}^{N_f}\left(\boldsymbol{y}_{f_i}(\boldsymbol{P}) - \boldsymbol{y}_{f_i}^{\mathbf{exp}}\right)^{\mathrm{T}} \boldsymbol{W}_i \left(\boldsymbol{y}_{f_i}(\boldsymbol{P}) - \boldsymbol{y}_{f_i}^{\mathbf{exp}}\right)} \end{aligned} \tag{72}$$

with the model result $\boldsymbol{y}_{f_i}(\boldsymbol{P})$ (c.f. Sections 3.1.1 and 3.1.2) and the experimental result $\boldsymbol{y}_{f_i}^{\mathrm{exp}}$ (c.f. Section 4.2) for frequency f_i. Here all $\boldsymbol{y}$ have four real-valued entries, i.e. separate entries for real and imaginary part of the pressure and temperature response. This is equivalent to the recommended multiplication of the complex-valued error with it complex conjugate (Bohn & Unbehauen, 2016) but has the advantage of allowing different weights for real and imaginary part. The total number of observations is $N = 4N_f$.

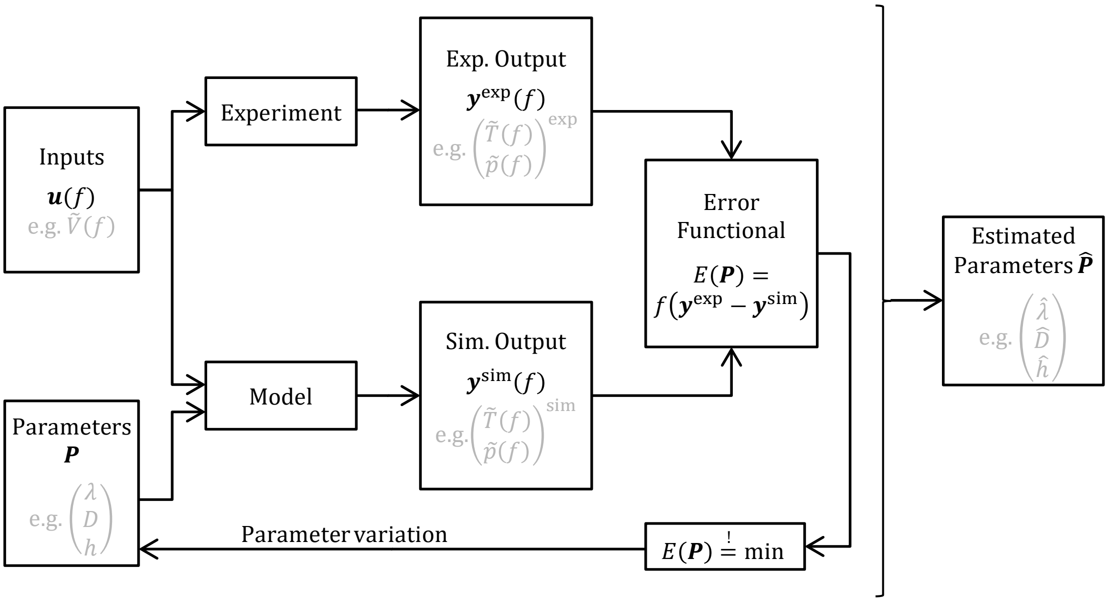

Figure 12: Schematic representation of the parameter identification procedure

Weighing is based on the inverse of the estimated standard measurement uncertainty of the response variable (c.f. Section 4.2.4.1) as recommended by e.g. Bohn & Unbehauen (2016) or Marsili-Libelli (2016). To avoid a bias in favour of the pressure signal arising from its generally lower uncertainty an equilibration between the pressure and temperature signal is applied. The weighing matrix is

$$\boldsymbol{W}_{f_i} = \mathrm{diag}\left(w_{\mathrm{Re}\left(\tilde{p}_{f_i}\right)}, w_{\mathrm{Im}\left(\tilde{p}_{f_i}\right)}, w_{\mathrm{Re}\left(\tilde{T}_{f_i}\right)}, w_{\mathrm{Im}\left(\tilde{T}_{f_i}\right)}\right) \tag{73}$$

with the individual weights

$$w_{k_{f_i}} = \left(\frac{1}{\sigma_{k_{f_i}}} \frac{\overline{\sigma_{\boldsymbol{k}}}}{\max(\boldsymbol{k}^{\mathrm{exp}}) - \min(\boldsymbol{k}^{\mathrm{exp}})}\right)^2. \tag{74}$$

The second term normalises the individual weights with the mean uncertainty $\overline{\sigma_{\boldsymbol{k}}}$ relative to the range of the experimental results. With this approach each (real-valued) response vector $\boldsymbol{k} \in \{\mathrm{Re}(\widetilde{\boldsymbol{p}}), \mathrm{Im}(\widetilde{\boldsymbol{p}}), \mathrm{Re}(\widetilde{\boldsymbol{T}}), \mathrm{Im}(\widetilde{\boldsymbol{T}})\}$ is equally emphasised (weighted with the inverse range) while data points of individual frequencies within one response vector are weighted according to their significance (with the inverse of $\sigma_{k_{f_i}}/\overline{\sigma_{\boldsymbol{k}}}$). The weights have the squared inverse unit of the actual measurand (e.g. $1/\mathrm{Pa}^2$ and $1/\mathrm{K}^2$) and thus ensure a non-dimensional error functional.

The value of $E(\widehat{\boldsymbol{P}})$ can be regarded as an average relative deviation between the best fitting model and the experiment of all N observations and is as such a meaningful value for result interpretation. For constant uncertainties ($\sigma_{k_{f_i}} = \overline{\sigma_{\boldsymbol{k}}}$) the error functional is equal to the root mean square deviation (RMSD) normalized with the range which has been used earlier as a "coefficient of variance" (Velte *et al.*, 2017) or "coefficient of variation" (Lanzerath, 2013)[4] for the calibration of different adsorption models.

The minimisation problem Eq. (72) needs to be solved numerically. The Levenberg–Marquardt algorithm (Levenberg, 1944; Marquardt, 1963) implemented in R as `nls.lm()` (Elzhov *et al.*, 2016) proved to be a reliable and efficient solution.

An additional measure for the quality of the identified parameters is the confidence region, i.e. the set of parameters in which the true parameters are expected with a certain probability. For a single parameter this is simply the confidence interval, whereas for two or three parameters, the confidence region becomes two or three dimensional. The uncertainties of different parameters are typically not independent from each other. Marsili-Libelli (2003; 2016) proposes to base the confidence regions on the contours of $E(\boldsymbol{P})$ which will be employed in this work. He relates the degree of confidence of given set of parameters $\boldsymbol{P}$ to the difference between the error functional at this point in the $\boldsymbol{P}$-space and to the minimum of the error functional:

$$\Delta E(\alpha) = E(\boldsymbol{P}) - E(\widehat{\boldsymbol{P}}) = E(\widehat{\boldsymbol{P}}) \frac{n_\mathrm{p}}{N - n_\mathrm{p}} F^{\alpha}_{n_\mathrm{p}, N-n_\mathrm{p}}, \tag{75}$$

where $n_\mathrm{p} = \dim(\boldsymbol{P})$ and $F^{\alpha}_{n_\mathrm{p}, N-n_\mathrm{p}}$ is the upper α critical level of the F-distribution[5] with the degrees of freedom n_p and $N - n_\mathrm{p}$. To find the 68% confidence region $E(\boldsymbol{P})$, which is comparable to the standard uncertainties reported for direct measurements, a parameter variation around $\widehat{\boldsymbol{P}}$ is performed and the level $E(\widehat{\boldsymbol{P}}) + \Delta E(\alpha = 0.32)$. For presentations of results with only one of the two parameters, simplified standard confidence limits for each parameter will be used. These are based on the outer extend of the 68% confidence region, as depicted in Figure 13.

This approach takes into account, three aspects:

1. the deviation between model and experiment in the form of the residual error $E(\widehat{\boldsymbol{P}})$,
2. the statistical power of the experiment through the second factor in Eq. (75), and
3. the sensitivity of the identification procedure with respect to the parameters through the extent of the confidence region corresponding to a given value of $E(\widehat{\boldsymbol{P}}) + \Delta E$ or, in other words, the "flatter" the form of $E(\boldsymbol{P})$, the larger the confidence region and, thus, the simplified confidence intervals of the parameters.

Alternatives to this direct calculation of the confidence region are approximation methods, which are based on the local partial derivatives at $\widehat{\boldsymbol{P}}$ of either $\boldsymbol{y}(\boldsymbol{P})$ (Fisher information matrix) or $E(\boldsymbol{P})$ (Hessian matrix). These are less computationally expensive as they do not require the calculation of $E(\boldsymbol{P})$ on a large grid of values (Marsili-Libelli *et al.*, 2003; Marsili-Libelli, 2016). However in the case of this work, they turned out to be not useful: Approximated regions often include negative, physically meaningless values for the estimated transport parameters, which is due to the strongly non-linear nature of the models and the relatively large uncertainty regions.

---

[4] Lanzerath used the arithmetic mean to normalise the RMSD of an always positive heat flow. In the case here the mean is not applicable as positive and negative values occur, thus the mean might be close to zero.

[5] The quantiles of the F-distribution are in available in R as `qf(1 - alpha, np, N - np)`.

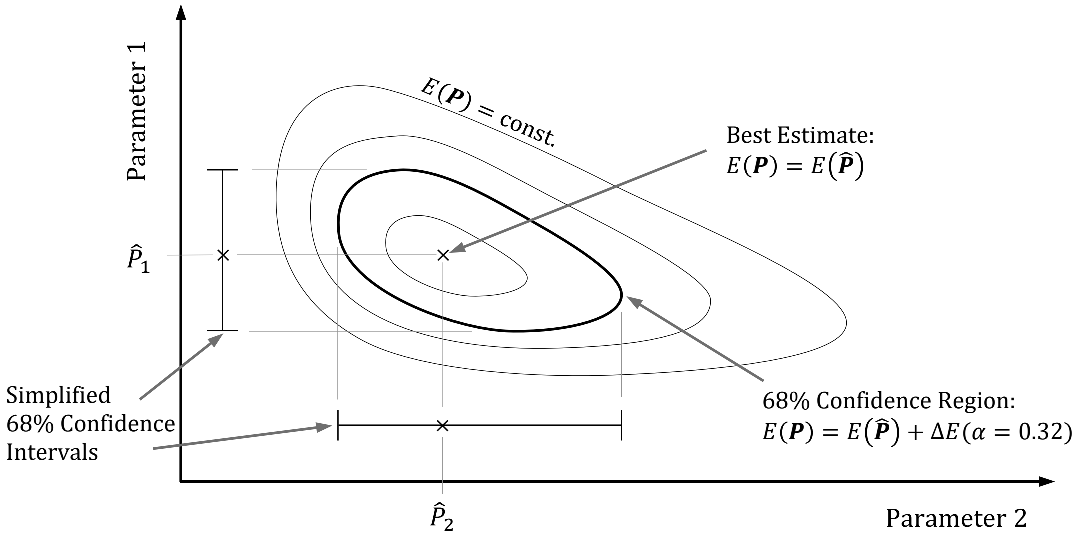

Figure 13: Schematic contour plot of the error functional $E(\boldsymbol{P})$ for the simultaneous identification of two parameters. The standard (68%) confidence region is highlighted with the definition of confidence limits used for simplified result presentation.

3.2 Concept of Effective Thermal Resistances

The concept of effective thermal resistances aims to provide a simplified design method for Ad-HX in the form of the basic heat exchanger design rule $\dot{Q} = \Delta T/R$, where $R = (UA)^{-1}$ is the overall heat transfer resistance. The external temperature levels of the target application are combined with the sorption equilibrium properties of the working pair to a meaningful driving temperature difference ΔT_{drv}, and the HMT properties to the effective thermal resistance R_{eff}. Both are combined to the expected heat flow in order to estimate the performance indicators without any empiric information about the characteristic time (c.f. Figure 14). This is an extension of the existing approach used for the empirical quantitative comparison of heat and mass transfer effects in the analysis of time domain experiments (Velte *et al.*, 2017; Ammann *et al.*, 2018) as will be discussed in the next section.

From the parameters used to describe the different HMT processes that occur in Ad-HXs, it is typically not possible to directly judge the practical relevance of these different processes nor the expected overall performance. Classically, the performance of an Ad-HX, especially in terms of SCP, is based on estimations of the heat flow from characteristic times Δt and uptakes ΔX (c.f. Eq. (57)), which both need to be obtained in the time domain either by simulations or by experiments, carried out for every set of boundary conditions of the target application. Thus, designing an Ad-HX becomes a complicated and laborious procedure, if, e.g., the adsorbate diffusion is to be modelled for the transient, non-linear and spatially distributed conditions of an adsorption cooling cycle. The experiment-based alternative, a more or less structured trial-and-error approach, merely shifts the effort to repeated prototyping and measurements. The novel concept presented here is intended to provide an alternative way, reducing the complicated adsorption dynamics to simple, application-relevant key parameters, which allow direct performance estimations and a quantitative judgement of limitations.

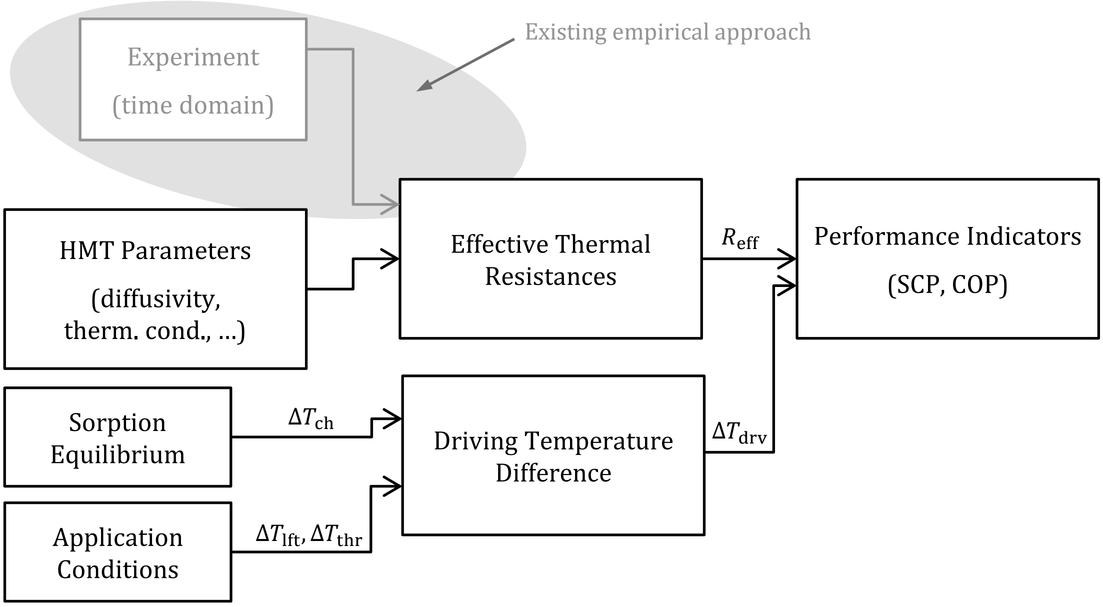

Figure 14: Principal concept of effective thermal resistances for performance estimation from heat and mass transfer (HMT) parameters (obtained, e.g., from FRA) compared to the existing empirical approach (Velte *et al.*, 2017; Ammann *et al.*, 2018)

The scope of this work are the heat and mass transfer processes occurring in an adsorbent or an adsorbent composite, which is a part of an Ad-HX. The Ad-HX as such has additional quantities to be accounted for, like a capacity flow of HTF and an accompanying temperature difference between in- and outlet. These HX-level effects will, however, not be considered in the following. They have been, e.g., recently analysed in depth by Velte (2019). Nevertheless, it should in principle be possible to integrate the concept developed in this section into classical heat exchanger design theories, like the ε-NTU method (Shah & Sekuli, 2003).

This section is organised along Figure 14: It starts with introducing the idea of effective thermal resistances for the quantitative comparison of heat and mass transfer in Ad-HXs, which is closely related to the existing empirical approach. In the next step, an approach is suggested how to directly derive the effective thermal resistances from the HMT parameters, like those identified by FRA in the last chapter, based in the underlying HMT models. Finally, the driving temperature difference ΔT_{drv} is derived from the sorption equilibrium and the application temperature boundary conditions, before relating the whole concept to the common performance indicators COP and SCP.

3.2.1 Comparison of heat and mass transfer

Initially, the introduction of effective thermal resistances was motivated by the quantitative comparison heat and mass transfer processes in adsorbents. The basic idea is to map any mass transfer resistance to an equivalent heat transfer resistance. This approach was first suggested by Wittstadt *et al.* (2017) and then further elaborated for the phenomenological interpretation of macro scale experimental data (Velte *et al.*, 2017; Ammann *et al.*, 2018) and is the starting point for the concept developed here.

Assume a quasi-isothermal adsorption process[6], i.e. with a small temperature change ($c_{p,\mathrm{eff}}\mathrm{d}T \ll \Delta h_\mathrm{s}\mathrm{d}X$), so that the associated heat flow is directly related to the mass flow adsorbed:

$$\dot{Q}_\mathrm{s} = m_\mathrm{s}\dot{X}\Delta h_\mathrm{s}. \tag{76}$$

In order to properly distinguish between resistive and capacitive effects, this definition slightly differs from that made by Ammann *et al.* (2018), who included an additional heat capacity term ($mc_p\mathrm{d}T$).

This process is running between a given bulk gas pressure p_e, e.g. provided by an ideal evaporator at T_L with $p_\mathrm{e} = p_\mathrm{sat}(T_\mathrm{L})$, and a fixed external heat reservoir at medium temperature level T_M, to which the heat released from the adsorption process is eventually transferred. As said above, effects of a finite HTF mass flow are neglected here. The adsorbent is characterised by X, T_s, and p_s, the loading, temperature, and pressure averaged over the places of adsorption. For the case of a microporous adsorbent, p_s is the pressure of a bulk gas phase that would exist in equilibrium with a place of adsorption. A place of adsorption may be any place where the loading changes, be it by actual adsorption or by adsorbate diffusion (c.f. Eq. (44), p42).

The overall heat transfer is governed by the temperature difference between the external reservoir, e.g. a heat exchanger fluid, and the adsorbent. It may be characterised by the heat transfer resistance

$$R_\mathrm{HT} = \frac{\Delta T_\mathrm{drv,HT}}{\dot{Q}_\mathrm{s}} = \frac{T_\mathrm{s} - T_\mathrm{M}}{m_\mathrm{s}\dot{X}\Delta h_\mathrm{s}}, \tag{77}$$

which relates the driving temperature difference to the adsorption associated heat flow $\dot{Q}_\mathrm{s}$.

The mass transfer occurring between p_e and p_s, may be accounted for by an equivalent heat transfer effect through the driving temperature equivalent (Wittstadt *et al.*, 2017), the difference between the equilibrium temperature $T_\mathrm{eq}(p_\mathrm{e}, X)$ and T_s. The resistance of this *mass transfer equivalent* heat transfer is

$$R_\mathrm{MT} = \frac{\Delta T_\mathrm{drv,MT}}{\dot{Q}_\mathrm{s}} = \frac{T_\mathrm{eq}(X, p_\mathrm{e}) - T_\mathrm{s}}{m_\mathrm{s}\Delta h_\mathrm{s}\dot{X}}. \tag{78}$$

It relates the driving temperature equivalent to the “enthalpy flow” associated to the gas mass flow being transferred between the bulk gas volume and the place of adsorption. With this definition, the overall effect on the sorption dynamics are equal: Considering the adsorption dynamics as a black box, where only the external quantities $\dot{Q}_\mathrm{s}$, T_M and p_e are visible, a fully mass transfer limited process cannot be distinguished from its heat transfer equivalent (Figure 15). This mapping of different kinds of mass transfer resistances to a heat transfer equivalents will be dealt with in detail in the next section.

---

[6] This approximation is especially valid for the isobaric phases of an adsorption cycle with a discrete sorption material, where the uptake is concentrated in a small temperature range.

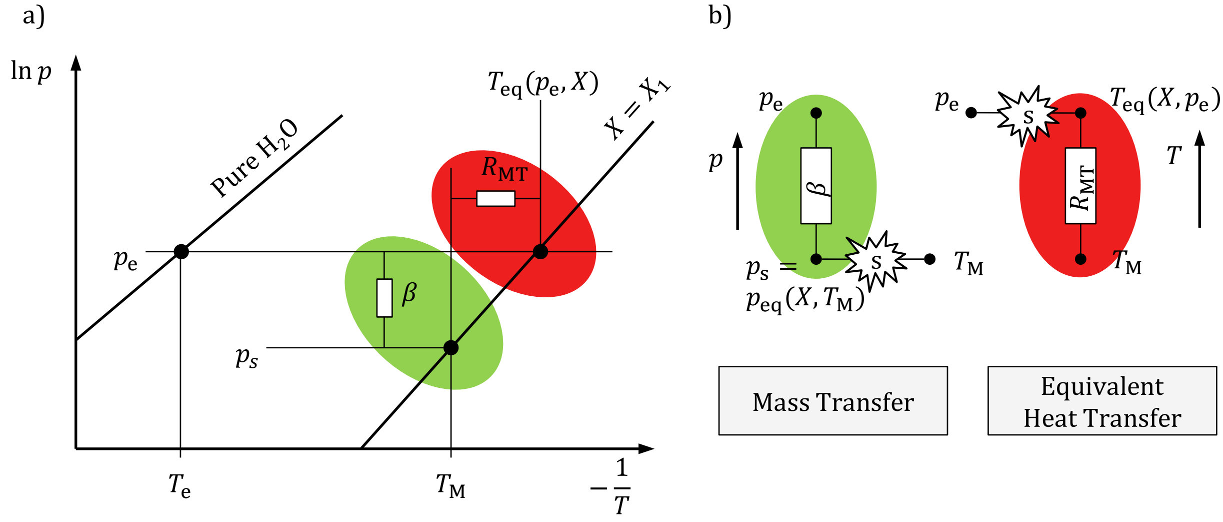

Figure 15: Representation of the mass-transfer-equivalent heat transfer resistance in a) the Clausius–Clapeyron plot and b) the thermal equivalent circuit as comparison of a mass transfer limited adsorption process, with a mass transfer resistance β inducing a pressure drop (green), and the equivalent heat transfer limited process, where the adsorbent pressure is equal to the bulk pressure provided by the evaporator (red), with the place of adsorption "s".

The overall resistance may be calculated by simple addition (Figure 16):

$$\begin{aligned} R_{\mathrm{eff}} &= R_{\mathrm{MT}} + R_{\mathrm{HT}} \\ &= \frac{\Delta T_{\mathrm{drv,MT}} + \Delta T_{\mathrm{drv,HT}}}{m_{\mathrm{s}} \Delta h_{\mathrm{s}} \dot{X}} \\ &= \frac{T_{\mathrm{eq}}(X, p_{\mathrm{e}}) - T_{\mathrm{M}}}{m_{\mathrm{s}} \Delta h_{\mathrm{s}} \dot{X}} \\ &= \frac{\Delta T_{\mathrm{drv,s}}}{\dot{Q}_{\mathrm{s}}}. \end{aligned} \tag{79}$$

Figure 16 shows, that this summation is only meaningful, if the effect of the heat capacity $C_s = m_s c_{p,\mathrm{eff}}$ can be neglected (see above). If that is not the case, e.g. during the isosteric phases of the cycle, the heat and mass transfer resistance must be treated separately, as the mass transfer becomes irrelevant. This is different in the definition suggested by Ammann *et al.* (2018), where C_{s} is included into the calculation of R_{MT}. In this case, Eq. (79) could seemingly – but wrongly – be applied to the isosteric phases.

Depending on the perspective of the analysis, R_{eff} may be referred to a reference quantity z, e.g. the adsorbent mass, the heat exchanger volume or the heat exchanger surface area, as

$$R_{\mathrm{eff}}^{z} = \frac{\Delta T_{\mathrm{eff}}}{\dot{Q}_s / z} = z R_{\mathrm{eff}}. \tag{80}$$

The derivation of resistances from Wittstadt *et al.*'s driving temperature equivalent was used for the phenomenological interpretation of macro scale experimental data (Ammann *et al.*, 2018). Ammann et el. referred to R_{eff}^{A} as "thermal impedance". This analogy to the electrical impedance, a complex quantity that takes into account resistance, capacitance and inductivity, is avoided here, as it suggests that the heat capacity is taken into account.

In the same formalism, the effective thermal resistance of a non-ideal and quasi-isothermal evaporator can be defined as

$$\begin{aligned} R_\mathrm{e} = (UA)_\mathrm{e}^{-1} &= \frac{T_\mathrm{L} - T_\mathrm{sat}(p_\mathrm{e})}{-\dot{m}_\mathrm{g}\Delta h_\mathrm{v}} \\ &= \frac{\Delta T_\mathrm{drv,e}}{\dot{Q}_\mathrm{e}}, \end{aligned} \tag{81}$$

where $-\dot{m}_\mathrm{g}$ is the refrigerant mass flow leaving the evaporator. In the same way, one may define R_c as the effective thermal resistance of the condenser.

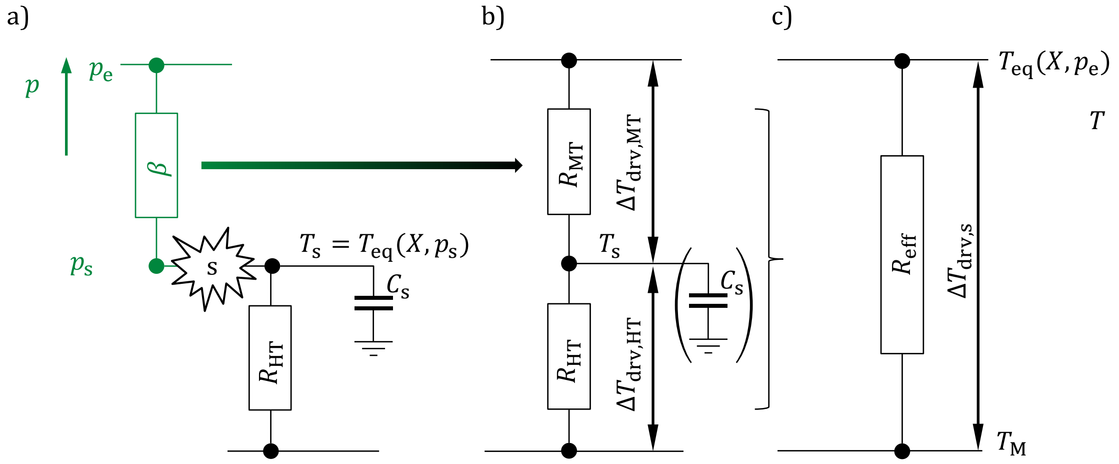

Figure 16: Thermal equivalent circuit of an adsorption process with heat and mass transfer limitations in three different representations: a) straightforward physical representation with mass transfer in the pressure (or concentration) dimension coupled to the heat transfer in the temperature dimension through the adsorption process ("s") at local equilibrium, b) mass transfer converted to the temperature dimension as equivalent heat transfer resistance and c) the overall effective heat transfer resistance as the sum of both resistances, if $\mathrm{d}TC_\mathrm{s}$ is small

3.2.2 Relation to transport parameters

The effective heat transfer resistances have proven useful for the evaluation of macroscopic adsorption experiments under application boundary conditions. However, from a design-and-optimisation perspective, it would be desirable to relate these effective resistances directly to transport parameters that are often available from literature or that may be obtained experimentally without restriction to explicit application boundary conditions.

This deduction with a general validity is difficult, and probably not possible, especially for strongly transient process phases with large gradients. However, for process phases where the temperature change is less rapid and the loading change $\dot{X}$ has equilibrated throughout the adsorbent, one may assume a quasi-isothermal case with a homogeneous distribution of $\dot{X}$. For this case, also the spatial state variation (X, T) is assumed small, so that coefficients are constant.

Under these assumptions, effective heat transfer resistance may be derived as shown in the Appendix A.3. The result is provided in Table 2 for the adsorbent mass related $R^{m_{\mathrm{s}}}$ and for $R^{A_{\mathrm{HX}}}$, which is related to the heat exchanger surface area A_{HX}, being either coated or covered with adsorbent pellets. Unlike $R^{m_{\mathrm{s}}}$ and for $R^{A_{\mathrm{HX}}}$, the volume related effective thermal resistance R^V cannot be calculated directly from local variables, as the reference volume usually also takes into account the volume occupied by the heat exchanger structure (e.g. fins, tubes, headers), which are out of scope here. However, once the volume-to-surface ratio of any specific HX design is available, it may easily be calculated from $R^{A_{\mathrm{HX}}}$:

$$R^V = \frac{V}{A_{\mathrm{HX}}} R^{A_{\mathrm{HX}}}. \tag{82}$$

Similarly, $R^{m_{\mathrm{s}}}$ may easily be converted to another reference mass with the respective mass ratio.

Table 2: Conversion of transport parameters to effective heat transfer resistances (d: thickness on the macro scale, r diffusion length, $\gamma = \sigma(\sigma + 2)$, c.f. Appendix A.3 for detailed derivation and variable definitions)

Parameter and Geometry		$(R^A)^{-1}$ (W/(m^2 K))	$(R^{m_{\mathrm{s}}})^{-1}$ (W/(kg K))
Lumped heat transfer h	Not applicable	h	$\frac{h}{d\rho_{\mathrm{eff}}}$
Thermal conductivity λ	Flat plate	$\frac{3\lambda}{d}$	$\frac{3\lambda}{d^2\rho_{\mathrm{eff}}}$
LDF coefficient k_{LDF}	Not applicable	$k_{\mathrm{LDF}}\frac{\partial X}{\partial T} d\rho_{\mathrm{eff}}\Delta h_{\mathrm{s}}$	$k_{\mathrm{LDF}}\frac{\partial X}{\partial T}\Delta h_{\mathrm{s}}$
Micropore transport diffusivity D_{mi} [i]	Flat plate, cylinder, sphere	$\frac{\gamma D_{\mathrm{mi}}}{r^2}\frac{\partial X}{\partial T} d\rho_{\mathrm{eff}}\Delta h_{\mathrm{s}}$	$\frac{\gamma D_{\mathrm{mi}}}{r^2}\frac{\partial X}{\partial T}\Delta h_{\mathrm{s}}$
Micropore adsorbate diffusivity D_{ad}	Flat plate, cylinder, sphere	$\frac{\gamma D_{\mathrm{ad}}}{r^2} X d\rho_{\mathrm{eff}}\frac{\Delta h_{\mathrm{s}}^2}{R_{\mathrm{w}}T^2}$	$\frac{\gamma D_{\mathrm{ad}}}{r^2} X \frac{\Delta h_{\mathrm{s}}^2}{R_{\mathrm{w}}T^2}$
Macropore eff. diffusivity D_{ma}	Flat plate, cylinder, sphere	$\frac{\gamma D_{\mathrm{ma}}}{r^2}\varepsilon_{\mathrm{P}} d\frac{p}{T}\left(\frac{\Delta h_{\mathrm{s}}}{R_{\mathrm{w}}T}\right)^2$	$\frac{\gamma D_{\mathrm{ma}}}{r^2}\frac{\varepsilon_{\mathrm{P}} p}{\rho_{\mathrm{eff}}T}\left(\frac{\Delta h_{\mathrm{s}}}{R_{\mathrm{w}}T}\right)^2$
	Flat plate	$\frac{3D_{\mathrm{ma}}}{d}\varepsilon_{\mathrm{P}}\frac{p}{T}\left(\frac{\Delta h_{\mathrm{s}}}{R_{\mathrm{w}}T}\right)^2$	$\frac{3D_{\mathrm{ma}}}{d^2}\frac{\varepsilon_{\mathrm{P}} p}{\rho_{\mathrm{eff}}T}\left(\frac{\Delta h_{\mathrm{s}}}{R_{\mathrm{w}}T}\right)^2$

---

[i] NB: For materials with a pronounced step-like isotherm, the loading dependency of D_{mi} can be large and so the assumption of constant coefficients may become weak. In this case the D_{ad}-based approximation will be more accurate.

3.2.3 Calculation of driving temperature differences

The driving temperature differences are directly related to the external temperature levels and the associated temperature thrust $\Delta T_{\mathrm{thr}} = T_{\mathrm{H}} - T_{\mathrm{M}}$ and temperature lift $\Delta T_{\mathrm{lft}} = T_{\mathrm{M}} - T_{\mathrm{L}}$ for an adsorption chiller cycle operating between a high (H), a medium (M) and a low (L) temperature level (c.f. Section 2.3.1).

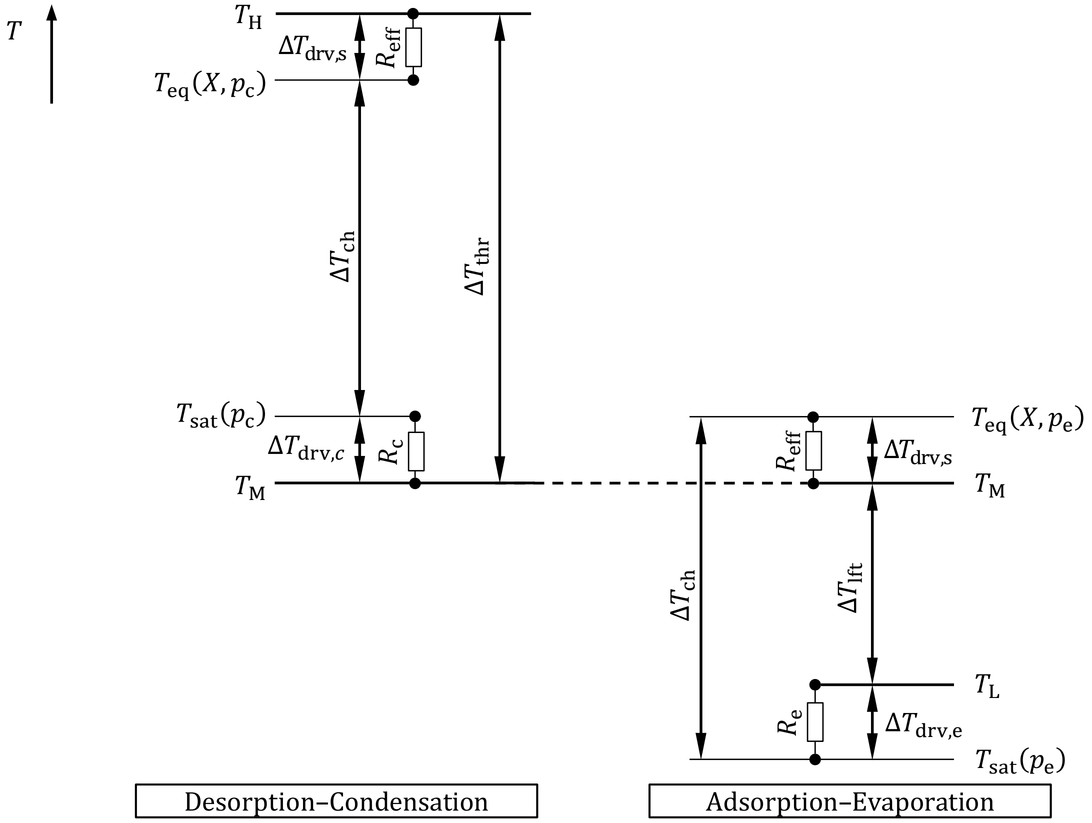

Figure 17: Relationship between principal temperature differences from external temperature conditions (ΔT_{lft}, ΔT_{thr}), from sorption equilibrium (ΔT_{ch}), and for driving heat and mass transfer (ΔT_{drv}) during both isobaric phases for quasi-isothermal conditions

During the adsorption half-cycle (Figure 17, right part), the temperature lift is composed of three principal temperature differences:

$$\begin{aligned}\Delta T_{\mathrm{lft}} &= T_{\mathrm{M}} - T_{\mathrm{L}} \\ &= \underbrace{\left(T_{\mathrm{eq}}(X, p_{\mathrm{e}}) - T_{\mathrm{sat}}(p_{\mathrm{e}})\right)}_{\Delta T_{\mathrm{ch}}} - \underbrace{\left(T_{\mathrm{eq}}(X, p_{\mathrm{e}}) - T_{\mathrm{M}}\right)}_{\Delta T_{\mathrm{drv,s}}} - \underbrace{\left(T_{\mathrm{L}} - T_{\mathrm{sat}}(p_{\mathrm{e}})\right)}_{\Delta T_{\mathrm{drv,e}}}. \qquad (83)\end{aligned}$$

The same relation may be applied – with different sign – to the desorption half-cycle (Figure 17, left part). For the sake of clarity, however, the following will be limited to the adsorption half-cycle.

$\Delta T_{\mathrm{drv,s}}$ and $\Delta T_{\mathrm{drv,e}}$ are the two temperature differences driving the process in the adsorber and the evaporator, introduced above. ΔT_{ch} is defined here as the characteristic temperature difference of the working pair at p_{e} and X. The latter may also be formulated as a function of either the adsorbent or the evaporator temperature, which might be more convenient in some cases:

$$\begin{aligned}\Delta T_{\mathrm{ch}}(T_{\mathrm{s}},X) &= T_{\mathrm{s}} - T_{\mathrm{sat}}\left(p_{\mathrm{eq}}(T_{\mathrm{s}},X)\right)\\ \Delta T_{\mathrm{ch}}(T_{\mathrm{e}},X) &= T_{\mathrm{eq}}\big(X,p_{\mathrm{sat}}(T_{\mathrm{e}})\big) - T_{\mathrm{e}}.\end{aligned} \tag{84}$$

This concept of temperature differences, combined with the effective thermal resistances, allows relating the external temperature levels, which are set by the application, to the heat flows during the isobaric phases. With the same assumption of a quasi-isothermal adsorption as above, the external heat flow and the adsorption associated heat flow are equal: $\dot{Q}_{\mathrm{M}} = \dot{Q}_{\mathrm{s}} = m_{\mathrm{s}}\Delta h_{\mathrm{s}}\dot{X}$. Further, $\dot{Q}_{\mathrm{s}}$ is coupled to the evaporator heat flow through the same gas mass flow ($-m_{\mathrm{g}} = m_{\mathrm{s}}\dot{X}$), but a different enthalpy change: $\dot{Q}_{\mathrm{e}} = \Delta h_{\mathrm{v}}/\Delta h_{\mathrm{s}} \cdot \dot{Q}_{\mathrm{M}}$. This allows rewriting Eq. (79) as

$$R_{\mathrm{e}}\frac{\Delta h_{\mathrm{v}}}{\Delta h_{\mathrm{s}}} = \frac{\Delta T_{\mathrm{drv,e}}}{\dot{Q}_{\mathrm{M}}} \tag{85}$$

so that it can be added to Eq. (79), yielding

$$\dot{Q}_{\mathrm{M}} = \frac{\Delta T_{\mathrm{drv,e}} + \Delta T_{\mathrm{drv,s}}}{R_{\mathrm{e}}\frac{\Delta h_{\mathrm{v}}}{\Delta h_{\mathrm{s}}} + R_{\mathrm{eff}}}. \tag{86}$$

With Eq. (83) this can be rewritten as

$$\dot{Q}_{\mathrm{M}}(T_{\mathrm{s}},X) = \frac{\Delta T_{\mathrm{ch}}(T_{\mathrm{s}},X) - \Delta T_{\mathrm{lft}}}{R_{\mathrm{e}}\frac{\Delta h_{\mathrm{v}}}{\Delta h_{\mathrm{s}}} + R_{\mathrm{eff}}}, \tag{87}$$

to get a simple Ohm's-law-like relation between external heat flow $\dot{Q}_{\mathrm{M}}$, and the overall driving temperature difference. The latter is determined by the easily accessible quantities ΔT_{lft} and $\Delta T_{\mathrm{ch}}(T_{\mathrm{s}},X)$, which characterise the application conditions and the sorption properties of the material, respectively. For the low temperature heat, the same approach yields:

$$\dot{Q}_{\mathrm{L}}(T_{\mathrm{s}},X) = \frac{\Delta T_{\mathrm{ch}}(T_{\mathrm{s}},X) - \Delta T_{\mathrm{lft}}}{R_{\mathrm{e}} + R_{\mathrm{eff}}\frac{\Delta h_{\mathrm{s}}}{\Delta h_{\mathrm{v}}}}. \tag{88}$$

For a discrete sorption material the loading dependency of ΔT_{ch} is small, since all (relevant) isosteres are close together or even superimposed. This allows to use $\Delta T_{\mathrm{ch}}(T_{\mathrm{s}},X) \approx \Delta T_{\mathrm{ch}}(T_{\mathrm{s}})$ as a first simplification. The dependency on the adsorbent temperature can be calculated through the Clausius–Clapeyron equation. A useful approximation, derived in Appendix A.4 based on a Taylor expansion, is

$$\frac{\partial \Delta T_{\mathrm{ch}}}{\partial T_{\mathrm{s}}} \approx 1 - \frac{\Delta h_{\mathrm{s}}}{\Delta h_{\mathrm{v}}}\left(1 - \frac{\Delta T_{\mathrm{ch}}}{T_{\mathrm{s}}}\right)^2. \tag{89}$$

The explorative evaluation of Eq. (89) indicates, that the temperature dependency of ΔT_{ch} is also small (Table 3). Thus, $\Delta T_{\mathrm{ch}}(T_{\mathrm{s}}, X) \approx \Delta T_{\mathrm{ch}}(T_{\mathrm{M}})$ may be used for the heat flow estimation in Eqs. (87) and (88). It is more convenient to use T_{M} here, as it is typically available a priori from the application conditions, while T_{s} is an internal process parameter, which itself depends on the complete design. For a first order approximation ΔT_{ch} might even be treated as a constant.

For the case of sorption materials with more continuous sorption equilibria, this simplification may not be made. Although out of scope here, Eqs. (87) and (88) could then still be useful if extended by an appropriate averaging in order to yield the mean heat flow expected per half-cycle.

It might be helpful to draw an analogy of this approach to common models of electrochemical batteries, where ΔT_{ch} corresponds to the open-circuit voltage (cell voltage in thermodynamic equilibrium), ΔT_{thr} to the charge voltage, ΔT_{lft} to the discharge voltage, and R_{e}, R_{c} and R_{s} to the internal resistances (Lasia, 2014). Also in batteries, the internal resistances include mass-transfer parts, e.g. related to the diffusive processes in the electrolyte, which are mapped to electrical resistances.

Table 3: Explorative evaluation of Eq. (89)

Working-pair	Δh_{s} (MJ/kg)	Δh_{v} (MJ/kg)	ΔT_{ch} (K)	T_{s} (K)	$\frac{\partial \Delta T_{\mathrm{ch}}}{\partial T_{\mathrm{s}}}$ (-)
SAPO-34–Water	3.2…3.5[ii]	2.5	45[ii,iii]	323	0.05…(−0.04)
Alfum–Water	2.9[iv]	2.5	22[iii,iv]	313	−0.002

[ii] Füldner (2015)

[iii] Calculated for the inflection point of the T_{s}-isotherm

[iv] This work

3.2.4 Relation to performance indicators

The concept of effective thermal resistances may be directly translated to the specific cooling power SCP (c.f. Section 2.3.3, p51), achieved during the isobaric phases. With the same assumption as above and the total effective resistance from the evaporator perspective $R_{\mathrm{e,tot}} = R_{\mathrm{e}} + R_{\mathrm{eff}}\frac{\Delta h_{\mathrm{s}}}{\Delta h_{\mathrm{v}}}$, the volume specific cooling power at loading X is

$$\begin{aligned} \mathrm{VSCP} &= \frac{\Delta T_{\mathrm{ch}}(T_{\mathrm{M}}, X) - \Delta T_{\mathrm{lft}}}{R^{V}_{\mathrm{e,tot}}} \\ &= \frac{\Delta T_{\mathrm{drv,tot}}}{R^{V}_{\mathrm{e,tot}}}, \end{aligned} \tag{90}$$

and the mass specific cooling power

$$\begin{aligned}\mathrm{MSCP} &= \frac{\Delta T_{\mathrm{ch}}(T_{\mathrm{M}}, X) - \Delta T_{\mathrm{lft}}}{R_{\mathrm{e,tot}}^{m}} \\ &= \frac{\Delta T_{\mathrm{drv,tot}}}{R_{\mathrm{e,tot}}^{m}}.\end{aligned} \tag{91}$$

This estimates the average cooling power during one adsorption half-cycle. If a complete cycle is to be assessed, the ratio between the durations of the adsorption half-cycle and the complete cycle must be taken into account.

4. Experimental

Experiments were carried out to fully characterise the sorption equilibrium and dynamics of aluminium fumarate coatings in different thicknesses. To this end, an extended FRA-based procedure was developed and applied with a specially designed and custom built setup. This "extended frequency response analysis" allows determining relevant material properties (namely the adsorption equilibrium and the adsorption enthalpy) together with the actual FR in a single integrated procedure. Finally, the remaining quantity of interest, the specific heat capacity, was measured with commercial DSC devices in a procedure, specially adapted to adsorbent measurements.

4.1 Material

An aqueous dispersion of 26.8 wt% aluminium fumarate (a.k.a. MIL-53(Al)-FA, sourced as "Basolite® A520" from BASF; Kiener *et al.*, 2009; Alvarez *et al.*, 2015) and 17.9 wt% silicone binder (SilRes® MP50E, Wacker Silicones) was processed by a knife coating applicator on 50 x 50 x 2 mm^3 AlMg3 sample plates (Table 4). The wet film thickness was varied by an octagonal stainless steel mask with a defined thickness (200, 350, 600 µm) and constant coating surface A_{ct} (18.7 cm^2). The samples were oven dried at 200 °C for 3 h, before measuring the coating thicknesses d_{ct} of the final samples at five points with a probe indicator (Table 4, Figure 18). The sample dry mass was determined directly after oven drying by quickly ($T \geq 160$ °C) weighing the hot samples under lab atmosphere. The total dry adsorbent content $w_{\mathrm{s,dry}}$ and the binder content w_{bnd} were first calculated from the suspension composition, based on experimentally determined dry masses of different suspension components, as shown by Kummer et al. (2015), and later cross checked by comparing the uptake of the samples to the uptake of pure adsorbent powder. The latter was measured manometrically before (AUTOSORB®, Quantachrome). The coating dry density was calculated as $\rho_{\mathrm{cmp}} = m_{\mathrm{cmp}}/(A_{\mathrm{ct}} d_{\mathrm{ct}})$.

Table 4: Sample mass, geometry and composition by dry mass , the adsorbent content was estimated when mixing the coating suspension and confirmed later by comparing the uptake of the sample with the pure adsorbent powder isotherm (c.f. Section 5.1)

				By suspension compositionx		By comparison to pure adsorbent uptake	
Sample	m_{cmp} (mg)	d_{ct} (mm)	ρ_{cmp} (g/cm^3)	$w_{\mathrm{s,dry}}$	w_{bnd}	$w_{\mathrm{s,dry}}$	w_{bnd}
Ct_140	134±3	0.14±0.04	0.51±0.15	0.75	0.25	0.72	0.28
Ct_240	217±4	0.24±0.05	0.48±0.10	0.75	0.25	0.79	0.21
Ct_610	563±11	0.61±0.07	0.49±0.06	0.75	0.25	0.80	0.20

The macro porosity of the coating ε_{P} is estimated at 0.47 based on the composite dry density, the mass fraction and density of the binder ($\rho = 1.1$ g/cm^3, calculated from Kummer et al. (2017a) where the same octagonal stainless steel masks were used), and the apparent dry density of the aluminium fumarate crystals. As reported measurements of the later are lacking, it was estimated based on the structural data that Alvarez et al. (2015) obtained by Rietveld refinement. They estimated the volume of a fully hydrated unit cell, consisting of two metal Al(OH) octahedrals ($m = 2 \cdot 44.0$ u) and four fumarate $C_4O_4H_2$ linkers ($m = 4 \cdot 114.1$ u), to 990 Å^3, yielding $\rho = 0.91$ g/cm^3. It should be noted that these values does not account for water induced shrinking or swelling nor for any defects or impurities that are likely to be found in the actual adsorbent particles.

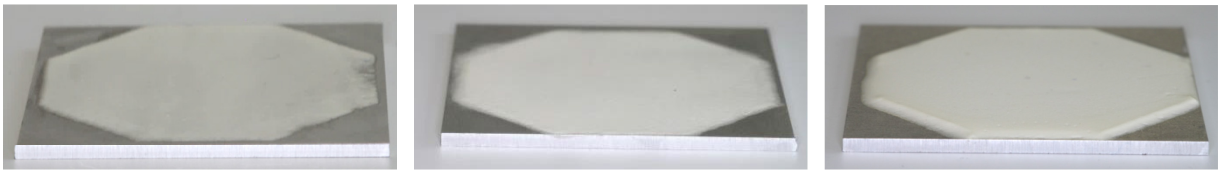

Ct_140 Ct_240 Ct_610

🅭 by Laurenz *et al.*, 2020 / CC BY 4.0

Figure 18: Photographs of samples for sorption dynamic experiments with different coating thicknesses on a 50 x 50 x 2 mm^3 AlMg3 sample plate

The particle size of the initial adsorbent power was measured before to be 18 µm on average (Appendix A.5, Figure 48).

4.2 Extended Frequency Response Analysis

The extended FRA, a custom built setup combined with a specially developed procedure, aims to determine the adsorption equilibrium and the adsorption enthalpy together with the FRA in a single time saving measurement. This allows for results that perfectly match the same thermodynamic state and for the same single sample. Errors from results interpolation to different thermodynamic states and possibly differing sample compositions are avoided.

4.2.1 Setup

Sorption kinetic measurements are done with a custom setup (schematic: Figure 19) under pure water vapour atmosphere allowing FR, LTJ, LPJ and SPJ experiments with water. Details on jump experiments with the setup have been reported extensively before (Schnabel, 2009; Füldner, 2015; Velte *et al.*, 2017).

For FR measurements in the course of this work, the existing setup is extended and partly redesigned (photograph: Figure 20). The closed measurement chamber volume ($\bar{V} = 885.4 \pm 1.3$ ml) is varied by 4.12% through a mechanically driven vacuum below, while the bellow position is recorded with a vacuum stable linear variable differential transformer (LVDT, Schreiber Messtechnik, $\tau = 1.3$ ms). The bellow position has been calibrated with a second order polynomial to the chamber volume by filling the evacuated and temperature controlled chamber with water of known mass. The sample, pre-conditioned to a given loading X_0 or pressure p_0, is thermally well connected (thermal grease TG20032, Müller Ahlhorn) to the cold plate kept isothermal ($\pm$ 0.01 K) by an external circuit. The absolute cold plate temperature is precisely measured with a 4-wired Pt100 sensor embedded in a bore.

The sinusoidal chamber pressure response can be recorded simultaneously with two pressure transducers: a slow high-precision capacitive sensor (MKS Baratron 627B, $\tau = 40$ ms) for practical reasons connected through long tubes, and a fast piezo-resistive sensor (STS ATM, $\tau = 1$ ms) directly mounted in the chamber wall (both sensors 0–100 mbar). The signal from the less long-term stable STS sensor is corrected for each set of measurements based on low frequency results ($f \leq 0.05$ Hz) where the low-pass filter (LPF) bias of the MKS is negligible.

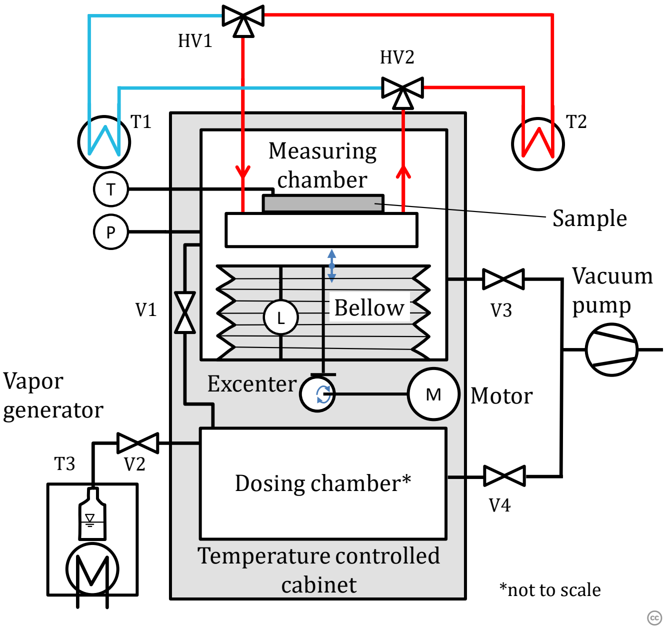

🄯 by Laurenz *et al.*, 2020 / CC BY 4.0

Figure 19: Schematic of the sorption kinetic setup for frequency response, large temperature jump and large pressure jump experiments with absolute and differential equilibrium measurement. Absolute sorption equilibria are measured manometrically by dosing in from the dosing chamber, differential equilibria by small temperature and pressure jumps around equilibrium. For frequency response measurements, the sample support is kept isothermal and small volume fluctuations are applied with a mechanically driven bellow, while the bellow position, chamber pressure and sample surface temperature are recorded.

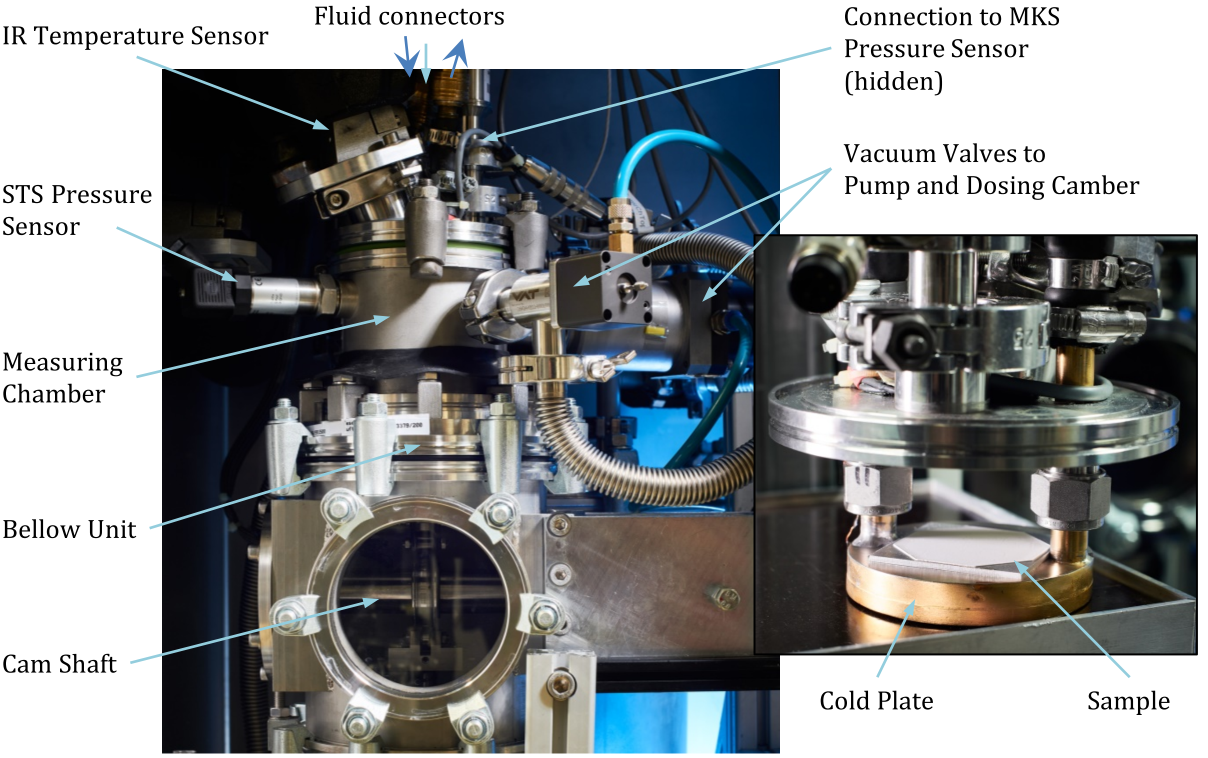

Figure 20: Photograph of the sorption kinetic setup for frequency response measurements with detail of the measuring chamber top when removed for sample installation

The sample surface temperature is recorded with an IR temperature sensor (Heitronics KT15, $\tau_{\text{min}} = 5$ ms) through a ZnSe vacuum viewport. The noise equivalent temperature difference (NETD) of the IR signal depends on the set response time with min. values of 25 mK at $\tau = 1$ s (temperature invariant) and max. values of 1.1 and 0.6 K at $\tau = 5$ ms depending on the sample temperature between 20 and 100 °C. The noise reduction is approximately proportional to $\tau^{-0.7}$ at 100 °C and $\tau^{-0.6}$ at 20 °C sample temperature. The response time is set to less than 1/1000 of the below period as long as possible. The measurement spot has a diameter of 6 mm (95%), and the spectral response maximum of the detector is between 8 and 14 µm, fitting to the transmissivity of the ZnSe viewport and the aimed sample temperature.

To avoid temperature gradients the whole vacuum setup is encapsulated in a temperature-controlled cabinet (± 0.1 K), which is set to the same temperature as the cold plate. Data acquisition from sensors not requiring high temporal resolution (e.g. cold plate temperature) is done with a high precision digital multi meter (Agilent 34970A). For FR-related sensors see Section 4.2.3. The key parameters of the setup are summarized in Table 5.

The setup can be classified as a volume swing thermal FRA inspired by typical approaches by other authors (Shen & Rees, 1994; Reyes *et al.*, 1997; Turner *et al.*, 2001; Song & Rees, 2008; Mohammad Iftekhar Hossain, 2014), but extended by a thorough control of the thermal contact of the sample and a temperature response measurement in order to discriminate between heat and mass transfer effects. In contrast to most applications, for AHT the heat effect is not a slight bias but purposely amongst the dominating mechanism for overall adsorption kinetics. To the author's knowledge, comparable measurements have been only performed at LIMSI-CNRS in the late 1990s (Bourdin *et al.*, 1996a; Bourdin *et al.*, 1996b; Bourdin *et al.*, 1998), but with immense effort on temperature measurement (liquid helium cooled detector) to reach an NETD of 1.5–15 mK at 5 ms response time. Driven by practical and economic considerations, the setup presented in this work employs an off-the-shelf temperature sensor, to the cost of a noise level, about two orders of magnitude higher than for the LIMSI-CNRS setup. The increased noise level is compensated by longer measurement times, in order to reach satisfying precision.

Table 5: Key parameters of the sorption kinetic setup used for frequency response experiments

Parameter	Value
Working fluid	Water
Sample adsorbent dry mass (typical)	50–500 mg
Max. sample geometry	$50 \times 70 \times 15$ mm^3
Temperature cold plate	5–95 °C
Temperature cabinet	20–80 °C
Mean pressure p_0	1–100 mbar
Measuring chamber volume mean $V_0 \pm$ amplitude $\hat{V}$	885.4 ± 36.5 ml
Frequency range	1×10^{-3}–5 Hz

4.2.2 Procedure

The measurement procedure consists of three steps: (i) pre-conditioning to the desired state, (ii) determination of the equilibrium slopes and (iii) the actual FR measurement. Throughout the measurement, the temperature-controlled cabinet is kept at the measurement mean temperature T_0. Measurements are carried out at 30–60 °C and in the entire loading range.

Table 6: Equilibrium set points for frequency response experiments

T_0 (°C)	X_0 (kg/kg$_s$)				
	0.05	0.13	0.2	0.28	0.35
30			●		
40	●	●	●	●	●
60			●		

4.2.2.1 Pre-conditioning and uptake measurement

Samples are fully desorbed and pre-conditioned to the desired state (Table 6), allowing for measuring the adsorption equilibrium manometrically, as detailed in the following.

Initially, samples are desorbed against a rotary vane pump ($p < 0.01$ mbar) at 95 °C overnight, to remove any co-adsorbed impurities. For aluminium fumarate this ensures an initial loading X_{init} of 0 kg/kg. After cooling down the closed chamber to T_0, the sample is pre-conditioned to a desired loading X_0 by dosing in vapour from the dosing chamber. X_0 is calculated manometrically from the mass balance of both chambers and the adsorbent dry mass $m_s = w_{s,\text{dry}} m_{\text{cmp}}$ following the ideal gas law, which is a very good approximation for water in the pressure and temperature region of the measurements:

$$X_0 = X_{\text{init}} + \frac{1}{T_0 R_w m_s} [V_D p_{D1} + V_{M1} p_{M1} - (V_{M2} p_{M2} + V_D p_{D2})]. \qquad (92)$$

Here, the indexes D and M denote the dosing chamber ($V_D = 41.815 \pm 0.021$ l) and the measuring chamber, where the volume depends on the bellow position, and the indexes 1 and 2 denote the equilibrium state before and after dosing in vapour. Set points for the pressures $p_{D,1}$ and $p_{D,2}$ are calculated beforehand, based on the isotherm of the pure adsorbent powder to approximately reach the set point for X_0. An automatic routine conditions the dosing chamber to p_{D1} by dosing in vapour from the vapour generator, and – if required – short evacuation for pressure reduction. Vapour dosing is started by opening V1 and stopped as soon as $p_{D,2}$ is reached. Eq. (92) is evaluated with the measured values of p_D to calculate X_0. The equilibrium pressure of the sample $p_0 = p_{M,2}$ will follow the equilibrium of the sorbent at T_0 and X_0, yielding a point on the T_0-isotherm. To calculate the effective loading X_{eff}, the composite mass m_{cmp} is used in Eq. (92) instead of m_s.

After pre-conditioning, the valve V1 remains closed throughout the rest of the measurement.

4.2.2.2 Differential sorption equilibrium and sorption Enthalpy

The differential sorption equilibrium, i.e. the slopes of the isotherm $\partial X/\partial p$ and the isobar $\partial X/\partial T$, is determined with small volume and temperature variations, respectively. This data allows calculating the sorption enthalpy (c.f. Section 2.1.2) and is required for the FRA models (Section 3.1.2). Further, the assumption of locally hysteresis-free sorption equilibria, which is fundamental to the FRA models, is checked by comparing the loading reached at V_0 and T_0 coming from above and from below.

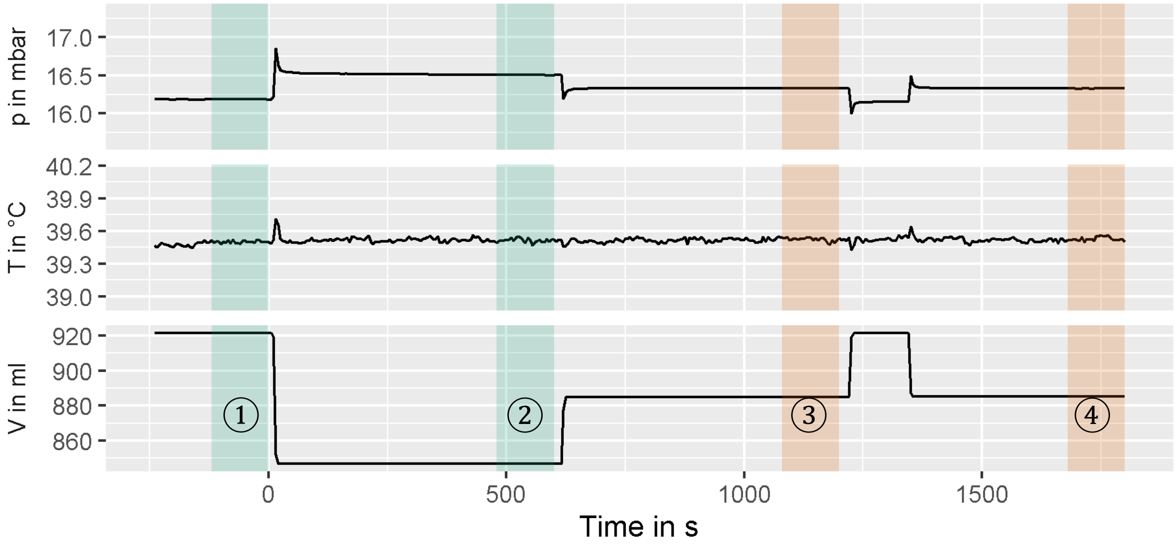

Figure 21: Typical signal used for determination of the isotherm slope $\mathrm{d}X/\mathrm{d}p$: The volume is changed with a rectangular pattern, temperature kept constant. Means of the highlighted equilibrium sections are evaluated for slope (green) and hysteresis check (orange).

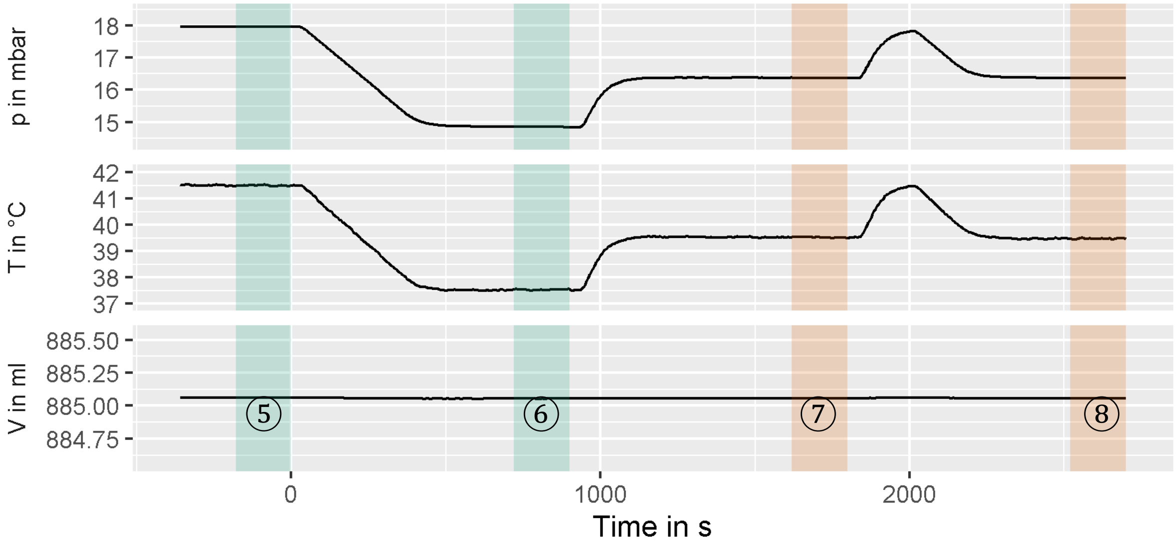

Figure 22: Typical signal used for determination of the isobar slope $\mathrm{d}X/\mathrm{d}T$: The volume is kept constant, while the temperature set point is changed with a rectangular pattern; the actual temperature is delayed by the limited thermostat power and controller characteristic. Highlighted sections as in Figure 21

To measure the equilibrium slopes a rectangular signal with small volume and temperature jumps is applied to the pre-conditioned sample and the equilibrium loading changes are evaluated manometrically (Figure 21 and Figure 22). The method is comparable to static gain evaluation from step response experiments e.g. in control systems.

The evaluation of the isotherm slope is straight forward from the isothermal (index T) volume change (Figure 21):

$$\frac{\partial X}{\partial p} \approx \frac{\Delta X_T}{\Delta p_T} = \frac{\Delta m_{\mathrm{a},T}}{m_\mathrm{s}\Delta p_T} = \frac{-(p_2V_2 - p_1V_1)}{m_\mathrm{s}R_wT(p_2 - p_1)}. \tag{93}$$

In some cases a very slow drift in pressure was observed which is due to parasitic effects of the setup already reported before (Schnabel, 2009; Füldner, 2015). This bias is corrected by fitting linear models to sections 1 and 2 and using the extrapolated values at the centre. The extrapolation takes into account the exponential form of the drift as detailed in Appendix A.6.

The slope of the isobar can be deduced from the isochoric (but not isobaric) temperature change (Figure 22) applying the first degree Taylor approximation of the loading change:

$$\Delta X_V \approx \frac{\partial X}{\partial p}\Delta p_V + \frac{\partial X}{\partial T}\Delta T_V. \tag{94}$$

Thus

$$\begin{aligned}\frac{\partial X}{\partial T} &\approx \frac{1}{\Delta T_V}\left(\frac{\Delta m_{\mathrm{a},V}}{m_\mathrm{s}} - \frac{\partial X}{\partial p}\Delta p_V\right)\\ &= \frac{1}{(T_6 - T_5)}\left(-\frac{V}{m_\mathrm{s}R_w}\left(\frac{p_6}{T_6} - \frac{p_5}{T_5}\right) - \frac{\partial X}{\partial p}(p_6 - p_5)\right).\end{aligned} \tag{95}$$

As the FR measurement would be strongly biased by any hysteresis of the equilibrium, hysteresis checks are included in the both experiments (Figure 21 and Figure 22): The equilibria reached for the same conditions “from below” and “from above” are compared and hysteresis is assumed negligible if the difference between ΔX_{34} and ΔX_{78} is below the measurement uncertainty.

From the obtained slopes of the isotherm and isobar, the differential adsorption enthalpy may be directly calculated using Eq. (18) (p. 30). However, this leads to unfavourable uncertainty propagation, especially for steep isotherms, where $\partial X/\partial p$ is difficult to measure as Δp_T becomes very small. Better results are obtained by directly using the differences obtained in the isothermal (sample uptake $\Delta m_T, \Delta p_T$) and isochoric (sample uptake $\Delta m_V, \Delta p_V, \Delta T_V$) step experiments around the mean values p and T:

$$\Delta h_s \approx \frac{RT^2}{p}\frac{1}{\Delta T_V}\left(\Delta p_V - \frac{\Delta m_{\mathrm{a},V}}{\Delta m_{\mathrm{a},T}}\Delta p_T\right). \tag{96}$$

For materials with a step-like isotherm ($\Delta p_T = 0$ for $\Delta m_T \neq 0$) this simplifies to:

$$\Delta h_s \approx \frac{RT^2}{p}\frac{\Delta p_V}{\Delta T_V}. \tag{97}$$

4.2.2.3 Frequency response analysis

The actual FR measurement consists of a set of single-frequency sinusoidal excitations of the measurement chamber volume spaced in a close-to-geometric sequence between 10^{-3} and 5 Hz. This is realised by rotating the stepper motor with constant velocity which is converted into a sinusoidal linear motion of the bellow through a specially designed cam. The stepper motor is controlled with the same data acquisition (DAQ) device (Keysight U2351A) that records the bellow position, chamber pressure and sample surface temperature so that data acquisition and volume excitation are synchronised. The single-frequency sinusoidals are chosen for the straight forward implementation and as the most robust excitation signal. The signal-to-noise ratio is maximised by concentrating the whole signal power to a single frequency (Bohn & Unbehauen, 2016). The number of periods is increased with frequency to compensate the reducing signal-to-noise ratio.

4.2.3 Data processing

For FRA, data needs to be filtered, transformed and corrected, while for the measurement of uptake and differential equilibrium, data processing is straight forward and already detailed above.

Signals from sensors for bellow position, chamber pressure and sample surface temperature are recorded at 10 kHz sampling rate and 16 bit resolution. During the measurement, the data is downsampled by integer averaging to a sampling rate of 1000 times the bellow frequency. This results in lower noise levels for lower bellow frequencies and considerably reduced amount of raw data while the filter disturbance on the signal remains negligible. The complex FR $\boldsymbol{y}_{f_i}^{\mathrm{exp}}$ of frequency f_i is obtained using fast Fourier transformation (FFT) implemented in R (R Core Team, 2020). Spectral leakage is avoided by carefully choosing bellow frequencies that allow for an integer amount of (averaged) samples per bellow period and cutting time series data to multiples of complete bellow periods.

Corrections are applied to the volume perturbation and the FR signals of sample surface temperature and measurement chamber pressure as detailed in the following.

4.2.3.1 Volume correction

The perturbation of the measurement chamber volume deduced from the measured bellow position is corrected for the slight LPF behaviour of the sensor (cut-off frequency $1/\tau_V = 800$ Hz) with a first order LPF:

$$\tilde{V}_{\mathrm{cor}} = (i2\pi f_{\mathrm{blw}}\tau_V + 1)\tilde{V}_{\mathrm{msr}}. \tag{98}$$

The correction rises linearly with f_{blw} affecting significantly only the phase shift (+2.2° at 5 Hz) but not the amplitude (+0.08% at 5 Hz).

4.2.3.2 Pressure correction

The measured chamber pressure response is corrected for drift and temperature dependency in a first and for dynamic non-idealities in a second step. The pressure is measured as $\tilde{p}_{\mathrm{STS}}$ with a fast STS ATM piezoresistive pressure sensor ($\tau = 1$ ms) introduced directly in the chamber wall next to the sample to allow for little damping. The drawbacks of this fast and inexpensive sensor are reduced long term stability (0.5–4 mbar per year) and high temperature drift. For the first correction step, the same pressure is also measured as $\tilde{p}_{\mathrm{MKS}}$ with a temperature compensated high precision MKS Baratron sensor placed outside the temperature controlled cabinet at lab ambient temperature. This second measurement has a strong LPF characteristic making it inappropriate for higher frequencies. However, for amplitudes at $f_{\mathrm{blw}} \leq 0.05$ Hz the damping is negligible ($\tau = 40$ ms, i.e. $|p_{\mathrm{out}}|/|p_{\mathrm{in}}| < 10^{-4}$)) and these data points can be used for correction. A simple linear model has proven useful to predict the corrected measured pressure amplitude $|p_{\mathrm{msr}}|$ with the measured $|\tilde{p}_{\mathrm{STS}}|$. No corrections are applied to the phase lag which is not affected by any drift effects. Thus:

$$\tilde{p}_{\mathrm{msr}} = (c_1|\tilde{p}_{\mathrm{STS}}| + c_0)e^{i\arg(\tilde{p}_{\mathrm{STS}})}. \tag{99}$$

The correction coefficients c_0 and c_1 are evaluated by linear regression ($R > 0.99$) for each measurement.

The second correction step takes into account the non-idealities of the empty measurement chamber. The result is the pressure that the experiment would yield in an ideal chamber as assumed by the models (c.f. Section 3.1.2). To do so, the empty measurement chamber has to be characterised for its non-ideal frequency response, i.e. deviations form an isothermal compression with constant gas mass and uniform spatial pressure distribution (Wang & LeVan, 2011). Examples for non-ideal effects are adsorption on the chamber walls, non-isothermal compression, damping effects of tubes connected to the chamber or the weak LPF behaviour of the STS ATM sensor.

Blank measurements were carried out at five temperatures between 30 and 70 °C, four pressures per temperature level and eight frequencies between 0.001 and 5 Hz per p-T-state. The pressures levels where chosen as a geometric sequence in p_{rel} between 0.03 and 0.43 covering the region of interest and accounting for the $\ln(p)$-dependency of most expected non-ideal effects.

All non-idealities are attributed to the pressure response. The indirect small disturbance of the surface temperature signal cannot be controlled with blank measurements (no temperature response) and is assumed to be negligible. A compensation of the temperature signal would require to differentiate between real (wall adsorption, damping), apparent (filter behaviour of sensors), and non-isothermal pressure effects which is not practically feasible.

The pressure correction consists of a simple multiplication of the measured pressure response $\tilde{p}_{\mathrm{msr}}$ with a complex correction factor:

$$\tilde{p}_{\mathrm{cor}} = \psi\tilde{p}_{\mathrm{msr}}. \tag{100}$$

The empty chamber pressure correction factor $\psi = -\frac{\tilde{V}}{V_0}\frac{p_0}{\tilde{p}_{\mathrm{cal}}}$ can be deduced from the chamber mass balance

$$
\begin{aligned}
0 &= \mathrm{d}m_{\mathrm{w,g}} - \mathrm{d}m_{\mathrm{err}} + \underbrace{\mathrm{d}m_{\mathrm{w,s}}}_{=0} \\
&= \frac{\mathrm{d}(pV)}{R_{\mathrm{w}}T_0} - \mathrm{d}m_{\mathrm{err}},
\end{aligned}
\tag{101}
$$

where no water is adsorbed ($\mathrm{d}m_{\mathrm{w,s}} = 0$) under the assumption that the mass balance error $\mathrm{d}m_{\mathrm{err}}$ is proportional to the measured pressure response $\tilde{p}_{\mathrm{msr}}$ (see Appendix A.7). Blank measurements yielded values in the range of 0.9–1.05 for $\mathrm{Re}(\psi)$ and (–0.075)–0 for $\mathrm{Im}(\psi)$. The dependency of ψ on mean temperature, mean pressure and frequency is fitted using a scaled and centred multivariate kriging model with noisy observations implemented in R (Roustant *et al.*, 2012). After correction, the non-idealities of the pressure response are below 2% of the relative pressure response $\tilde{p}/p_0$. Details are given in Appendix A.7. The typical pressure response (measured and corrected) in Figure 23 illustrates how correction and uncertainties mainly apply to higher frequencies.

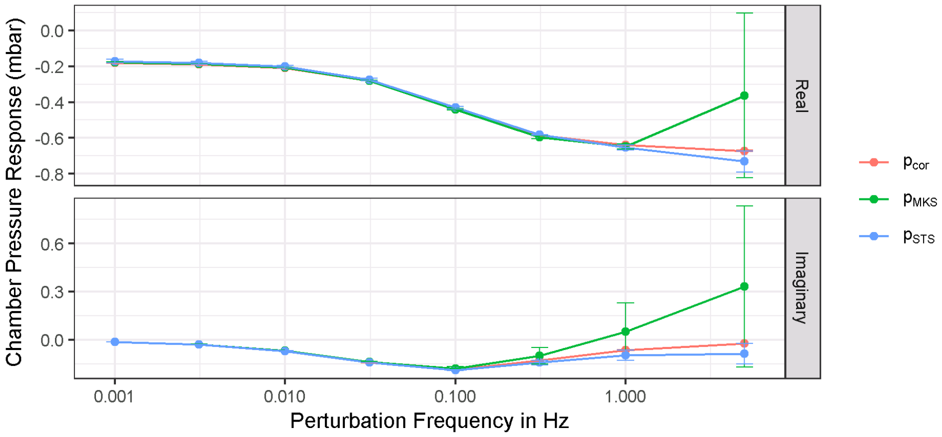

Figure 23: Comparison of the corrected pressure response to measured signals for a typical case, illustrating changes in uncertainties over frequency. The uncertainty of the measured signals (MKS and STS) take into account the missing corrections amongst others (c.f. Section 4.2.4.1).

4.2.3.3 Temperature correction

The response of the surface temperature is corrected for linearity errors arising from the IR measurement principle (complicated non-linear radiation mechanism and deviations of assumed optical surface properties) and the sensor LPF ($\tau_T = 5$ ms). Significant gas heating effects (Bourdin *et al.*, 1998) could not be observed in blank experiments with a graphite coated (GRAPHIT 33, Kontakt Chemie) aluminium sheet and are therefore not corrected. To correct the linearity error, the change in the measured IR signal $\Delta T_{\mathrm{smpSrf,msr}}$ is compared to the change in the cold plate temperature $\Delta T_{\mathrm{cldPlt}}$ at small increments (± 2 K) around the measurement temperature after reaching a steady state at the same state (pressure, loading) as the FR measurement. Deviations are in the order of some percentage points. For the LPF correction see above (Section 4.2.3.1). The overall correction function is:

$$\tilde{T}_{\mathrm{smpSrf,cor}} = \frac{\Delta T_{\mathrm{cldPlt}}}{\Delta T_{\mathrm{smpSrf}}} (i2\pi f_{\mathrm{blw}} \tau_T + 1) \tilde{T}_{\mathrm{smpSrf,msr}}. \qquad (102)$$

4.2.4 Uncertainty analysis

Uncertainty analysis has been carried out using the *Guide to the expression of uncertainty in measurement* (GUM) as a basis (JCGM, 2008).

4.2.4.1 Frequency response

The FR encompasses the measurement of the complex system response and excitation ($\tilde{p}_{\mathrm{ch}}, \tilde{T}_{\mathrm{smpSrf}}$ and $\tilde{V}_{\mathrm{ch}}$) and the absolute mean values ($p_0 = \bar{p}_{\mathrm{ch}}, T_0 = \bar{T}_{\mathrm{smpSrf}}, V_0 = \bar{V}_{\mathrm{ch}}$).

Mean values

Standard uncertainties of mean chamber volume, chamber pressure and sample temperature are estimated by combining all applicable uncertainties of sensors and DAQ. Uncertainties stated as temperature dependent are assumed interdependent and thus combined linearly. All other uncertainties are assume independent and combined quadratically. In all cases, uncertainties of the mean (Type A uncertainties) are negligible due to the great number of samples (> 10^4) per evaluated data point.

The mean chamber volume is about 885 ml for all measurements and is calculated based on the measurement of the bellow position with a LVDT sensor. Its total uncertainty varies with measurement temperature between 0.4 ml (20 °C) and 1.3 ml (80 °C). This includes contributions from the calibration between chamber volume and bellow position (0.4 ml), the absolute non-reproducibility of the LVDT sensor (0.07 ml) and the DAQ (0.01 ml), the temperature drift of the LVDT sensor (< 0.2 ml) and its electronic module (< 0.04 ml) and thermal expansion effects (< 0.9 ml), including the absolute thermal expansion of the chamber and the difference in thermal expansion of the chamber (stainless steel) and the LVDT sensor core rod (brass).

The mean chamber pressure is evaluated from the MKS Baratron signal independent of frequency. Its uncertainty varies between 0.05 mbar ($\bar{p} = 5$ mbar) and 0.15 mbar ($\bar{p} = 100$ mbar) including sensor uncertainty with temperature drift and zero shift (0.04 – 0.15 mbar) and DAQ uncertainty (0.03 – 0.04 mbar).

The mean sample temperature is measured with a Pt100 sensor placed inside a blind hole in the cold plate. Its uncertainty is estimated at 0.07 K including uncertainties from calibration[7] (0.03 K) and DAQ (0.06 K).

Complex responses

Standard uncertainties of the measured complex responses of the measurement chamber pressure and the sample surface temperature as well as the complex excitation of the measurement chamber volume have been estimated with a procedure based as much as possible on GUM (JCGM, 2008). The different contributions to the overall

---

[7] Calibrated against the Pt100 reference thermometer Physics 1000 ($\sigma_T = 0.02$ K)

uncertainty are described in the second part of this section after a short introduction on complex error propagation.

Complex uncertainty propagation is not explicitly treated by GUM (JCGM, 2008). However, it can be carried out as bivariate combination of real and imaginary part uncertainties; whereas a combination of modulus and argument uncertainties has a strong bias for values close to $0 + i0$ and are advised against (Ridler & Salter, 2002). It is assumed that the influence of covariances between real and imaginary part can be neglected. Further elaborated methods of complex uncertainty propagation can be found e.g. in Hall (2004).

The complex error propagation under these assumptions can be illustrated for the simple case of a complex output quantity $\tilde{y} = y_1 + iy_2$ that depends on an input quantity $\tilde{x} = x_1 + ix_2$ with the functional relationship

$$\tilde{y} = f(\tilde{x}) \tag{103}$$

as follows. The functional relationship can be rewritten with real variables as

$$y_1 + iy_2 = f_1(x_1, x_2) + if_2(x_1, x_2). \tag{104}$$

Where f_1 and f_2 denote the real and imaginary part of the complex function f. The uncertainty of $\tilde{y}$ is then

$$\begin{pmatrix} u^2(y_1) \\ u^2(y_2) \end{pmatrix} = \begin{pmatrix} \left(\frac{\partial f_1}{\partial x_1} u(x_1)\right)^2 + \left(\frac{\partial f_1}{\partial x_2} u(x_2)\right)^2 \\ \left(\frac{\partial f_2}{\partial x_1} u(x_1)\right)^2 + \left(\frac{\partial f_2}{\partial x_2} u(x_2)\right)^2 \end{pmatrix}. \tag{105}$$

The partial derivatives in Eq. (105) are solved numerically with appropriate step widths as part of the data evaluation routine. If required, the real and imaginary uncertainty of the output variable are also expressed as uncertainty of amplitude and phase (i.e. modulus and argument) following a transformation algorithm by Hall (2007).

Uncertainties of the complex response may arise from time lags in the DAQ, hysteresis effects, random effects (noise), linearity uncertainty and imperfect corrections. All effects contributing to the absolute uncertainty only (offsets, temperature drifts) are not relevant as the Fourier transform is insensitive to changes of the mean value. In contrast, linear errors of the values measured in time are directly fed through as linear errors of the Fourier transformed values.

The time-lag-related uncertainties are negligible. The sampling rate per channel was 10 kHz for all measurements, thus the between-channels time lag is < 0.1 ms, < 0.05% of the shortest bellow period (200 ms).

Hysteresis was observed to be insignificant compared to the uncertainty from other sources for pressure and chamber volume measurements in specially designed tests[8]. In contrast to pressure measurements, were a moving diaphragm may be prone to some

---

[8] Using the direct control of the stepper motor the same position was attained from above and below.

kind of stiction, for IR surface temperature measurements no physical mechanism for hysteresis could be identified. In addition, a coarse hysteresis testing[9] was carried out showing no significant effect.

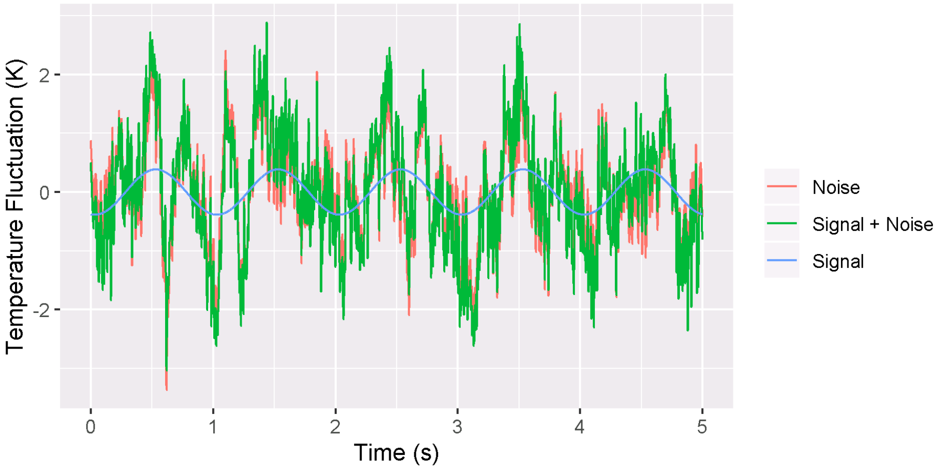

Figure 24: Example of a section of the temporal signal and noise used in the Monte Carlo simulation to estimate uncertainty (here for the surface temperature) from random effects ($f_{blw} = 1$ Hz, $\hat{T} = 0.39$ K, 40 °C, 16.6 mbar) showing 5 of 35 evaluated periods

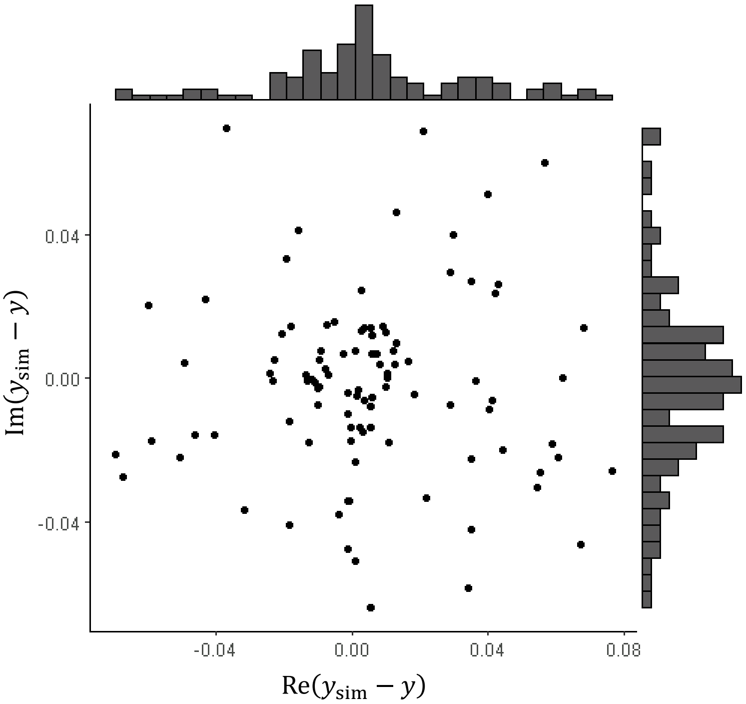

Figure 25: Result of the Monte Carlo simulation for the example shown in Figure 24 as complex scatter plot of the difference between the actual signal y and the signal found in the noisy time series y_{sim} in K ($\sigma_T = 0.030 + i0.025$ K)

Uncertainties arising from random effects were estimated for all signals with a Monte Carlo simulation based on steady state measurements (pure noise) under the same conditions as the actual measurement (sample, temperature, loading). For the

---

[9] Using the lab thermostats the same temperature set point was attained from above and below.

simulation, an artificial signal of the same amplitude and length as in the actual measurement was superposed to the pure noise. Then, the noisy signal is processed like the measurement (Figure 24). Finally, the uncertainty was deduced from the variance between the detected signal and the actual signal for a large number of runs (Figure 25). For each run ($n \geq 1000$), the section of the pure noise used and the phase of the artificial signal were shifted in random draws from a uniform distribution based on the "Mersenne twister" algorithm (Matsumoto & Nishimura, 1998) implemented in R (R Core Team, 2020) in order to avoid interference bias.

For the chamber volume perturbation, the linearity uncertainty arises from the DAQ like for all measurands (0.04%) and from the LVDT sensor (0.1%). The imperfect calibration between chamber volume and bellow position accounts for an uncertainty of 1.1% ($\pm$0.4 ml per 37 ml amplitude). The uncertainty of the correction of the sensor LPF characteristic (cut-off frequency 800 Hz) is assumed with 25% of the correction factor. This yields uncertainty contributions to the imaginary part for higher frequencies of 0.4 ml (5 Hz) to 0.04 ml (0.5 Hz). The uncertainty contribution to the real part is negligible. So is the effect of thermal expansion on the volume perturbation.

The pressure response is calculated with a two-step correction based on the measured signal from the STS ATM sensor (c.f. Section 4.2.3.2). The uncertainty estimation includes the random and DAQ uncertainty of the uncorrected pressure sensor signal. The uncertainty contributions from the amplitude correction (per-measurement calibration of amplitudes from STS to MKS at low frequencies using a linear model) and from the empty chamber correction are estimated based on the standard uncertainty estimation of the respective correction models as implemented[10] in R and random uncertainties of the measurements the corrections are based upon. All uncertainty contributions are combined with complex uncertainty propagation methods (Hall, 2004).

The sample surface temperature is based on the IR-sensor measurement, corrected for LPF effects and linearity errors (c.f. Section 4.2.3.3). The random effect of the background noise in the signal is taken into account with Monte Carlo simulations (see above), which is by far the biggest uncertainty contribution for higher frequencies. The uncertainty arising from the low-pass-filter correction is assumed to be 25% of the correction factor, to account for the uncertainty of the time constant and deviations from the assumed first order LPF. The uncertainty of the calibration-based linearity correction takes into account the linearity error of the calibration reference (the cold plate temperature T_{cldPlt}) and the random noise during calibration.

4.2.4.2 Sorption equilibrium and enthalpy

The uncertainty of the equilibrium slopes is based on the uncertainty of the means of the measured values for each section (c.f. Section 4.2.2.2) and straight forward uncertainty propagation. In contrast to the above-mentioned mean values of the FR measurements, here, the limited number of samples is relevant. Thus, the standard uncertainty of the mean is taken into account as type A uncertainty for temperature and volume. For the extrapolated pressure, the uncertainty of the extrapolation is taken into account as based on the propagation of the measured value and slope uncertainties through Eq. (165). Uncertainties of slopes and values can be obtained from the linear regression in the respective sections (Chambers & Hastie, 1992). All other signals (temperature and

---

[10] For both, the simple linear model and the multivariate kriging model, the function `predic(…, se.fit = TRUE)$se.fit` returns estimates for the standard uncertainty of the model return values.

pressure where no correctable background signal was observed) are extrapolated with a constant value (zero slope) and, in order to take into account any uncorrected drift effects, the small slope measured is assumed to be the standard uncertainty of this zero slope.

The uncertainty of the adsorbent dry mass is assumed to be 5%, if not otherwise stated.

4.3 Differential Scanning Calorimetry

Table 7: Conditions for DSC-based specific heat capacity measurements

Quantity		Range
Loading	X	0.05, 0.2 and 0.35 $\mathrm{kg/kg_s}$
Effective loading	X_{eff}	0.04, 0.15 and 0.26 $\mathrm{kg/kg_{cmp}}$
Temperature	T	30, 50, 70 and 90 °C
Principle	-	Temperature steps

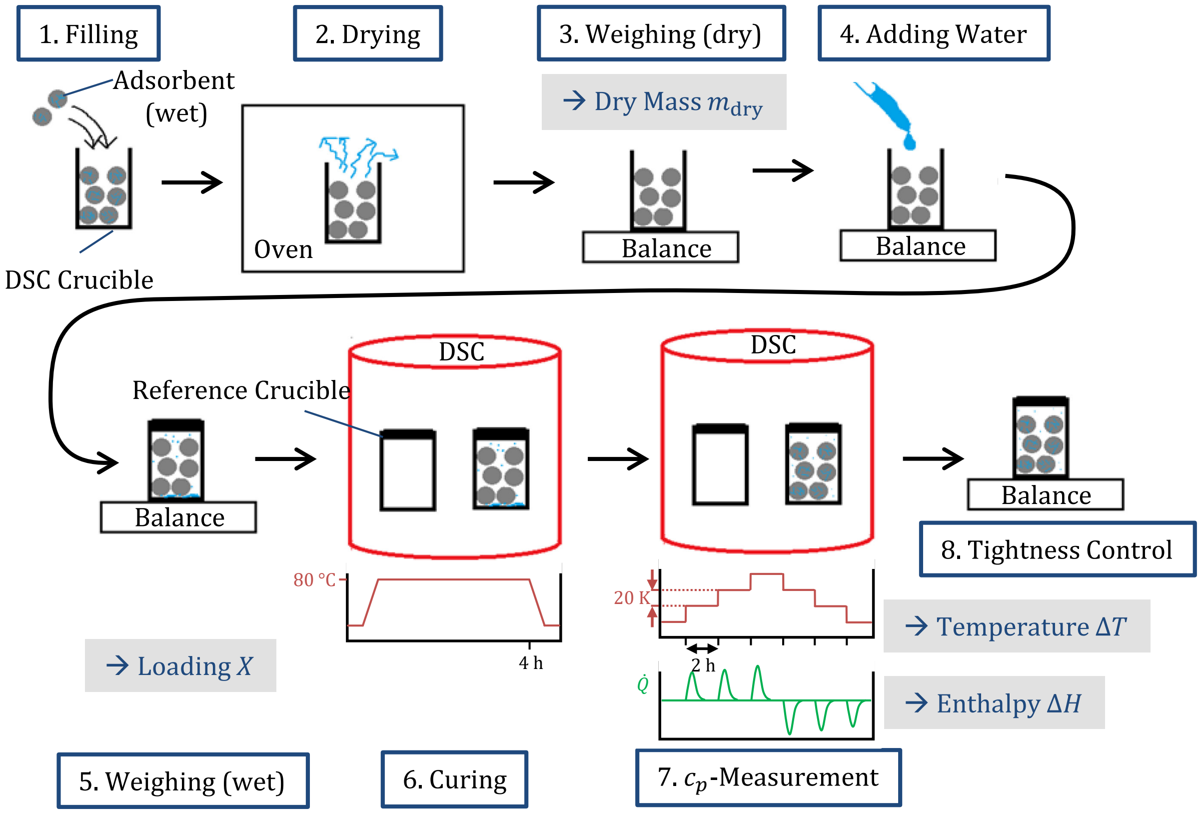

Figure 26: Procedure for loading dependent c_p measurement by DSC, principal measurement quantities obtained are highlighted in grey, calibration measurements with empty crucible and sapphire reference are not shown for clarity

The specific heat capacity (c.f. Section 2.1.3) of the adsorbent coating is measured by DSC for different temperatures and loadings given in Table 7. Samples are taken from the same well mixed dispersion used for coatings (c.f. Section 4.1) to ensure equal composition. Measurements were performed using two commercial devices: “micro DSC III” (Setaram) and “µSC” (Setaram).

A specially adapted procedure is used for sample preparation and measurement, in order to realise measurements at different loadings. The approach, based on tightly sealed crucibles, is comparable to those reported in literature (Aristov *et al.*, 1997; Cacciola *et al.*, 1998; Aristov, 2012), but with a step-wise temperature profile, to rule out temperature lag (c.f. Section 2.1.4).

The procedure (c.f. Figure 26), which is performed for each loading point, consists of several preparatory steps, in order to set, measure, and control the loading set point. The sample in unknown state is filled (1) into the crucible of known mass, minimising the void volume. After drying overnight in a vacuum oven (2), the hot sample is quickly weighted (3) to determine the sample dry mass m_{dry}. Subsequently, deionised water is dosed in with a micropipette (4) until the target mass is reached, which is calculated from the dry mass and the loading set point. Then, the crucible is quickly and thoroughly sealed with a lid of know mass and weighted again (5). The mass of the sealed crucible is used to calculate the actual loading X, which might differ slightly due to water evaporating during the sealing procedure. In order to ensure an even adsorbate distribution, a curing step at 80 °C for 4 h (6) is set before the actual DSC measurement (7). The latter is performed with a sequence of increasing and decreasing temperature steps, which is repeated twice to check for settling effects. The reported temperature is the mean temperature per step, e.g., 30 °C for the step of 20→40 °C. Increasing and decreasing temperatures are an additional check for the effect of bias from ad- and desorption (c.f. Section 2.1.4): Desorption into the air filled void volume (with increasing temperature) should occur faster than adsorption (with decreasing temperature), as in the latter case a dry air film is built up on the adsorbent surface creating an additional diffusion barrier. This should manifest as a difference between results from increasing and decreasing temperatures under otherwise same conditions. Finally, the crucible is weighted a last time after dismounting (8) to exclude leakage of water during the measurement. Standard calibration routines are observed, including measurements with empty crucibles and with a sapphire reference. For dry measurements steps 4 and 5 were omitted.

4.4 Large Temperature Jump

Large temperature jump experiments serve as a reference to validate the FR-based investigation of adsorption dynamics (c.f. Section 5.4.4) and for performance assessment under application conditions (c.f. Section 5.5.3). The measurements are carried out on the same sorption kinetic setup (c.f. Section 4.2.1). The procedure consists of initial desorption against the vacuum pump, and pre-conditioning to a desired starting temperature and pressure, where the latter is directly defined through the vapour generator. After closing the valve to the vapour generator and an additional equilibration time, the cold plate temperature is changed rapidly (~1 s) by switching between thermostat T1 and T2 (c.f. Figure 19). After this jump, the temporal evolution of the sample surface temperature and the pressure in the two connected chambers is measured until a new equilibrium is reached, in order to calculate the loading difference over time from the mass balance. This method was implemented on the setup and extensively documented before (Velte *et al.*, 2017; Velte, 2019).

5. Results and Discussion

The results are presented in three main parts: The chapter starts with the material properties of the coating, identified in-situ with the pre-procedure of the extended FRA (sorption equilibrium and enthalpy) and measured externally by DSC (specific heat capacity). Then, the actual FRA results are presented alongside with the identified heat and mass transfer (HMT) parameters. Finally, the concept of effective thermal resistances is applied to the obtained transport coefficients, which translates them into intuitive and application-relevant quantities that allow a simplified performance estimation of exemplary Ad-HX designs.

LTJ measurements under application-like temperature conditions are used as a validation reference for both, the material properties and HMT parameters identified by the extended FRA, and for the simplified performance estimation based on effective thermal resistances. For the validation of the model obtained by the extended FRA, all identification results are fed into a transient non-linear adsorption dynamic model that is used to predict the temporal evolution of the LTJ, which is then compared to the actual experimental observation. The simplified performance estimation, on the other hand, is compared to the conventional performance estimation based on the characteristic times and uptakes obtained from the LTJ results.

Results of the extended FRA, the sorption equilibrium and enthalpy (Laurenz *et al.*, 2020) as well as the FRA itself (Laurenz *et al.*, 2021), have partly been published in journal papers before.

5.1 Adsorption Equilibrium

🅭 by Laurenz *et al.*, 2020 / CC BY 4.0

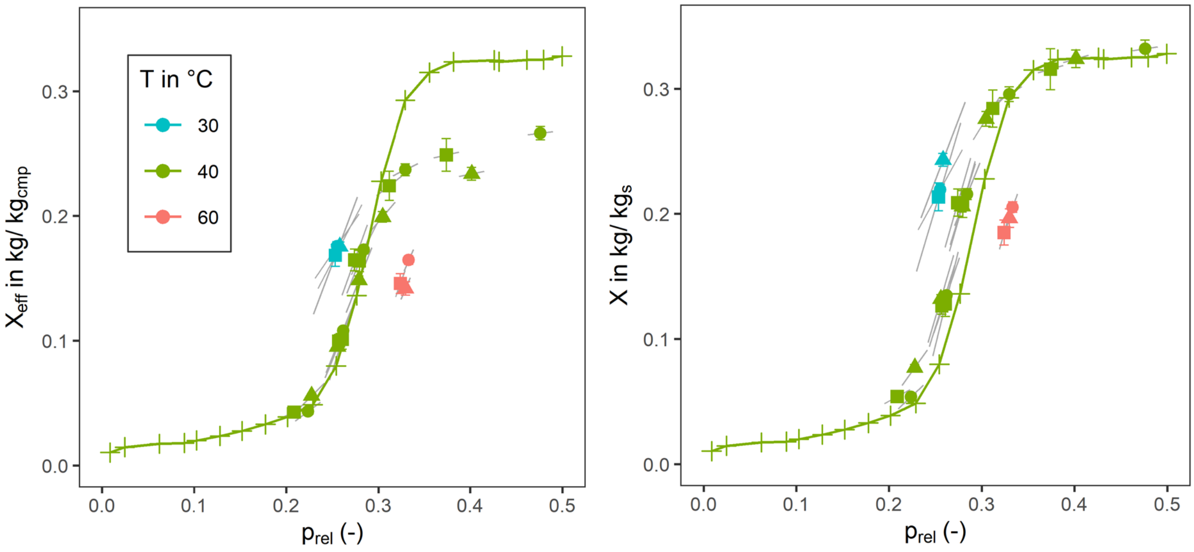

Figure 27: Sorption equilibrium points from FR measurements for Ct_140 (▲), Ct_240 (■) and Ct_610 (●) at 30, 40 and 60 °C in comparison with the 40 °C isotherm of the pure adsorbent powder (+), as effective loading X_{eff}, i.e. related to the total sample dry mass, (left) and as loading X, i.e. related to the adsorbent mass only, (right); grey lines indicate the local equilibrium slope measured by small volume jumps

The water isotherm of the adsorbent powder at 40 °C (Figure 27, Table 12 in Appendix A.10) show the characteristic step-like uptake, at a relative pressure of about 0.25–0.3, to a plateau at 0.32 kg/kg and is in line with (Kummer *et al.*, 2017b) or slightly lower than (Jeremias *et al.*, 2014; Elsayed *et al.*, 2016) previous results. Measured local isotherm slopes are in agreement with the tangent for 40 °C. The position of the uptake step is reproducibly within the samples and shows a strong temperature dependency that persists when applying a Dubinin transformation (Dubinin & Astakhov, 1971). Hence, the assumption of a temperature invariant characteristic curve is a strong simplification for aluminium fumarate and should be applied with caution. The exact position of the uptake step is an important information for application as it determines the available driving forces and finally the resulting equipment power (Wittstadt *et al.*, 2017).

No significant hysteresis was observed, neither locally by the procedure explained before (Section 4.2.2.2) nor globally. For the latter, the vapour dosing procedure was modified starting with the saturated sample ($p_{\text{rel}} = 0.5$, $T = 40$ °C, $X_{\text{init}} = 0.33$ kg/kg$_\text{s}$) and desorbing into the dosing chamber. Probably, the hysteresis found in previous results is due to incomplete equilibrium and/or pore condensation occurring at $p_{\text{rel}} \gg 0.5$. This region of high relative pressures was disregarded here due its limited relevance for heat transformation applications.

The adsorbent content $w_{\text{s,dry}}$, which is calculated by comparing the uptake of the sample to that of the powder (Figure 27, right), fits on average the values calculated at sample preparation (Table 4) showing that the binder has no significant influence on adsorption equilibrium. The results show good agreement between the two thicker samples and a slight deviation of the thinnest sample Ct_140, which could be explained by a slightly lower adsorbent content of the coating. The difference to the uptake of the pure adsorbent can be explained by the inert binder, loss due to the coating process, differences in the production process and measurement uncertainty of the manometric adsorption measurement.

An evaluation in the form a characteristic curve in the Dubinin formalism (c.f. Section 2.1.1), which is presented in the Appendix A.8, shows clearly that the required temperature-invariance assumption may not be made for Alfum–water. While highly relevant, this deviation is small and barely visible if the data is presented with a large range of the adsorption potential on the x-axis as it is commonly encountered in literature (Ammann *et al.*, 2019).

5.2 Adsorption Enthalpy

The calculated differential enthalpy of adsorption is 2.90±0.05 MJ/kg (52.2±1.0 kJ/mol) on average (Figure 29). The calculation with Eq. (19) is based on either the local equilibrium slope or on a linear fit of the quasi isosteric points ($X_{\text{eff}} \approx 0.16$ g/g) measured at 30, 40 and 60 °C. The Clausius–Clapeyron plot (Figure 28) shows that local slopes coincidence well with the multi-temperature fit, and so do the calculated enthalpies. Temperature and loading dependencies are negligible in the parameter range evaluated (Figure 29). Calorimetric measurements of water on SAPO-34, which also exhibits a step-like isotherm but at a lower relative pressure, found a similar plateau in the loading dependency of the differential adsorption enthalpy at 63.0 ± 2.5 kJ/mol for the region of the uptake step (Jänchen *et al.*, 2005).

The adsorption enthalpy is about 10–15% higher than expected by a simple Dubinin approximation (c.f. Eq. (20), Section 2.1.2), which is in accordance to the observed temperature variance of the isotherm. Thus, the application of both concepts, that of a characteristic curve to describe the sorption equilibrium and that of the adsorption potential to describe the sorption enthalpy, result in a rather rough approximation for the case of aluminium fumarate. This is also in line with similar observations made for SAPO-34 (Jänchen *et al.*, 2005).

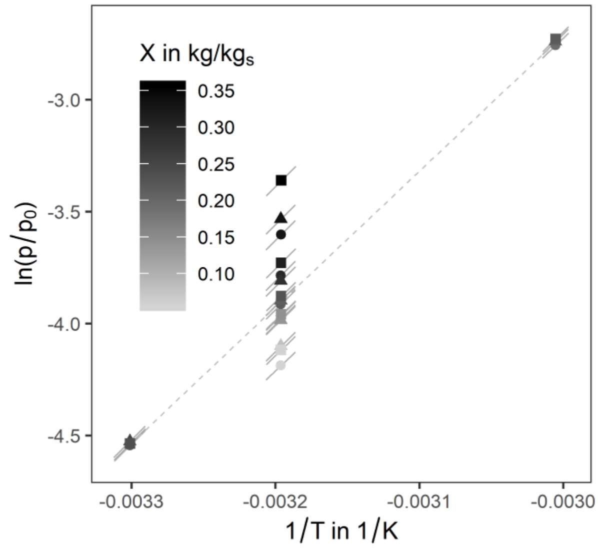

© by Laurenz *et al.*, 2020 / CC BY 4.0

Figure 28: Clausius–Clapeyron plot with measured equilibrium points ($p_0 = 1\,\mathrm{bar}$) for different samples (▲ Ct_140, ■ Ct_240, ● Ct_610) and isostere slope calculated from measured local deviations (short grey lines) and linear fit of points with $X_{\mathrm{eff}} \approx 0.16$ g/g (- - -), uncertainties of T and p are bellow point size; Right:

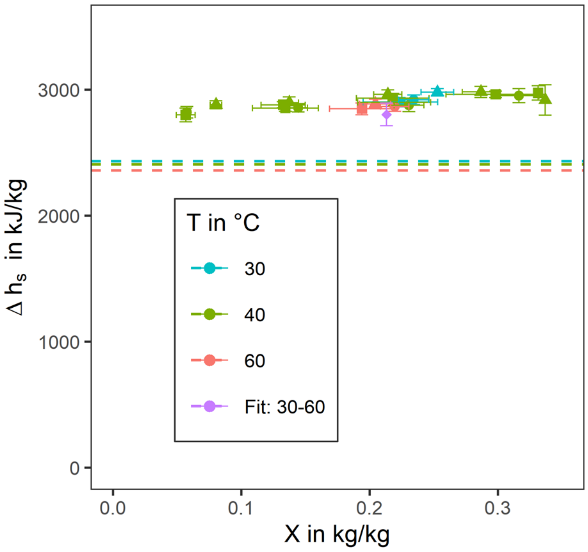

© by Laurenz *et al.*, 2020 / CC BY 4.0

Figure 29: Differential adsorption enthalpy calculated from isostere slopes of local equilibria and 0.16-g/g-fit over corrected loading with the evaporation enthalpy of water (- - -), symbols as in Figure 28

5.3 Specific Heat Capacity

The specific heat capacity of the adsorbent composite samples shows the expected pronounced loading dependency (Figure 30). Here, the heat capacity is reported as $c_{p,\mathrm{cmp+a}}$, i.e. specific to the total composite dry mass, as it is not possible to distinguish between the composite constituents, binder and adsorbent. While in the first measurement cycle a slight discrepancy between de- and adsorption direction (rising and falling temperature) is observed, this vanishes in the second cycle, which is therefore used for the evaluation shown here. Only for the highest loading and temperatures beyond 50 °C, a slight direction dependency persists and rises with temperature. Here, the pressures and thus the amount of adsorptive in the void volume is the highest, which is a plausible explanation for this observation. Overall, the results from all samples, including the repeated measurement of sample Ct_240, agree well.

The lines indicated in Figure 30 show the results of a non-linear fit to the ansatz

$$c_{p,\mathrm{cmp+a}} = \underbrace{k_0 + (T - 25\,^\circ\mathrm{C})k_T}_{c_{p,\mathrm{cmp,dry}}} + X_{\mathrm{eff}}\underbrace{\left(k_X + (T - 25\,^\circ\mathrm{C})k_{XT} + Xk_{X^2}\right)}_{"c_{p,\mathrm{a}}"}, \tag{106}$$

derived from a Taylor expansion around 25 °C, 0 kg/kg. While this fitting approach is equivalent to Eq. (29) with $b_2 = 0$ (Aristov, 2012), the formulation in analogy to Eq. (25) (c.f. p32) allows to directly derive the apparent specific heat capacity of the adsorbate

$c_{p,\mathrm{a}}$ through the specific heat capacity of the dry composite $c_{p,\mathrm{cmp,dry}}$. This heat capacity relies on the assumption of an inert adsorbent, which may not necessarily be physically true here. Thus, the fitting parameter k_{X^2} should be zero or at least insignificant. As both is not the case (c.f. Table 8), it can be deduced that this assumption may not be made for aluminium fumarate. This observation is in line with the measured adsorption equilibrium and enthalpy, which both does not follow the simple Dubinin approximation Eq. (23) (c.f. p31) that is also based on the assumption of an inert adsorbent.

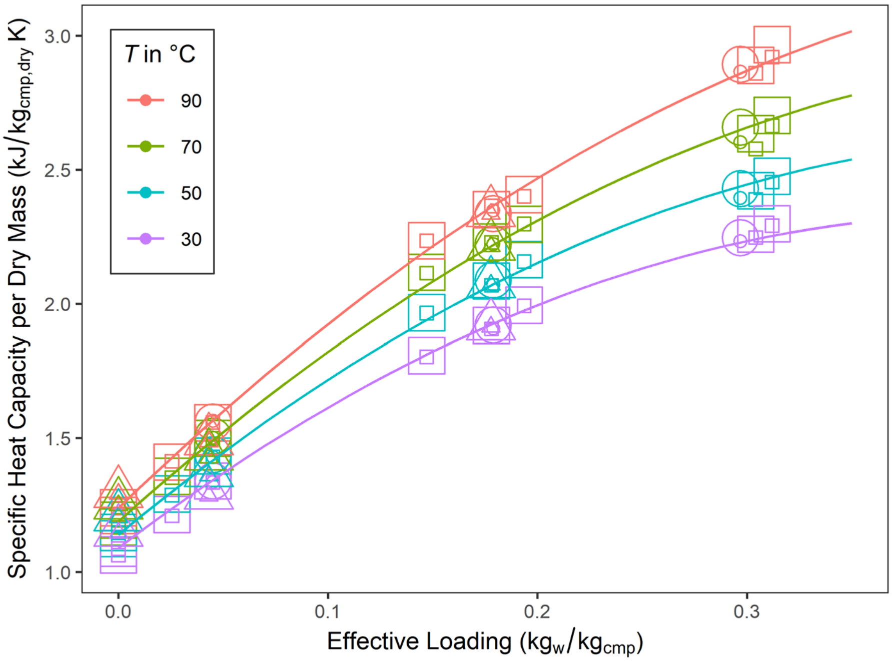

Figure 30: Specific heat capacity of the binder based aluminium fumarate coating $c_{p,\mathrm{cmp+a}}$ (related to the composite dry mass) for different coating batches (▲ Ct_140, ■ Ct_240, ● Ct_610), points: experimental results, lines: non-linear fit , small symbols: direction of decreasing temperature (adsorption), large symbols: increasing temperature (desorption), direction independence is given, if small and large symbols superimpose, error bars omitted for clarity

Table 8: Fitting parameter for Eq. (106), the loading and temperature dependent specific heat capacity of aluminium fumarate coating as used for adsorption dynamic models.

Fitting parameter	Estimate	Std. Error
k_0	1.077 kJ/(kg K)	0.008
k_T	0.00248 kJ/(kg K^2)	0.00018
k_X	5.81 kJ/(kg K)	0.10
k_{XT}	0.0271 kJ/(kg K^2)	0.0011
k_{X^2}	−7.11 kJ/(kg K)	0.28

The same conclusion can be made if the experimental results and the deduced non-linear fit are compared with the common inert-adsorbent-based approximation, which assume for the adsorbate either the specific heat capacity of ice or water at the respective temperature (Figure 31). Here, the approximation was made based on the temperature dependent c_p of the dry composite (Figure 32), i.e. the deviations are zero at dry conditions ($X_{\mathrm{eff}} = 0$). While for 30 °C the water-based approximation seems to fairly match the experimental data, for 90 °C the maximum deviation is in the order of −20%. The ice-based approximation is even worse with deviations for higher loadings of about −20% and −30% at 30 °C and 90 °C, respectively.

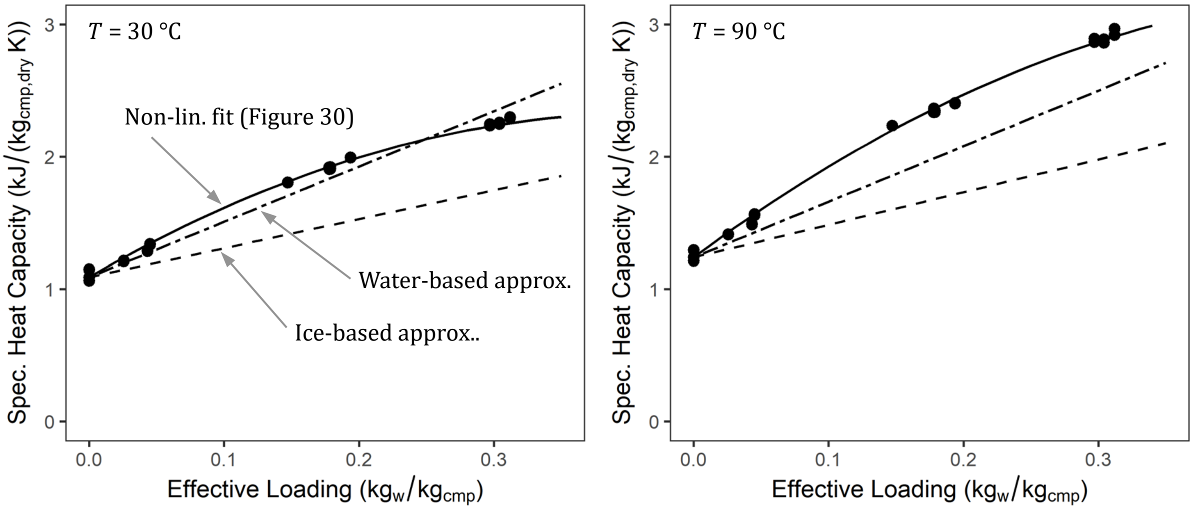

Figure 31: Comparison of the specific heat capacity of the adsorbent–adsorbate system as fitted based on measurement data (points, same data as Figure 30) with different common approximations based on inert adsorbent with a water- or ice-like adsorbate, the c_p of ice was linearly temperature-extrapolated

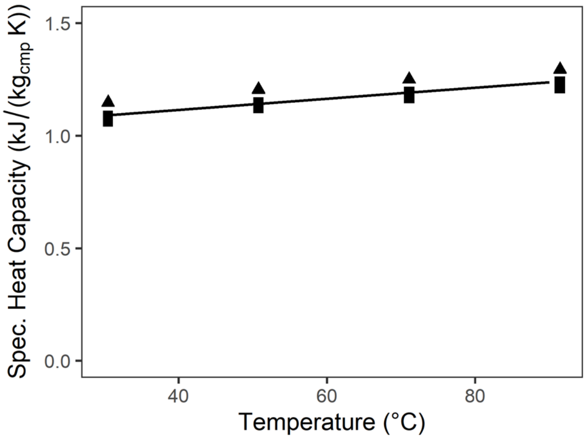

Figure 32: Heat capacity of the dry adsorbent coating $c_{p,\mathrm{cmp+a}}(X_{\mathrm{eff}} = 0)$ for different coating batches (▲ Ct_140, ■ Ct_240), points: measurement data, line: result from overall fit

In practice, the findings made here are relevant to the estimation of overall application efficiencies (c.f. p55) and for the estimation of heat transfer parameters, as adsorption dynamic experiments typically yield some kind of thermal time constants that must be split into a capacitive and a resistive part. The efficiency estimation is little sensitive to the specific heat capacity of the adsorbent, and so the deviations resulting from the water- or ice-based approximation, may be barely above the overall uncertainty. This applies at least to typical configurations with high loading spreads, where the amount of heat required for desorption is much greater than for the isosteric heat-up. However, for the identification of heat transfer parameters, the case is different, and the observed deviations from the simplified approximations must be taken into account. Otherwise, the deviations in c_p will directly propagate to the identified heat transfer parameters.

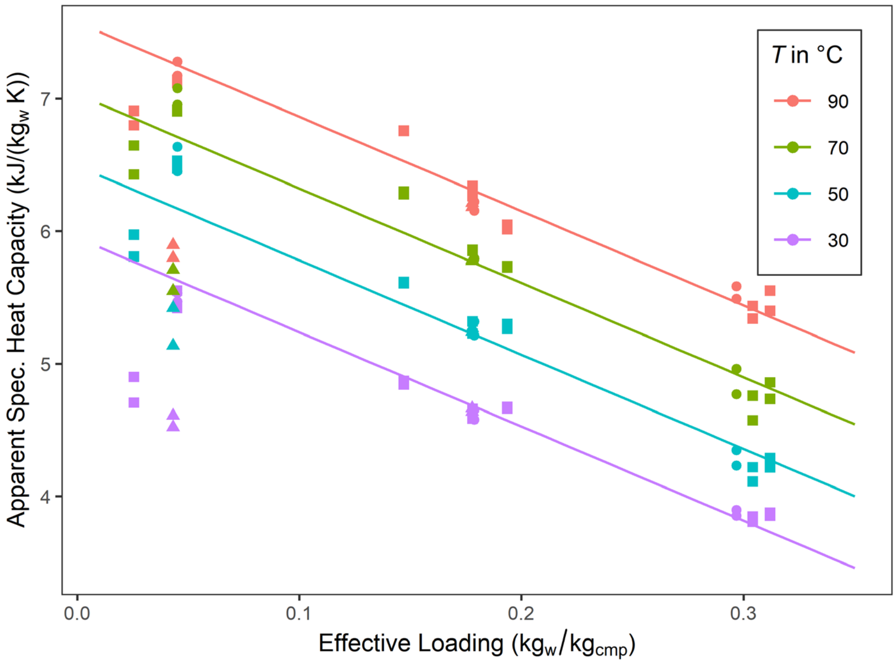

Figure 33: Apparent specific heat capacity of the adsorbate $c_{p,\mathrm{a}}$ as a function of loading and temperature: Lines are calculated with the overall fit, points are based on measurement data for different coating batches (▲ Ct_140, ■ Ct_240, ● Ct_610) and fitted heat capacity of the dry adsorbent coating

The apparent specific heat capacity of the adsorbate $c_{p,\mathrm{a}}$ can be analysed more in depth. In order to calculate $c_{p,\mathrm{a}}$ from Eq. (30), the specific heat capacity of the (assumingly) inert composite $c_{p,\mathrm{cmp}}$ is derived from the "dry" measurements (Figure 32). Although highly scattered for small loadings, the $c_{p,\mathrm{a}}$ points evaluated with Eq. (30) confirm the lines derived from the overall fit Eq. (106) as shown in Figure 33. Values for $c_{p,\mathrm{a}}$ are significantly higher than those for either pure water or ice, with a particularly pronounced loading dependency. The results confirm earlier results that also showed higher values for $c_{p,\mathrm{a}}$ than for pure water (c.f. Section 2.1.4, p36). This result is difficult to explain by an actual physical specific heat capacity of the adsorbed water. It seems more likely that the adsorption of water leads to a change of the specific enthalpy of the adsorbent, e.g., by slightly altering the crystalline structure, i.e. the adsorbent being not inert. Since an inert adsorbent was nevertheless assumed for the calculation of $c_{p,\mathrm{a}}$, this change in the adsorbent is attributed to the adsorbate. For a non-inert adsorbent, the actual specific heat capacity of the adsorbate may not be calculated without further knowledge about $\partial H_\mathrm{s}/\partial m_\mathrm{a}$, which is experimentally impossible up to now.

5.4 Adsorption Dynamics – Frequency Response Analysis

In this section, the measurement results will be first compared to different models in order to identify the relevant transport mechanisms. The best-fitting model will then be used to quantify the transport parameters, with a special attention on the interpretation of the mass transfer results. Finally, the loading and temperature dependent transport parameters are fed into a non-linear time domain model. This allows to simulate a large temperature jump (LTJ) under realistic application conditions and to validate the parametrised model by comparing the simulation to experimental results.

The measured FR (Figure 35) shows the typical bimodal shape observed before for non-isothermal adsorption systems (Sun & Bourdin, 1993; Bourdin *et al.*, 1996b). Note that here $\mathrm{Im}(\tilde{p})$ and $\mathrm{Im}(\tilde{T})$ are proportional to the negative "out-of-phase curves" due to different phase shift definition. The maximum temperature amplitude is in the order of several 100 mK, which is typical of adsorption with water measured in the apparatus presented here and allows for a good signal-to-noise ratio. It is about one order of magnitude higher than the values reported by Bourdin et al. (1996b), making it easier to reach similar data quality with the higher noise levels of the simpler temperature measurement used in this work.

The signal-to-noise ratio is sufficient, and for lower frequencies more than sufficient. This might allow further reduction of the measurement time, e.g., by replacing the single-frequency sinusoidal signal by a phase shifted multisine with a high signal power, i.e. a low crest factor (Bohn & Unbehauen, 2016).

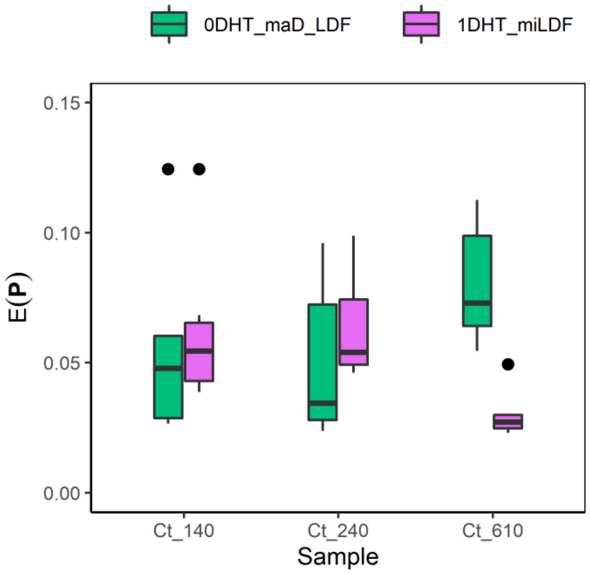

© by Laurenz *et al.*, 2021 / CC BY 4.0

Figure 34: Box plot of the residual error for the two best-fitting models over the coating thickness (horizontal line: median, box: lower/upper quartile, whisker: full extend, dots: outliers)

5.4.1 Model comparison

The different models shown in Figure 11 are compared following two criteria: Their ability to reproduce the data, i.e. the residual error of the best estimate, and the plausibility of the identified transport parameters, especially when looking at the dependency on the coating thickness.

For the example shown in Figure 35, the simple macro- and micropore diffusion models 0DHT_maD and 0DHT_miD fail to represent the experimental data (weighted residual error $E(\widehat{\boldsymbol{P}}) = 0.20$). Due to the mathematically similar structure, both models yield the same best-fit shape for all measurements. As the mismatch is observed throughout all experiments, both models will be disregarded in the following. A better fit $(E(\widehat{\boldsymbol{P}}) = 0.08)$ is achieved with the macropore diffusion + micro-LDF model (0DHT_maD_1D_LDF). However, the best fit $(E(\widehat{\boldsymbol{P}}) = 0.04)$ is obtained when discretising the heat transfer with the 1DHT_miLDF model. The simple 0DHT_LDF model returns the same fit result as 0DHT_maD_LDF, indicating that the macropore diffusion is not relevant to the example shown. For a similar reason the 0DHT_LDF model converges toward the results from the 1DHT_miLDF model when fitting other experiments: For large values of λ (small Biot numbers), the solution of the 1DHT_miLDF model simplifies to that of the 0DHT_LDF model, as the temperature distribution becomes homogeneous. Therefore, and for its limited information content, the 0DHT_LDF is disregarded in the following.

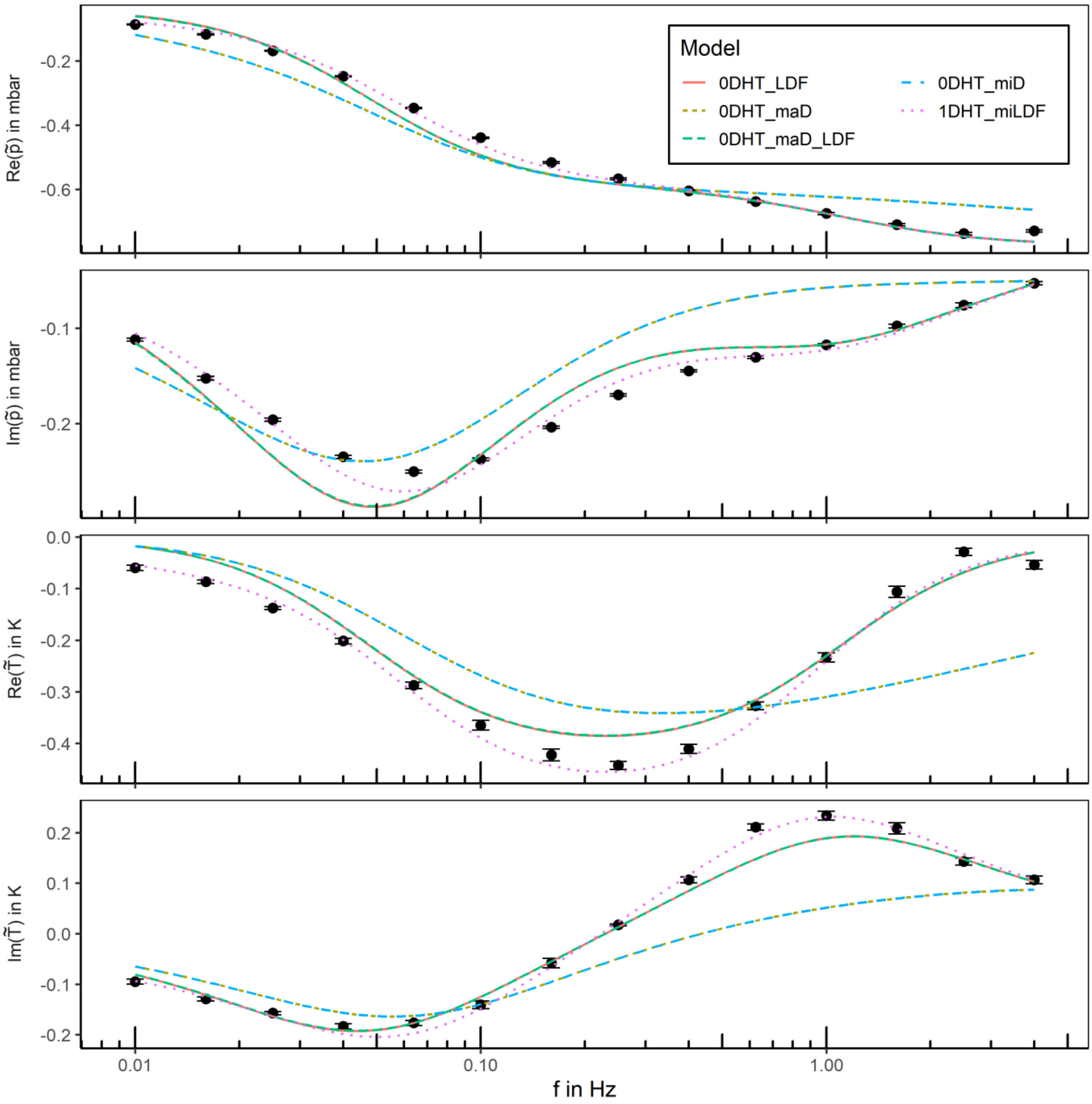

Figure 35: Example for measured frequency response of water on the Alfum-coated sample Ct_610 at $p = 18.5$ mbar, $T = 40$ °C and $X_{\mathrm{eff}} = 0.09$ g/g in comparison to best-fit results of different models for a geometric sequence of 14 frequencies between 0.01 and 4 Hz, shown as non-normalized real and imaginary part of the complex deviation variables of the chamber pressure $\tilde{p}$ and surface temperature $\tilde{T}$

Further assessment shows that the model 1DHT_miLDF is more appropriate than the model 0DHT_maD_LDF to plausibly represent the observed behaviour of all measurements. To this end, both models are further analysed looking at two aspects: the relative residual error $E(\widehat{\boldsymbol{P}})$ (Figure 34, Figure 52 in Appendix A.9) and the identified parameters $\widehat{\boldsymbol{P}}$ (Figure 36). Starting with $E(\widehat{\boldsymbol{P}})$, the overall best-fitting model is 1DHT_miLDF (Figure 52). Furthermore, with the sample layer thickness, the residual error $E(\widehat{\boldsymbol{P}})$ rises for 0DHT_maD_LDF and drops for 1DHT_miLDF (Figure 34). The difference between the two models lies in whether the heat conduction or the macropore diffusion is the dominant transport mechanism perpendicular to the coating layer. This becomes more relevant in the case of thicker coatings, indicating that the heat transport discretisation (1DHT_miLDF) is more relevant to catch the overall behaviour.

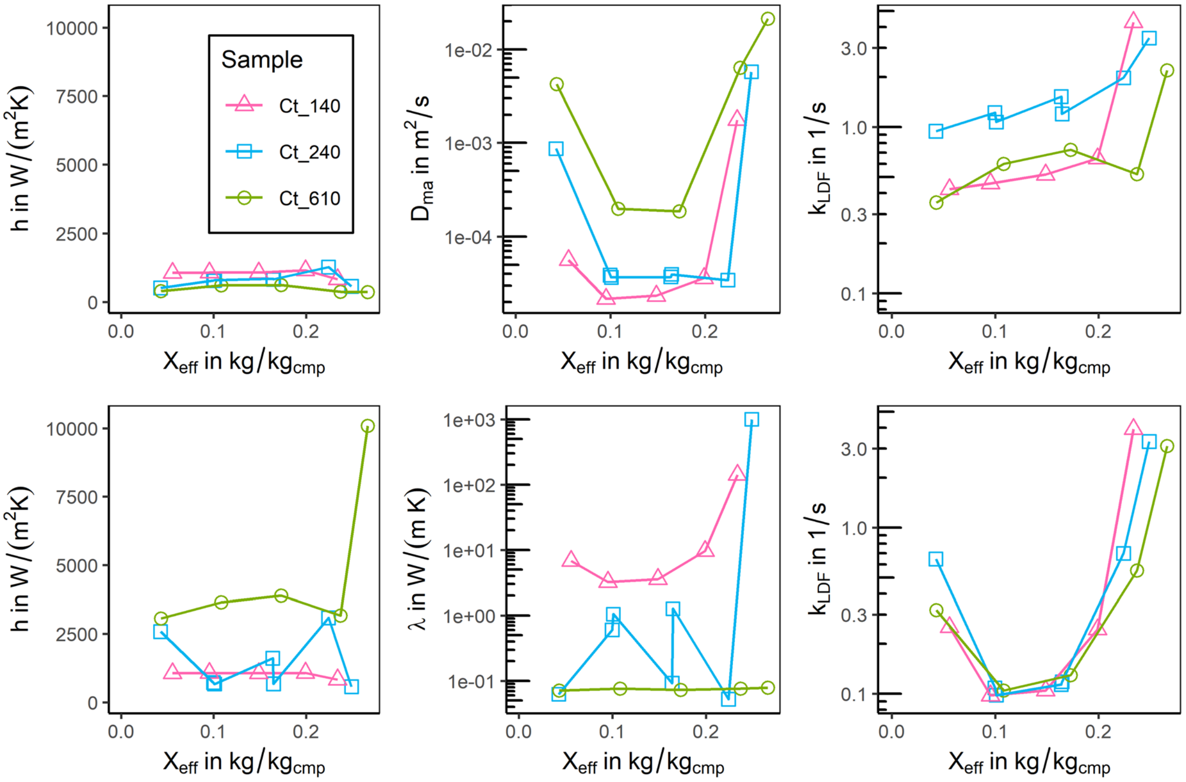

© by Laurenz *et al.*, 2021 / CC BY 4.0

Figure 36: Identified parameters using different models (first row: 0DHT_maD_LDF; second row: 1DHT_LDF) over the effective loading for $T = 40\,°\mathrm{C}$ and different coating thicknesses (colours and symbols); Lines are only meant as guides to the eye.

The second aspect, the identified transport parameters (Figure 36), supports this hypothesis by showing plausible results only for 1DHT_miLDF. Distributed transport parameters, like diffusivities, micro-level LDF-coefficients and thermal conductivities, should not depend on the coating thickness. However, for the 0DHT_maD_LDF model, a coating-thickness dependency is found for all parameters, whereas it is only plausible for the overall heat transfer coefficient h to drop with rising coating thickness; k_{LDF} and D_{ma} should be independent of the thickness, as all samples have the same composition. D_{ma} is expected to rise with the pressure, but it shows an implausible U-shaped loading dependency. The heat transfer coefficient is expected to depend on the pressure and the grain–grain contact properties, but it also shows a slightly chaotic U-shape-like loading dependency, which also is not plausible. For the 1DHT_LDF model, a coating-thickness-independent U-shaped loading dependency is found for the LDF-coefficient k_{LDF}. Assuming that the underlying mass transfer process is related to the micropore transport diffusivity, this can plausibly be explained by the strong change of the thermodynamic factor, as will be discussed later. Yet, the two heat transfer-related parameters, λ and h, are fluctuating arbitrarily by orders of magnitude for the thinner samples. Only fits to measurements of the thickest sample yield a plausible thermal conductivity in the order of 0.1 W/(m K), independent of the loading.

In the following, the evaluation will thus focus on the 1HT_miLDF model.

5.4.2 Identified transport parameters

Based on the model with discretised heat transfer and LDF-simplified micro-scale mass transfer (1DHT_miLDF), the thermal conductivity λ of the samples was identified as about 0.07 W/(m K). Values for k_{LDF} are between 0.1 and 3 s^{-1} at 40 °C with a characteristically U-shaped loading dependency (Figure 39). The heat transfer coefficient h for the contact between coating and support was identified as $\geq 4 \times 10^3$ W/(m^{2}K). An upper boundary for h cannot be given, as it proved to be irrelevant to the overall transport process (non-identifiable). Details will be discussed in the following.

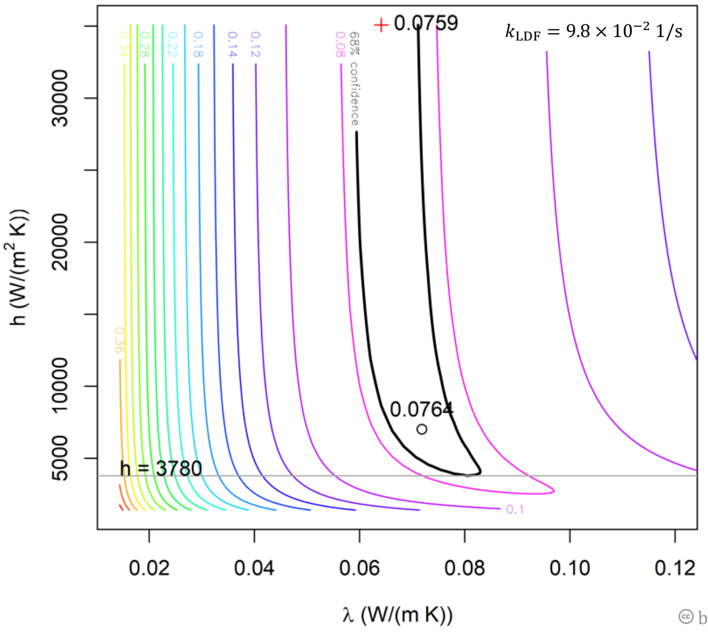

🅭 by Laurenz *et al.*, 2021 / CC BY 4.0

Figure 37: Contour plot of $E(\boldsymbol{P})$ over λ and h for the simultaneous fit of measurement results of the three samples (Ct140, Ct240, Ct610) under similar conditions ($X_{0,\mathrm{eff}} \approx 0.16$ g/g, T_0 = 40 °C, $p_0 \approx 20.7$ mbar) to the model 1DHT_miLDF with k_{LDF} fixed at the best estimate (9.8×10^{-2} 1/s), open circle: minimum found by the fitting algorithm, red cross: minimum found by parameter variation for creating this plot, bold line: standard confidence limit (c.f. Eq (75), p68)

The sensitivity of the individual fit results to h is extremely low (Figure 53 in Appendix A.9). For the thinner samples, any combination of λ and h, resulting in the same total heat transfer resistance, yields similar values of the error functional, whereas for the thicker sample, only high enough values of h yield good fits. This explains the arbitrary oscillation of λ and h for Ct_240 in Figure 36: The fitting algorithm will arbitrarily return any value from the long stretched minimum "valley" of $E(\boldsymbol{P})$. As λ, h and k_{LDF} should be equal for all samples and to increase the power of the parameter identification procedure, the fit procedure was applied to find a single set of parameters fitting well to multiple samples ("multi-fit"). For this, experimental results from all three samples were pooled for similar X, T-states and fitted to a single $\boldsymbol{P}$ while all other specific model parameters were kept at the precise state of each individual measurement and sample. The contour plot of $E(\boldsymbol{P})$ in the $\hat{k}_{\mathrm{LDF}}$-plane (Figure 37) reveals that values below 4×10^3 W/(m²K) are unlikely for h, but no upper boundary can be given.

In the following, the model results will therefore be presented based on an ideal (i.e. non-limiting) thermal contact (i.e. $h \to \infty$). As the values obtained for λ rise with decreasing h, this approach yields conservative estimates for λ. In the case analysed in Figure 37, this leads to a maximum underestimation of less than 0.02 W/(m K) which is within the standard confidence level.

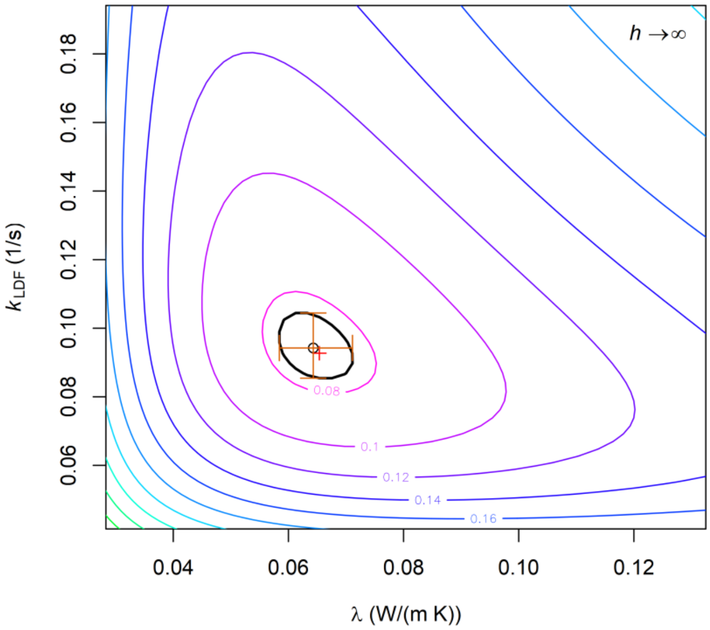

Figure 38: Contour plot of $E(\boldsymbol{P})$ over k_{LDF} and λ for the same fit as in Figure 37 for model 1DHT_miLDF with ideal thermal contact ($h \to \infty$), bold line: standard (68%) confidence limit, error bars depict the definition confidence limits used in the other plots, open circle: minimum found by the fitting algorithm, red cross: minimum found by parameter variation for creating this plot

For the ideal-contact model, the form of the confidence region of k_{LDF} and λ shows that the two variables can be distinguished clearly (Figure 38). The maximal extent of the standard confidence region as depicted will be used as a definition for error bars in the following plots. A three-dimensional evaluation of the standard confidence region is possible in principle, but omitted here for computational constraints and limited insight gain.

The parameter values identified with the ideal-contact model do not show any significant dependency on the coating thickness (Figure 39). The thermal conductivity of the coating is found to be constant throughout all measurement points, with values around 0.07 W/(m K), which seems plausible if compared to, e.g., the true thermal conductivity of 0.14–0.2 W/(m K) reported for silica gels (Kast, 1988; Bathen & Breitbach, 2001). It can be expected that the thermal conductivity is lower for the porous coating than for the pure solid adsorbent, due to contact resistances and increased path lengths. The missing loading and pressure dependency that one might expect, and which was reported before for, e.g., granular beds of silica gel–water (Gurgel *et al.*, 2001), could be explained by a heat transfer, which is limited by binder–adsorbent contact resistances and conduction in the binder and/or the gas phase. The – possibly loading dependent – thermal conductivity of the adsorbent crystal would just add a low, thus invisible at macro scale, conductive resistance in series. Assuming macropores in the order of the adsorbent particles (d = 18 µm), the inverse Knudsen number under experimental conditions is in the order of 5–25, which leads to only minor deviations from the (pressure-independent) gas phase thermal conductivity (Kaganer, 1969). Given that the macropore diffusion is not limiting the overall dynamics, the thermal conductivity might be worth addressing by, e.g., densifying the coating. The results for micro-scale mass transfer hardly differ from the non-idealised model (Figure 36).

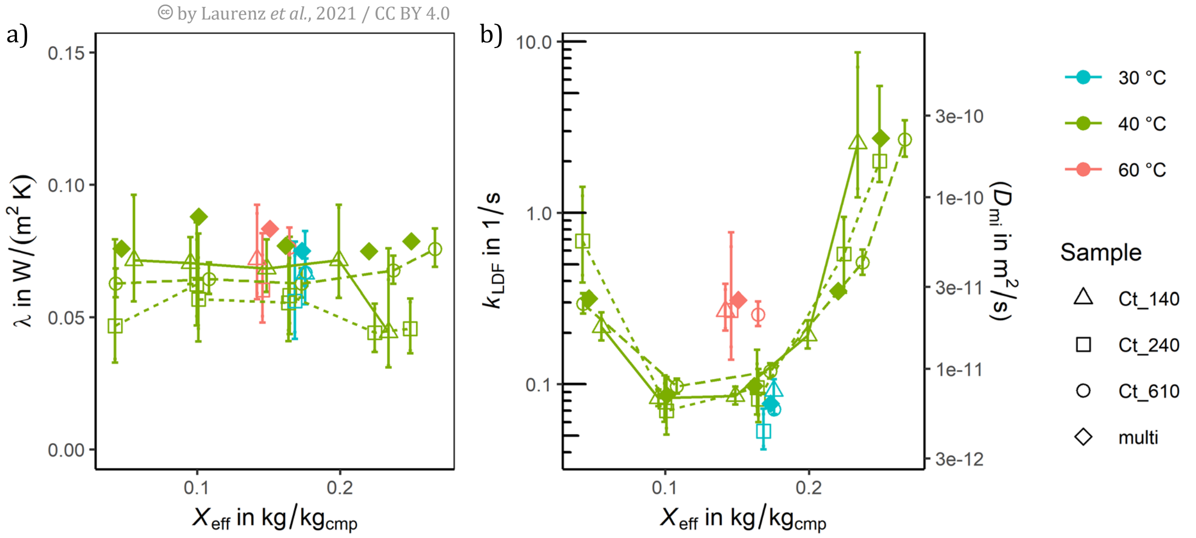

© by Laurenz *et al.*, 2021 / CC BY 4.0

Figure 39: Estimated parameters from the model 1DHT_LDF with ideal thermal contact between support and coating for different coating thicknesses over the effective loading, "multi" (filled symbols) indicates results from simultaneous fit of all samples for similar X, T conditions with non-ideal thermal contact. D_{mi} tentatively calculated form k_{LDF}, see Section 5.4.3 for details. Lines are only meant as guides to the eye.

5.4.3 Interpretation of micro-scale mass transfer

Even though the mass transfer at micro level can be successfully described with an LDF-approach, this does not determine its physical nature. In a first hypothesis, it could be adsorbate diffusion, which, in the model, is approximated by the LDF-approach.

In this case, the micropore transport diffusivity D_{mi} (secondary y-axis of Figure 39b) could be calculated from k_{LDF} according to Eq. (49) with the mean particle radius as the diffusion length (9 µm, c.f. Appendix A.5, Figure 48), and a curvature factor $\sigma = 1$, accounting for the 1D channel structure of Alfum. Further, the adsorbate diffusivity D_{ad}, i.e. the self-diffusivity, could be calculated through the Darken factor $\Gamma = \mathrm{d}\ln p / \mathrm{d}\ln X$ with Eq. (45). Interestingly, this correction compensates for most of the loading dependency observed for k_{LDF}, with values for D_{ad} of about 1×10^{-11} m²/s at 40 °C (Figure 40).

This supposed adsorbate diffusivity may be compared to literature data for the same material. PFG-NMR measurements (c.f. Section 2.2.3.3) of water in saturated Alfum at 25 °C yielded self-diffusivities of $D_{\parallel} = (6.0 \pm 0.4) \times 10^{-10}$ m²/s and $D_{\perp} = (5.0 \pm 0.4) \times 10^{-12}$ m²/s for the diffusion in the direction of the 1D channels and perpendicular to them (Splith *et al.*, 2018), while the overall diffusion is dominated by $D_{\parallel}$. In Figure 40, the estimate of D_{ad}, which is thought equivalent to $D_{\parallel}$, directly depends on the assumptions of the validity of the LDF approximation and the diffusion path length. However, a wrong diffusion path length is not able to explain the discrepancy of about two orders of magnitude between D_{ad}, shown in Figure 40, and the PFG-NMR-based $D_{\parallel}$: The diffusion path length would need to be in the order of 100 µm instead of 9 µm, which is impossible, given the results of the particle size measurements (c.f. Appendix A.5).

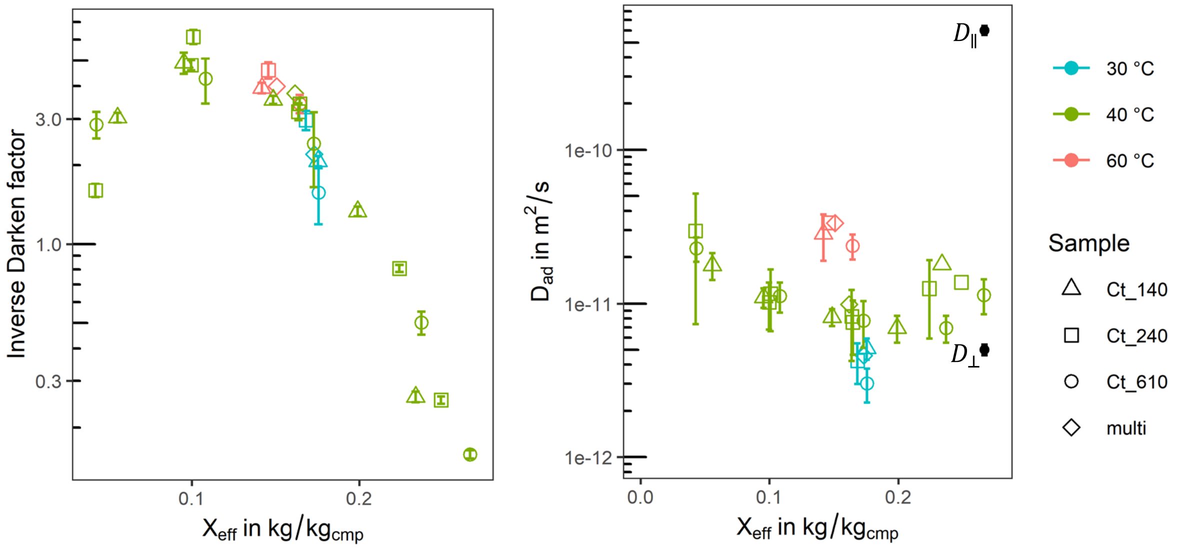

© by Laurenz *et al.*, 2021 / CC BY 4.0

Figure 40: Inverse Darken factor calculated from Figure 27 and adsorbate diffusivity tentatively calculated from identified micro transport diffusivity (Figure 39). $D_{\parallel}$ and $D_{\perp}$ are values reported by Splith *et al.* (2018) for the diffusion in the 1D channels and perpendicular to them

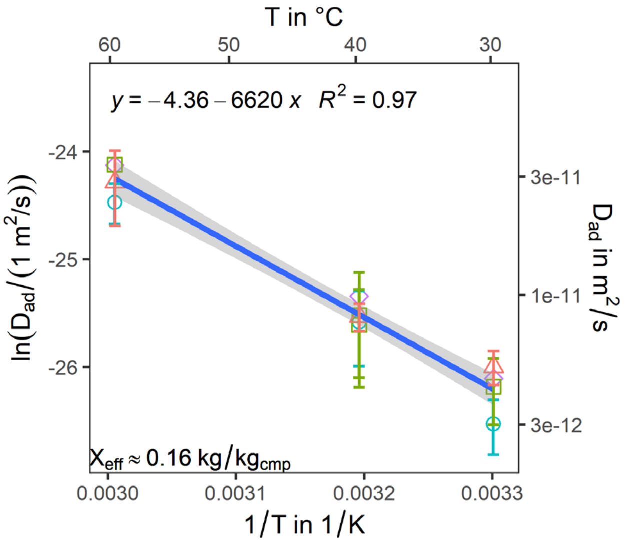

© by Laurenz *et al.*, 2021 / CC BY 4.0

Figure 41: Arrhenius plot of the adsorbate (self) diffusion of water in aluminium fumarate with linear fit and standard error (blue line, grey area) for points with similar loading ($X_{\mathrm{eff}} = 0.16 \pm 0.02$ kg/kg$_{\mathrm{cmp}}$) of all three coating thicknesses evaluated, the fit refers to the bottom and left axes

It seems more likely that deriving a micropore diffusion coefficient from the LDF approximation is misleading here, especially as the derivation of Eq. (49), the relation between LDF and diffusion, is based on the assumption of homogeneous uptake distribution ($\dot{X}(x) = \text{const.}$). This assumption becomes weak in FR experiments for frequencies above the diffusion time constant, when the deeper layers are no longer reached by the fluctuation at the surface.

Irrespective of the physical interpretation, the data allows an Arrhenius-plot of points with similar loading $X_{\mathrm{eff}} \approx 0.16$ g/g and different temperatures (Figure 41). It shows the linear form of the inverse temperature dependency, expected according to Eq. (47), with an activation energy E_{a} of 55.0 ± 3.1 kJ/mol. As the Darken factor is barely temperature dependent, this evaluation also describes the temperature dependency of k_{LDF}. The supposed activation energy is higher than, e.g., the 28–36 kJ/mol found for water in Chabazite B, Gmelinite and Heulandite (Barrer & Fender, 1961), or the 2–12 kJ/mol measured by PFG-NMR for water in MIL-100(Al) (Splith *et al.*, 2017).

While the LDF model reproduces the experimental FR results particularly well, k_{LDF} might have a different physical meaning. In any case, this unknown mass transfer barrier exhibits some kind of Darken-like loading, and an Arrhenius-like temperature dependency. However, this open question to be further investigated, does not affect the quality of the description of the macroscopic processes, as shown in the next section.

5.4.4 Validation with LTJ results

The identified transport and thermodynamic parameters were used for a non-linear simulation of an LTJ response, using an existing implementation of the 1DHT_miLDF model (Figure 11f) in the time domain (Velte *et al.*, 2017). The results are compared to LTJ results on the same samples, which have been published elsewhere before (Laurenz *et al.*, 2019). The simulation is based on a loading- and temperature-dependent LDF coefficient, constant thermal conductivity, constant adsorption enthalpy and the fitted adsorption equilibrium; all as identified above. Details of the parametrization are given in Appendix A.10. The simulation is solely based on parameters identified by FRA, without any fitting in the time domain.

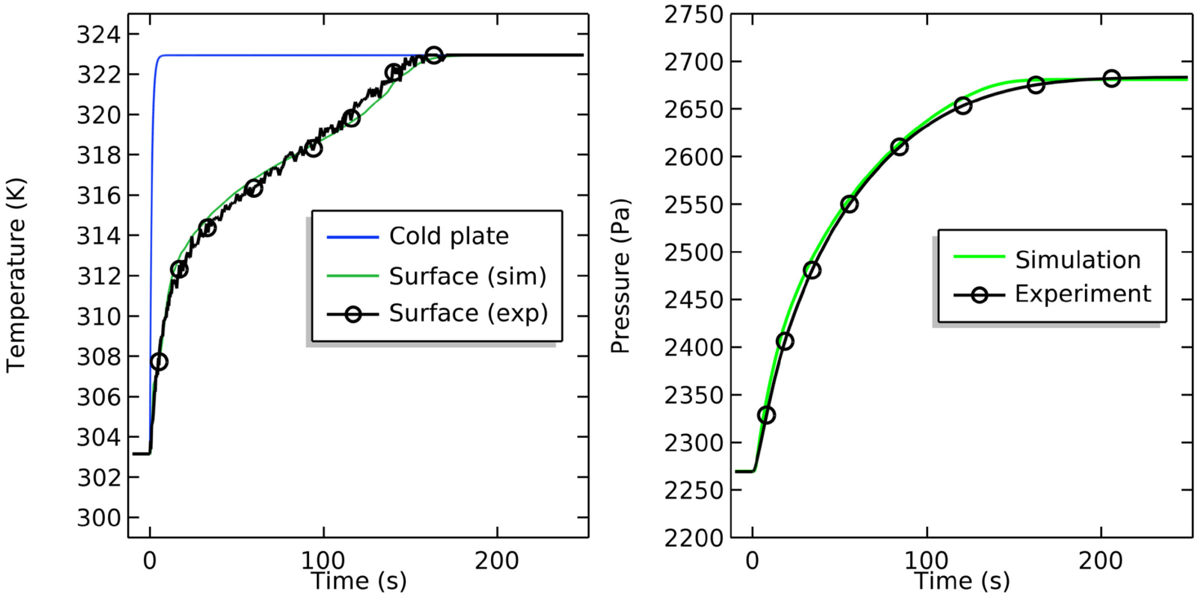

© by Laurenz *et al.*, 2021 / CC BY 4.0

Figure 42: Response of surface temperature (left) and chamber pressure (right) on a large jump of the cold plate temperature (desorption) measured for sample Ct_610 and simulated with the T, X-dependent transport and equilibrium parameters identified in this work

The results show very good agreement (Figure 42), validating the aforementioned procedures and identification results. The deviation between measurement and simulation show an improvement compared to previous works where similar transport models were fitted directly in the time domain (Frazzica *et al.*, 2014; Velte *et al.*, 2017). One might suggest that the deviations observed before were rather due to the incompletely mapped state dependency of the transfer coefficients and not due to the general model simplification like the reduction of particle size and layer thickness distributions to single values.

5.5 Expected Ad-HX Performance

In this section, the identified transport parameters, presented in the last section, are put in perspective to an actual application. On the basis of the concept of effective thermal resistances developed in this work (Section 3.2), the overall relevance shall be measured on a coarse and accessible level. After calculating the effective thermal resistances, they are combined with the characteristic temperature difference, obtained from the measured adsorption equilibrium, to estimate the expected performance (c.f. Section 3.2.4). Finally, the results will be compared to the performance deduced from LTJ measurements under application conditions.

5.5.1 Effective thermal resistances

The relevant effective thermal resistances are the heat transfer resistance R_{HT} and the mass transfer resistance R_{MT}, calculated from the obtained thermal conductivity and the LDF coefficient, respectively, with the relations derived before (Table 2). Both are expressed according to Eq. (80) with respect to heat exchanger area and with respect to the mass of adsorbent composite. These two perspectives are related to component volume and heat exchanger costs, and to adsorbent composite costs, respectively.

The results in Figure 43 show that the total effective thermal resistance is strongly dependent on the layer thickness, but also on the thermodynamic state: For the thinnest coating Ct_140 the resistance is more than halved between 30 and 60 °C. For this sample also a pronounced loading dependency is observed with the resistance strongly decreasing with loading. Moreover, the dominating resistance depends on layer thickness and temperature: At 40 °C the thinnest sample Ct_140 is dominated by mass transfer, the thicker sample Ct_610 is completely governed by heat transfer, and the intermediate sample Ct_240 is roughly equilibrated. The layer thickness dependency is straight forward for the conductive heat transfer resistance. For the mass transfer resistance this effect is due to the mass-per-area ratio: In order to provide the same adsorption power per area, the same vapour flow has to penetrate into less adsorbent particles. This results in a higher molar flux on microscopic level, which can only be realised with larger driving forces. The mass transfer resistance drops with rising temperature and loading, whereas the heat transfer resistance barely changes with both, temperature and loading. The trends in terms of layer thickness, temperature and loading (i.e. pressure) have been also observed for binder based SAPO-34 coatings (Ammann *et al.*, 2019). However, the results show that the loading dependency may be neglected in a first approximation, especially for the thicker cases, where the heat transfer resistance dominates. In this case, constant resistances may be used for a given operational point, where temperature does not change much throughout a half-cycle. Though, different effective resistances for ad- and desorption may be advisable to reflect the temperature dependency.

The total area related effective thermal resistance is in the order of 1–4 (m^2 K)/kW. This result is comparable to the reported values of 1.5–3.5 (m^2 K)/kW for binder based SAPO-34 coatings of 60–460 µm (Ammann *et al.*, 2019), slightly higher than the 0.4–1.8 (m^2 K)/kW for sintered aluminium fibres coated by partial support transformation (Velte, 2019), and significantly lower than the 10–20 (m^2 K)/kW for different layers of silica grains (Ammann *et al.*, 2018).

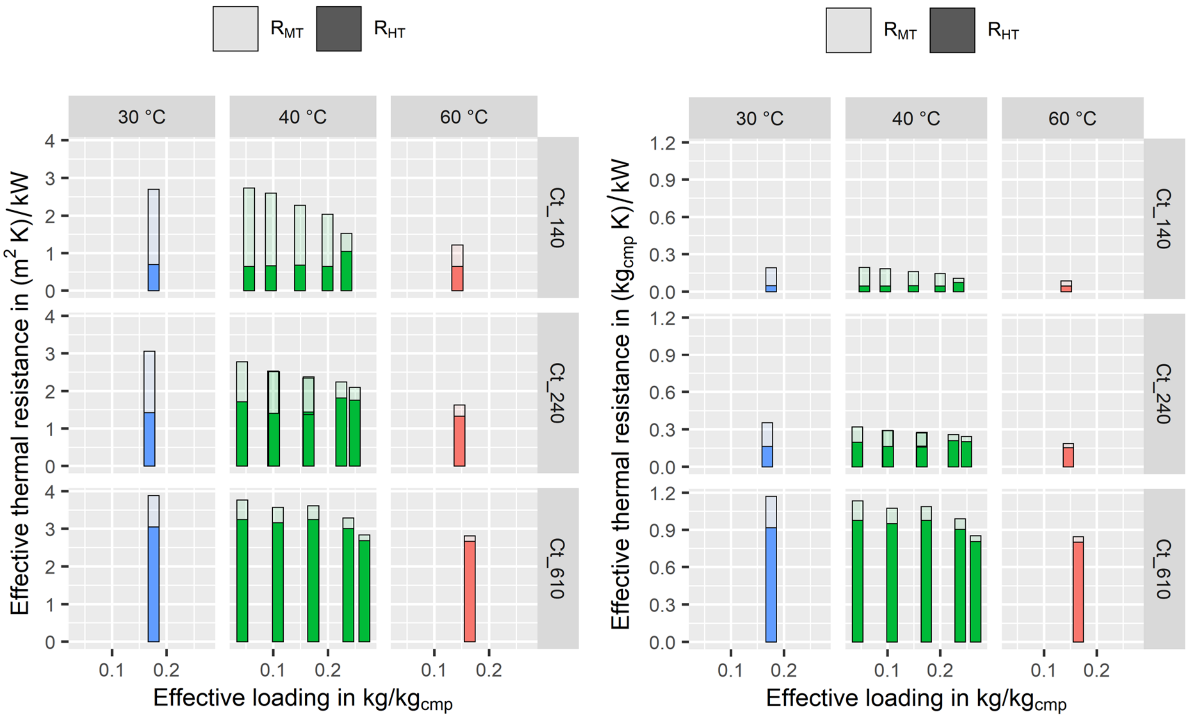

Figure 43: Equivalent thermal resistances of aluminium fumarate coating over loading for different temperature (colours) and thicknesses differentiated by resistance from mass transfer (LDF-approximated) R_{MT} and heat transfer (conduction in the composite layer) R_{HT}, i.e. the coated area (left) or composite dry mass (right) required to provide 1 kW adsorption power at 1 K of driving temperature difference between support (fin) surface and equilibrium temperature

In the mass related perspective (Figure 43, right) the differences in resistance, between thinner and thicker coatings, are much more pronounced for the heat transfer resistance and vanishes for mass transfer resistance. Thus, the *material usage* (power output per material input) is much better for thinner coatings, given that the low resistances may be leveraged by appropriately low resistances in the rest of the system. These other resistances, like the heat transfer in the remaining Ad-HX (conduction in fins, convection to the HTF), the heat and mass transfer in the evaporator/condenser or the pressure drop in the free vapour flow, can be quantified and compared with the same framework in a practical design process.

In all cases the achievable power will need to be balanced with efficiency that is reduced with thinner coatings (Schnabel *et al.*, 2018). An overall improvement would be achieved by improved thermal conductivity, as this would especially improve the performance of thicker coatings, where efficiency is high and mass transfer resistance is already low.

5.5.2 Estimation of expected SCP and COP

In the following the effective heat transfer resistances are combined with the measured adsorption equilibrium to predict the specific cooling power (SCP) of an adsorption cycle with the method proposed in this work (c.f. Section 3.2.4). The coefficient of performance (COP) prediction is straightforward with the conventional energy balance approach (c.f. p55). Exemplary results are given for a fin-and-tube Ad-HX design and two sets of cycle conditions, which determine the effective driving temperature difference and the loading spread.

The assumed cycle conditions are $T_1/T_{23}/T_4$ = 65/35/20 °C (A) and 60/30/20 °C (B), representing a variation of driving and rejection temperature for the same cooling temperature. These are the conditions at the level of the adsorbent coating, i.e.:

T_1	temperature of the metal support (fin) during desorption,
T_{23}	temperature of the metal support (fin) during adsorption and saturation temperature (pure water) of the surface pressure during desorption, and
T_4	saturation temperature (pure water) of the pressure at the coating surface during adsorption.

Note that the conditions at the level of the external heat sources and sinks are different, as additional driving temperature differences as well as necessary temperature differences between heat exchanger in- and outlet need to be taken into account. Table 9 summarises the cycle conditions and derived parameters, with an assumed additional overall difference of 5 K between the conditions at coating level and the external conditions. The variants are basically a variation of the temperature lift $\Delta T_{\mathrm{lft}} = T_3 - T_4$, while the temperature thrust $\Delta T_{\mathrm{thr}} = T_1 - T_2$ is kept constant (c.f. p53).

Table 9: Assumed cycle conditions for SCP and COP prediction

Variant	Conditions at Coating Level			External Conditions		
	$T_1/T_{23}/T_4$ (°C)	ΔT_{lft}	ΔT_{thr}	$T_1/T_{23}/T_4$ (°C)	ΔT_{lft}	ΔT_{thr}
A	65/35/20	15 K	30 K	70/30/25	5 K	40 K
B	60/30/20	10 K	30 K	65/25/25	0 K	40 K

The plot of ΔT_{ch} vs. X (Figure 44) shows the equilibrium properties of aluminium fumarate together with the cycle conditions at coating level (Variant A only). The data confirms that the temperature dependency of ΔT_{ch} is negligible in a first approximation as expected (c.f. Table 3). The loading dependency is little pronounced in the mid-range and steeply rising to wards both end of the loading scale.

By adding the external temperature differences ΔT_{thr} and ΔT_{lft}, the plot allows deducing some important parameters for performance approximation, as discussed in the following by going through the adsorption cycle: The desorption process starts at high loadings, ideally at X_{max}, where the effective driving temperature difference ($\Delta T_{\mathrm{drv,tot}} = \Delta T_{\mathrm{thr}} - \Delta T_{\mathrm{ch}}$) is the highest (red arrows). During the desorption half-cycle the loading decreases down to X_{min}, where $\Delta T_{\mathrm{ch}} = \Delta T_{\mathrm{thr}}$. Here, the desorption process reaches equilibrium, i.e. no driving force is available anymore to further desorb the adsorbent, and the cycle is switched to adsorption. At this low loading, the adsorption half-cycle starts with a high absolute value of $\Delta T_{\mathrm{drv,tot}}$ (green arrows), that decreases until the adsorption process reaches equilibrium at the maximal loading X_{max}, where $\Delta T_{\mathrm{ch}} = \Delta T_{\mathrm{lft}}$ and the cycle is switched to desorption again. The isosteric phases are barely visible in this representation, as ΔT_{ch} is nearly temperature independent. However, and in contrast to the classical Clausius–Clapeyron plot (c.f. Figure 6), this plot allows deducing directly the two parameters required for SCP and COP prediction, respectively: the available effective driving temperature difference ΔT_{drv}, and the available loading spread ΔX.

The maximum loading spread ΔX_{max} is a theoretical value reached at equilibrium, which results very low average heat flows, and that will be avoided in most applications. Thus, the exact position of X_{min} and X_{max} is less relevant, and so is the higher uncertainty and the apparently higher temperature dependency of T_{ch} in this area. To allow for this, 15% of ΔX_{max} will be cut off at each end, based on an approach from Velte (2019). Similarly, the driving temperature differences will be roughly deduced from the inflection point of T_{ch} at about 22.5 K and assumed constant.

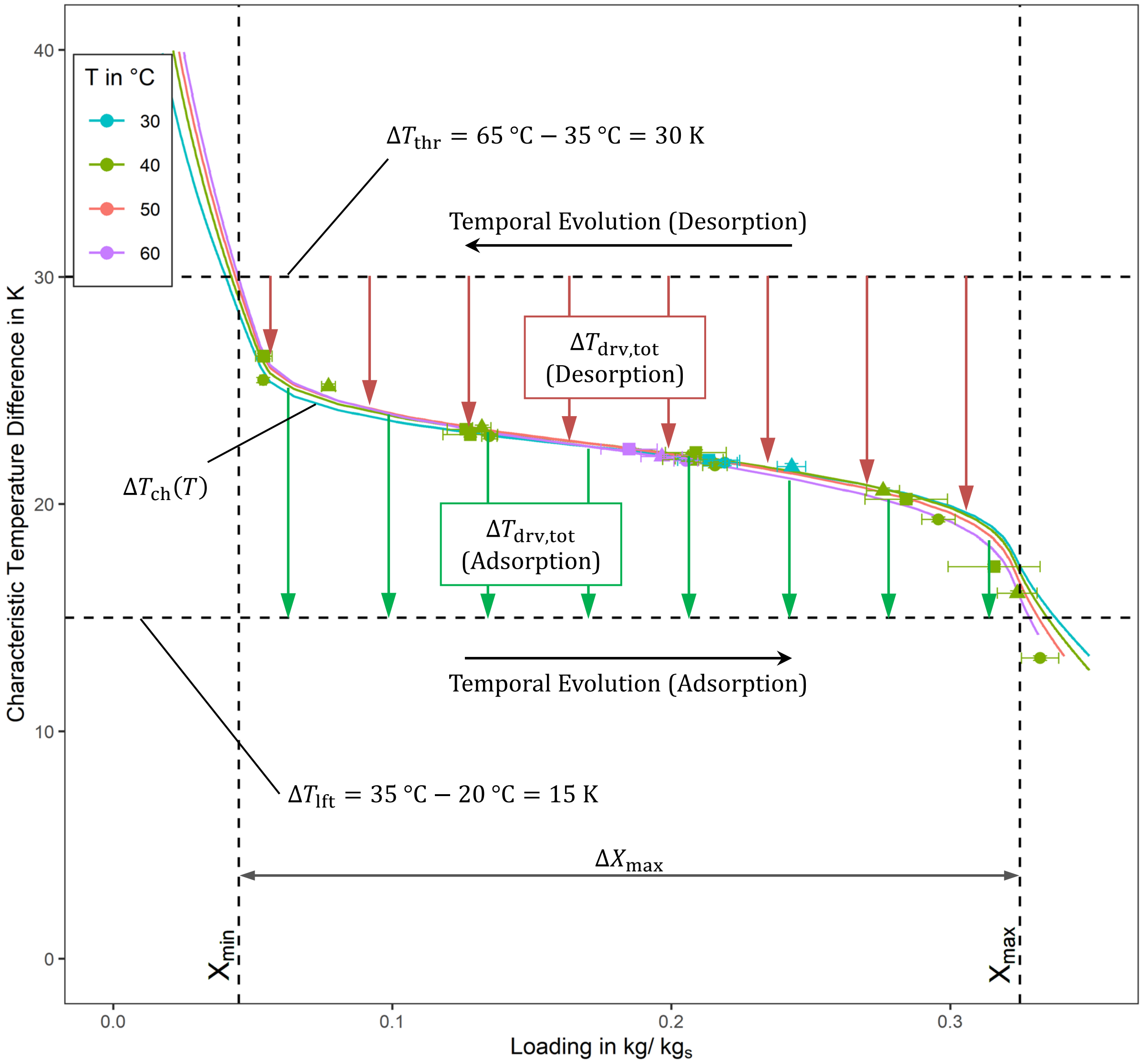

Figure 44: Characteristic temperature difference of Alfum–water over loading for different adsorbent temperatures (colour legend in °C), calculated from measured data (points, c.f. Figure 27) and fitted equilibrium (lines, c.f. Appendix A.10) for temperatures between 30 and 60 °C with the temperature lift and thrust of the Variant A cycle, i.e. 65/35/20 °C (temperature differences in K as dashed horizontal lines), coloured arrows indicate the available effective driving temperature difference for adsorption and desorption half-cycle.

The exemplary Ad-HX design is adopted from a heat exchanger assessed in detail by Wittstadt (2018), which is depicted in Figure 45. The fins are assumed to be covered with the aluminium fumarate coating analysed before. The fin spacing is varied with coating thickness, in order to allow for 2 mm free vapour channels between the fins. This results in area-to-volume-ratios of 0.34–0.25 $\mathrm{m^2/l}$ for coating thicknesses of 140–610 µm. For this range, the overall heat capacity per adsorbent mass is 9.5–4.0 $\mathrm{kJ/(kg_s\ K)}$, based on tube and fin masses from Wittstadt (2018) (c.f. Appendix A.11).

With these assumptions, the Ad-HX performance is estimated for both cycle variants and for the thinnest and the thickest coating assessed as shown in Table 10. The effective thermal resistances are (roughly) loading-averaged and taken for 40 °C, which is more relevant to the given cycle conditions. For the whole range of conditions measured, the range of R_eff is 1.2–3.7 $\mathrm{kW/(m^2\ K)}$ for the thinnest and 2.8–3.9 $\mathrm{kW/(m^2\ K)}$ for the thickest coating.

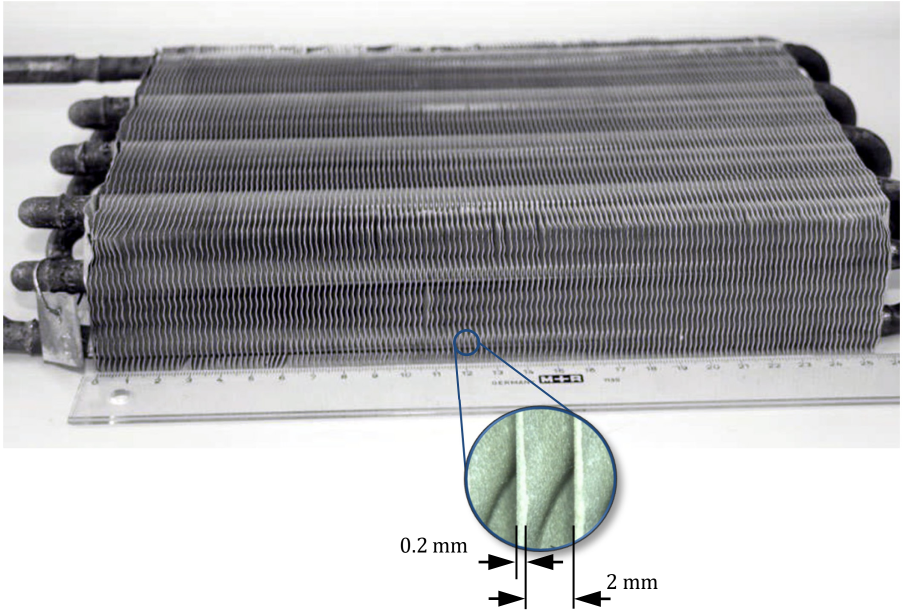

Figure 45: Example adsorption heat exchanger for result extrapolation adopted from Wittstadt (2018), the thickness of the coating (not shown) is added to the fin spacing, in order to allow for a 2 mm free vapour channel between fins.
Adopted from Wittstadt (2018) under license CC BY 4.0.

The expected cooling power is calculated directly from R^A_eff, as the evaporator effect is already included in the defined cycle conditions, according to Eq. (88) with the enthalpy ratio of $\Delta h_\mathrm{v}/\Delta h_\mathrm{s}$ = 2.45/2.90 = 0.84. The "loss" attributed to the isenthalpic expansion of the working fluid is just about 3% of Δh_v here, and can be neglected in this coarse approximation. Further, the ratio between the adsorption half-cycle time and the total cycle time has to be taken into account. For Variant A, where the driving forces are roughly equal for both half-cycles, this ratio is assumed to be 0.5. For Variant B the case is less straight forward as during adsorption ΔT_ch is 1.7 times larger than during desorption. Assuming, in a first approximation and neglecting the temperature dependency of R^A_eff, that the half-cycle time is inverse to the driving force, 0.4 is assumed for the ratio. This yields a VSCP in the range of 0.2–0.7 kW/l for the Alfum coating.

This VSCP result can be compared to literature values: For the state-of-the-art silica gel granular bed (Ammann *et al.*, 2018), the expected range is 0.02–0.08 kW/l, under the same boundary conditions and the same geometrical assumptions (c.f. Appendix A.12). Kummer *et al.* (2017b) investigated a complete Ad-HX with a similar Alfum coating as investigated here (d_ct = 300–330 µm, $w_\mathrm{s,dry}$ = 0.77) by LPJ experiments on heat exchanger level. For the cycle conditions of 90 °C/30 °C/18 °C, which corresponds to $\Delta T_{\mathrm{thr}} = 60\ \mathrm{K}$ and $\Delta T_{\mathrm{lft}} = 12\ \mathrm{K}$, an average VSCP of 0.1 kW/l is reported for a cut-off uptake of 90% and with respect to the volume of the finned part (headers excluded). The applied temperature thrust allowed for a complete desorption so that the initial conditions for the adsorption are comparable to the assumption made here. The temperature lift determined the available driving temperature difference during adsorption ($\Delta T_{\mathrm{drv}} = \Delta T_{\mathrm{ch}} - \Delta T_{\mathrm{lft}} \approx 22.5\ \mathrm{K} - 12\ \mathrm{K} = 10.5\ \mathrm{K}$), which is roughly in between Variant A and Variant B (Table 10). Also the coating thickness was in the range of the FRA-investigated samples. Still, the reported VSCP is considerably lower. This can be explained by the additional heat transfer resistances on the path from the fin surface to the HTF (conduction in the fins and convection inside the tubes), i.e. the ΔT_{drv} available at the level of the coating would have actually been much smaller than for Variant A. Moreover, the available ΔT_{drv} was further reduced by the necessary temperature difference between the in- and outlet of the Ad-HX, which is explicitly neglected in the estimations shown in Table 10.

The COP is estimated conventionally according to Eq. (55), based on the thermal mass of the heat exchanger and the reduced loading spread ΔX_{15-85}, and assuming that evaporator and condenser are separated, i.e. without the effect of C_{CE}.

These values should be treated with caution. They are meant as rough approximation and therefore necessarily include several simplifying assumptions.

Table 10: Estimated Ad-HX performance based on effective thermal resistances

Cycle conditions		**Variant A**		**Variant B**	
Temperature lift ΔT_{lft}	K	15		10	
Temperature thrust ΔT_{thr}	K	30		30	
Coating thickness d_{ct}	**µm**	**140**	**610**	**140**	**610**
Eff. driving temp. difference ΔT_{drv}	K	7.5		12.5	
Effective thermal resistance R_{eff}^{A}	$(\mathrm{m}^2\ \mathrm{K})/\mathrm{kW}$	2	3.5	2	3.5
Adsorption power per coated area[v]	$\mathrm{kW/m}^2$	3.8	2.1	6.3	3.6
Relative adsorption half-cycle duration	-	0.5		0.4	
Cooling power per coated area[vi]	$\mathrm{kW/m}^2$	1.6	0.9	2.1	1.2
Coated area per overall-volume	m^2/l	0.34	0.25	0.34	0.25
Volume specific cooling power (VSCP)	**kW/l**	**0.54**	**0.23**	**0.72**	**0.30**
(LTJ-based VSCP, c.f. Section 5.5.3)	kW/l	(0.44)	(0.22)	(0.70)	(0.36)
Mass of pure adsorbent per coated area	$\mathrm{kg/m}^2$	0.052	0.24	0.052	0.24
Heat capacity per adsorbent mass[vii]	kJ/(kg K)	10.2	4.5	10.2	4.5
Maximum loading spread $\Delta X_{\max}$	$\mathrm{kg_w/kg_s}$	0.28		0.28	
Reduced loading spread ΔX_{15-85}	$\mathrm{kg_w/kg_s}$	0.20		0.20	
Coefficient of performance (COP)	**-**	**0.54**	**0.67**	**0.54**	**0.67**
(LTJ-based COP, c.f. Section 5.5.3)	-	(0.54)	(0.66)	(0.56)	(0.68)

5.5.3 Comparison to LTJ measurement

The same samples were analysed with LTJ measurements, as published before (Laurenz *et al.*, 2019). For this study, two temperature jumps at a pressure around $p_{\mathrm{sat}}(20\ °\mathrm{C})$

---

[v] Per coated area, averaged over the adsorption half-cycle

[vi] Per coated area, averaged over the complete cycle

[vii] Including headers, tubes, fins, binder and dry adsorbent

were measured: the first from 45 °C to 35 °C, the second from 50 °C to 30 °C. This corresponds closely to the cycle conditions of Variant A and B detailed above. The measured temporal uptake evolution (Figure 46) was used to estimate a hypothetical cooling power per coated surface area based on Δt_{15-85}, the duration between 15% and 85% of relative uptake $\Delta X/\Delta X_\infty$, with Eq. (57). A slightly different assumption about the relative adsorption half-cycle time was used with 0.5 for both cases. These results were then further used to estimate a VSCP for the same Ad-HX geometry from Wittstadt (2018). The results[11] (Figure 47 and also included in Table 10) show comparable values to those estimated in the last section based on effective thermal resistances, especially given the intended coarseness of the latter.

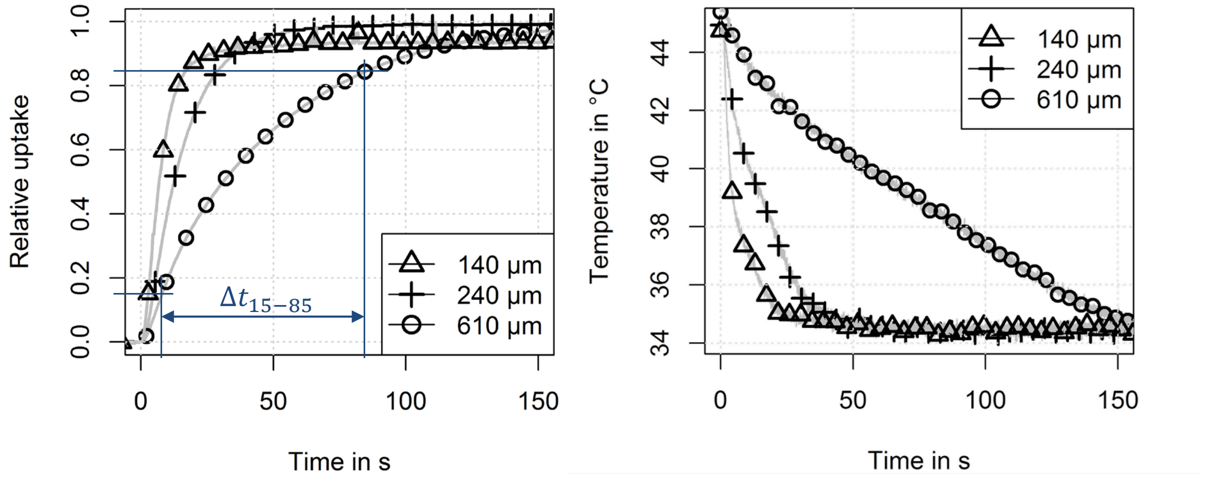

Figure 46: Temporal evolution from LTJ measurements for different coating thickness measured at an average pressure of $p_{\mathrm{sat}}(20\ °\mathrm{C})$ for cycle conditions comparable to Variant A (Table 9)

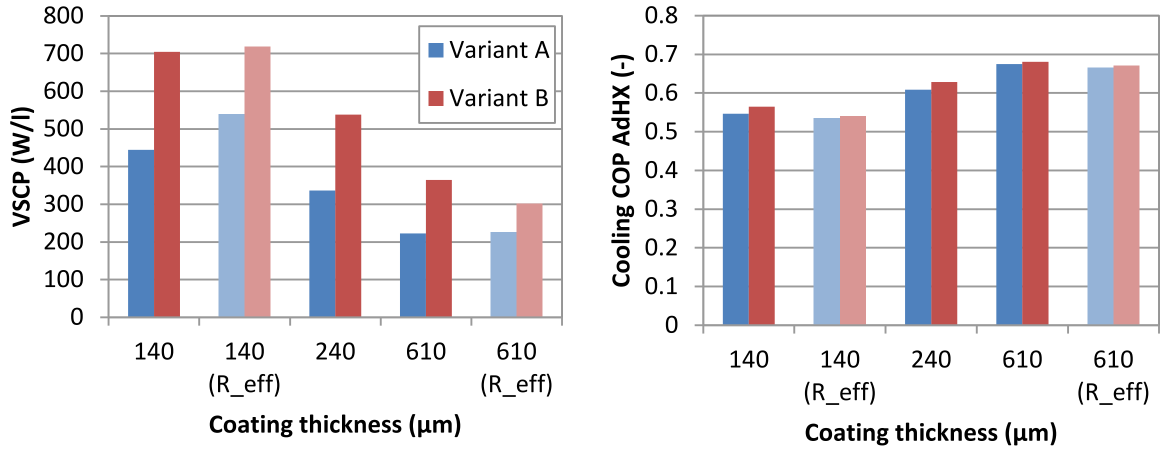

Figure 47: Volume specific cooling power (VSCP) and cooling COP estimated from LTJ measurements (strongly coloured; Laurenz *et al.*, 2019) compared to R_{eff}-based estimate as given in Table 10 (lightly coloured)

---

[11] The originally published results included a minor implementation error and simple Dubinin approximation for the differential adsorption enthalpy in stead the consisten values given before (c.f. Section 5.2), which both have been corrected here.

6. Conclusion and Outlook

"[...] if this merely helps a little towards dispelling the metaphysical fog that seems to be engulfing us, it will have attained its object." (Buckingham, 1914)

The first aim of this work was to quantify the relevant heat and mass transfer (HMT) parameters for the adsorption dynamics of water, with a special focus on their dependency on the thermodynamic state. A binder-based aluminium fumarate (Alfum) coating served as a model material investigated in this research. The HMT parameters with their state dependency allow the precise non-linear modelling of application-relevant processes in the time domain. They should be independent from geometrical design parameters to be directly useable for design and optimisation.

Based on the frequency response analysis (FRA), the coating thermal conductivity and the micro-scale mass transfer could be identified as the mechanisms governing the adsorption dynamics. The corresponding transport parameters were determined in their loading (entire range) and temperature (30–60 °C) dependency as detailed below, and they proved to be independent from the coating thickness. Further, with an extension of the FRA procedure, the adsorption equilibrium and the differential adsorption enthalpy were measured at the same time. For model and parameter validation, all information obtained was fed into a non-linear simulation of a large temperature jump, which was perfectly confirmed by experimental results under the same application-like conditions.

The second aim of this research was to present the resulting HMT parameters in a simplified form, allowing a direct interpretation of their relevance for adsorption heat transformation applications and rough estimates of principle performance indicators for efficiency and compactness.

With the concept of effective thermal resistances, which was further extended theoretically and related to HMT parameters, it was shown that resistances from both, heat and mass transfer, were comparably relevant, with the heat transfer becoming more relevant for thicker coatings, whereas the mass transfer is dominating in thinner coatings. The mass transfer resistance reduces considerably with loading and temperature. The analysis allowed a clear and simple distinction between the influence of the transfer resistances, the equilibrium properties and the external temperature boundary conditions with respect to the achievable performance of a given adsorption heat exchanger (Ad-HX) design. A case study, carried out for typical boundary conditions of a data centre cooling application and an exemplary Ad-HX design, showed the technological potential of this Alfum coating: The approximated volume specific cooling power was between 0.2 kW/l and 0.7 kW/l with a coefficient of performance between 0.67 and 0.54, respectively, compared to 0.02–0.08 kW/l expected for a state-of-the-art silica gel granular bed.

The FRA method was realised in a custom built setup, combined with newly derived models and integrated into an extended measurement procedure for a holistic characterisation of the adsorption dynamics. The setup included a measurement of the surface temperature response for improved heat transfer characterisation, making it the second of its kind in adsorption dynamics literature, with a much more economic approach compared to the previous one.

Four heat-transport-focused HMT models were employed for the first time in combination with FRA, including a deduction of their complex transfer functions, i.e. generally applicable analytical solutions in the Laplace domain. From these newly proposed models, the best fitting one combined 1-dimensional heat conduction with a linear driving force (LDF) approximated micro-scale mass transfer. While this model proved to be very well suited for the description of the Alfum coating, the generalizability of this model may be limited as other adsorbent coating might require different approaches, e.g., a model with additional mass transport in the macro pores. An explicit transfer function for such a model was shown to exist in principle; however, the implementation remains an open question as it showed to be irrelevant for this research.

With the extension of the FRA measurement procedure, including manometric adsorption measurement and small equilibrium excitations around the set measurement point, the absolute and differential adsorption equilibrium of aluminium fumarate was determined in-situ. The results basically confirmed literature data and show that the adsorbent in the coating remained fully accessible. However, an application-relevant hysteresis, which was reported by other authors, could be evidently ruled out.

The adsorption enthalpy was consistently calculated with two different methods to a value of 2.90 ± 0.05 MJ/kg (52.2 ± 1.0 kJ/mol) on average, based on either the classical approach of interpolating the isostere pitch from several isotherms or the newly proposed “local” method based on the differential adsorption equilibrium. Although for the Alfum sample no significant dependency on loading or temperature could be observed within the range of thermodynamic states investigated, the new local method allows in principal to resolve this state dependency to a much higher degree. The research clearly shows that the common Dubinin approximation may not be made for aluminium fumarate–water as the temperature-invariance criterion is not met. Although, the physical reason for this behaviour remains an open question.

The specific heat capacity of the Alfum coating, required for the FRA evaluation, was measured with differential scanning calorimetry as loading and temperature dependent quantity. While the results for the dry coating are inconspicuous (1.05 kJ/(kg K) at 25 °C with a temperature coefficient of 2×10^{-3} kJ/(kg K^2)), the loading dependent results are in strong disagreement with the common assumption of an inert adsorbent with an adsorbate that behaves like water or ice. The apparent heat capacity of the adsorbed phase is up to a factor 2 higher than that of pure water. Consistent with the aforementioned temperature-variance in the Dubinin formalism, this indicates a strong feedback effect of the adsorption on the adsorbent itself. While this is especially relevant to the estimation of heat transfer resistances from sorption dynamic experiments, overall efficiency-estimations of most applications will have a low sensitivity to the adsorbate heat capacity. As direct external measurements are costly and literature on the heat capacity of sorption materials, especially as a function of loading, is scarce, the inclusion in the extended FRA measurement procedure should be aimed at in future research.

The details of the adsorption dynamics of water in the Alfum coating revealed a micro-scale mass transfer with a Darken-like loading and Arrhenius-type temperature dependency ($E_\mathrm{a} = 55.0 \pm 3.1\,\mathrm{kJ/mol}$). Through a variation of the coating thickness (140–610 µm), it was possible to discriminate between different plausible transfer processes. The micro-scale mass transfer is described by an LDF coefficient k_LDF with values between 0.1 and 3 s^{-1} at 40 °C and a U-shaped loading dependency, which could be explained by the thermodynamic (Darken) factor. The underlying mechanism at the scale of the adsorbent particles (average size 18 µm) could be narrowed down to a surface barrier resistance rather than adsorbate diffusion process. However, the exact physical effect remains an open question. Counterintuitively, the macropore diffusion was shown to be irrelevant, at least for the coating thicknesses investigated. Values for the thermal conductivity are around 0.07 W/(m K), a low but plausible value that exhibited neither a significant temperature nor a loading dependency. The heat transfer coefficient of the thermal contact between coating and support is larger than 4×10^3 W/(m^{2}K), but no upper limit can be given as it is not limiting the adsorption dynamics.

Based on these results, practical improvements of this coating should consider, firstly, to reduce the macro porosity in order to increase the thermal conductivity to the bearable cost of a further limited macropore transport, and secondly, to reduce the size of the adsorbent particles in order to improve the micro-scale mass transfer.

The concept of effective thermal resistances was extended by the definition of two fundamental temperature differences for adsorption heat transformation (AHT), characterising the applied external temperatures and the internal adsorption equilibrium. This allows first-order estimations of the power density with a new simple Ohm's-law-like approach for engineering-level design decisions, without requiring experiments or simulations in the time domain. This concept could be demonstrated to yield results comparable to LTJ-based state-of-the-art estimations for working pairs with S-shaped (type IV) isotherms exhibiting isobaric phases with little temperature change. Current limitations include its applicability to adsorbents with linear isotherms, the extent to which the isosteric phases are taken into account and the assumption of a constant HTF temperature. They should be addressed in future research, e.g., based on a thermal time constant, calculated from the heat capacity and the overall thermal transfer resistance or the ε-NTU method, respectively.

For the case of the Alfum coatings, the effective thermal resistances are found to be between 1–4 (m^2 K)/kW with respect to the coated heat exchanger area and the effective driving temperature difference, showing the high application potential from a technological point of view. Lower resistances are only reported for sintered aluminium fibres coated by partial support transformation, but here the fabrication process is considerably more resource and know-how intensive.

The practical recommendations for improving the coating can be further refined, based on the quantitative comparison of heat and mass transfer resistances: If the aim is a very high specific cooling power, thinner coating are preferred, where the micro-scale mass transfer should be targeted as the principal limitation by reducing the adsorbent particle size. However, if the aim includes a high COP, thicker coatings are more appropriate, where the heat transfer is limiting and can be improved by compacting the coating or by addition of thermally highly conductive material to the coating.

Finally, it seems worth mentioning that with the foundation laid in this research it should in principle be possible to combine both methods, the FRA and the concept of effective thermal resistances, to directly obtain the frequency response of the (complex) effective thermal impedance. This approach has a strong analogy to the vast field of electrical impedance spectroscopy and might allow using parts of this elaborated field of research for the means of analysing and improving components for AHT.

To sum up, this research has shown the high potential of the FRA for quantitative and differentiated assessment of heat and mass transfer processes that govern adsorption dynamics and how the concept of effective heat transfer resistances can help to transform this information directly into a practical design process for improved adsorption heat pumps, chillers and thermal storages.

A Appendix

A.1 Energy Balance of the Isothermal Adsorbent–Adsorbate System

The general energy balance of the adsorbent–adsorbate system (Figure 1) is

$$\mathrm{d}U_{\mathrm{s+a+g}} = h_{\mathrm{g}}\mathrm{d}m_{\mathrm{g}} + \mathrm{d}Q \tag{107}$$

where $\mathrm{d}U_{\mathrm{s+a+g}}$ is the combined internal energy of the adsorbent, the adsorbate and the gas phase within the system. The following assumptions have been described before:

- No effect of the gas phase on the mass balance, $\mathrm{d}m_{\mathrm{g}} = \mathrm{d}m_{\mathrm{a}}$
- No effect of the gas phase on the energy balance, $\mathrm{d}U_{\mathrm{s+a+g}} = \mathrm{d}U_{\mathrm{s+a}}$
- No effect of the adsorbent–adsorbate volume on the energy balance, $\mathrm{d}U_{\mathrm{s+a}} = \mathrm{d}H_{\mathrm{s+a}}$

This leads to

$$\mathrm{d}H_{\mathrm{s+a}} = h_{\mathrm{g}}\mathrm{d}m_{\mathrm{a}} + \mathrm{d}Q, \tag{108}$$

and with Eq. (10) to

$$\left(\frac{\partial H_{\mathrm{s+a}}}{\partial T}\right)_{m_{\mathrm{s}},m_{\mathrm{a}}}\mathrm{d}T + \left(\frac{\partial H_{\mathrm{s+a}}}{\partial m_{\mathrm{a}}}\right)_{m_{\mathrm{s}},T}\mathrm{d}m_{\mathrm{a}} = h_{\mathrm{g}}\mathrm{d}m_{\mathrm{a}} + \mathrm{d}Q. \tag{109}$$

This simplifies for the isothermal case, and may be rearranged to

$$\begin{aligned} -\mathrm{d}Q &= h_{\mathrm{g}}\mathrm{d}m_{\mathrm{a}} - \left(\frac{\partial H_{\mathrm{s+a}}}{\partial m_{\mathrm{a}}}\right)_{m_{\mathrm{s}},T}\mathrm{d}m_{\mathrm{a}} \\ &= \mathrm{d}m_{\mathrm{a}}\left(h_{\mathrm{g}} - \left(\frac{\partial H_{\mathrm{s+a}}}{\partial m_{\mathrm{a}}}\right)_{m_{\mathrm{s}},T}\right) \\ &= \mathrm{d}m_{\mathrm{a}}\left(h_{\mathrm{g}} - \bar{h}_{\mathrm{s+a}}\right) \\ &= \mathrm{d}m_{\mathrm{a}}\Delta h_{\mathrm{s}}. \end{aligned} \tag{110}$$

For the case of an inert adsorbent, where $(\partial H_{\mathrm{s}}/\partial m_{\mathrm{a}})_{m_{\mathrm{s}},T} = 0$, the enthalpy difference simplifies as follows

$$\begin{aligned} h_\mathrm{g} - \left(\frac{\partial H_\mathrm{s+a}}{\partial m_\mathrm{a}}\right)_{m_\mathrm{s},T} &= h_\mathrm{g} - \left(\frac{\partial (H_\mathrm{s} + H_\mathrm{a})}{\partial m_\mathrm{a}}\right)_{m_\mathrm{s},T} \\ &= h_\mathrm{g} - \left(\frac{\partial H_\mathrm{s}}{\partial m_\mathrm{a}}\right)_{m_\mathrm{s},T} - \left(\frac{\partial H_\mathrm{a}}{\partial m_\mathrm{a}}\right)_{m_\mathrm{s},T} \\ &= h_\mathrm{g} - \left(\frac{\partial H_\mathrm{a}}{\partial m_\mathrm{a}}\right)_{m_\mathrm{s},T} \\ &= h_\mathrm{g} - \bar{h}_\mathrm{a}, \end{aligned} \tag{111}$$

i.e. to the definition of the differential adsorption enthalpy with inert adsorbent (c.f. Eq (14)).

A.2 Solutions of Heat and Mass Transfer Models (Table 1)

A.2.1 Lumped HT w. even-layer micropore diffusion (0DHT_miD)

Adsorbate diffusion is considered as the transport mechanism on crystal level:

$$\frac{\partial X(x,t)}{\partial t} = D_\mathrm{mi} \frac{\partial^2 X(x,t)}{\partial x^2} \tag{112}$$

with the no-flux condition in the crystal centre $(x = 0)$ and equilibrium with the chamber atmosphere, i.e. p_ch, at the surface $(x = r)$ as boundary conditions:

$$\frac{\partial X(0,t)}{\partial x} = 0 \qquad X(r,t) = X_\mathrm{eq}\big(p_\mathrm{ch}(t), T(t)\big). \tag{113}$$

The equilibrium loading can be linearized as usual (Wang 2011, Bourdin 1998) to

$$X_\mathrm{eq}(x,t) - X_0 \approx K_T(T(x,t) - T_0) + K_p(p_\mathrm{ch}(t) - p_0) \tag{114}$$

with the slopes of the isobar and isotherm $K_T = \partial X/\partial T$ and $K_p = \partial X/\partial p$. Taking the Laplace transform with deviation variables from Eq. (60) yields

$$\begin{gathered} s\tilde{X} = D_\mathrm{mi} \frac{\partial^2 \tilde{X}(x)}{\partial x^2} \\ \frac{\partial \tilde{X}(0)}{\partial x} = 0 \qquad \tilde{X}(r) = K_T\tilde{T} + K_p\tilde{p}_\mathrm{ch}, \end{gathered} \tag{115}$$

which can be solved to

$$\tilde{X}(x) = \frac{e^{-\frac{x}{\sqrt{D_{\mathrm{mi}}/s}}+\frac{r}{\sqrt{D_{\mathrm{mi}}/s}}}\left(1+e^{\frac{2x}{\sqrt{D_{\mathrm{mi}}/s}}}\right)\left(K_p\tilde{p}_{\mathrm{ch}} + K_T\tilde{T}\right)}{1+e^{\frac{2r}{\sqrt{D_{\mathrm{mi}}/s}}}}. \tag{116}$$

and integrated to

$$\tilde{\tilde{X}} = \frac{1}{r}\int_0^r \tilde{X}(x)\mathrm{d}x = \sqrt{\left(\frac{D_{\mathrm{mi}}}{r^2 s}\right)\left(K_p\tilde{p}_{\mathrm{ch}} + K_T\tilde{T}\right)\tanh\left(\sqrt{\frac{r^2 s}{D_{\mathrm{mi}}}}\right)}. \tag{117}$$

Combination with the chamber mass balance Eq. (61) and the lumped energy balance Eq. (64) allows solving for the loading volume transfer function

$$\begin{aligned} G_{XV}(s) &= \frac{\tilde{\tilde{X}}}{\tilde{V}} \\ &= \frac{\frac{K_p p_0}{V_0}\left(-\sqrt{\frac{k_{\mathrm{mi}}}{s}}\tanh\left(\sqrt{\frac{s}{k_{\mathrm{mi}}}}\right)\right)}{\left(1+\left(\frac{m_{\mathrm{s}}K_pR_{\mathrm{w}}T_0}{V_0}-\frac{m_{\mathrm{s}}\Delta h_{\mathrm{s}}K_T s}{Ah+c_p m_{\mathrm{s}} s}\right)\sqrt{\frac{k_{\mathrm{mi}}}{s}}\tanh\left(\sqrt{\frac{s}{k_{\mathrm{mi}}}}\right)\right)} \\ &= \frac{\frac{K_p p_0}{V_0}\,(-1)}{\left(\sqrt{\frac{s}{k_{\mathrm{mi}}}}\coth\left(\sqrt{\frac{s}{k_{\mathrm{mi}}}}\right)+\frac{m_{\mathrm{s}}K_pR_{\mathrm{w}}T_0}{V_0}-\frac{m_{\mathrm{s}}\Delta h_{\mathrm{s}}K_T s}{Ah+c_p m_{\mathrm{s}} s}\right)} \end{aligned} \tag{118}$$

with $k_{\mathrm{mi}} = D_{\mathrm{mi}}/r^2$ and $s = j\omega$. $G_{XV}(s)$ may be substituted in Eqs. (66) and (67) to yield the pressure and temperature response actually measured.

It can be shown that the result is equivalent to the solution Sun & Bourdin (1993) provided earlier for the "in-phase and out-of-phase components" of the same model. Although, the compact complex formulation of Eq. (118) is preferred here, as it may be implemented straight forward in parameter identification procedures.

A.2.2 Lumped HT w. even-layer macropore diffusion (0DHT_maD)

For this model, the governing mass transfer process is the diffusion within isotropic macropores of an even coating layer with the thickness d, the (constant) effective macro diffusivity D_{ma} and the gas concentration in the pores as driving force:

$$\frac{\partial c(x,t)}{\partial t} = D_{\mathrm{ma}}\frac{\partial^2 c(x,t)}{\partial x^2} - \frac{\partial X(x,t)}{\partial t}\frac{\rho_{\mathrm{eff}}}{\varepsilon_{\mathrm{P}} M} \tag{119}$$

with the molar mass M, the effective adsorbent density $\rho_{\mathrm{eff}} = m_{\mathrm{s}}/(Ad)$, the macro porosity ε_{P} (i.e. macropore volume per coating volume) and the usual boundary conditions at the coating bottom ($x = 0$) and surface ($x = d$):

$$\frac{\partial c(0,t)}{\partial x} = 0 \qquad\qquad c(d,t) = c_{\mathrm{ch}}(t) = \frac{p_{\mathrm{ch}}(t)}{MR_{\mathrm{w}}T_0}. \tag{120}$$

Laplace transformation with deviation variables yields

$$\begin{gathered} s\tilde{c}(x) = D_{\mathrm{ma}}\frac{\partial^2 \tilde{c}(x)}{\partial x^2} - s\tilde{X}(x)\frac{\rho_{\mathrm{eff}}}{\varepsilon_{\mathrm{P}}M} \\ \frac{\partial \tilde{c}(0)}{\partial x} = 0 \qquad\qquad \tilde{c}(d) = \frac{\tilde{p}_{\mathrm{ch}}}{MR_{\mathrm{w}}T_0}. \end{gathered} \tag{121}$$

As the model assumes local equilibrium in the macropores, the linearized equilibrium in concentration form (c.f. Eq. (114), assuming ideal gas behaviour)

$$\tilde{X} = \tilde{X}_{\mathrm{eq}} \approx MR_{\mathrm{w}}T_0K_p\tilde{c} + K_T\tilde{T} \tag{122}$$

can be used to substitute $\tilde{c}$ in Eq. (121):

$$\begin{gathered} s\frac{-K_T\tilde{T} + \tilde{X}(x)}{MR_{\mathrm{w}}T_0K_p} = \frac{D_{\mathrm{ma}}}{MR_{\mathrm{w}}T_0K_p}\frac{\partial^2 \tilde{X}(x)}{\partial x^2} - s\tilde{X}(x)\frac{\rho_{\mathrm{eff}}}{\varepsilon_{\mathrm{P}}M} \\ \frac{\partial \tilde{X}(0)}{\partial x} = 0 \qquad\qquad \frac{-K_T\tilde{T} + \tilde{X}(d)}{K_p} = \tilde{p}_{\mathrm{ch}}. \end{gathered} \tag{123}$$

Solving for $\tilde{X}(x)$ and integrating yields the mean loading as a function of $\tilde{p}_{\mathrm{ch}}$ and $\tilde{T}$

$$\bar{\tilde{X}} = \frac{K_TT}{1+\alpha} + \sqrt{\frac{k_{\mathrm{ma}}}{s}}\frac{K_p\tilde{p} + \alpha\left(K_p\tilde{p} + K_T\tilde{T}\right)}{(1+\alpha)^{3/2}}\tanh\left(\sqrt{\frac{s}{k_{\mathrm{ma}}}}\sqrt{1+\alpha}\right) \tag{124}$$

with $\alpha = K_p\rho_{\mathrm{eff}}R_{\mathrm{w}}T_0/\varepsilon_{\mathrm{P}}$ and $k_{\mathrm{ma}} = D_{\mathrm{ma}}/d^2$. Equation (124) can be solved together with Eq. (61) and Eq. (64) to yield the required loading volume transfer function

$$
\begin{aligned}
G_{XV}(s) &= \frac{\tilde{\bar{\tilde{X}}}}{\tilde{\bar{V}}} \\
&= -\frac{K_p p_0}{V_0}\left[\sqrt{\frac{s}{k_{\mathrm{ma}}}(1+\alpha)}\left(1-\frac{s}{\beta(1+\alpha)}\right)\coth\left(\sqrt{\frac{s}{k_{\mathrm{ma}}}(1+\alpha)}\right)\right. \\
&\qquad \left. +\,\alpha\left(\frac{\varepsilon_{\mathrm{P}} m_{\mathrm{s}}}{\rho_{\mathrm{eff}} V_0}-\frac{s}{\beta(1+\alpha)}\right)\right]^{-1}
\end{aligned}
\tag{125}
$$

with $\beta = \left(Ah + c_p m_{\mathrm{s}} s\right)/(\Delta h_{\mathrm{s}} K_T m_{\mathrm{s}})$.

A.2.3 Lumped HT w. macropore diffusion and micro LDF (0DHT_maD_LDF)

This model extends the macropore diffusion model above by a local linear driving force model to account for a micro transport process in a simplified way. It is assumed that the local rate of uptake from the micropores is proportional to the difference between the actual loading and the equilibrium loading under the conditions in the micropore. This model has already been presented and solved for the isothermal case on a spherical geometry by Wang & LeVan (2011). Here, it is extended by a lumped heat transfer model and solved on an even-plate geometry.

The Laplace transformed LDF equation with deviation variables and locally linearized equilibrium

$$
\begin{aligned}
s\tilde{X}(x) &= k_{\mathrm{LDF}}\left(\tilde{X}_{\mathrm{eq}}(x)-\tilde{X}(x)\right) \\
&= k_{\mathrm{LDF}}\left(MR_{\mathrm{w}}T_0K_p\tilde{c}(x)+K_T\tilde{T}-\tilde{X}(x)\right)
\end{aligned}
\tag{126}
$$

is used to substitute $\tilde{c}$ in the macro diffusion equation Eq. (121) yielding:

$$
\begin{aligned}
s\frac{1}{K_c}&\left(\frac{s\tilde{X}(x)}{k_{\mathrm{LDF}}}+\tilde{X}(x)-K_T T\right) \\
&\qquad = \frac{D}{K_c}\left(\frac{s}{k_{\mathrm{LDF}}}+1\right)\frac{\partial^2\tilde{X}(x)}{\partial x^2}-\frac{\rho_{\mathrm{eff}} s\tilde{X}(x)}{\varepsilon_{\mathrm{P}} M}
\end{aligned}
\tag{127}
$$

$$
\frac{\partial\tilde{X}(0)}{\partial x}=0 \qquad \frac{1}{K_c}\left(\left(\frac{s}{k_{LDF}}+1\right)X(d)-K_T T\right)=\frac{\tilde{p}_{\mathrm{ch}}}{MR_{\mathrm{w}}T_0}
$$

where $K_c = MR_{\mathrm{w}}T_0K_p$. With the same solution procedure as in the last section, the loading volume transfer function is

$$G_{XV}(s) = -\frac{K_p p_0}{V_0}\left[\sqrt{\frac{s}{k_{\mathrm{ma}}}\frac{\alpha+\gamma}{\gamma}}\gamma\left(1-\frac{s}{\beta(\alpha+\gamma)}\right)\coth\left(\sqrt{\frac{s}{k_{\mathrm{ma}}}\frac{\alpha+\gamma}{\gamma}}\right)\right.$$
$$\left.+\alpha\left(\frac{\varepsilon_{\mathrm{P}} m_{\mathrm{s}}}{\rho_{\mathrm{eff}}V_0}-\frac{s}{\beta(\alpha+\gamma)}\right)\right]^{-1} \qquad (128)$$

with $\gamma = 1 + s/k_{\mathrm{LDF}}$ and the same definition of k_{mi}, α and β as before. For $k_{\mathrm{LDF}} \to \infty$ (i.e. $\gamma = 1$), Eq. (128) simplifies to Eq. (125), the solution for macro diffusion with local equilibrium and lumped heat transfer. For $h \to \infty$ (i.e. $\beta \to \infty$), it simplifies to the isothermal solution of the even-plate macro diffusion model.

A.2.4 1D HT with distributed LDF (1DHT_miLDF)

For thicker coatings and lower thermal conductivity the assumption of a homogeneous temperature distribution becomes more and more inaccurate. Therefore, in this model the heat transfer will be discretized in space, whereas the mass transfer will be simplified with a LDF approach. This is, to keep the model still more convenient for fast parameter identification than a coupled model discretizing both, heat and mass transfer, in space.

Again, an even layer of adsorbent coating is assumed. The conductive heat transfer in the layer can be described with a constant conductivity λ as:

$$\rho_{\mathrm{s}} c_p \frac{\partial T(x,t)}{\partial t} = \lambda\frac{\partial^2 T(x,t)}{\partial x^2} + \rho_{\mathrm{s}}\Delta h_{\mathrm{s}}\frac{\partial X(x,t)}{\partial t}. \qquad (129)$$

At the coating bottom ($x = 0$) an imperfect thermal contact with the heat transfer coefficient h, and at the surface ($x = x_{\mathrm{s}}$) thermal insulation, i.e. negligible convective and radiative heat transfer, are assumed:

$$-\lambda\frac{\partial T(0,t)}{\partial x} = -h[T(0,t) - T_0] \qquad -\lambda\frac{\partial T(x_{\mathrm{s}},t)}{\partial x} = 0. \qquad (130)$$

Taking the Laplace transform in deviation variables yields the ODE

$$\rho_{\mathrm{s}} c_p s\tilde{T}(x) = \lambda\frac{\partial^2\tilde{T}(x)}{\partial x^2} + \rho_{\mathrm{s}}\Delta h_{\mathrm{s}} s\tilde{X}(x)$$
$$-\lambda\frac{\partial\tilde{T}(0)}{\partial x} = -h\tilde{T}(0) \qquad -\lambda\frac{\partial\tilde{T}(x_{\mathrm{s}})}{\partial x} = 0. \qquad (131)$$

The “distributed” and Laplace transformed LDF approach for the mass transfer at the scale of the adsorbent particles is

$$\begin{aligned} s\tilde{X}(x) &= k_{\mathrm{LDF}}\left(\tilde{X}_{\mathrm{eq}}(x) - \tilde{X}(x)\right) \\ &= k_{\mathrm{LDF}}\left(K_p\tilde{p}_{\mathrm{ch}} + K_T\tilde{T}(x) - \tilde{X}(x)\right) \end{aligned} \tag{132}$$

with the linearized equilibrium loading from Eq. (114). Note that for this model the local pressure outside the adsorbent (i.e. in macropores) is constant throughout the coating and equal to the chamber pressure p_{ch}.

The solution procedure is slightly different from before, mainly because, unlike in all cases before, it is not possible anymore to apply the simplification of the energy balance Eq. (64): The temperature at the interface to the support T_{btm} and the mean temperature $\bar{T}$ may be different, and so is the actually measured surface temperature T_{srf}. Instead of $G_{XV}(s)$ as a single “master curve” (Wang & LeVan, 2011) that allows to calculate both, the temperature and the pressure response, explicit results for the two signal are required.

To do so, the ODE system of Eqs. (131) and (132) is solved, allowing then to compute the average loading and temperature as

$$\tilde{\tilde{X}} = \frac{1}{x_{\mathrm{s}}}\int_0^{x_{\mathrm{s}}} \tilde{X}(x)\mathrm{d}x \qquad\qquad \tilde{\tilde{T}} = \frac{1}{x_{\mathrm{s}}}\int_0^{x_{\mathrm{s}}} \tilde{T}(x)\mathrm{d}x. \tag{133}$$

And to insert them into the overall mass and energy balance Eqs. (61) and (64). These can then be solved explicitly for the temperature volume transfer function $G_{TV}(s) = \tilde{T}_{\mathrm{srf}}/\tilde{V}$ and the pressure volume transfer function $G_{pV}(s) = \tilde{p}_{\mathrm{ch}}/\tilde{V}$.

The explicit results of $G_{pV}(s)$ and $G_{TV}(s)$ are so long that there is no advantage in math typing them here. Instead, the results are provided as a pseudo code for implementation in a programming environment. The following code fragment may be directly used in R. For other programming environments, modifications, e.g. of the hyperbolic functions, might be required. Note that the Laplace variable s needs to be replaced by the complex $i\omega$ for the FR and all variables need to be entered in consistent units, e.g. SI units.

```
G_pV = (h*p0*sqrt(rho)*sqrt(s)*(k + s)*(-(hs*k*KT) + cp*(k +
  s))**1.5*xs*cosh((sqrt(rho)*sqrt(s)*sqrt(-(hs*k*KT) + cp*(k +
  s))*xs)/(sqrt(lambda)*sqrt(k + s))) + sqrt(lambda)*p0*rho*s*sqrt(k + s)*
  (-(hs*k*KT) + cp*(k + s))**2*xs*sinh((sqrt(rho)*sqrt(s)*sqrt(-(hs*k*KT) +
  cp*(k + s))*xs)/(sqrt(lambda)*sqrt(k + s))))/(-(h*sqrt(rho)*sqrt(s)*(k +
  s)*sqrt(-(hs*k*KT) + cp*(k + s))*(cp*k*Kp*ms*Rw*T0 + (-(hs*k*KT) + cp*(k +
  s))*V0)*xs*cosh((sqrt(rho)*sqrt(s)*sqrt(-(hs*k*KT) + cp*(k +
  s))*xs)/(sqrt(lambda)*sqrt(k + s)))) + sqrt(lambda)*sqrt(k +
  s)*(h*hs*k^2*Kp*KT*ms*Rw*T0 - rho*s*(-(hs*k*KT) + cp*(k + s))*
  (cp*k*Kp*ms*Rw*T0 + (-(hs*k*KT) + cp*(k + s))*V0)*xs)*
  sinh((sqrt(rho)*sqrt(s)*sqrt(-(hs*k*KT) + cp*(k + s))*xs)/
  (sqrt(lambda)*sqrt(k + s))))


G_TV = (2*hs*k*Kp*p0*sqrt(rho)*sqrt(s)*sqrt(-(hs*k*KT) + cp*(k + s))*xs*
  sinh((sqrt(rho)*sqrt(s)*sqrt(-(hs*k*KT) + cp*(k + s))*xs)/(2.*sqrt(lambda)*
  sqrt(k + s)))*(sqrt(lambda)*sqrt(rho)*sqrt(s)*sqrt(k + s)*sqrt(-(hs*k*KT) +
  cp*(k + s))*cosh((sqrt(rho)*sqrt(s)*sqrt(-(hs*k*KT) + cp*(k + s))*xs)/
  (2.*sqrt(lambda)*sqrt(k + s))) + h*(k + s)*sinh((sqrt(rho)*sqrt(s)*
  sqrt(-(hs*k*KT) + cp*(k + s))*xs)/(2.*sqrt(lambda)*sqrt(k + s)))))* (h*(k + s)*
  cosh((sqrt(rho)*sqrt(s)*sqrt(-(hs*k*KT) + cp*(k + s))*xs)/(sqrt(lambda)*
```

```
sqrt(k + s))) + sqrt(lambda)*sqrt(rho)*sqrt(s)*sqrt(k + s)*sqrt(-(hs*k*KT) +
cp*(k + s))*sinh((sqrt(rho)*sqrt(s)*sqrt(-(hs*k*KT) + cp*(k + s))*xs)/
(sqrt(lambda)*sqrt(k + s)))))/(sqrt(k + s)*(h*sqrt(k + s)*cosh((sqrt(rho)*
sqrt(s)*sqrt(-(hs*k*KT) + cp*(k + s))*xs)/(sqrt(lambda)*sqrt(k + s))) +
sqrt(lambda)*sqrt(rho)*sqrt(s)*sqrt(-(hs*k*KT) + cp*(k + s))*sinh((sqrt(rho)*
sqrt(s)*sqrt(-(hs*k*KT) + cp*(k + s))*xs)/(sqrt(lambda)*sqrt(k + s))))*
(-(h*sqrt(rho)*sqrt(s)*(k + s)*sqrt(-(hs*k*KT) + cp*(k + s))*(cp*k*Kp*ms*Rw*T0 +
(-(hs*k*KT) + cp*(k + s))*V0)*xs*cosh((sqrt(rho)*sqrt(s)*sqrt(-(hs*k*KT) +
cp*(k + s))*xs)/(sqrt(lambda)*sqrt(k + s)))) + sqrt(lambda)*sqrt(k + s)*
(h*hs*k^2*Kp*KT*ms*Rw*T0 - rho*s*(-(hs*k*KT) + cp*(k + s))*(cp*k*Kp*ms*Rw*T0 +
(-(hs*k*KT) + cp*(k + s))*V0)*xs)* sinh((sqrt(rho)*sqrt(s)*sqrt(-(hs*k*KT) +
cp*(k + s))*xs)/(sqrt(lambda)*sqrt(k + s)))))
```

A.3 Derivation of Effective Heat Transfer Resistances

Effective heat transfer resistances related to area R^{A}, and adsorbent mass R^{m_s} are derived for different heat and mass transfer coefficients on different standard geometries as summarised in Table 2.

Lumped heat transfer

For the lumped heat transfer coefficient h, R_{h}^{A} is directly defined:

$$R_{h}^{A} = \frac{1}{h}. \tag{134}$$

On a macroscopic flat plate geometry, $R_{h}^{m_\mathrm{s}}$ is calculated with $V = dA$:

$$R_{h}^{m_\mathrm{s}} = R_{h}^{A} \frac{V \rho_\mathrm{eff}}{A} = \frac{d \rho_\mathrm{eff}}{h}, \tag{135}$$

where ρ_eff is the effective adsorbent density, i.e. the adsorbent mass per volume of the flat plate, which might include non-adsorbent volumes like macropores, a binder or additives.

Heat conduction

For a homogeneous uptake distribution on a flat plate geometry, also the heat released is homogeneous ($\Delta h_\mathrm{s} \dot{X}(x)$ = const.). The mean thermal path associated to the thermal conductivity λ is then $\frac{d}{3}$, thus

$$R_{\lambda}^{A} = \frac{d}{3\lambda}, \tag{136}$$

and with the same approach as above:

$$R_\lambda^{m_\mathrm{s}} = R_\lambda^A \frac{V\rho_\mathrm{eff}}{A} = \frac{d^2\rho_\mathrm{eff}}{3\lambda}. \tag{137}$$

Linear driving force

For a (locally) linear isotherm, the driving loading difference $\Delta X = X_\mathrm{eq}(T,p) - X$ can be converted to an equivalent driving temperature difference with the inverse slope of the isotherm. Combined with the LDF ansatz ($\dot{X} = k_\mathrm{LDF}\Delta X$), the driving temperature equivalent is

$$\begin{aligned} \Delta T &= \Delta X \left(\frac{\partial X}{\partial T}\right)^{-1} \\ &= \frac{\dot{X}}{k_\mathrm{LDF}\frac{\partial X}{\partial T}} \end{aligned} \tag{138}$$

The adsorption associated heat flow per unit area can be derived similar as before from the loading change for a flat plate geometry:

$$\frac{\dot{Q}}{A} = \frac{\dot{X}m_\mathrm{s}\Delta h_\mathrm{s}}{A} = \dot{X}d\rho_\mathrm{eff}\Delta h_\mathrm{s}. \tag{139}$$

Thus:

$$\begin{aligned} R_\mathrm{LDF}^A &= \frac{\dot{X}}{k_\mathrm{LDF}\frac{\partial X}{\partial T}} \cdot \frac{1}{\dot{X}d\rho_\mathrm{eff}\Delta h_\mathrm{s}} \\ &= \left(k_\mathrm{LDF}\frac{\partial X}{\partial T}d\rho_\mathrm{eff}\Delta h_\mathrm{s}\right)^{-1}, \end{aligned} \tag{140}$$

and with the same approach as above:

$$\begin{aligned} R_\mathrm{LDF}^{m_\mathrm{s}} &= R_\mathrm{LDF}^A d\rho_\mathrm{eff} \\ &= \left(k_\mathrm{LDF}\frac{\partial X}{\partial T}\Delta h_\mathrm{s}\right)^{-1}. \end{aligned} \tag{141}$$

Micropore diffusion on different geometries

Under the assumption of homogeneous uptake distribution and a quasi-isothermal process, the LDF approximation $D_\mathrm{mi} \approx k_\mathrm{LDF}r^2/[\sigma(\sigma+2)]$ (c.f. p43) may be applied to simplify the micropore diffusion. Here r is a length on the micro scale, as opposed to d, the thickness on the macro scale, and σ a curvature factor (1: flat plate, 2: cylinder, 3: sphere). Hence, based on the LDF solutions above:

$$R_{\mathrm{mi}}^{A} = \left(\frac{D_{\mathrm{mi}}}{r^2}\sigma(\sigma+2)\frac{\partial X}{\partial T}d\rho_{\mathrm{eff}}\Delta h_{\mathrm{s}}\right)^{-1}, \tag{142}$$

$$R_{\mathrm{mi}}^{m_{\mathrm{s}}} = \left(\frac{D_{\mathrm{mi}}}{r^2}\sigma(\sigma+2)\frac{\partial X}{\partial T}\Delta h_{\mathrm{s}}\right)^{-1}. \tag{143}$$

With the Darken equation Eq. (45) this becomes

$$\begin{aligned} R_{\mathrm{mi}}^{A} &= \left(\frac{D_{\mathrm{ad}}}{r^2\dfrac{\partial X}{\partial p}\dfrac{p}{X}}\sigma(\sigma+2)\frac{\partial X}{\partial T}d\rho_{\mathrm{eff}}\Delta h_{\mathrm{s}}\right)^{-1} \\ &= \left(\frac{D_{\mathrm{ad}}}{r^2}\ \sigma(\sigma+2)\frac{X}{p}\frac{\partial X}{\partial T}\left(\frac{\partial X}{\partial p}\right)^{-1} d\rho_{\mathrm{eff}}\Delta h_{\mathrm{s}}\right)^{-1}, \end{aligned} \tag{144}$$

and with the Clausius–Clapeyron equation Eq. (19):

$$\begin{aligned} R_{\mathrm{mi}}^{A} &= \left(\frac{D_{\mathrm{ad}}}{r^2}\ \sigma(\sigma+2)\frac{X}{p}\frac{\Delta h_{\mathrm{s}}p}{R_{\mathrm{w}}T^2}d\rho_{\mathrm{eff}}\Delta h_{\mathrm{s}}\right)^{-1} \\ &= \left(\frac{D_{\mathrm{ad}}}{r^2}\ \sigma(\sigma+2)Xd\rho_{\mathrm{eff}}\frac{\Delta h_{\mathrm{s}}^2}{R_{\mathrm{w}}T^2}\right)^{-1}, \end{aligned} \tag{145}$$

$$R_{\mathrm{mi}}^{m_{\mathrm{s}}} = \left(\frac{D_{\mathrm{ad}}}{r^2}\ \sigma(\sigma+2)X\frac{\Delta h_{\mathrm{s}}^2}{R_{\mathrm{w}}T^2}\right)^{-1}. \tag{146}$$

Note, that for all microscopic shapes (plate, cylinder, or sphere), the macroscopic shape is always a flat plate. The effective density ρ_{eff} accounts for the arrangement of the microscopic particles within this plate.

Macropore diffusion on a flat-plate geometry

Macropore diffusion can also be referred to the LDF approximation with the same principal assumptions as for micropore diffusion. The LDF form of macropore diffusion can be derived from the isothermal simplification of the Laplace transformed and loading substituted macropore diffusion equation Eq. (123), which can be rearranged to

$$
\begin{aligned}
s\frac{\tilde{X}(x)}{MR_\mathrm{w}T_0K_p} &= \frac{D_\mathrm{ma}}{MR_\mathrm{w}T_0K_p}\frac{\partial^2\tilde{X}(x)}{\partial x^2} - s\tilde{X}(x)\frac{\rho_\mathrm{eff}}{\varepsilon_\mathrm{P}M} \\
s\tilde{X}(x)\left(\frac{1}{MR_\mathrm{w}T_0K_p} + \frac{\rho_\mathrm{eff}}{\varepsilon_\mathrm{P}M}\right) &= \frac{D_\mathrm{ma}}{MR_\mathrm{w}T_0K_p}\frac{\partial^2\tilde{X}(x)}{\partial x^2} \\
s\tilde{X}(x)\left(1 + \frac{R_\mathrm{w}T_0K_p\rho_\mathrm{eff}}{\varepsilon_\mathrm{P}}\right) &= D_\mathrm{ma}\frac{\partial^2\tilde{X}(x)}{\partial x^2} \\
s\tilde{X}(x) &= D_\mathrm{ma}\left(1 + \frac{\rho_\mathrm{eff}R_\mathrm{w}T_0K_p}{\varepsilon_\mathrm{P}}\right)^{-1}\frac{\partial^2\tilde{X}(x)}{\partial x^2}.
\end{aligned}
\tag{147}
$$

This equation is equivalent to the micropore diffusion equation Eq. (115) with a differently scaled diffusivity. Applying this equivalence to the LDF approximation Eq. (49) under the same assumptions as for micropore diffusion yields:

$$
\begin{aligned}
k_\mathrm{LDF} &\approx \frac{D_\mathrm{ma}}{r^2}\frac{\sigma(\sigma+2)}{1 + \frac{\rho_\mathrm{eff}R_\mathrm{w}T_0}{\varepsilon_\mathrm{P}}\frac{\partial X}{\partial p}} \\
&\approx \frac{D_\mathrm{ma}}{r^2}\frac{\sigma(\sigma+2)}{\frac{\rho_\mathrm{eff}R_\mathrm{w}T_0}{\varepsilon_\mathrm{P}}\frac{\partial X}{\partial p}},
\end{aligned}
\tag{148}
$$

where r is the diffusion path length. It is assumed that $\rho_\mathrm{eff}R_\mathrm{w}T/\varepsilon_\mathrm{P}\cdot\partial X/\partial p \gg 1$, which is a very good approximation for the cases in the scope of this work (and for most heat transformation applications). For a globally linear sorption isotherm, i.e. $\partial X/\partial p = X_0/p_0$, and with the ideal gas law $R_\mathrm{w}MT = p/c$ this denominator becomes $(\rho_\mathrm{eff}X/M)/(\varepsilon_\mathrm{P}c)$, which is the form initially used by Glueckauf & Coates (1947).

The effective resistances can then be calculated as before, using again the Clausius–Clapeyron Equation:

$$
\begin{aligned}
R_\mathrm{ma}^{A} &= \left(\frac{D_\mathrm{ma}}{r^2}\frac{\sigma(\sigma+2)}{\frac{\rho_\mathrm{eff}R_\mathrm{w}T_0}{\varepsilon_\mathrm{P}}\frac{\partial X}{\partial p}}\frac{\partial X}{\partial T}d\rho_\mathrm{eff}\Delta h_\mathrm{s}\right)^{-1} \\
&= \left(\frac{D_\mathrm{ma}}{r^2}\frac{\sigma(\sigma+2)}{R_\mathrm{w}T}\frac{\Delta h_\mathrm{s}p}{R_\mathrm{w}T^2}\varepsilon_\mathrm{P}d\Delta h_\mathrm{s}\right)^{-1} \\
&= \left(\frac{D_\mathrm{ma}}{r^2}\sigma(\sigma+2)\varepsilon_\mathrm{P}d\frac{p}{T}\left(\frac{\Delta h_\mathrm{s}}{R_\mathrm{w}T}\right)^2\right)^{-1},
\end{aligned}
\tag{149}
$$

$$
R_\mathrm{ma}^{m_\mathrm{s}} = \left(\frac{D_\mathrm{ma}}{r^2}\sigma(\sigma+2)\frac{\varepsilon_\mathrm{P}p}{\rho_\mathrm{eff}T}\left(\frac{\Delta h_\mathrm{s}}{R_\mathrm{w}T}\right)^2\right)^{-1}.
\tag{150}
$$

Even if both lengths, the diffusion path length r and the layer thickness d, are both on the same macro scale they might differ. E.g., for a layer of spherical granules, r is the granule radius, d the layer thickness, ρ_eff accounts for the voids in the layer, and $\sigma = 3$. However, for the flat plate case, where $d = r$, and $\sigma = 1$, one may further simplify to

$$R_{\mathrm{ma}}^{A} = \left(\frac{3D_{\mathrm{ma}}}{d}\frac{\varepsilon_{\mathrm{P}}p}{T}\left(\frac{\Delta h_{\mathrm{s}}}{R_{\mathrm{w}}T}\right)^{2}\right)^{-1}, \tag{151}$$

$$R_{\mathrm{ma}}^{m_{\mathrm{s}}} = \left(\frac{3D_{\mathrm{ma}}}{d^{2}}\frac{\varepsilon_{\mathrm{P}}p}{\rho_{\mathrm{eff}}T}\left(\frac{\Delta h_{\mathrm{s}}}{R_{\mathrm{w}}T}\right)^{2}\right)^{-1}. \tag{152}$$

A.4 Temperature Dependency of the Char. Temperature Difference

The change of the characteristic temperature difference with respect to the adsorbent temperature is

$$\frac{\partial \Delta T_{\mathrm{ch}}}{\partial T_{\mathrm{s}}} \approx \frac{\Delta(\Delta T_{\mathrm{ch}})}{\Delta T_{\mathrm{s}}}. \tag{153}$$

The equilibrium pressure $p_{\mathrm{eq}}(T^{*},X)$ of an adsorbent, where ideal gas behaviour may be assumed for the adsorptive, changes according to the integrated Clausius–Clapeyron equation Eq. (17):

$$\ln\frac{p_{\mathrm{eq}}(T_1^{*},X)}{p_{\mathrm{eq}}(T_2^{*},X)} = \frac{\Delta h_{\mathrm{s}}}{R_{\mathrm{w}}}\left(\frac{1}{T_2^{*}} - \frac{1}{T_1^{*}}\right), \tag{154}$$

The same applies to the saturation pressure $p_{\mathrm{sat}}(T')$ of the pure working fluid:

$$\ln\frac{p_{\mathrm{sat}}(T_1')}{p_{\mathrm{sat}}(T_2')} = \frac{\Delta h_{\mathrm{v}}}{R_{\mathrm{w}}}\left(\frac{1}{T_2'} - \frac{1}{T_1'}\right). \tag{155}$$

The characteristic temperature differences are $\Delta T_{\mathrm{ch1}} = T_1^{*} - T_1'$ and $\Delta T_{\mathrm{ch2}} = T_2^{*} - T_2'$. From the definition of ΔT_{ch} the pressure $p_{\mathrm{sat}}(T')$ and $p_{\mathrm{eq}}(T^{*},X)$ are equal. Thus, the exact change in ΔT_{ch} is given implicitly by

$$\Delta h_{\mathrm{s}}\left(\frac{1}{T_2^{*}} - \frac{1}{T_1^{*}}\right) = \Delta h_{\mathrm{v}}\left(\frac{1}{T_2'} - \frac{1}{T_1'}\right). \tag{156}$$

In order to yield an explicit approximation, a 2nd order Taylor expansion of the inverse function

$$\begin{aligned}\frac{1}{T_1+\Delta T} &\approx \frac{1}{T_1}-\frac{\Delta T}{T_1^2}\\ &=\frac{T_1-\Delta T}{T_1^2}\end{aligned} \tag{157}$$

can be employed. With $T_2 = T_1 + \Delta T$, this allows rewriting Eq. (156) to

$$\begin{aligned}\Delta h_\mathrm{s}\left(\frac{T_1^*-\Delta T^*}{{T_1^*}^2}-\frac{1}{T_1^*}\right) &\approx \Delta h_\mathrm{v}\left(\frac{T_1'-\Delta T'}{{T_1'}^2}-\frac{1}{T_1'}\right)\\ \Delta h_\mathrm{s}\left(\frac{1}{T_1^*}-\frac{\Delta T^*}{{T_1^*}^2}-\frac{1}{T_1^*}\right) &\approx \Delta h_\mathrm{v}\left(\frac{1}{T_1'}-\frac{\Delta T'}{{T_1'}^2}-\frac{1}{T_1'}\right)\\ \Delta h_\mathrm{s}\frac{\Delta T^*}{{T_1^*}^2} &\approx \Delta h_\mathrm{v}\frac{\Delta T'}{{T_1'}^2}\\ \Delta T' &\approx \frac{\Delta h_\mathrm{s}}{\Delta h_\mathrm{v}}\left(\frac{T_1'}{T_1^*}\right)^2\Delta T^*.\end{aligned} \tag{158}$$

The change in ΔT_ch is

$$\begin{aligned}\Delta(\Delta T_\mathrm{ch}) &= \Delta T_\mathrm{ch,2}-\Delta T_\mathrm{ch,1}\\ &= T_2^*-T_2'-(T_1^*-T_1')\\ &= \Delta T^*-\Delta T',\end{aligned} \tag{159}$$

which finally yields the required temperature dependency with $T_\mathrm{s} = T^*$:

$$\begin{aligned}\frac{\partial \Delta T_\mathrm{ch}}{\partial T_\mathrm{s}} &\approx \frac{\Delta(\Delta T_\mathrm{ch})}{\Delta T^*}\\ &= \frac{\Delta T^*-\Delta T'}{\Delta T^*}\\ &= 1-\frac{\Delta T'}{\Delta T^*}\\ &= 1-\frac{\Delta h_\mathrm{s}}{\Delta h_\mathrm{v}}\left(\frac{T'}{T^*}\right)^2\\ &= 1-\frac{\Delta h_\mathrm{s}}{\Delta h_\mathrm{v}}\left(\frac{T^*-\Delta T_\mathrm{ch}}{T^*}\right)^2\\ &= 1-\frac{\Delta h_\mathrm{s}}{\Delta h_\mathrm{v}}\left(1-\frac{\Delta T_\mathrm{ch}}{T_\mathrm{s}}\right)^2.\end{aligned} \tag{160}$$

A.5 Particle Size Distribution of Aluminium Fumarate

Particle sizes were measured by laser diffraction analysis using a Beckman Coulter LS 13 320® on samples dispersed in water.

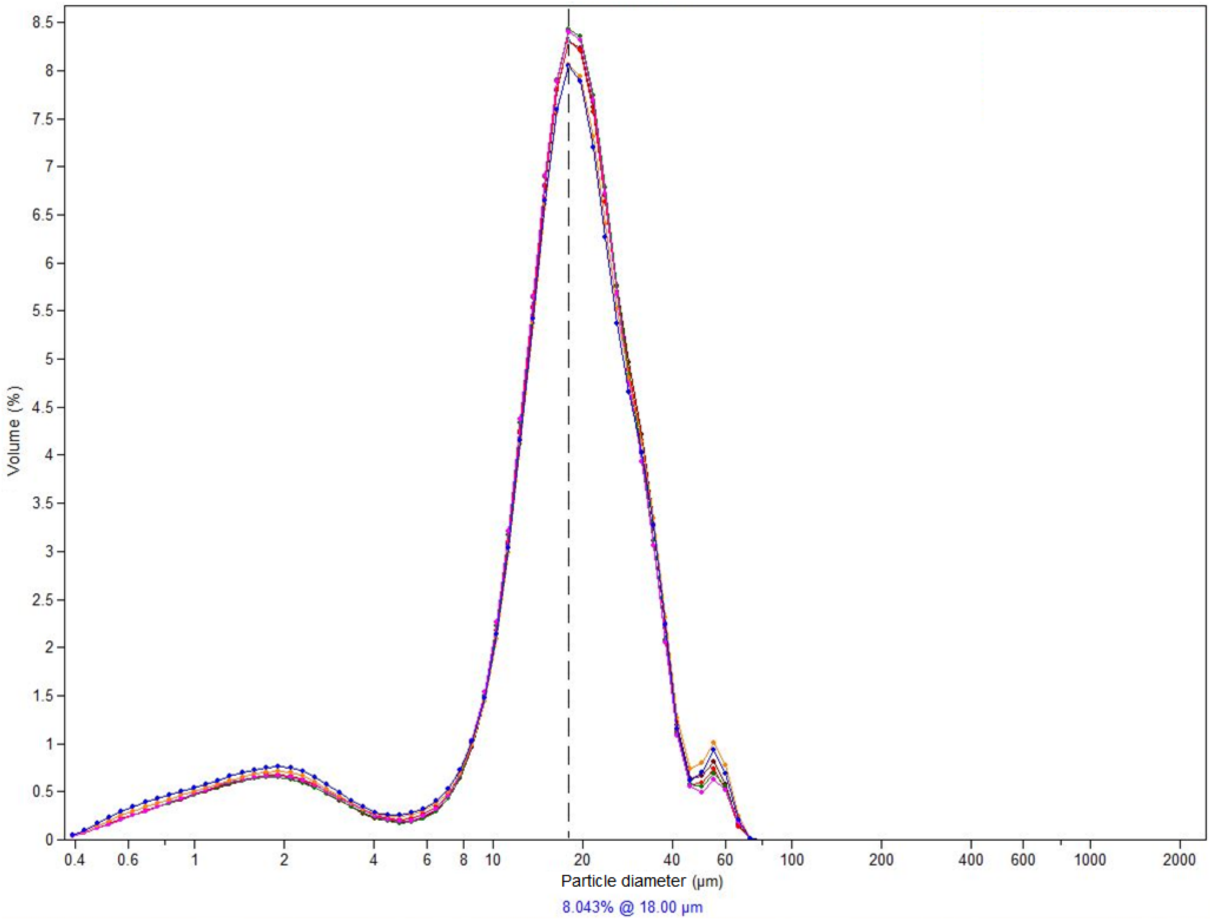

Figure 48: Particle size distribution of the initial adsorbent powder measured for different samples drawn

A.6 Exponential Drift Correction

The measurement pressure signal might be overlaid by a slow exponential decline that can be observed after filling the evacuated chamber with water vapour regardless of whether a sample is installed or not. The measured pressure is the sum of the equilibrium pressure p_0 and this background signal, that starts at time t_0 with a pressure Δp and attenuates with the time constant τ:

$$p(t) = p_0 + \Delta p e^{-\frac{(t-t_0)}{\tau}}. \tag{161}$$

For the correction of the small jump measurements (4.2.2.2) it can be assumed that the background drift is not affected by the small jumps. From the measurement, the value and slope are known at t_1 (p_1, p_1') and t_2 (p_1, p_2') and the corrected (extrapolated) pressures at an intermediate time $p_1(t_\mathrm{m})$ and $p_2(t_\mathrm{m})$ are needed.

For this correction the actual values of t_0 and Δp are not required so Eq. (161) can be reduced to

$$\begin{aligned} p(t) &= p_0 + \Delta p e^{\frac{t_0}{\tau}} e^{-\frac{t}{\tau}} \\ &= p_0 + a e^{-\frac{t}{\tau}}. \end{aligned} \tag{162}$$

This yields for the slope

$$p'(t) = -\frac{a}{\tau} e^{-\frac{t}{\tau}} \tag{163}$$

which can be used to set up a system of two equation with $p'(t_1)$, $p'(t_2)$ to solve for τ and a:

$$\tau = \frac{t_2 - t_1}{\ln\left(\frac{p'(t_1)}{p'(t_2)}\right)} \qquad\qquad a = -p'(t_1)\tau e^{\frac{t_1}{\tau}} \tag{164}$$

The extrapolated value for p_1 (where $p_1(t_1)$ is known) is then

$$p_1(t_\mathrm{m}) = p_1(t_1) + a\left(e^{-\frac{t_\mathrm{m}}{\tau}} - e^{-\frac{t_1}{\tau}}\right). \tag{165}$$

For the jump-free baseline signal the extrapolation follows exactly the signal:

$$\begin{aligned} p_1(t_\mathrm{m}) &= \left(p_0 + a e^{-\frac{t_1}{\tau}}\right) + a\left(e^{-\frac{t_\mathrm{m}}{\tau}} - e^{-\frac{t_1}{\tau}}\right) \\ &= p_0 + a e^{-\frac{t_\mathrm{m}}{\tau}} \end{aligned} \tag{166}$$

and both extrapolations $p_1(t_\mathrm{m}) = p_2(t_\mathrm{m})$ match as expected.

A.7 Empty Chamber Pressure Correction Factor

The empty chamber pressure correction factor ψ can be deduced based on Eq. (101) in the Laplace domain

$$\tilde{m}_\mathrm{err,cal} = \frac{\tilde{p}_\mathrm{cal} V_0 + \tilde{V} p_0}{R_\mathrm{w} T_0}, \tag{167}$$

with the complex mass balance error and the pressure response of the calibration experiments $\tilde{m}_\mathrm{err,cal}$ and $\tilde{p}_\mathrm{cal}$. The expected mass balance error of a measurement at same T_0, p_0, V_0 and $\tilde{V}$ follows as

$$\tilde{m}_{\mathrm{err,msr}} = \tilde{m}_{\mathrm{err,cal}} \frac{\tilde{p}_{\mathrm{msr}}}{\tilde{p}_{\mathrm{cal}}} \tag{168}$$

taking into account the assumed linear dependency on the pressure response. To deduce the corrected pressure signal $\tilde{p}_{\mathrm{cor}}$, the overall mass balance of the corrected measurement can be defined analogously to Eq. (101) as

$$0 = \mathrm{d}m_{\mathrm{w,g,cor}} + \mathrm{d}m_{\mathrm{w,s}}. \tag{169}$$

Hence:

$$\begin{aligned}
\mathrm{d}m_{\mathrm{w,g,cor}} &= \mathrm{d}m_{\mathrm{w,g}} - \mathrm{d}m_{\mathrm{err,msr}} \\
\frac{\mathrm{d}(pV)_{\mathrm{cor}}}{R_{\mathrm{w}}T_0} &= \frac{\mathrm{d}(pV)_{\mathrm{msr}}}{R_{\mathrm{w}}T_0} - \mathrm{d}m_{\mathrm{err,msr}} \\
\frac{\tilde{p}_{\mathrm{cor}}V_0 + \tilde{V}p_0}{R_{\mathrm{w}}T_0} &= \frac{\tilde{p}_{\mathrm{msr}}V_0 + \tilde{V}p_0}{R_{\mathrm{w}}T_0} - \tilde{m}_{\mathrm{err,cal}}\frac{\tilde{p}_{\mathrm{msr}}}{\tilde{p}_{\mathrm{cal}}} \\
\frac{\tilde{p}_{\mathrm{cor}}V_0 + \tilde{V}p_0}{R_{\mathrm{w}}T_0} &= \frac{\tilde{p}_{\mathrm{msr}}V_0 + \tilde{V}p_0}{R_{\mathrm{w}}T_0} - \frac{\tilde{p}_{\mathrm{cal}}V_0 + \tilde{V}p_0}{R_{\mathrm{w}}T_0}\frac{\tilde{p}_{\mathrm{msr}}}{\tilde{p}_{\mathrm{cal}}} \\
\tilde{p}_{\mathrm{cor}}V_0 &= \tilde{p}_{\mathrm{msr}}V_0 - \left(\tilde{p}_{\mathrm{cal}}V_0 + \tilde{V}p_0\right)\frac{\tilde{p}_{\mathrm{msr}}}{\tilde{p}_{\mathrm{cal}}} \\
\tilde{p}_{\mathrm{cor}} &= \tilde{p}_{\mathrm{msr}} - \left(\tilde{p}_{\mathrm{cal}} + \frac{\tilde{V}}{V_0}p_0\right)\frac{\tilde{p}_{\mathrm{msr}}}{\tilde{p}_{\mathrm{cal}}} \\
\tilde{p}_{\mathrm{cor}} &= \tilde{p}_{\mathrm{msr}} - \tilde{p}_{\mathrm{cal}}\frac{\tilde{p}_{\mathrm{msr}}}{\tilde{p}_{\mathrm{cal}}} - \frac{\tilde{V}}{V_0}p_0\frac{\tilde{p}_{\mathrm{msr}}}{\tilde{p}_{\mathrm{cal}}} \\
\tilde{p}_{\mathrm{cor}} &= -\frac{\tilde{V}}{V_0}\frac{p_0}{\tilde{p}_{\mathrm{cal}}}\tilde{p}_{\mathrm{msr}} \\
\tilde{p}_{\mathrm{cor}} &= \psi\tilde{p}_{\mathrm{msr}}.
\end{aligned} \tag{170}$$

As the deviation of $\tilde{p}_{\mathrm{cal}}$ from the ideal pressure response $-p_0\tilde{V}/V_0$ is small, $\mathrm{Re}(\psi) \approx 1$ and $\mathrm{Im}(\psi) \approx 0$.

The fit and data pre-treatment of $\psi = f(T_0, p_0, f_{\mathrm{blw}})$ were performed separately for real and imaginary part as the kriging model only handles real numbers. The observed values of each part where scaled with the respective range and centred to the mean (real part only) to improve the numerical performance of the fit. Noise (0.1% of the respective range) was introduced to avoid problematic oscillations between the data points that are otherwise typical for the cubic spline interpolation underlying the kriging model.

The fit result in Figure 49 and Figure 50 shows very good agreement to the data with a realistic shape between data points. The slight deviations at the outer edges of the dataset (e.g. 0.001 Hz, 30 °C, 0.04 mbar/mbar) as a results from the noise introduced are a necessary evil to avoid oscillation.

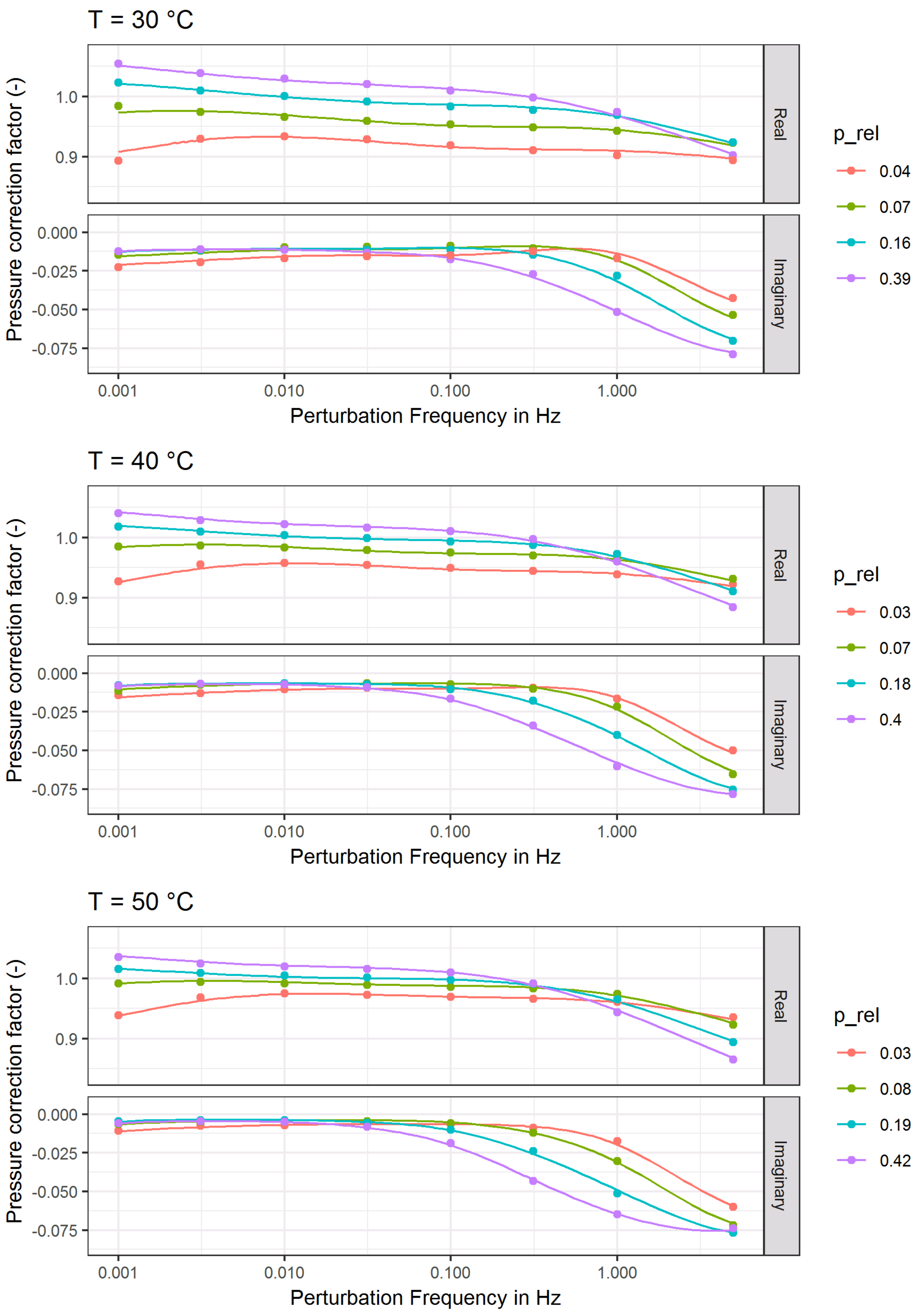

Figure 49: Pressure correction factor ψ over frequency from measurements (dots) and multivariate kriging model (lines) for different temperatures and relative pressures, showing smooth and realistic (oscillation free) interpolation between data points

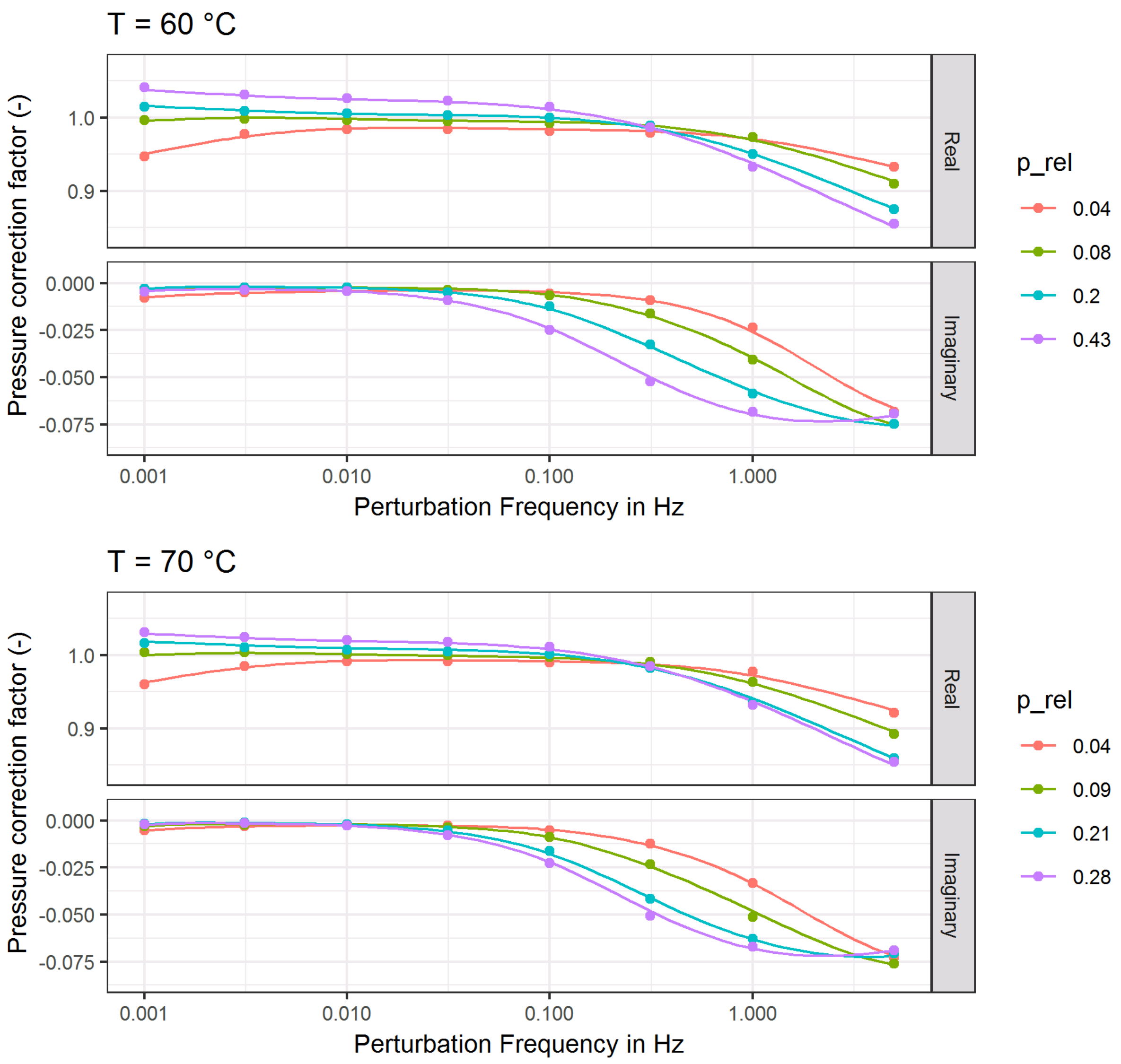

Figure 49: (continued)

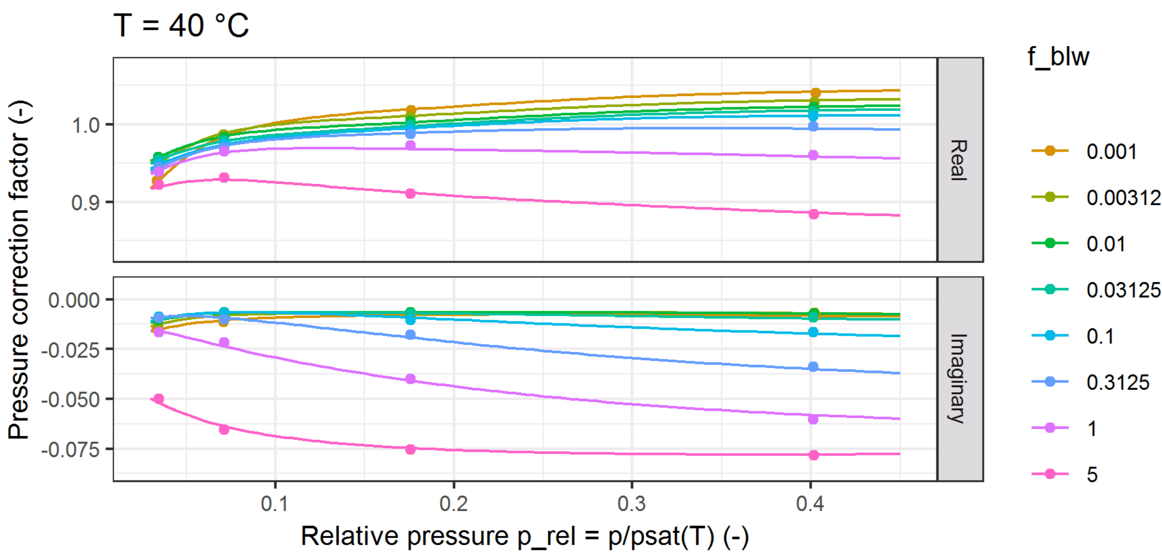

Figure 50: Pressure correction factor ψ over relative pressure for different bellow frequencies f_{blw} (in Hz) and constant temperature of 40 °C showing smooth and realistic (oscillation free) interpolation between data points

A.8 “Characteristic Curve” of Aluminium Fumarate

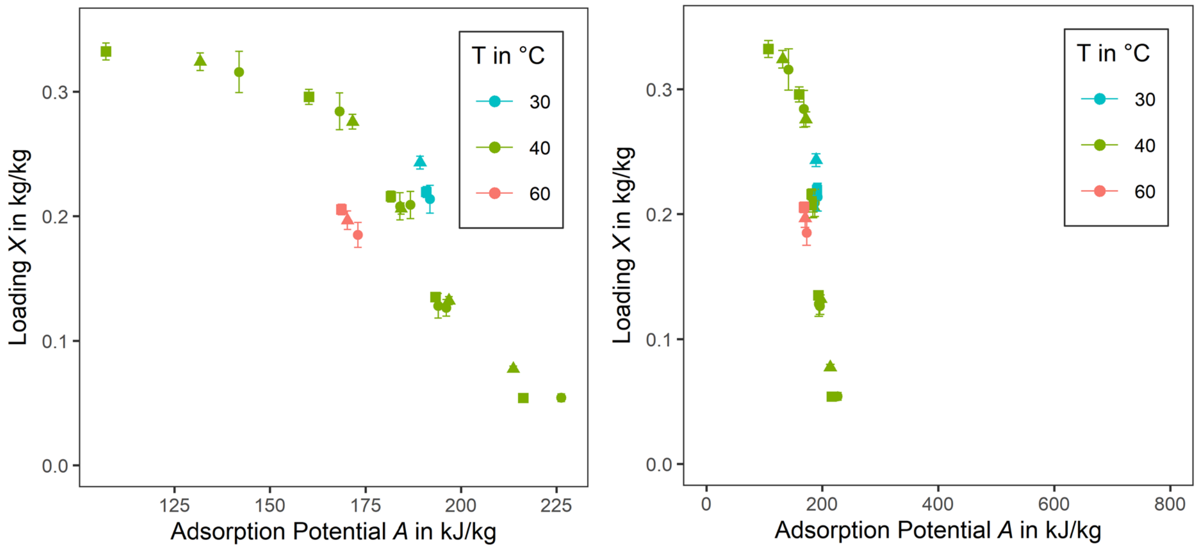

Figure 51: Loading over adsorption potential calculated with the data from Figure 27, presented for two different limits of the A-axis, left: data-tied limits, right: limits as typically used in literature (e.g., Ammann *et al.*, 2019); the violation of the temperature invariance assumption is only visible in the presentation on the left hand side

Figure 51 shows the equilibrium data obtained from FR measurements for Alfum in a plot, typically used for characteristic curves (c.f. p26). As the density of the adsorbate and, especially, its temperature dependency are unknown, the loading $X(A)$ is presented instead of a somehow approximated adsorbate volume $W(A)$. Anyhow, the temperature effect on the density in the small temperature region of 30–60 °C would be small, so that the W-points relative position would literally be the same.

While the same data is presented in both plots, only the higher resolution on the left hand side reveals that the data is not temperature-invariant, and thus, no characteristic curve may be given for aluminium fumarate.

A.9 Additional Parameter Identification Results

The results given in the following are additions to Sections 5.4.1 and 5.4.2.

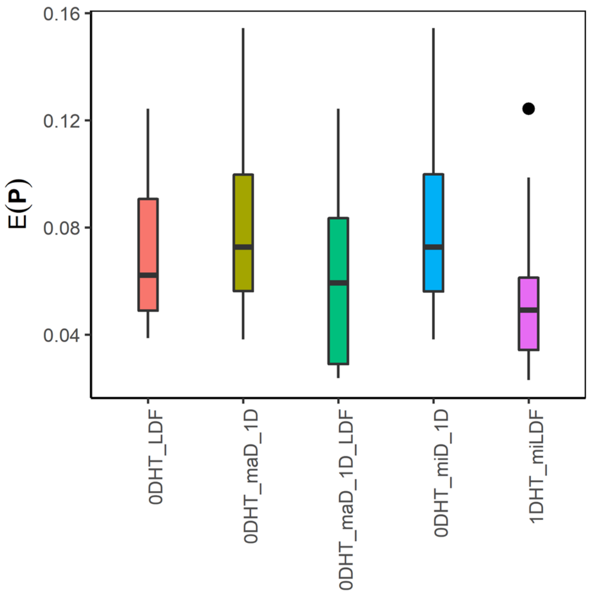

Figure 52: Boxplot of the residual relative error $E(\widehat{\boldsymbol{P}})$ for different models used over all measurement points

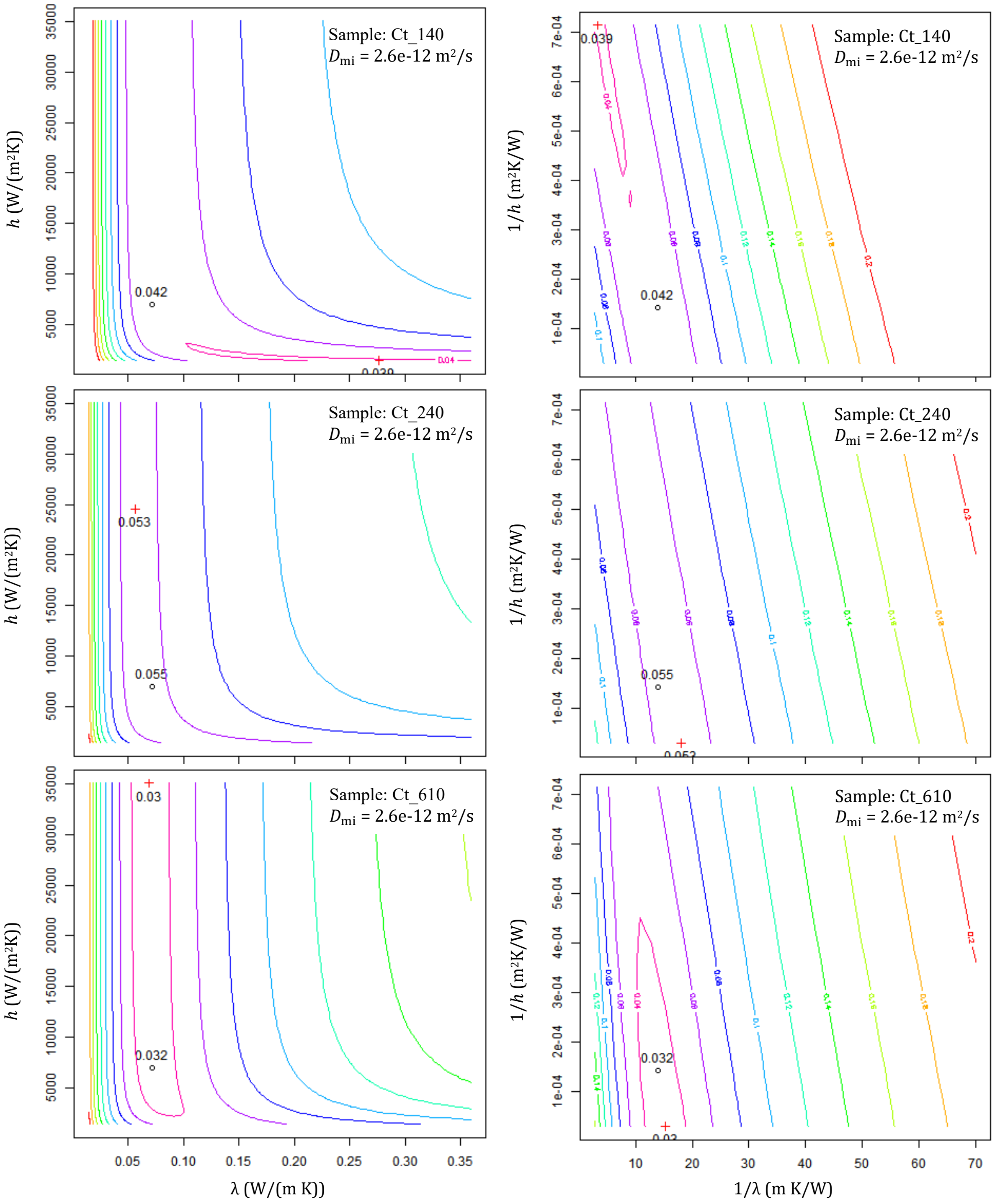

Figure 53: Contour plots of $E(P)$ for individual samples at conditions as in Figure 37 over parameters $\boldsymbol{h}$ and $\boldsymbol{\lambda}$ (left) and their reciprocal values (right) for the same parameter range, open circle: best estimate as returned from the fitting algorithm for the multi fit, red cross: minimum of $\boldsymbol{E}(\boldsymbol{P})$ found by parameter variation for these plots. Lines in increments of 0.02. Parameters varied by factors of [0.2, 5] around the multi fit best estimate.

A.10 Parametrization Used for Non-Linear Alfum Modelling

Table 11: Parametrization for non-linear LTJ simulation of coated aluminium fumarate samples

Initial conditions	As measured
Temperature of the cold plate	As measured
Heat capacity	$c_{p_\mathrm{eff}} \Big/ \frac{\mathrm{kJ}}{\mathrm{kg_{cmp,dry}}} = c_{p0} + \left(\frac{T}{\mathrm{K}} - 298.15\right)\frac{\mathrm{d}c_{p0}}{\mathrm{d}T}$ $+ X_\mathrm{eff}\left(c_{pa0} + \left(\frac{T}{\mathrm{K}} - 298.15\right)\frac{\mathrm{d}c_{pa}}{\mathrm{d}T} + X_\mathrm{eff}\frac{\mathrm{d}c_{pa}}{\mathrm{d}X_\mathrm{eff}}\right)$ c_{p0}: 1.0766888 $\frac{\mathrm{d}c_{p0}}{\mathrm{d}T}$: 0.0024788 c_{pa0}: 5.8137812 $\frac{\mathrm{d}c_{pa}}{\mathrm{d}T}$: 0.0270763 $\frac{\mathrm{d}c_{pa}}{\mathrm{d}X_\mathrm{eff}}$: -7.1141313
Thermal conductivity	0.07 W/mK (constant)
Thermal contact resistance	0 $\mathrm{m^2K/W}$
Adsorption enthalpy	51.2 kJ/mol (constant)
Equilibrium loading	As detailed below
LDF coefficient	$k_\mathrm{LDF}(X_\mathrm{eff}, T) = k_{\mathrm{LDF,40^\circ C}}(X_\mathrm{eff}) \cdot \exp\left(-\frac{E_\mathrm{a}}{R}\left[\frac{1}{T}-\frac{1}{313.15\ \mathrm{K}}\right]\right)$ $k_{\mathrm{LDF,40^\circ C}}(X_\mathrm{eff}) \Big/ \frac{1}{\mathrm{s}} = 1.87 + 35.4 \cdot X_\mathrm{eff} + 151 \cdot X_\mathrm{eff}^2$ E_a: 66.8 kJ/mol (c.f. Section 5.3.3)

In order to calculate X for any T and p, the Clausius– Clapeyron approach for the isostere was used to calculate the pressure $p_{40^\circ\mathrm{C}}$ at 40 °C on the same isostere:

$$\ln p_{40^\circ\mathrm{C}}(X) = \ln p(X) - \frac{\Delta h_\mathrm{s}}{R}\left(\frac{1}{313.15\ \mathrm{K}} - \frac{1}{T}\right). \qquad (171)$$

With $p_\mathrm{rel} = p_{40^\circ\mathrm{C}}/p_\mathrm{sat}(40\ ^\circ\mathrm{C})$ the loading X can then be looked up in Table 12. The adsorption enthalpy is assumed constant with a value of 51.2 kJ/mol (c.f. Section 5.2).

Table 12: Values of the 40 °C isotherm as used for LTJ simulations: interpolated from uptake results of all coated samples relative to the total coating dry mass (c.f. Figure 27, left panel, p95)

p_{rel} (-)	X_{eff} (g/g_{cmp})	p_{rel} (cont.)	X_{eff} (cont.)	p_{rel} (cont.)	X_{eff} (cont.)
0	0	0.17	0.03328	0.34	0.24247
0.01	0.00200	0.18	0.03513	0.35	0.24550
0.02	0.00400	0.19	0.03698	0.36	0.24745
0.03	0.00600	0.2	0.03880	0.37	0.24882
0.04	0.00800	0.21	0.04060	0.38	0.25010
0.05	0.00999	0.22	0.04325	0.39	0.25148
0.06	0.01198	0.23	0.04982	0.4	0.25297
0.07	0.01396	0.24	0.06210	0.41	0.25455
0.08	0.01594	0.25	0.08067	0.42	0.25621
0.09	0.01791	0.26	0.10608	0.43	0.25793
0.1	0.01987	0.27	0.13797	0.44	0.25971
0.11	0.02182	0.28	0.16640	0.45	0.26153
0.12	0.02376	0.29	0.18856	0.46	0.26339
0.13	0.02569	0.3	0.20681	0.47	0.26526
0.14	0.02761	0.31	0.22102	0.48	0.26714
0.15	0.02951	0.32	0.23109	0.49	0.26902
0.16	0.03140	0.33	0.23787	0.5	0.27090

A.11 Example Heat Exchanger Properties

Table 13: Principal parameters of Ad-HX designs derived from measured coating samples

Quantity	Unit	Value[viii]			Comment
Mass additional copper	kg	0.17			Wittstadt, 2018
Mass finned copper tubes	kg	0.34			Wittstadt, 2018
Mass aluminium per fin	kg	0.00488			Wittstadt, 2018
Overall HX volume	l	5.2			Wittstadt, 2018
Finned tube length	mm	255			Wittstadt, 2018
Fin thickness	mm	0.2			Wittstadt, 2018
Width free vapour channel	mm	2			Assumption
Area per fin	m^2	0.0173			Wittstadt, 2018
Coating thickness	mm	0.14	0.24	0.61	c.f. Table 4
Fin spacing	mm	2.48	2.68	3.42	Calculated
Number of fins	-	103	95	75	Calculated
Mass aluminium	kg	0.501	0.464	0.363	Calculated
Coating volume	l	0.249	0.395	0.787	Calculated
Coating mass	kg	0.127	0.190	0.386	Calculated[ix]
Adsorbent mass	kg	0.092	0.150	0.309	Calculated[ix]
HX area	m^2	1.78	1.65	1.29	Calculated
HX area per total HX volume	m^2/l	0.342	0.317	0.248	Calculated
Adsorbent mass per HX area	kg/m^2	0.051	0.091	0.239	Calculated
Total heat capacity	kJ/K	0.93	1.04	1.40	Calculated[x]
Heat capacity per adsorbent mass	kJ/(kg K)	10.2	7.0	4.5	Calculated
Heat capacity per HX area	kJ/(m^2 K)	0.52	0.63	1.08	Calculated

---

[viii] Single values are equal for all three designs

[ix] Based on measured coating density and adsorbent content (c.f. Table 4)

[x] With constant specific heat capacities: aluminium: 0.90 kJ/(kg K); copper: 0.38 kJ/(kg K); coating: 2.27 kJ/(kg K)

A.12 Expected VSCP of a Silical Gel Granular Bed Ad-HX

For comparison to the expected values for the Alfum coating, the results of state-of-the-art silica gel granular beds, as reported by Ammann *et al.* (2018), are used for the same calculation. Ammann et al. investigated mono- and bilayers of two differently sized silica gel granules with average diameters of 1.3 and 1.9 mm. The monolayer of the smaller granules and the bilayer of the larger granules were the best and worst performing configuration with effective thermal resistances R_{eff}^{A} of 10 and 20 (m^2 K)/kW, respectively. For the estimation of the VSCP, the same assumptions for the Ad-HX are made, as for the Alfum coating (c.f. Section 5.5.2 and Appendix A.11). This implicitly includes the optimistic assumption that the granular layers may be evenly distributed on all sides of the fins leaving an open vapour channel between the fins, knowing that this will be practically challenging.

Table 14: Assumed configuration of silica gel Ad-HXs

Quantity	**Unit**	**Value**	
Configuration	-	Monolayer small	Bilayer large
Bed thickness (Ammann *et al.*, 2018)	mm	1.3	3.2
Fin spacing	mm	4.8	8.7
Number of fins	-	53	29
Mass aluminium	kg	0.260	0.143
Bed volume	l	0.119	0.165
Bed mass	kg	n.a.	n.a.
Adsorbent mass	kg	n.a.	n.a.
HX area	m^2	0.92	0.51
HX area per total HX volume	m^2/l	0.18	0.10

Table 15: Estimated performance of silica gel Ad-HXs based on effective thermal resistances

Cycle conditions		**Variant A**		**Variant B**	
Temperature lift ΔT_{lft}	K	15		10	
Temperature thrust ΔT_{thr}	K	30		30	
Bed thickness	**µm**	**1300**	**3200**	**1300**	**3200**
Eff. driving temp. difference ΔT_{drv}	K	7.5		12.5	
Effective thermal resistance R_{eff}^{A}	(m^2 K)/kW	10	20	10	20
Adsorption power per coated area[xi]	kW/m^2	0.8	0.4	1.3	0.6
Relative adsorption half-cycle duration	-	0.5		0.4	
Cooling power per coated area[xii]	kW/m^2	0.3	0.2	0.4	0.2
Coated area per overall-volume	m^2/l	0.18	0.1	0.18	0.1
Volume specific cooling power (VSCP)	**kW/l**	**0.06**	**0.02**	**0.08**	**0.02**

The heat exchanger area-to-volume-ratio calculated (Table 14) can be combined with R_{eff}^{A} and the driving temperature differences for Variant A and Variant B. In a first approximation, the same driving temperature differences are assumed, as they are

---

[xi] Per coated area, averaged over the adsorption half-cycle

[xii] Per coated area, averaged over the complete cycle

primarily dependent on the external temperature differences. This yields, with the same approach as shown in Table 10, VSCP in the range of 0.02–0.08 kW/l (Table 15).

The analysis of the COP is omitted here, as it would require additional data on the adsorption equilibrium. While the better metal-to-adsorbent mass ratio would indicate a COP increase compared to the Alfum coated Ad-HXs, the lower uptake due to the linear isotherm of silica gel would indicate a decrease.

References

Alvarez E., Guillou N., Martineau C., Bueken B., Van de Voorde B., Le Guillouzer C., Fabry P., Nouar F., Taulelle F., de Vos D., Chang J.-S., Cho K.H., Ramsahye N., Devic T., Daturi M., Maurin G. & Serre C. (2015) The Structure of the Aluminum Fumarate Metal-Organic Framework A520. *Angewandte Chemie International Edition,* **54,** 3664–3668. DOI: 10.1002/anie.201410459.

Ammann J., Michel B. & Ruch P.W. (2019) Characterization of transport limitations in SAPO-34 adsorbent coatings for adsorption heat pumps. *International Journal of Heat and Mass Transfer,* **129,** 18–27. DOI: 10.1016/j.ijheatmasstransfer.2018.09.053.

Ammann J., Ruch P., Michel B. & Studart A.R. (2018) Quantification of heat and mass transport limitations in adsorption heat exchangers: Application to the silica gel/water working pair. *International Journal of Heat and Mass Transfer,* **123,** 331–341. DOI: 10.1016/j.ijheatmasstransfer.2018.02.076.

Aristov Y., Dawoud B., Glaznev I.S. & Elyas A. (2008) A new methodology of studying the dynamics of water sorption/desorption under real operating conditions of adsorption heat pumps: Experiment. *International Journal of Heat and Mass Transfer,* **51,** 4966–4972. DOI: 10.1016/j.ijheatmasstransfer.2007.10.042.

Aristov Y.I. (2012) Adsorptive transformation of heat: Principles of construction of adsorbents database. *Applied Thermal Engineering,* **42,** 18–24. DOI: 10.1016/j.applthermaleng.2011.02.024.

Aristov Y.I. (2013) Challenging offers of material science for adsorption heat transformation: A review. *Applied Thermal Engineering,* **50,** 1610–1618. DOI: 10.1016/j.applthermaleng.2011.09.003.

Aristov Y.I. (2017a) Adsorptive transformation and storage of renewable heat: Review of current trends in adsorption dynamics. *Renewable Energy,* **110,** 105–114. DOI: 10.1016/j.renene.2016.06.055.

Aristov Y.I. (2017b) Adsorptive transformation of ambient heat: A new cycle. *Applied Thermal Engineering,* **124,** 521–524. DOI: 10.1016/j.applthermaleng.2017.06.051.

Aristov Y.I. (2020) Dynamics of adsorptive heat conversion systems: Review of basics and recent advances. *Energy,* **205. DOI:** 10.1016/j.energy.2020.117998.

Aristov Y.I., Kovalevskaya Y.A., Tokarev M.M. & Paukov I.E. (2011) Low temperature heat capacity of the system "silica gel–calcium chloride–water". *Journal of Thermal Analysis and Calorimetry,* **103,** 773–778. DOI: 10.1007/s10973-010-0981-8.

Aristov Y.I., Tokarev M.M., Cacciola G. & Restuccia G. (1997) Heat Capacity and Heat Conductivity of Aqueous Solutions of Calcium Chloride in Silica Gel Pores. *Russ. J. Phys. Chem,* **71,** 327–330.

Baehr H.D. & Kabelac S. (2009) *Thermodynamik: Grundlagen und technische Anwendungen.* Springer, Berlin, Heidelberg.

Barrer R.M. & Fender B. (1961) The diffusion and sorption of water in zeolites—II. Intrinsic and self-diffusion. *Journal of Physics and Chemistry of Solids,* **21,** 12–24. DOI: 10.1016/0022-3697(61)90207-4.

Bathen D. & Breitbach M. (2001) *Adsorptionstechnik.* Springer, Berlin, Heidelberg.

Bläker C., Luckas M., Pasel C., Dreisbach F. & Bathen D. (2016) Entwicklung eines Messgeräts zur Kopplung von kalorimetrischen und volumetrischen Sorptionsmessungen. *Chemie Ingenieur Technik,* **88,** 282–290. DOI: 10.1002/cite.201500142.

Bläker C., Pasel C., Luckas M., Dreisbach F. & Bathen D. (2017) Investigation of load-dependent heat of adsorption of alkanes and alkenes on zeolites and activated carbon. *Microporous and Mesoporous Materials,* **241,** 1–10. DOI: 10.1016/j.micromeso.2016.12.037.

Bohn C. & Unbehauen H. (2016) *Identifikation dynamischer Systeme: Methoden zur experimentellen Modellbildung aus Messdaten.* Springer Vieweg, Wiesbaden.

Bourdin V., Germanus A., Grenier P. & Kärger J. (1996a) Application of the thermal frequency response method and of pulsed field gradient NMR to study water diffusion in zeolite NaX. *Adsorption,* **2,** 205–216. DOI: 10.1007/BF00128302.

Bourdin V., Gray P.G., Grenier P. & Terrier M.F. (1998) An apparatus for adsorption dynamics studies using infrared measurement of the adsorbent temperature. *Review of Scientific Instruments,* **69,** 2130–2136. DOI: 10.1063/1.1148911.

Bourdin V., Grenier P., Meunier F. & Sun L.M. (1996b) Thermal frequency response method for the study of mass-transfer kinetics in adsorbents. *AIChE Journal,* **42,** 700–712. DOI: 10.1002/aic.690420311.

Brancato V., Frazzica A., Sapienza A., Gordeeva L. & Freni A. (2015) Ethanol adsorption onto carbonaceous and composite adsorbents for adsorptive cooling system. *Energy,* **84,** 177–185. DOI: 10.1016/j.energy.2015.02.077.

Brunauer S., Emmett P.H. & Teller E. (1938) Adsorption of Gases in Multimolecular Layers. *Journal of the American Chemical Society,* **60,** 309–319. DOI: 10.1021/ja01269a023.

Buckingham E. (1914) On Physically Similar Systems; Illustrations of the Use of Dimensional Equations. *Physical Review,* **4,** 345–376. DOI: 10.1103/PhysRev.4.345.

Cacciola G., Maggio G. & Restuccia G. (1998) Misura della capacità termica di adsorbenti e calcolo delle prestazioni di pompe di calore ad adsorbimento. *La Termotecnica,* **Aprile 1998,** 67–72.

Cahill D.G. & Pohl R.O. (1987) Thermal conductivity of amorphous solids above the plateau. *Physical review. B, Condensed matter,* **35,** 4067–4073. DOI: 10.1103/physrevb.35.4067.

Calvet E. & Prat H. (1963) *Recent Progress in Microcalorimetry.* Elsevier Science, Burlington.

Chambers J.M. & Hastie T.J., editors (1992) *Statistical Models in S.* Wadsworth & Brooks/Cole, Pacific Grove, California.

Chmelik C., Hibbe F., Tzoulaki D., Heinke L., Caro J., Li J. & Kärger J. (2010) Exploring the nature of surface barriers on MOF Zn(tbip) by applying IR microscopy in high temporal and spatial resolution. *Microporous and Mesoporous Materials,* **129,** 340–344. DOI: 10.1016/j.micromeso.2009.06.006.

Clark A. (1970) *The theory of adsorption and catalysis.* Academic Press, New York, NY.

Darken L.S. (1948) Diffusion, Mobility, and Their Interrelation Through Free Energy in Binary Metallic Systems. *Trans. AIME,* **175,** 184ff.

Dawoud B., Vedder U., Amer E.-H. & Dunne S. (2007) Non-isothermal adsorption kinetics of water vapour into a consolidated zeolite layer. *International Journal of Heat and Mass Transfer,* **50,** 2190–2199. DOI: 10.1016/j.ijheatmasstransfer.2006.10.052.

Deng J., Wang R.Z. & Han G.Y. (2011) A review of thermally activated cooling technologies for combined cooling, heating and power systems. *Progress in Energy and Combustion Science,* **37,** 172–203. DOI: 10.1016/j.pecs.2010.05.003.

Dubinin M.M. (1975) Physical Adsorption of Gases and Vapors in Micropores. In: *Progress in Surface and Membrane Science: Volume 9* (ed. by D.A. Cadenhead, J.F. Danielli & M.D. Rosenberg), pp. 1–70. Elsevier Science, Burlington.

Dubinin M.M. & Astakhov V.A. (1971) Description of Adsorption Equilibria of Vapors on Zeolites over Wide Ranges of Temperature and Pressure. In: *Molecular sieve zeolites. 2: International conference on molecular sieves 2* (ed. by E.M. Flanigen & L.B. Sand), pp. 69–85. American Chemical Society, Washington, D.C.

Elsayed E., AL-Dadah R., Mahmoud S., Elsayed A. & Anderson P.A. (2016) Aluminium fumarate and CPO-27(Ni) MOFs: Characterization and thermodynamic analysis for adsorption heat pump applications. *Applied Thermal Engineering,* **99,** 802–812. DOI: 10.1016/j.applthermaleng.2016.01.129.

Elzhov T.V., Mullen K.M., Spiess A.-N. & Bolker B. (2016) minpack.lm: R Interface to the Levenberg-Marquardt Nonlinear Least-Squares Algorithm Found in MINPACK, Plus Support for Bounds. URL https://CRAN.R-project.org/package=minpack.lm [accessed on 25 January 2021].

Frazzica A., Füldner G., Sapienza A., Freni A. & Schnabel L. (2014) Experimental and theoretical analysis of the kinetic performance of an adsorbent coating composition for use in adsorption chillers and heat pumps. *Applied Thermal Engineering,* **73,** 1022–1031. DOI: 10.1016/j.applthermaleng.2014.09.004.

Freni A., Dawoud B., Bonaccorsi L., Chmielewski S., Frazzica A., Calabrese L. & Restuccia G. (2015) Adsorption Heat Exchangers. In: *Characterization of zeolite-based coatings for adsorption heat pumps* (ed. by A. Freni), pp. 35–53. Springer, Cham.

Freni A., Sapienza A., Glaznev I.S., Aristov Y.I. & Restuccia G. (2012) Experimental testing of a lab-scale adsorption chiller using a novel selective water sorbent “silica modified by calcium nitrate”. *International Journal of Refrigeration,* **35,** 518–524. DOI: 10.1016/j.ijrefrig.2010.05.015.

Fubini B. (1988) Adsorption calorimetry in surface chemistry. *Thermochimica Acta,* **135,** 19–29. DOI: 10.1016/0040-6031(88)87364-7.

Füldner G. (2015) *Stofftransport und Adsorptionskinetik in porösen Adsorbenskompositen für Wärmetransformationsanwendungen.* Doctoral dissertation, Universiät Freiburg.

Fumey B., Weber R. & Baldini L. (2019) Sorption based long-term thermal energy storage – Process classification and analysis of performance limitations: A review. *Renewable and Sustainable Energy Reviews,* **111,** 57–74. DOI: 10.1016/j.rser.2019.05.006.

Giesy T.J. (2014) *Characterization of Mass Transfer in Adsorbents for Use in Oxygen Separation from Air.* Doctoral dissertation, Vanderbilt University.

Giesy T.J. & LeVan M.D. (2013) Mass transfer rates of oxygen, nitrogen, and argon in carbon molecular sieves determined by pressure-swing frequency response. *Chemical Engineering Science,* **90,** 250–257. DOI: 10.1016/j.ces.2012.12.029.

Giesy T.J., Wang Y. & LeVan M.D. (2012) Measurement of Mass Transfer Rates in Adsorbents: New Combined-Technique Frequency Response Apparatus and Application to CO_2 in 13X Zeolite. *Industrial & Engineering Chemistry Research,* **51,** 11509–11517. DOI: 10.1021/ie3014204.

Glaznev I.S. & Aristov Y. (2008) Kinetics of water adsorption on loose grains of SWS-1L under isobaric stages of adsorption heat pumps: The effect of residual air. *International Journal of Heat and Mass Transfer,* **51,** 5823–5827. DOI: 10.1016/j.ijheatmasstransfer.2008.04.061.

Glueckauf E. (1955) Theory of chromatography. Part 10.—Formulæ for diffusion into spheres and their application to chromatography. *Trans. Faraday Soc.,* **51,** 1540–1551. DOI: 10.1039/TF9555101540.

Glueckauf E. & Coates J.I. (1947) 241. Theory of chromatography. Part IV. The influence of incomplete equilibrium on the front boundary of chromatograms and on the effectiveness of separation. *J. Chem. Soc.,* 1315–1321. DOI: 10.1039/JR9470001315.

Gordeeva L.G. & Aristov Y.I. (2012) Composites ‘salt inside porous matrix’ for adsorption heat transformation: a current state-of-the-art and new trends. *International Journal of Low-Carbon Technologies,* **7,** 288–302. DOI: 10.1093/ijlct/cts050.

Graf S., Eibel S., Lanzerath F. & Bardow A. (2020) Validated Performance Prediction of Adsorption Chillers: Bridging the Gap from Gram-Scale Experiments to Full-Scale Chillers. *Energy Technology,* 1901130. DOI: 10.1002/ente.201901130.

Graf S., Lanzerath F., Sapienza A., Frazzica A., Freni A. & Bardow A. (2016) Prediction of SCP and COP for adsorption heat pumps and chillers by combining the large-temperature-jump method and dynamic modeling. *Applied Thermal Engineering,* **98,** 900–909. DOI: 10.1016/j.applthermaleng.2015.12.002.

Gurgel J.M., Filho L.A., Grenier P. & Meunier F. (2001) Thermal Diffusivity and Adsorption Kinetics of Silica-Gel/Water. *Adsorption,* **7,** 211–219. DOI: 10.1023/A:1012732817374.

Gustavsson M., Karawacki E. & Gustafsson S.E. (1994) Thermal conductivity, thermal diffusivity, and specific heat of thin samples from transient measurements with hot disk sensors. *Review of Scientific Instruments,* **65,** 3856–3859. DOI: 10.1063/1.1145178.

Hall B.D. (2004) On the propagation of uncertainty in complex-valued quantities. *Metrologia,* **41,** 173–177. DOI: 10.1088/0026-1394/41/3/010.

Hall B.D. (2007) Some considerations related to the evaluation of measurement uncertainty for complex-valued quantities in radio frequency measurements. *Metrologia,* **44,** L62-L67. DOI: 10.1088/0026-1394/44/6/N04.

Handy B.E., Sharma S.B., Spiewak B.E. & Dumesic J.A. (1993) A Tian-Calvet heat-flux microcalorimeter for measurement of differential heats of adsorption. *Measurement Science and Technology,* **4,** 1350–1356. DOI: 10.1088/0957-0233/4/12/007.

Hauer A. (2002) *Beurteilung fester Adsorbentien in offenen Sorptionssystemen für energetische Anwendungen.* Doctoral dissertation, Technische Universität Berlin.

Henninger S.K. (2008) *Untersuchungen von Neuen Hochporösen Sorptionsmaterialien für Wärmetransformationsanwendungen.* Dissertation, Universität Freiburg.

Henninger S.K., Ernst S.-J., Gordeeva L., Bendix P., Fröhlich D., Grekova A.D., Bonaccorsi L., Aristov Y. & Jaenchen J. (2017) New materials for adsorption heat transformation and storage. *Renewable Energy,* **110,** 59–68. DOI: 10.1016/j.renene.2016.08.041.

Henninger S.K., Jeremias F., Kummer H. & Janiak C. (2012) MOFs for Use in Adsorption Heat Pump Processes. *European Journal of Inorganic Chemistry,* **2012,** 2625–2634. DOI: 10.1002/ejic.201101056.

Hossain M.I. & Glover T.G. (2019) Kinetics of Water Adsorption in UiO-66 MOF. *Industrial & Engineering Chemistry Research,* **58,** 10550–10558. DOI: 10.1021/acs.iecr.9b00976.

IEA (2012) Technology Roadmap - Solar Heating and Cooling. Paris. URL https://www.iea.org/reports/technology-roadmap-solar-heating-and-cooling [accessed on 23 October 2020].

IEA (2018) The Future of Cooling: Opportunities for energy-efficient air conditioning. Paris. URL https://webstore.iea.org/download/direct/1036 [accessed on 23 October 2020].

Iglesia E. & Reyes S.C. (1994) Frequency Response Techniques for the Characterization of Porous Catalytic Solids. In: *Catalysis, Specialist Periodical Reports* (ed. by J.J. Spivey, S.K. Agarwal & H.H. Kung). Royal Society of Chemistry, Cambridge.

Jänchen J., Ackermann D., Weiler E., Stach H. & Brösicke W. (2005) Calorimetric investigation on zeolites, $AlPO_4$'s and $CaCl_2$ impregnated attapulgite for thermochemical storage of heat. *Thermochimica Acta,* **434,** 37–41. DOI: 10.1016/j.tca.2005.01.009.

JCGM (2008) Guide to the expression of uncertainty in measurement - GUM 1995 with minor corrections. Joint Committee for Guides in Metrology (BIPM, IEC, IFCC, ILAC, ISO, IUPAC, IUPAP and OIML).

Jeremias F., Fröhlich D., Janiak C. & Henninger S.K. (2014) Advancement of sorption-based heat transformation by a metal coating of highly-stable, hydrophilic aluminium fumarate MOF. *RSC Advances,* **4,** 24073–24082. DOI: 10.1039/C4RA03794D.

Jordi R.G. & Do D.D. (1993) Analysis of the Frequency Response Method for Sorption Kinetics in Bidispersed Structured Sorbents. *Chemical Engineering Science,* **6,** 1103–1130. DOI: 10.1016/0009-2509(93)81040-3.

Kaganer M.G. (1969) *Thermal Insulation in Cryogenic Engineering.* Israel Program for Scientific Transl., Jerusalem.

Kärger J., Ruthven D.M. & Theodorou D.N. (2012) *Diffusion in nanoporous materials.* John Wiley & Sons, Hoboken.

Kärger J., Vasenkov S. & Auerbach S.M. (2003) Diffusion in Zeolites. In: *Handbook of zeolite science and technology* (ed. by K.A. Carrado, P.K. Dutta & S.M. Auerbach). M. Dekker, New York.

Karmakar S., Dechnik J., Janiak C. & De S. (2016) Aluminium fumarate metal-organic framework: A super adsorbent for fluoride from water. *Journal of hazardous materials,* **303,** 10–20. DOI: 10.1016/j.jhazmat.2015.10.030.

Kast W. (1988) *Adsorption aus der Gasphase: Ingenieurwissenschaftliche Grundlagen und technische Verfahren.* VCH, Weinheim.

Kiener C., Müller U. & Schubert M. (2009) Organometallic Aluminum Fumerate Backbone Material.

Kolokathis P.D. (2020) Personal Communication: Density calculation from atomic structure.

Kummer H., Baumgartner M., Hügenell P., Fröhlich D., Henninger S.K. & Gläser R. (2017a) Thermally driven refrigeration by methanol adsorption on coatings of HKUST-1 and

MIL-101(Cr). *Applied Thermal Engineering,* **117,** 689–697. DOI: 10.1016/j.applthermaleng.2016.11.026.

Kummer H., Füldner G. & Henninger S.K. (2015) Versatile siloxane based adsorbent coatings for fast water adsorption processes in thermally driven chillers and heat pumps. *Applied Thermal Engineering,* **85,** 1–8. DOI: 10.1016/j.applthermaleng.2015.03.042.

Kummer H., Jeremias F., Warlo A., Füldner G., Fröhlich D., Janiak C., Gläser R. & Henninger S.K. (2017b) A Functional Full-Scale Heat Exchanger Coated with Aluminum Fumarate Metal–Organic Framework for Adsorption Heat Transformation. *Industrial & Engineering Chemistry Research,* **56,** 8393–8398. DOI: 10.1021/acs.iecr.7b00106.

Langmuir I. (1918) The Adsorption of Gases on plane Surfaces of Glass, Mica and Platium. *Journal of the American Chemical Society,* **40,** 1361–1403. DOI: 10.1021/ja02242a004.

Lanzerath F. (2013) *Modellgestützte Entwicklung von Adsorptionswärmepumpen.* Doctoral dissertation, RWTH Aachen.

Lasia A. (2014) *Electrochemical Impedance Spectroscopy and its Applications.* Springer, New York.

Laurenz E. (2012) *Untersuchung der Relevanz von Wärme- und Stofftransportparametern einzelner Komponenten für die Optimierung einer Adsorptionswärmepumpe.* Diplomarbeit, TU Hamburg-Harburg.

Laurenz E., Füldner G. & Schnabel L. (2014) Heat Transfer in Adsorption Heat Exchangers between Fins and Monolayer Pellet Beds. In: *Proceedings of the Comsol Conference 2014* (ed. by COMSOL Inc.). Cambridge.

Laurenz E., Füldner G. & Schnabel L. (2016) Assessment of thermodynamic equilibrium properties of salt hydrates for heat transformation applications at different temperature levels. In: *Proceedings of the Heat Powered Cycles Conference 2016.* Nottingham, 2016-06.

Laurenz E., Füldner G., Schnabel L. & Schmitz G. (2020) A Novel Approach for the Determination of Sorption Equilibria and Sorption Enthalpy Used for MOF Aluminium Fumarate with Water. *Energies,* **13,** 3003. DOI: 10.3390/en13113003.

Laurenz E., Füldner G., Velte A., Schnabel L. & Schmitz G. (2021) Frequency response analysis for the determination of thermal conductivity and water transport in MOF adsorbent coatings for heat transformation. *International Journal of Heat and Mass Transfer,* **169,** 120921. DOI: 10.1016/j.ijheatmasstransfer.2021.120921.

Laurenz E., Velte A., Kummer H., Füldner G. & Schnabel L. (2019) Adsorption dynamics of MOF coatings for waste heat driven cooling. In: *Proceedings of the 25th IIR International Congress of Refrigeration* (ed. by International Institute of Refrigeration (IIR)). Montréal, Canada, August 24-30. France.

Lenzen D., Zhao J., Ernst S.-J., Wahiduzzaman M., Ken Inge A., Fröhlich D., Xu H., Bart H.-J., Janiak C., Henninger S., Maurin G., Zou X. & Stock N. (2019) A metal-organic framework for efficient water-based ultra-low-temperature-driven cooling. *Nature communications,* **10,** 3025. DOI: 10.1038/s41467-019-10960-0.

Levenberg K. (1944) A method for the solution of certain non-linear problems in least squares. *Quarterly of Applied Mathematics,* **2,** 164–168. DOI: 10.1090/qam/10666.

Llano-Restrepo M. & Mosquera M.A. (2009) Accurate correlation, thermochemistry, and structural interpretation of equilibrium adsorption isotherms of water vapor in zeolite 3A by means of a generalized statistical thermodynamic adsorption model. *Fluid Phase Equilibria,* **283,** 73–88. DOI: 10.1016/j.fluid.2009.06.003.

Marquardt D.W. (1963) An Algorithm for Least-Squares Estimation of Nonlinear Parameters. *Journal of the Society for Industrial and Applied Mathematics,* **11,** 431–441. DOI: 10.1137/0111030.

Marsili-Libelli S. (2016) *Environmental Systems Analysis with MATLAB®.* CRC Press, Boca Raton.

Marsili-Libelli S., Guerrizio S. & Checchi N. (2003) Confidence regions of estimated parameters for ecological systems. *Ecological Modelling,* **165,** 127–146. DOI: 10.1016/S0304-3800(03)00068-1.

Matsumoto M. & Nishimura T. (1998) Mersenne twister: a 623-dimensionally equidistributed uniform pseudo-random number generator. *ACM Transactions on Modeling and Computer Simulation,* **8,** 3–30. DOI: 10.1145/272991.272995.

Metcalf S.J., Critoph R.E. & Tamainot-Telto Z. (2012) Optimal cycle selection in carbon-ammonia adsorption cycles. *International Journal of Refrigeration,* **35,** 571–580. DOI: 10.1016/j.ijrefrig.2011.11.006.

Meunier F. (2013) Adsorption heat powered heat pumps. *Applied Thermal Engineering,* **61,** 830–836. DOI: 10.1016/j.applthermaleng.2013.04.050.

Mohammad Iftekhar Hossain (2014) *Volume Swing Frequency Response Method For Determining Mass Transfer Mechanisms in Microporous Adsorbents.* Doctoral dissertation, University of South Carolina - Columbia.

Naphtali L.M. & Polinski L.M. (1963) A Novel Technique for Characterization of Adsorption Rates on Heterogeneous Surfaces. *The Journal of Physical Chemistry,* **67,** 369–375. DOI: 10.1021/j100796a038.

Núñez T. (2001) *Charakterisierung und Bewertung von Adsorbentien für Wärmetransformationsanwendungen.* Doctoral dissertation, Albert-Ludwigs-Universität.

Ovoshchnikov D.S., Glaznev I.S. & Aristov Y.I. (2011) Water sorption by the calcium chloride/silica gel composite: The accelerating effect of the salt solution present in the pores. *Kinetics and Catalysis,* **52,** 620–628. DOI: 10.1134/S0023158411040124.

Pang S.C., Masjuki H.H., Kalam M.A. & Hazrat M.A. (2013) Liquid absorption and solid adsorption system for household, industrial and automobile applications: A review. *Renewable and Sustainable Energy Reviews,* **28,** 836–847. DOI: 10.1016/j.rser.2013.08.029.

Parker W.J., Jenkins R.J., Butler C.P. & Abbott G.L. (1961) Flash Method of Determining Thermal Diffusivity, Heat Capacity, and Thermal Conductivity. *Journal of Applied Physics,* **32,** 1679–1684. DOI: 10.1063/1.1728417.

Pillai R.S. & Jasra R.V. (2010) Computational Study for Water Sorption in $AlPO_4$-5 and $AlPO_4$-11 Molecular Sieves. *Langmuir,* **26,** 1755–1764. DOI: 10.1021/la902629g.

Pinheiro J.M., Salústio S., Rocha J., Valente A.A. & Silva C.M. (2020) Adsorption heat pumps for heating applications. *Renewable and Sustainable Energy Reviews,* **119,** 109528. DOI: 10.1016/j.rser.2019.109528.

Pinheiro J.M., Salústio S., Valente A.A. & Silva C.M. (2018) Adsorption heat pump optimization by experimental design and response surface methodology. *Applied Thermal Engineering,* **138,** 849–860. DOI: 10.1016/j.applthermaleng.2018.03.091.

Pires J., Cavalho M.B. de, Carvalho A.P., Guil J.M. & Perdigón-Melón J.A. (2000) Heats of Adsorption of N-Hexane by Thermal Gravimetry with Differential Scanning Calorimetry (TG-DSC): A Tool for Textural Characterization of Pillared Clays. *Clays and Clay Minerals,* **48,** 385–391. DOI: 10.1346/CCMN.2000.0480309.

Qinglin H., Sundaram S.M. & Farooq S. (2003) Revisiting Transport of Gases in the Micropores of Carbon Molecular Sieves. *Langmuir,* **19,** 393–405. DOI: 10.1021/la026451+.

Qiu S., Pang W., Kessler H. & Guth J.-L. (1989) Synthesis and structure of the $[AlPO_4]_{12}$ Pr_4NF molecular sieve with AFI structure. *Zeolites,* **9,** 440–444. DOI: 10.1016/0144-2449(89)90101-2.

R Core Team (2020) R: A Language and Environment for Statistical Computing. R Foundation for Statistical Computing, Vienna, Austria. URL https://www.R-project.org/.

Reyes S.C., Sinfelt J.H., DeMartin G.J., Ernst R.H. & Iglesia E. (1997) Frequency modulation methods for diffusion and adsorption measurements in porous solids. *The Journal of Physical Chemistry B,* **101,** 614–622. DOI: 10.1021/jp961036+.

Ridler N.M. & Salter M.J. (2002) An approach to the treatment of uncertainty in complex S-parameter measurements. *Metrologia,* **39,** 295. DOI: 10.1088/0026-1394/39/3/6.

Riffel D.B., Wittstadt U., Schmidt F.P., Núñez T., Belo F.A., Leite A.P. & Ziegler F. (2010) Transient modeling of an adsorber using finned-tube heat exchanger. *International Journal of Heat and Mass Transfer,* **53,** 1473–1482. DOI: 10.1016/j.ijheatmasstransfer.2009.12.001.

Rigaud L., Kindbeiter F. & Tadiotto D. (2015) Solution innovante pour la logistique à température dirigée: Production de froid autonome par procédé thermochimique solide-gaz. *Revue générale du Froid et du Conditionnement d'air,* **104,** 47–53.

Rouquerol F., Rouquerol J. & Sing K.S. (2014) Thermodynamics of Adsorption at the Gas/Solid Interface. In: *Adsorption by powders and porous solids: Principles, methodology and applications* (ed. by F. Rouquerol), pp. 25–56. Elsevier/Academic Press, Amsterdam.

Rouquerol F., Rouquerol J. & Sing K.S.W. (2002) The Experimental Approach. In: *Handbook of Porous Solids* (ed. by F. Schüth, K.S. Sing & J. Weitkamp), pp. 236–275. Wiley, Weinheim.

Rouquerol J., Avnir D., Fairbridge C.W., Everett D.H., Haynes J.M., Pernicone N., Ramsay J.D.F., Sing K.S.W. & Unger K.K. (1994) Recommendations for the characterization of porous solids (Technical Report). *Pure and Applied Chemistry,* **66,** 1739–1758. DOI: 10.1351/pac199466081739.

Rouquerol J. & Rouquerol F. (2014) Methodology of Gas Adsorption. In: *Adsorption by powders and porous solids: Principles, methodology and applications* (ed. by F. Rouquerol), pp. 57–104. Elsevier/Academic Press, Amsterdam.

Roustant O., Ginsbourger D. & Deville Y. (2012) DiceKriging, DiceOptim: Two R Packages for the Analysis of Computer Experiments by Kriging-Based Metamodeling and Optimization. *Journal of Statistical Software,* **51,** 1–55.

Sapienza A., Frazzica A., Freni A. & Aristov Y. (2016) Dramatic effect of residual gas on dynamics of isobaric adsorption stage of an adsorptive chiller. *Applied Thermal Engineering,* **96,** 385–390. DOI: 10.1016/j.applthermaleng.2015.09.031.

Sapienza A., Santamaria S., Frazzica A., Freni A. & Aristov Y.I. (2014) Dynamic study of adsorbers by a new gravimetric version of the Large Temperature Jump method. *Applied Energy,* **113,** 1244–1251. DOI: 10.1016/j.apenergy.2013.09.005.

Schicktanz M. & Núñez T. (2009) Modelling of an adsorption chiller for dynamic system simulation. *International Journal of Refrigeration,* **32,** 588–595. DOI: 10.1016/j.ijrefrig.2009.02.011.

Schnabel L. (2009) *Experimentelle und numerische Untersuchung der Adsorptionskinetik von Wasser an Adsorbens-Metallverbundstrukturen.* Doctoral dissertation, TU Berlin.

Schnabel L., Füldner G., Velte A., Laurenz E., Bendix P., Kummer H. & Wittstadt U. (2018) Innovative Adsorbent Heat Exchangers: Design and Evaluation. In: *Innovative Heat Exchangers* (ed. by H.-J. Bart & S. Scholl), pp. 363–394. Springer International Publishing, Cham.

Schnabel L., Tatlier M., Schmidt F. & Erdem-Şenatalar A. (2010) Adsorption kinetics of zeolite coatings directly crystallized on metal supports for heat pump applications (adsorption kinetics of zeolite coatings). *Applied Thermal Engineering,* **30,** 1409–1416. DOI: 10.1016/j.applthermaleng.2010.02.030.

Schwamberger V. & Schmidt F.P. (2013) Estimating the Heat Capacity of the Adsorbate–Adsorbent System from Adsorption Equilibria Regarding Thermodynamic Consistency. *Industrial & Engineering Chemistry Research,* **52,** 16958–16965. DOI: 10.1021/ie4011832.

Shah R.K. & Sekuli D.P. (2003) *Fundamentals of Heat Exchanger Design.* John Wiley & Sons, Inc, Hoboken, NJ, USA.

Shen D. & Rees L.V.C. (1994) Study of fast diffusion in zeolites using a higher harmonic frequency response method. *Journal of the Chemical Society, Faraday Transactions,* **90,** 3011–3015. DOI: 10.1039/FT9949003011.

Song L. & Rees L.V.C. (2008) Frequency Response Measurements of Diffusion in Microporous Materials. In: *Adsorption and diffusion* (ed. by H.G. Karge & J. Weitkamp), pp. 235–276. Springer, Berlin.

Splith T., Fröhlich D., Henninger S.K. & Stallmach F. (2018) Development and application of an exchange model for anisotropic water diffusion in the microporous MOF aluminum fumarate. *Journal of magnetic resonance,* **291,** 40–46. DOI: 10.1016/j.jmr.2018.04.009.

Splith T., Pantatosaki E., Kolokathis P.D., Fröhlich D., Zhang K., Füldner G., Chmelik C., Jiang J., Henninger S.K., Stallmach F. & Papadopoulos G.K. (2017) Molecular Dynamics Phenomena of Water in the Metalorganic Framework MIL-100(Al), as Revealed by Pulsed Field Gradient NMR and Atomistic Simulation. *The Journal of Physical Chemistry C,* **121,** 18065–18074. DOI: 10.1021/acs.jpcc.7b06240.

Stryi-Hipp G. & Dias P. (2014) Solar Heating and Cooling Technology Roadmap. European Technology Platform on Renewable Heating and Cooling, Brussels. URL https://www.rhc-platform.org/content/uploads/2019/05/Solar_Thermal_Roadmap.pdf [accessed on 23 October 2020].

Sun L.M. & Bourdin V. (1993) Measurement of Intracrystalline Diffusion by the Frequency Response Method: Analysis and Interpretation of Bimodal Response Curves. *Chemical Engineering Science,* **22,** 3783–3793.

Sun L.M. & Meunier F. (1987) A detailed model for nonisothermal sorption in porous adsorbents. *Chemical Engineering Science,* **42,** 1585–1593. DOI: 10.1016/0009-2509(87)80163-X.

Sun L.M., Meunier F., Grenier P. & Ruthven D.M. (1994) Frequency response for nonisothermal adsorption in biporous pellets. *Chemical Engineering Science,* **49,** 373–381. DOI: 10.1016/0009-2509(94)87008-X.

Sun L.M., Meunier F. & Kärger J. (1993) On the heat effect in measurements of sorption kinetics by the frequency response method. *Chemical Engineering Science,* **48,** 715–722. DOI: 10.1016/0009-2509(93)80138-G.

Sward B.K. & LeVan M.D. (2003) Frequency Response Method for Measuring Mass Transfer Rates in Adsorbents via Pressure Perturbation. *Adsorption,* **9,** 37–54. DOI: 10.1023/A:1023863213893.

Tamainot-Telto Z. & Critoph R.E. (2001) Monolithic carbon for sorption refrigeration and heat pump applications. *Applied Thermal Engineering,* **21,** 37–52. DOI: 10.1016/S1359-4311(00)00030-2.

Teng W.S., Leong K.C. & Chakraborty A. (2016) Revisiting adsorption cooling cycle from mathematical modelling to system development. *Renewable and Sustainable Energy Reviews,* **63,** 315–332. DOI: 10.1016/j.rser.2016.05.059.

Tian M. (1923) Utilisation de la méthode calorimétrique en dynamique chimique: emploi d'un micro-calorimétre á compensation. *Bulletin de la Société Chimique de France,* **33,** 427–428.

Tierney M., Ketteringham L., Selwyn R. & Saidani H. (2016) Calorimetric measurements of the dynamics of a finned adsorbent: early assessment of the activated carbon cloth–ethanol pair with prismatic aluminium fins. *Applied Thermal Engineering,* **93,** 1264–1272. DOI: 10.1016/j.applthermaleng.2015.10.009.

Tokarev M.M. & Aristov Y. (2017) A new version of the Large Temperature Jump method: The thermal response (T–LTJ). *Energy,* **140,** 481–487. DOI: 10.1016/j.energy.2017.08.093.

Turner M.D., Capron L., Laurence R.L. & Conner W.C. (2001) The design and construction of a frequency response apparatus to investigate diffusion in zeolites. *Review of Scientific Instruments,* **72,** 4424–4433. DOI: 10.1063/1.1408931.

Uddin K., Amirul Islam M., Mitra S., Lee J., Thu K., Saha B.B. & Koyama S. (2018) Specific heat capacities of carbon-based adsorbents for adsorption heat pump application. *Applied Thermal Engineering,* **129,** 117–126. DOI: 10.1016/j.applthermaleng.2017.09.057.

Velte A. (2019) *Experimentelle Arbeiten und Entwicklung von numerischen Modellen zur Analyse und Optimierung von erweiterten Adsorptionskreisläufen für die Wärmeversorgung von Gebäuden.* Doctoral dissertation, Universiät Freiburg.

Velte A., Füldner G., Laurenz E. & Schnabel L. (2017) Advanced Measurement and Simulation Procedure for the Identification of Heat and Mass Transfer Parameters in Dynamic Adsorption Experiments. *Energies,* **10,** 1130. DOI: 10.3390/en10081130.

Velte A., Munz G., Bendix P., Baumgartner M., Ernst S.-J., Hügenell P.P. & Henninger S. (2018) MAKSORE: Materialien und Komponenten für Sorptionswärmespeicher mit hoher Energiedichte, Schlussbericht (Final Report). Fraunhofer-Institut für Solare Energiesysteme (ISE), Freiburg im Breisgau. DOI: 10.2314/KXP:1670261913.

Vučelić V. & Vučelić D. (1983) The heat capacity of water near solid surfaces. *Chemical Physics Letters,* **102,** 371–374. DOI: 10.1016/0009-2614(83)87058-4.

Wagner W., Cooper J.R., Dittmann A., Kijima J., Kretzschmar H.-J., Kruse A., Mareš R., Oguchi K., Sato H., Stöcker I., Šifner O., Takaishi Y., Tanishita I., Trübenbach J. & Willkommen T. (2000) The IAPWS Industrial Formulation 1997 for the Thermodynamic Properties of Water and Steam. *Journal of Engineering for Gas Turbines and Power,* **122,** 150. DOI: 10.1115/1.483186.

Walton K.S. & LeVan M.D. (2005) Adsorbed-Phase Heat Capacities: Thermodynamically Consistent Values Determined from Temperature-Dependent Equilibrium Models. *Industrial & Engineering Chemistry Research,* **44,** 178–182. DOI: 10.1021/ie049394j.

Wang D.C., Li Y.H., Li D., Xia Y.Z. & Zhang J.P. (2010) A review on adsorption refrigeration technology and adsorption deterioration in physical adsorption systems. *Renewable and Sustainable Energy Reviews,* **14,** 344–353. DOI: 10.1016/j.rser.2009.08.001.

Wang L., Zhu D. & Tan Y. (1999) Heat Transfer Enhancement of the Adsorber of an Adsorption Heat Pump. *Adsorption,* **5,** 279–286. DOI: 10.1023/A:1008964013879.

Wang L.W., Wang R.Z. & Oliveira R.G. (2009) A review on adsorption working pairs for refrigeration. *Renewable and Sustainable Energy Reviews,* **13,** 518–534. DOI: 10.1016/j.rser.2007.12.002.

Wang Y. & LeVan M.D. (2008) Nanopore Diffusion Rates for Adsorption Determined by Pressure-Swing and Concentration-Swing Frequency Response and Comparison with Darken's Equation. *Industrial & Engineering Chemistry Research,* **47,** 3121–3128. DOI: 10.1021/ie070673r.

Wang Y. & LeVan M.D. (2011) Master curves for mass transfer in bidisperse adsorbents for pressure-swing and volume-swing frequency response methods. *AIChE Journal,* **57,** 2054–2069. DOI: 10.1002/aic.12420.

Wicke E. & Kallenbach R. (1941) Die Oberflächendiffusion von Kohlendioxyd in aktiven Kohlen. *Kolloid-Zeitschrift,* **97,** 135–151. DOI: 10.1007/BF01502640.

Wilde T., Ott M., Auweter A., Meijer I., Ruch P., Hilger M., Kuhnert S. & Huber H. (2017) CooLMUC-2: A supercomputing cluster with heat recovery for adsorption cooling. In: *Proceedings of the 33rd Thermal Measurement, Modeling & Management Symposium (SEMI-THERM)* (ed. by IEEE), pp. 115–121. San Jose, CA, USA.

Wittstadt U. (2018) *Experimentelle und modellgestützte Charakterisierung von Adsorptionswärmeübertragern.* Doctoral dissertation, Technische Universität Berlin.

Wittstadt U., Füldner G., Andersen O., Herrmann R. & Schmidt F. (2015) A New Adsorbent Composite Material Based on Metal Fiber Technology and Its Application in Adsorption Heat Exchangers. *Energies,* **8,** 8431–8446. DOI: 10.3390/en8088431.

Wittstadt U., Füldner G., Laurenz E., Warlo A., Große A., Herrmann R., Schnabel L. & Mittelbach W. (2017) A novel adsorption module with fiber heat exchangers: Performance analysis based on driving temperature differences. *Renewable Energy,* **110,** 154–161. DOI: 10.1016/j.renene.2016.08.061.

Wittstadt U., Laurenz E., Füldner G. & Schnabel L. (2014) A 2D Model of a Fin-Tube Adsorption Heat Exchanger. In: *Proceedings of the International Sorption Heat Pump Conference (ISHPC 2014).* College Park, Maryland, USA. Curran, Red Hook, NY.

Yasuda Y. (1982) Determination of vapor diffusion coefficients in zeolite by the frequency response method. *The Journal of Physical Chemistry,* **86,** 1913–1917. DOI: 10.1021/j100207a036.

Yong L. & Sumathy K. (2002) Review of mathematical investigation on the closed adsorption heat pump and cooling systems. *Renewable and Sustainable Energy Reviews,* **6,** 305–338. DOI: 10.1016/S1364-0321(02)00010-2.

Ziegler F. (1999) Recent developments and future prospects of sorption heat pump systems. *International Journal of Thermal Sciences,* **38,** 191–208. DOI: 10.1016/S1290-0729(99)80083-0.

Zimmermann S., Meijer I., Tiwari M.K., Paredes S., Michel B. & Poulikakos D. (2012) Aquasar: A hot water cooled data center with direct energy reuse. *Energy,* **43,** 237–245. DOI: 10.1016/j.energy.2012.04.037.